2018

Experimental Investigation of Advanced Ignition Systems for High Efficiency Combustion

Bader Almansour
University of Central Florida

EXPERIMENTAL INVESTIGATION OF ADVANCED IGNITION SYSTEMS FOR HIGH EFFICIENCY COMBUSTION

by

BADER ALMANSOUR

M.S. University of Central Florida, 2015

M.Eng. University of Leeds, 2010

B.Sc. Kuwait University, 2004

A dissertation submitted in partial fulfillment of the requirements
for the degree of Doctor of Philosophy
in the Department of Mechanical and Aerospace Engineering
in the College of Engineering and Computer Science
at the University of Central Florida
Orlando, Florida

Spring Term

2018

Major Professor: Subith S. Vasu

ABSTRACT

Consumption of fossil and bio-derived fuels is growing due to energy demands associated with increase in population and standard of living across the globe. Power generation and transportation sectors are the primary two sources of fuel consumption, which have raised the demand for crude oil and led to serious environmental pollution issues. This demand for energy forced various government agencies to strengthen the allowable exhaust pollutant concentration limits. Recently, CO, CO_2, particulate matter, and nitrogen oxides (NO_x) emission restrictions have become more stringent to the extent that engines must operate at higher energy densities and efficiencies. Towards this goal, this doctoral study focused on evaluating advanced ignition systems and testing new biofuels for automotive combustion applications. First, a natural gas lean combustion mode was assessed by using advance ignition systems to provide higher brake power while maintaining the exhaust limits. A rigorous combustion data analysis was performed to identify the main reasons leading to improved performance in the case of prechamber equipped laser ignition. An overall efficiency improvement of 2.1% points was observed, compared to spark ignition, which in turn leads to save 633 PJ per year. In the second part of this dissertation, a spherical chamber was designed and validated to measure the laminar burning velocity (LBV) of a promising biofuel: 2,4-Dimethyl-3-pentanone, (DIPK), for homogenous charge compression ignition engines. LBV measurements were carried out with various diluent species (N_2, Ar, and He) in order to provide several data points for development and validation of DIPK chemical kinetic mechanisms. It has been found that DIPK does not only have higher temperature and pressure sensitivities (compared to iso-octane), but additionally enabled a faster laminar burning velocity which leads to higher rate of heat release in reciprocating engines.

ACKNOWLEDGMENTS

First and foremost, I would like to thank my wife Sara for her love, encouragement and quiet patience during my doctorate study. Her support during the last five years of my life by taking care of my kids while I was away doing experiments is unforgettable; words cannot express how grateful I am to you.

It is with immense gratitude that I acknowledge the support and help of my advisors, Dr. Subith Vasu, and Dr. Sreenath Gupta for their guidance, valuable advices, and steadfast encouragement. This study would not have been possible without their useful insights and help. I also would like to thank my dissertation committee members, Dr. Mani Sarathy, Dr. Jayanta Kapat, and Dr. Alain Kassab for their willingness to be in my thesis committee, their time and effort to serve on my dissertation.

Also, I am grateful for all my past and present lab mates at the University of Central Florida for their valuable discussions throughout my doctorate study, especially those who helped during the spherical chamber assembly and experiments Anthony Terracciano, Luke Thompson, Joseph Lopez, Sami Alawadhi, Gihun Kim, Batikan Koroglu, Ghazal Barari, Owen Pryor, and Samuel Barak. Also, I would like to thank Tim Lindner, Robert Wong and Charles Price for their help in the spherical chamber and spark plug development. Finally, and most importantly, I would like to thank and dedicate this dissertation to my parents.

TABLE OF CONTENTS

LIST OF FIGURES

LIST OF TABLES

NOMENCLATURE

2P-LI	single-point 2 pulse laser ignition
A_f	flame surface area
ATDC	after top dead center
B_D	laser beam diameter
BMEP	brake mean effective pressure
BSCO	brake specific carbon monoxide
BSFC	brake specific fuel consumption
BSHC	brake specific hydrocarbons
$BSNO_x$	brake specific NO_x emission
BTDC	before top dead center
c_p	specific heat at constant pressure
c_v	specific heat at constant volume
CAD	crank angle degrees
CCD	combustion chamber deposits
CCS	carbon capture and storage
CDI	capacitance discharge ignition
CNG	compressed natural gas
COV	coefficnect of variation
CR	compression ratio
CV	constant volume
CW	continues wave
D	oxygen ratios
D_f	laser beam diameter within the focal region
d_m	diameter of unsupported area
DAQ	data acquisition
DIPK	2,4-Dimethyl-3-pentanone
E	internal energy
e	specific internal energy
E_p	laser pulse energy

EGR	exhaust gas recirculation
EPA	Enviromental Protection Agency
f	focal length
FWHM	full width at half maximum
HCCI	homogenous charge compression engine
HCEP	high efficiency side pump
I	laser intensity
I_{thr}	critical threshold value
IMEP	indicated mean effective pressure
IT	ignition timing
K	stretch rate
k	average heat conductivity
L	Markstein length
L_e	Lewis number
LBV	laminar burning velocity
LED	light emitting diode
LI	laser ignition
LOMP	location of maximum pressure
m	number of photons required for ionization
m	mass
M	total mass
M^2	beam quality factor
MBT	maximum brake torque
MFB	mass fraction burned
MIE	minimum ignition energy
MPE	minimum pulse energy
N_e	number of electrons
$N_{e,o}$	initial number of electrons
Nd:YAG	neodymium-doped yttrium aluminum garnet
P	pressure
PCLI	prechamber equipped laser ignition

PLNG	pipeline natural gas
PQL	passively Q-switched lasers
R	radius of the combustion chamber
R_f	flame radius
ROHR	rate of heat release
S	design safety factor
S_b	stretched flame speed
S_b^o	unstretched flame speed
S_u	stretched laminar burning velocity
S_u^o	laminar burning velocity
SAE	Society of Automotive Engineers
SDT	spectroscopy diagnostic techniques
SI	spark Ignition
T	temperature
T_f	kernel temperature
T_u	unburned gas temperature
t	time
t_d	minimum required window thickness
t_p	pulse duration
TDC	top dead center
TIT	turbine inlet temperature
U	velocity
UCF	University of Central Florida
UHC	unburned hydrocarbons
UV	ultraviolet
V	chamber volume
v	specific volume
v_d	diffusion rate of electrons escaping from the plasma
v_f	propagation velocity
VCSEL	vertical cavity surface emitting laser
X	mass fraction burned

Greek

η	efficiency
θ	divergence half angle
λ	wavelength
λ	excess air ratio
ρ_f	density
Φ	equivalence ratios
τ_e	time constant
δ_f	characteristic flame thickness
σ_{tf}	allowable tensile strength
γ	specific heat ratio
σ	density jump
δ_f	flame thickness

Subscripts

ad	adiabatic
b	burned mixture
e	equilibrium state
f	flame
i	initial condition
u	unburned mixture

CHAPTER 1: INTRODUCTION

1.1 Motivation

Tremendous development had been carried out for internal combustion engines since their invention in the 19th century. Strategies such as turbocharging [1], downsizing [2], variable valve timing [3], variable intake length [4], and direct injection systems [5] were used to increase the cyclic efficiency without compromising exhaust emissions. Even though a dramatic increase of engine efficiency has been achieved, the massive demand for the automotive application and power generation in our modern life forced the U.S. Environmental Protection Agency (EPA) to strengthen the allowable exhaust pollutant concentration limits. Recently, carbon monoxide, carbon dioxide, particulate matter, and NO_x emission restrictions have become more stringent to the extent that engines must operate at higher energy densities; and future requirements in 2025 of California State pushes the exhaust limit even further [6-8].

It is getting extremely challenging to improve reciprocating engine efficiency because of the limitations set by fuel properties, ignition strategies, and combustion stability. To meet some of these engineering challenges, the United States Department of Energy proposed the Co-Optimization (Co-Optima) project, where novel fuel formulations and combustion concepts are developed simultaneously to optimize engine operation at higher loads [9]. Towards this goal, this dissertation focused on the two aspects of Co-Optima program, testing new biofuels and investigating innovative engine strategies that deliver higher thermal efficiencies. First, natural gas lean combustion mode was assessed by using a prechamber equipped laser ignition (PCLI) to operate with leaner mixtures and provide higher brake power while maintaining the exhaust limits.

Second, a new combustion chamber was developed and validated to measure the laminar burning velocity of a promising biofuel for homogenous charge compression ignition engines (HCCI).

1.1.1 Internal Combustion Engine Research

Natural gas is a promising fuel to reduce exhaust gas emission (compared to coal and petroleum), exhibiting a low carbon to hydrogen ratio (1:3.89), and a high-octane number (RON $\geq$ 110). Those are needed properties to reduce CO_2 emissions and to operate at a higher load without engine knock. Recently, several natural gas shale reserves were found within the United States, and the extraction rate increased significantly since 2006 (see Figure 1.1A) [10]. Also, advancements in fuel cracking technology [11] and the implementation of natural gas distribution grids promote natural gas utilization over other energy resources. In fact, the latest Energy Information Agency report shows that the natural gas production is expected to account for 40% of U.S. production in 2040 [10]. Hence, natural gas availability and its excellent properties increased its consumption relative to other fuels in the past; and higher growth is predicted in the future as shown in Figure 1.1B. Clearly, there is a good market for natural gas reciprocating engines for automotive and power generation sectors; and improvement in engine efficiency is crucial of the path forward.

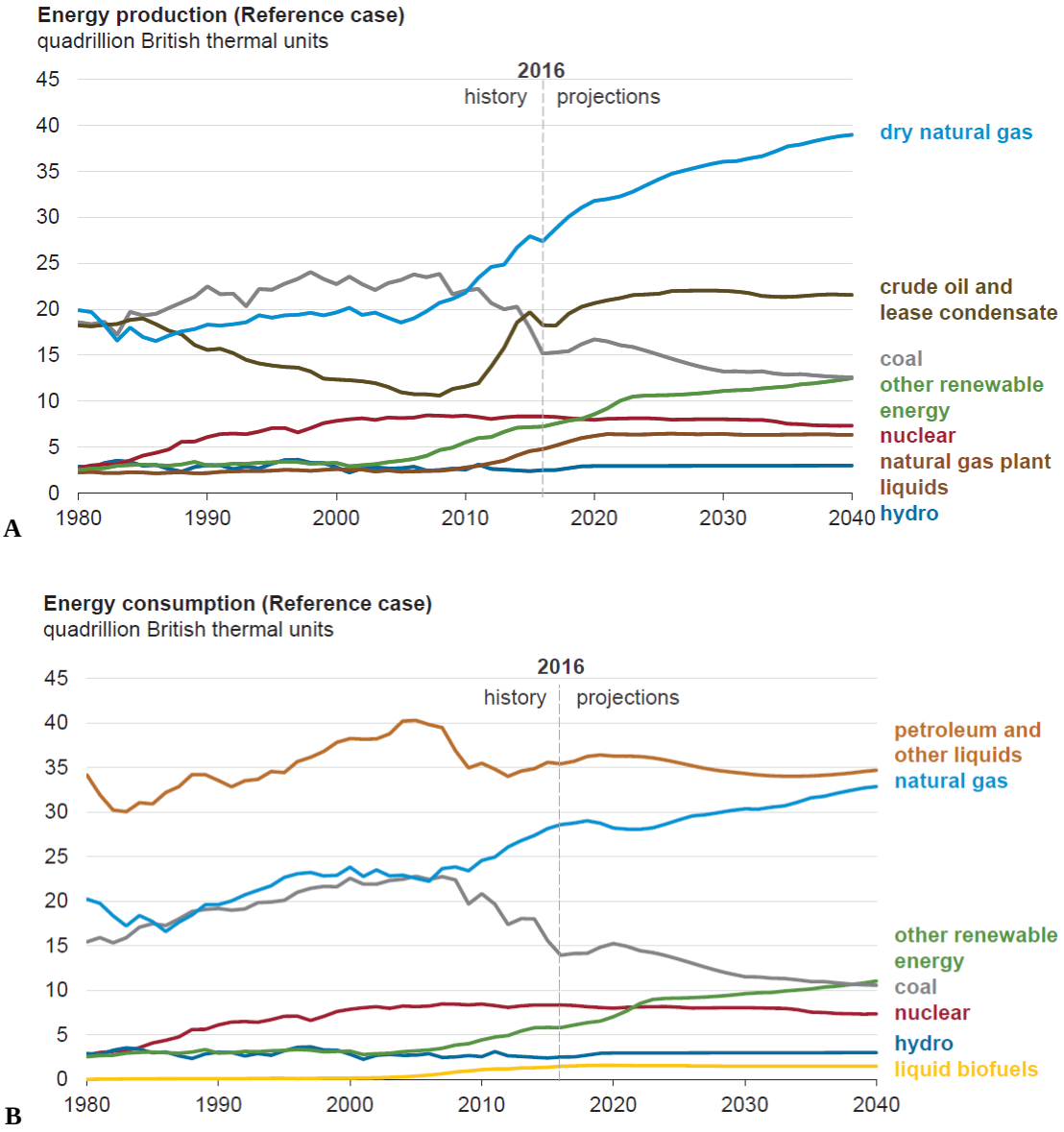

Figure 1.1. Energy production and consumption of The United States (adapted from [10]).

Lean combustion is a promising strategy that delivers higher thermal efficiency over stoichiometric and rich combustion [12-18]. For example, in lean combustion the combustion chamber temperature drops by igniting lean mixtures and results in lower dissociation and heat transfer losses. As engine knock is directly related to the in cylinder temperatures, it is believed that this combustion mode can enable engine operation at higher loads without knock. Lean mixtures also provide higher specific heat ratios which in turn increases the compression and cyclic

efficiencies. In addition, pumping losses can be reduced by controlling the fuel flow rate instead of throttling the intake air which improves the fuel economy.

While it is evident that there are numerous advantages of lean combustion, most reciprocating engines operate near the stoichiometric ratio because of the three-way catalytic converter requirements [13]. Namely, the three-way catalytic converter efficiently oxidizes CO and unburned hydrocarbons while reducing NO_x using a catalytically assisted reaction which becomes feasible at engine exhaust temperatures only nearby the stoichiometric ratio. Additionally, NO_x emissions increase for slightly lean mixtures because of both high combustion chamber temperatures and excess oxygen avaliability in the exhaust gases. Currently, no practical after-treatment system is available for spark-assisted lean burn combustion mode [16]. This limitation requires the air to fuel ratio be pushed further toward the lean limit, where the maximum temperature drops significantly and provides acceptable NO_x emission even without using a catalytic converter [19, 20]. Unfortunately, due to the lower temperatures the maximum chemical reaction rates decrease which in turn reduces, the laminar burning velocity that is directly related to the combustion duration. However, there are several means to reduce the combustion duration which will be discussed later.

Furthermore, it is very difficult to ignite lean mixtures, not only because the required ignition energy increases exponentially nearby the lean limit [21] but, also because the energy density of a lean charge is lower than a stoichiometric mixture; requiring the use of higher boost pressures or compression ratios to compensate. Due to this fact, ignition is compromised as the lean mixtures are under sufficiently high pressures at the time of ignition. The situation demands spark gap voltages in excess of 40 kV, which standard electrical ignition systems cannot reliably transmit. This is attributed to increases in the breakdown voltage which is directly related to the gas density,

and the mean free path of impact electron ionization [12]. Even if a high voltage system is employed, corrosion of spark plug electrodes increases maintenance cost [22]. An increase in indicated mean effective pressure (IMEP) from 17 to 22 bar reduces the service life of a spark ignition system to the half [23]. This is in contrast to current trends in which engine manufacturers would like to increase the maintenance interval to 8000 hrs, which is more than double the current used period [16].

Market demands for lower fueling costs and higher specific powers in reciprocating engines have engine designs trending towards higher in-cylinder pressures and leaner combustion operation. Stationary natural gas engine loads increased from 12 bar in 1994 to 24 bar in 2013 to provide 9% gain in engine efficiency [7]; this trend is expected to increase further in order to comply with anticipated future emission regulations [23]. However, ignition remains as the main limiting factor in achieving further performance improvements in these engines. To comply with future emission regulations, several ignition systems are proposed in the literature to overcome the limitations with a spark ignition system [13, 24]: plasma ignition [14], pilot fuel injection [25], rail plugs [15], and laser ignition [12, 22, 26-29] among others [30]. Out of those listed ignition systems, laser ignition is the most favorable as it exhibits several benefits [28, 31, 32]:

(i) enables ignition under higher pressures,

(ii) extends the lean ignition limit,

(iii) enables multi-pulse ignition, i.e., use of consecutive multiple pulses,

(iv) enables multi-point ignition, i.e., multiple spatially separated ignition locations, and further

(v) allows optimal placement of the ignition kernel in the combustion chamber.

Moreover, under lean conditions, flame speed is slow thereby offsetting any efficiency gains resulting from the higher ratio of specific heats. The laminar burning velocity (LBV) values calculated by using CHEMKIN PRO [33] tool employing the GRI-Mech 3.0 [34] chemical kinetic mechanism for typical pressure and temperature conditions at the time of ignition are shown in Figure 1.2. It is clear that the laminar burning velocity strongly decreases at lean mixtures, for example, LBV at $\lambda = 1.75$ are about 40% lower as compared to similar values at $\lambda = 1.54$. The actual combustion rate, however, is influenced by local turbulence and mixing in addition to laminar burning velocity. The decreased combustion rate offsets any potential gains with lean combustion mode. To compensate for this effect, one could use a prechamber in tandem with laser ignition to promote volumetric ignition under extremely lean conditions. This concept minimizes the flame travel path, and hence lowers the dependence on LBV.

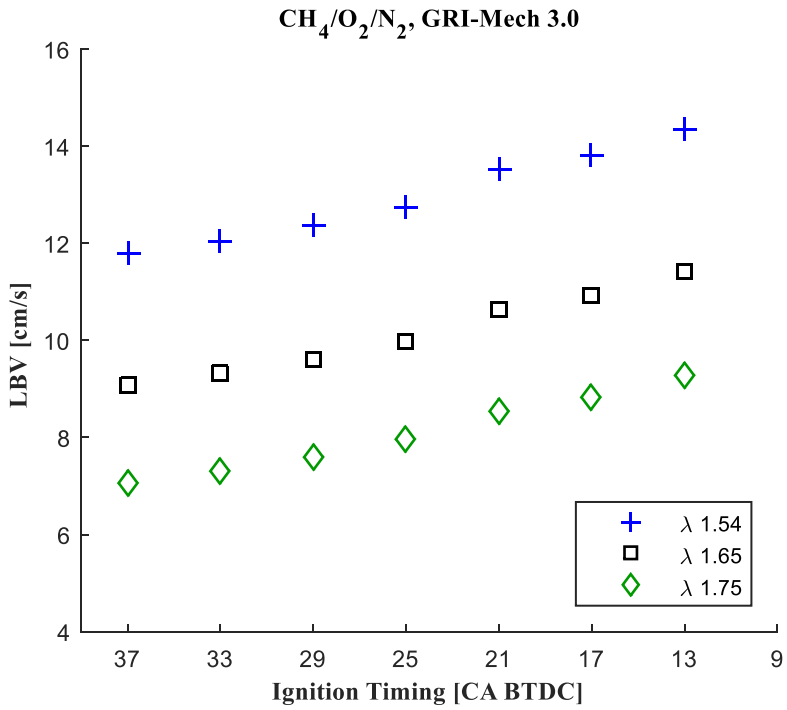

Figure 1.2. Laminar burning velocities calculated for typical conditions at the time of ignition for three different excess air ratios

In an unscavenged prechamber (see Figure 1.3), residual exhaust gases from previous combustion cycle are displaced by fresh combustible mixture during the upward compression stroke. After that, when an ignition kernel is created, it ignites the mixture within the prechamber, and the pressure is locally increased. Jets of radical partially combusted gases issue from the prechamber nozzle holes, each of which acts as an ignition source for the lean mixture in the main combustion chamber and provides the following advantages [35-37]:

(i) Volumetric ignition – spatial distribution of the jets leads to faster combustion in the main combustion chamber

(ii) In-cylinder turbulence enhancement – each of the partially combusted jets issues from the prechamber nozzles at very high velocities (Reynolds numbers in excess of 30,000) and in turn enhance the turbulence within the main combustion chamber [38].

(iii) Ignition energy amplification – depending upon the amount of the fuel-air mixture trapped in the prechamber at the time of ignition, amplification of ignition energy occurs up to 300 fold.

One of the objectives of this dissertation was to evaluate the efficiency of prechamber when used in tandem with laser ignition to overcome all challenges in lean combustion mode. First, the prechamber geometry was optimized through several tests in a single cylinder research engine. Subsequently, tests were performed comparing the performance of the three ignition systems: Standard spark ignition (SI), single point laser ignition (2P-LI), and prechamber equipped laser ignition (PCLI). Figure 1.3 illustrates ignition points for the three-tested ignition systems in this study as well as the partially combusted jets with the prechamber ignition system.

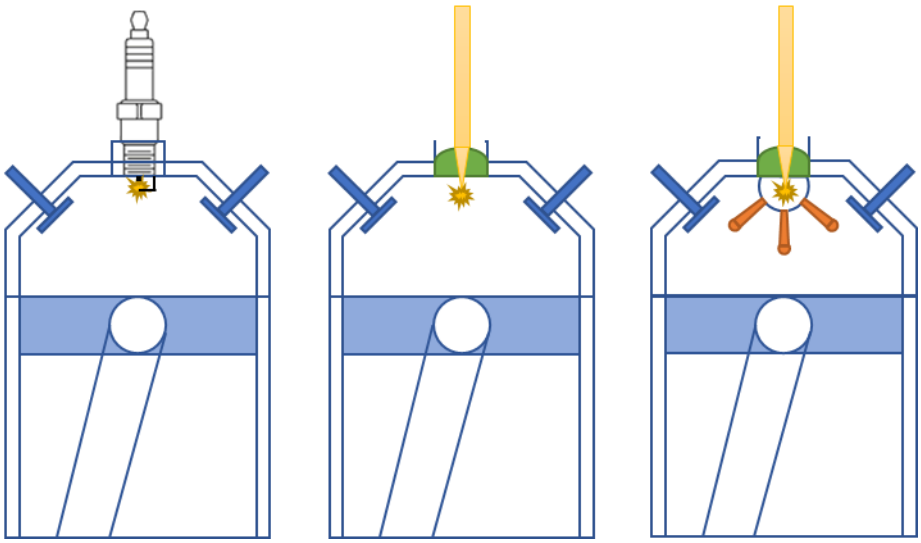

Figure 1.3. Schematic representation of the combustion chamber with three ignition systems. PCLI reduces the dependence on LBV by providing distributed jets

1.1.2 Advanced Biofuel Development

The transportation sector is a primary source of liquid fuel consumption, which has raised the demand for crude oil and led to severe environmental problems [39-42]. These reasons, along with new government legislation increasing regulations on exhaust emissions are the driving forces for researchers to find new fuel alternatives (e.g. biofuels) [40]. Due to the fact that internal combustion engines will still dominate the market for the immediate future [41], biofuels research [43, 44] is vital in order to investigate their fundamental properties such as ignition energy, flammability limit, octane number, ignition delay, and laminar burning velocity.

As mentioned earlier, one reason due to limited engine performance is the fuel combustion characteristics (engine knock at high load, combustion instability in lean combustion, and fuel sensitivity in homogeneous charge compression ignition engines); it is belived that biofuels could extent that margin. To investigate the benefit of biofuels, the Co-Optimization (Co-optima) project [9] was initiated, where fuel and combustion concepts are developed simultaneously to meet more

stringent exhaust emissions regulations, without compromising engine efficiency. Recently, the United States government incentives program increased biofuel utilization for automotive application to account for 5% of the total fuel consumed. Under this program, annual ethanol as fuel consumption went from 1.4 billion gallons in 1995 to 14.4 billion gallons in 2016; and those numbers are expected to increase further in the future [45]. Figure 1.4 presents the percentage of each fuel utilized in 2016 for the transportation sector. Oxygenated fuels like methanol and ethanol have been used as an octane booster or to reduce emissions by inhibiting soot formation [46, 47]; in the United States and part of Europe ethanol is blended with gasoline at 10% by volume [48].

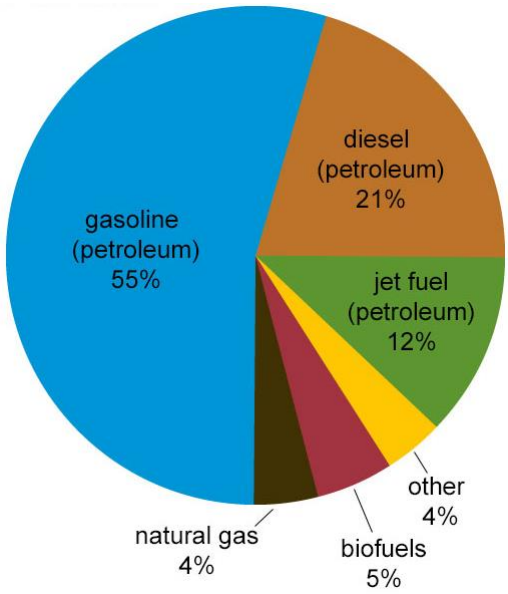

Figure 1.4. Liquid fuel consumption for transportation sector in the United States [45].

The biofuel and engine co-development framework which was initiated earlier than the Co-optima effort at Sandia National Labs [49] had similar goals. Here, the synthetic biologists develop and engineer a new platform for drop-in fuel production from lignocellulosic biomass, using several endophytic fungi. Hence this process has the potential advantage that expensive pretreatment and fuel refining stages can be optimized thereby allowing scalability and cost reduction; two major considerations for widespread biofuel utilization. Large concentrations of

ketones along with other volatile organic compounds were produced by fungi grown over switchgrass media. The combustion and emission properties of these new large ketones are poorly known. Therefore, fundamental measurements of representative molecules are needed to provide feedback on their desirability in advanced combustion engines (e.g., HCCI: homogeneous charge compression ignition engines [50, 51]) and their impact on emissions, as well as other combustion devices such as micro-combustors.

There is a vast potential for these new biofuels in automotive applications due to their advantages in mitigating greenhouse gases, improve air quality, and reduce the dependence on foreign oil (energy security) [52]; however, their oxidation chemistry is not well understood. The 2,4-Dimethyl-3-pentanone, also known as diisopropyl ketone (DIPK), is a promising candidate biofuel for automotive applications produced by the fungal conversion process [52]. The auto-ignition enhancement at increasing boost pressures and DIPK's higher temperature and pressure sensitivities provide significant advantages over gasoline for HCCI [52, 53]. The high pressure-sensitivity reduces the required inlet temperature for DIPK as the inlet pressure increases in HCCI engines; which allows for more advanced combustion timing. As a result, DIPK provides a higher thermal efficiency compared to gasoline at high-load boosted conditions $P_{in} \geq 2.36$ atm [52].

There are few studies in the literature on ignition delay times of DIPK, but no laminar burning velocity (LBV) measurement was found. LBV is defined as: *the velocity at which unburned gas moves through the combustion wave in the direction normal to the wave surface* [54]; LBV is a function of local composition, temperature, and pressure. LBV is not only important in understanding several aspects of combustion in spark ignition engines, and fuel comparisons; it is commonly used to validate chemical kinetic schemes [54, 55]. Therefore, LBV measurements are

needed for DIPK at low/high pressure conditions to understand the heat release rate in reciprocating engines, and deliver several validation points for chemical kinetic mechanisms.

A new combustion chamber has been designed, assembled, and post processing validated with iso-octane & synthetic air mixture a well-known fuel in the literature, before conducting experiments with the fuel of interest. Experiments at a wide range of equivalence ratios, and initial conditions were carried out by diluting the mixture with N_2, He, and Ar. The constant volume approach with multilayer thermodynamic model was used in the analysis of data points to provide accurate LBV measurements. Since flame develops diffusional-thermal instability as the pressure increases, several diluents have been used to suppress flame instability and offer a wider range of useful data points along one isentrope. Also, flame propagation was captured to determine the onset of hydrodynamic flame instability in order to eliminate those data points from the LBV values. This investigation aims to provide values in the range of pressure 1 to 10 atm and temperature 400 to 500 K for representing reciprocating engine initial conditions.

1.2 Scope and Organization of Dissertation

Chapter 2 includes theory behind the use of a laser ignition system and design consideration of optical components. The limitations of spark ignition and advantages of laser ignition systems are also discussed in detail. A literature review of laser ignition in constant volume combustion chamber and reciprocating engines is presented. Advanced laser ignition concepts are presented to show their promising benefits for future reciprocating engine research. Thereafter results of three laser ignition investigation studies are discussed.

The first study shows the laser characterization process as well as the measurements of methane LBV at atmospheric pressure and two initial temperatures 297 K and 393 K. Laser and spark

ignition systems were used to initiate the combustion process, and LBV values were compared to determine the accuracy of values obtained with laser ignition. Also, this study investigates the effect of laser ignition energy on the LBV, pressure traces, and methane flammability limits. These experimental results were compared with numerical predictions by GRI-Mech 3.0 [34] and ARAMCO-Mech 1.3 [56] kinetic mechanisms for a wide range of equivalence ratios (Φ 0.7-1.4). Additionally, the benefit of laser ignition for initiating combustion in CH_4/O_2 mixtures diluted with CO_2 was investigated in a separate section of this dissertation (Appendix B).

The results of reciprocating engine tests utilizing a water-cooled, passively Q-switched, Nd:YAG µlasers are discussed in the second study. The µlasers were installed in the individual cylinders of Cummins engine (QSK19G), 350 kW, inline 6-cylinder, open-chamber, spark ignited engine and tests were conducted. The operating conditions were held constant at 298 kW load, and 1800 RPM rated speed, while sweeps of ignition timing and excess air ratio were performed by keeping the NO_x emissions below the EPA regulated value ($BSNO_x$ < 1.34 g/kW-hr), and while maintaining ignition stability at industry acceptable values (COV_IMEP < 5%). A rigorous combustion data analysis was made and the main reasons leading to improved performance in the case of laser ignition was presented.

The third study in chapter 2 investigates the capabilities of a prechamber equipped laser ignition (PCLI) system to extend the lean limit of a natural gas research engine. The optimal geometry of PCLI was identified through several tests in a single-cylinder engine as a compromise between autoignition, NO_x and soot formation. Subsequently, tests were conducted to compare the performance of three ignition systems: standard electrical spark ignition (SI), single-point laser ignition (2P-LI), and prechamber equipped laser ignition (PCLI). Efficiency gain of 2.1% points

could be achieved while complying with EPA regulation and the industry standard for ignition stability.

Chapter 3 gives a comparison of methods used in the literature for determining the laminar burning velocity in combustion chamber. The latest thermodynamic models for the constant volume approach were evaluated with methane and compared against a numerical prediction using CHEMKIN PRO [33]. After that, LBV measurements of a new promising biofuel candidates for automotive applications have been introduced in Chapter 3. Experiments were conducted at a wide range of initial condition by employing SI system and utilizing three diluents (N_2, Ar, and He). Flame propagation was captured using schlieren imaging to ensure that the flame is spherical and stable in order to provide accurate data points. This chapter also includes flame instability discussion and suggests a diluent to suppress flame instability and increase the range of useful data point along one isentrope. Finally, it provides DIPK LBV values in the range of 1 to 10 atm, 400 to 500 K, and equivalence ratio 0.8 to 1.6.

Chapter 4 summarizes the conclusions of the main findings of this doctoral study. Also, publications made during this doctoral study are listed and recommendations for future work are provided.

CHAPTER 2: LASER IGNITION FUNDAMENTALS AND EXPERIMENTS

2.1 Theory and Background

Many proposed combustion schemes have the potential to increase the thermal efficiency and to lower exhaust gas emissions for reciprocating engines. The latest proposed concepts are direct injection, lean combustion, and homogeneous charge compression ignition (HCCI) engines. However, those concepts suffer from flame instabilities that result in high cyclic variation and limited operating ranges. Laser ignition can be used to enhance the combustion process in all those cases. For instance, in lean combustion, the laser ignitor offers a reliable ignition source without conduction heat transfer losses which will extend the lean limit (wider equivalence ratio range) and provides better initial flame propagation. Similarly, in HCCI engines, a small energy can be deposited to assist flame initiation in order to deliver a wider range of engine speed, and reduce the cyclic variation (spark assisted HCCI engines). Lastly, optimal placement of the ignition kernel in direct injection gasoline engines reduces the time for complete combustion; hence, the maximum output power can be increased.

The combustion process can be initiated by several methods such as compression, evaporation, or depositing energy based on the application/reciprocating engine type. In a diesel engine, fuel is injected near the top dead center (TDC) where the temperature is high enough to start the combustion process. However, fuel evaporation and the mixing processes control the diffusion flame in this concept. The HCCI engine compresses the premixed lean combustible mixture to an extent where auto-ignition occurs instantaneously. Alternatively, spark ignition (SI) engine compresses the premixed mixture to an extent below the auto-ignition temperature to prevent the occurrence of engine-knocking in a slightly rich mixture. In this type of combustion, energy must

be introduced to provide heat generation quicker than the losses associated with heat transfer to electrodes and the unburned mixture [57].

Ignition is defined as an unsteady event where chemical reaction rates dramatically increase enabling the onset of stabilized combustion [19, 21, 58] by depositing a thermal or electronic energy into the combustible mixture. The minimum ignition energy (MIE), is the energy required to raise a sphere of gas with characteristic flame thickness (δ_f) to the adiabatic flame temperature [19, 21, 58]. Here, the MIE and minimum kernel radius can be estimated using equations (2.1) and (2.2) respectively [21]. Where ρ_f, c_p, k, v_f, and δ_f are density, specific heat at constant pressure, average heat conductivity, propagation velocity and minimum kernel radius respectively; while $T_f, and\ T_u$ are the kernel and unburned gas temperature. This energy enables sustained combustion where the heat generation in excess of net heat losses. In the early stage of the combustion process, the shape of the flame is called flame kernel [21] that exists after the transition from plasma to self-sustained flame. Engine turbulence influences the flame kernel shape and spreads flame propagation, however, in extreme cases, turbulence might extinguish the flame kernel [59].

$$MIE \approx \frac{4\pi\delta_f^3}{3}\rho_f c_p\left(T_f - T_u\right) \tag{2.1}$$

$$\delta_f \approx \frac{k}{\rho_u c_p v_f} \tag{2.2}$$

Like wise, many parameters affect the ignition process such as the air to fuel ratio, impurities, homogeneity, pressure, and temperature [21]. It is evident from equation (2.1) that an increase in unburned gas temperature reduces the MIE. Similarly, initial pressure changes the gas density as well as the quenching distance (minimum gas volume that can be ignited) that results in indirect relationship between MIE and pressure shown in equation (2.3), this behavior has been observed

in numerical and experimental studies for a wide range of pressure 1-10 atm [60-62]. However, the limiting factor in spark ignition system is the required breakdown voltage that increases with pressure according to Paschen's law. The air to fuel ratio must be within the flammability limit for the mixture, otherwise, combustion will not be initiated even at very high ignition energy. These boundaries exist because in very lean and rich mixtures the amount of energy released is not enough to sustain flame [21]; Tauer *et al.* observed that the flammability limits increases with pressure and temperature until the auto-ignition temperature is reached [21].

$$MIE \; \alpha \; P_i^{-2} \tag{2.3}$$

The maximum energy released in the combustion process occurs at slightly rich mixture; and decreases for both lean and rich mixtures due to the reduction of hydrocarbons and oxygen molecules respectively. Also, if a mixture is not homogeneous, having a spatially dependent concentration gradient, the local equivalence ratio (Φ) deviates and reduces the fuel reactivity. Under extreme conditions, the non-homogeneity might prevent the ignition process.

Historically, spark ignition systems were used to initiate the combustion process by utilizing a high voltage current across the spark plug electrodes in both gas turbines and reciprocating engines [19]. In an ideal case of a homogenous mixture near the stoichiometric ratio, a 1 mJ spark energy pulse delivered for a few micro seconds would be sufficient to initiate the combustion [19]. However, non-homogeneity and turbulence, among other reasons inhibit ignition in reciprocating engines. Generally, a 40-50 mJ spark energy for 0.5 ms provides reliable ignition source in entire engine working range [19]. Also, the required energy increases during the life span of a spark plug due to the erosion problem. Spark plug gap is usually in between 0.7 to 0.9 mm which might be increased to 1.2 mm for extremely diluted mixture [19]. The spark ignition system works properly

with current cycles. However, market demands for lower fueling costs and higher specific powers have engine designs trending towards higher in-cylinder pressures that requires more innovative ignition techniques to overcome the limitation of SI system.

Many researchers [18, 21-23, 28, 63-66] have reviewed the advantages of laser over spark ignition systems. All SI system limitations discussed earlier can be eliminated by using laser ignition (LI) system as LI provides greater timing control. LI processes are on the order of 5~ 10 ns that offers a proper combustion phasing to achieve the maximum brake torque over the entire engine speed. Also, the absence of electrodes in LI results in a longer life span and a reduction in the conduction heat losses during the combustion event. The life span of a conventional SI system is in between 2000-4000 h while a diode-pumped laser ignition system has a potential lifetime up to 10,000 h [28].

The plasma location in LI can be adjusted by changing the lens focal length to provide an optimum position of the ignition kernel. A reduction in flame travel path helps in faster burning rates (compare Figure 2.1A and B), which is a concern in a lean combustion mode due to a slower flame speed. In addition, multi-point LI reduces the combustion duration substantially; in this process multiple laser paths are used to generate multiple ignition sources Figure 2.1C and D [23]. The most motivating feature of LI system is the indirect relationship between initial pressure and the required pulse energy to start the combustion process [22, 64]. This feature is significant because engines running with lean mixtures must increase the boost pressure to compensate for the reduction of energy density, hence, lower ignition energy can be deposited [64].

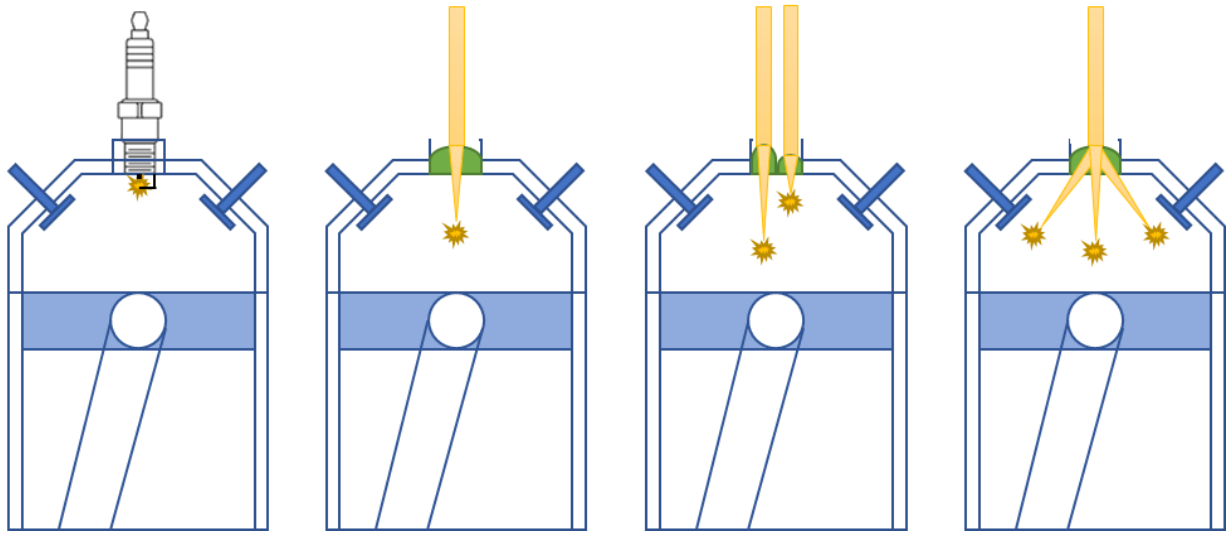

Figure 2.1. Schematics of reciprocating engines ignited by (A) a spark plug, (B) a laser ignitor with a single pulse, (C) two laser ignitors with two focal lengths (D) a laser ignitor with multi-point ignition.

In a reciprocating engine, turbulence is used to increase the burn rate, however, the heat transfer to the wall also increases due to high gas velocity. Ronney [64] proposed the multi-point ignition to enhance the combustion process in a laminar flow field in order to develop engines with high burn rate and low heat transfer losses. In another study, Dearden and Shenton [66] suggested laser ignition for automotive application with high exhaust gas recirculation (EGR). Diluting combustible mixtures with EGR lowers the NO_x formation and rises thermal efficiency. However, the poor ignitability of highly diluted mixture limited its use in spark ignition engine. In a similar manner, laser ignition can be employed for lean (near the flammability limit) combustion mode because of the seam reason.

In gasoline direct injection systems, studies showed that optimum spark position is within the spray cone [67]. However, the spark plug electrodes erode in such circumstance. Therefore, laser ignition system can circumvent this issue by forming a plasma within the spray cone. Since, an optical plug can be designed to be smaller than a regular spark plug, cylinder heads can be

optimized to enhance engine turbulence, and to increase the overall volumetric efficiency. Without a doubt LI is capable of eliminating all SI limitation (more examples are given in section 2.1.3) and delivers higher engine efficiencies because it can be used in a wider range of operating conditions. However, there are some drawbacks like the cost, windows durability and the propagation of laser beam, which are going to be discussed later [22].

The basic idea of the LI system is to direct Q-switched short laser pulses of a few nanosecond toward a bi-convex lens to focus the beam; optical breakdown occurs if the intensity in the focal region exceeds a threshold value 10^{10}-10^{11} W/cm^2 in atmospheric pressure [18, 21, 22, 28, 32, 63]. Figure 2.2 illustrates the laser induced plasma formation process and the minimum cross sectional dimeter. The laser pulse is characterized by the wavelength, pulse energy, profile, and duration (full width at half maximum, FWHM). Several authors [21, 47] have noticed a bigger plasma expansion toward the incoming laser after the optical breakdown. Approximately after 0.5 μs from the laser pulse, an acoustic shockwave detaches from the plasma [68] and transports energy away from the focal region and causes a temperature rise to the surrounding. The shockwave energy losses are predicted to be bigger than 60% of the deposited energy [47]. After that, if the deposited energy is high enough, a smooth transition occurs around 10-50 μs from plasma to a developing flame kernel [21]. The plasma size and the required MIE does not only depend on the mixture properties but also on the specification of the laser beam as well as the optical setup (mirrors, lenses) [28].

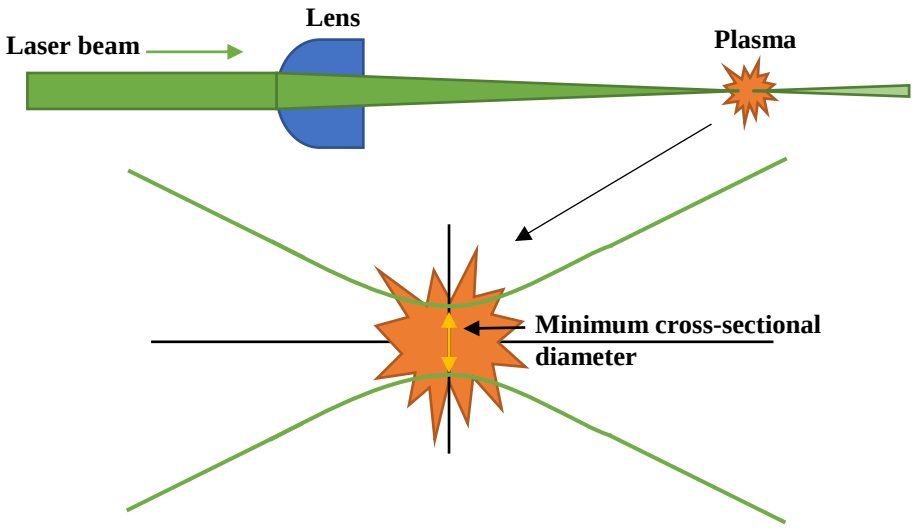

Figure 2.2. Laser-induced plasma formation.

2.1.1 Laser Ignition Theory

There are four mechanisms by which laser radiation may interact with the combustible mixture: (i) thermal ignition (ii) photochemical ignition (iii) resonant ignition (iv) non-resonant breakdown [18, 28, 32, 66]. In thermal ignition, the mixture absorbs thermal energy through vibrational and rotational modes without generating an electrical breakdown [63]. This method is often plagued by low radiant intensity, which results in a longer ignition delay. Therefore, it is not appropriate for practical propulsion applications [31] where ignition has to be controlled precisely. In some cases, a strong target absorber (solid) is placed in the beam path to absorb and transfer energy to the gases [18]. However, erosion problem such as those exist with a SI system limits its utilization.

Photochemical ignition occurs when laser radiation dissociates a molecule and ionizes its constituents to initiate combustion [18]. This mechanism requires highly energetic photons to target a certain molecule. Lasers in the range of ultraviolet (VU) or shorter wavelengths must be employed in this mechanism to provide the necessary energy for ionization. Even though this is a

promising technique, the close match between laser radiation and molecule absorption, laser cost, size, and weight currently prohibits its use in reciprocating engines [18].

The most favorable LI mechanism is non-resonant breakdown; this process starts when electrons absorb laser irradiance from a focused high laser pulse to generate a plasma. Plasma formation requires a free seed electron that might exist because of impurities in the mixture, or by multi-photon ionization of few gas molecules that releases an electron. Thereafter, electrons absorb more photons easily to increase their kinetic energy. As a result, more collisions between the electrons and molecules leads to an electron avalanche and breakdown [18, 28, 63]. This mechanism does not have a wavelength dependence. Namely, the laser wavelength is not corresponding to any absorption line of the medium. Conversely, the resonant breakdown starts by non-resonant breakdown; followed by a resonant photoionization of atoms [18, 63]. This type has a higher energetic efficiency than the non-resonant ignition. However, it is not commonly used because it requires a precise spectral selection to target certain molecules [28].

In non-resonant breakdown, the plasma is generated by focusing a high laser pulse energy to a very small volume, if the intensity exceeds 10^{10}-10^{11} W/cm^2 a breakdown occurs. In this type, high energy is required because it was found that laser interacts weakly with gases, and ionizations was responsible for its absorption [32]. Gas ionization can be achieved by either multi-photon ionization where an electron absorbs photons to an extent that provide a free state electron (extract it from the atom). Or by cascade ionization which requires at least one seed free electron that absorbs energy by laser radiation. It is worth to note here that the initial seed electron is available in practical applications because of impurities present in the combustible gas mixture (aerosol particles, dust, vapor, or soot) [18, 21]. After that, the accelerated electrons collide with neutral atoms to ionize them [21, 32, 69].

In multi-photon ionization (MPI), the electron absorbs a sufficient number of photons for ionization. This process is proportional to the photon flux and depends on electric field state (quasi-static or not during the pulse duration). However, the MPI occurs only at a very short wavelength (λ < 1 μm) or at very low pressure (P < 10 mbar) where electron-atom collision effect is negligible [21, 32]. The multi-photon ionization may provide the initial electrons, but, the cascade breakdown mechanism is the dominant mechanism for practical combustion application where the mixture is ignited at high pressure.

Cascade breakdown increases the electron energy and eventually ionizes the atom by inelastic collisions that lead to avalanche process. When the laser intensity reaches a critical threshold value I_{thr}, the medium absorbs the energy efficiently by the discussed mechanism [21, 32]. The number of electrons increases exponentially with time as shown in equation (2.4). Where t_p, τ_e, N are the pulse duration, time constant, and number of electrons respectively. It is obvious that the final number of electrons have a weak and a strong dependence on the initial electrons number and time constant respectively. Equation (2.5) can be used to calculate the time constant that depends on the laser intensity (I) and diffusion losses represented by the diffusion rate of electrons escaping from the plasma (v_d). It is clear that, the time constant decreases as the laser intensity increases, more detail analysis can be found in appropriate references [18, 21, 32].

$$N_e = N_{e,o} \exp\left(\frac{t_p}{\tau_e}\right) \tag{2.4}$$

$$\tau_e = \left[v_d \left(\frac{I}{I_{thr}} - 1\right)\right]^{-1} \tag{2.5}$$

The critical threshold laser intensity (I_{thr}) is indirectly proportional to the laser wavelength and initial pressure. The cascade ionization threshold value can be estimated using equation (2.6). For sub ns laser pulses, the diffusion losses are negligible and the constant, n equals 1. However, for

longer pulses, which are common in affordable lasers today, the diffusion losses of the electron must be considered, and the constant n is 2. Under extremely high pressure, the critical intensity behaves differently; the critical intensity increases with pressure due to electrons collisions losses [70], however, this range is also outside the scope of our work for the reciprocating engines.

$$I_{thr} \propto \frac{1}{p^n}\frac{1}{\lambda^2} \tag{2.6}$$

2.1.1.1 Optical Geometry

The laser intensity (irradiance) is defined as the laser power per beam cross section area; that is mainly because beam divergence prevents a theoretical point focused beam (see Figure 2.2). Since plasma requires high laser intensity that cannot be delivered with an unfocused laser beam, an optical setup is used to concentrate the beam cross sectional area, and hence provides the required intensity. Intensities as high as trillions W/cm^2 can be reached with a proper optical setup and pulse duration in the order of ns or fs [32]. Laser intensity depends on several parameters as described below, and can be evaluated after determining the beam cross sectional area within the focused volume.

The beam quality is reflected by the quality factor (M^2) which is a measure of the beam profile compared with the fundamental Gaussian mode. Equation (2.7) provides the quality factor by using the laser beam diameter (B_D), divergence half angle (θ), and wavelength (λ). The quality factor of a pure Gaussian mode is 1, any divergence from that mode results in a bigger focal volume and hence, reduces the laser intensity [32]. The beam quality factor value increases with the deviation from Gaussian mode, typical values used in the literature varies from 1.3-10 [32].

$$M^2 = \frac{\pi B_D \theta}{2\lambda} \tag{2.7}$$

In a similar manner, the beam cross sectional area within the focused volume is a function of the lens focal length, wavelength, laser beam diameter, and source profile. After evaluating the quality factor by equation (2.7), equation (2.8) can be used to estimate the diameter of the focal spot, neglecting aberrations. Under the assumption of perfect focusing conditions, the field intensity is proportional to the square of the focal diameter, which compensates for the larger threshold intensity value [21, 32].

$$D_f \approx \frac{4\lambda M^2 f}{\pi B_D} \tag{2.8}$$

Tauer *et al.* showed that for a fixed focal length, the required breakdown intensity of a 532nm wavelength is less than that required for 1064 nm. Conversely, a compassion under the same focal diameter by employing different focal lenses revealed an opposite trend. This observation demonstrates the importance of the focal volume in LI which can be controlled using several parameters given in equation (2.8). Also, if the pulse energy is varied, there will be a point where the absorption of the 1064 nm radiation exceeds the 532 nm even though the minimum pulse energy (MPE) at 1064 nm is larger than at 532 nm. This effect is due to the wavelength dependency of absorption process by inverse bremsstrahlung lying somewhere between λ^2 and λ^3 [21].

The laser intensity can be calculated by using equation (2.9). In stationary natural gas engines, a MPE of 15 mJ is needed to initiate the combustion as will be shown in section 2.3, however, only part of that energy is available for ignition due to the absorption and reflection losses. In an ideal case where windows/lenses losses are neglected, and the laser profile assumed to be Gaussian, 15 mJ, 1064 nm, 2 mm diameter, 4.72 ns pulse with 12 mm focal length provides a minimum cross-sectional area of 5.19×10^{-7} cm^2, and a laser intensity in the order of 6.12×10^{12} W/cm^2. This value is two order of magnitude less than the value suggested for multiphoton

ionization (10^{14} W/cm^2) [69]. Therefore it is valid to conclude that the cascade ionization is the mechanism behind plasma formation.

$$I = \frac{E_p \pi B_D^2}{4\lambda^2 (M^2)^2 f^2 t_p} \tag{2.9}$$

2.1.1.2 Window/lens Considerations

There are currently two approaches to deliver laser ignition in an automotive applications, a diode-pumped solid-state laser mounted directly on the cylinder head, with necessary cooling [71] or by transporting laser pulse by fiber which has its own challenges pertaining to beam degradation and pulse energy limitations. Regardless, the laser ignitor is located outside the combustion chamber, which requires a window for laser beam transmission. Accordingly combined and separated configurations are employed in the literature (see Figure 2.3). A combined design provides an optimum seal, but it is expensive compared with the separate configuration. As the name implies, in the separate configuration, the window and focusing lens are separated by a gasket (or a spacer) that can be used to change the focusing point inside the combustion chamber. This is a great advantage for research engines, but, reflective losses and sealing are the drawbacks of this concept. The author used a separate configuration optics with a laser ignition in section 2.2 while a combined configuration was employed in sections 2.3 and 2.4 for the reciprocating engine tests.

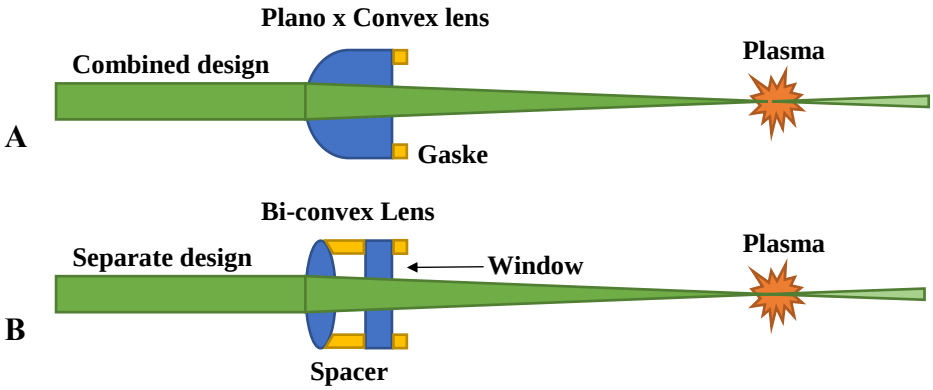

Figure 2.3. Schematic representation of combined (a) and separated (b) focusing optical configurations for laser beams

In a LI system, the window does not only have to withstand the harsh engine environment, but also must provide a long term operation with minimal reduction of pulse energy due to window fouling [21]. Window fouling is a phenomenon that exists if combustion chamber deposit (CCD) forms on the window surface causing a reduction of window transmission. Therefore, a high optical transparency for the laser wavelength and no reaction with the combustion are desired substrate properties. An estimation of the minimum required window thickness [21] can be determined by using equation (2.10). where d_m, P, S, and σ_{tf} are the diameter of unsupported area, pressure, design safety factor (8-10 for windows), and the allowable tensile strength respectively.

$$t_d = 0.55 d_m \sqrt{\frac{pS}{\sigma_{tf}}} \tag{2.10}$$

Durability of windows depends on the material properties, geometry, and the design thickness. Sapphire windows are preferred over other materials, espically at high cylnder pressures, because of its high tensile strength and thermal shock resistance. Harris [72] examined the durability, reflectivity, emissivity, and transmissivity for several infrared window materials under high temperature. The emissivity was found to be linearly proportional to the absorptivity and increases

with temperature. The refractive index of fused silica, sapphire, and aluminum oxynitride (AlON) are 1.46 1.77 and 1.8 respectively at a 0.5-μm wavelength, the lower the refractive index, the lower the losses. In regards to thermal stress resistance, the relative resistance was calculated to be 9.7, 2.6 and 1.2 for fused silica, sapphire, and AlON, respectively. A higher relative resistance indicates that the material can withstand thermal shock without facing problems [72]. Even though sapphire has a higher refractive index than fused silica, properties such as tensile strength and excellent thermal resistivity promote the substrate for high pressure and temperature applications.

In another study, Lackner *et al.* [73] reviewed four types of windows: quartz, sapphire, zinc selenide (ZnSe), and AlON by conducting experiments with spark ignition system for 2 hours. Table 2.1 presents substrates specification used in their study. The windows were mounted on the cylinder head (by copper rings/mica gaskets) to estimate the effect of conduction heat transfer on combustion chamber deposits (CCD). The difference in the windows weight before and after each test was utilized to determine the accumulated CCD mass. Lackner *et al.* [73] found that CCD decreases by increasing the window temperature. Since the temperature is a function of mounting position, engine load and speed, sealing material, and the thermal conductivity of the windows, all those factors contribute to CCD formation.

It has been found that CCD increases with decreasing substrate thermal conductivity (the lower the thermal conductivity, the lower the heat losses are) [73]. Similarly, a sealing material with low thermal conductivity lowers CCD. It has been noticed that with a better thermal insulation (for the window) the CCD formations are very low; the benefit of Klingersil gaskets instead of copper was shown. Lackner *et al.* [73] also showed that the Calcium Sulfonate in the lubricating oil is a reason behind deposits even in four stroke engines. That being said, several studies in the literature proved

that the combustion chamber deposits could be removed by laser ablation as will be shown in the window fouling section of this dissertation.

Table 2.1. Specification of windows material (taken from [73]).

Material	**Sapphire**	**AlON**	**ZnSe**	**Quartz**
Tensile strength, [Mpa]	800	380	100	80
Melting point, [C]	2000	2150	1850	1550
Thermal conductivity, [W/mK]	42	12.6	18	1.4
Hardness, [kg/mm^2]	2000	1950	105	600
Coefficient of thermal expansion, [10^{-6}/K]	5	7.5	7.3	0.13

The next two subsections provide a literature review of experiments conducted in constant volume chamber and reciprocating engine, respectively, to appreciate and deliver the latest technologies in that field to the reader. The constant volume chamber tests provide a general understating of laser parameters on the plasma formation, the effect of absorption and reflection losses on the minimum ignition energy. Also, flame propagation shape was illustrated to realize the reasons behind the toroidal shape formation and to understand its advantage for combustion applications. After that, the improvement of engine efficiency and combustion stability will be addressed in the reciprocating engine section. Solutions for combustion chamber deposits, laser delivering systems, and high laser temperature problems are discussed later.

2.1.2 Laser Ignition in Constant Volume Chamber

2.1.2.1 Effect of Optics, Laser Parameters, and Initial Conditions

The steady state nature of experiments conducted by constant volume combustion chamber provided a repeatable and accurate platform for studying the effect of laser parameters and optics configurations on LI. This fact motivated several authors in the literature [21, 28, 31, 69, 74-78] to evaluate the effect of initial conditions, focal length, wavelength, ignition energy, beam

diameter, quality factor, reflection, and absorption losses on laser ignition. Srivastava *et al.* [28] studied the behavior of natural gas combustion by utilizing Q-switched Nd:YAG laser at the fundamental wavelength. The beam quality M^2 was 4.6, and a plano-convex lens with a focal length of 100 mm were used to ignite the mixture at several initial pressures. It has been noticed that the minimum pulse energy for 100% ignition probability decreased from 17 to 7 mJ by increasing the initial pressure from 1 to 10 bar. This fact is beneficial for lean burn engine, where energy density can be compensated by increasing the pressure. Srivastava *et al.* [28] justified this behavior by the increase of absorption efficiency for a denser mixture (higher number of gas molecules in the focal volume).

Strozzi *et al.* [31] determined the MIE of n-decane air mixtures at several initial condition and equivalence ratios. Nd:YAG laser at the fundamental wavelength with a beam quality factor of 1.95, and 150 mm focal length lens were employed in experiments. MIE values were corrected for the windows absorption (4.5% per window) of the incoming beam. The mixture composition versus the MIE gave a U-shaped trend where the minimum value is near stoichiometric ratio, and the ignition energy increases for lean and rich mixtures. However, MIE increases at a faster rate for lean mixtures. Initial pressure was inversely proportional to the minimum ignition energy; the required energy was reduced from 104 to 48 mJ by increasing the initial pressure from 0.5 to 4 bar [31].

In another study, Rudz *et al.* [74] evaluated the MIE of α-pinene/air mixtures at atmospheric pressure and 347 K. An overlap between the breakdown and ignition energies were noticed in the range of Φ (0.9 – 1.7). However, mixtures outside that region require higher pulse energy to initiate combustion. This behavior can be understood because breakdown at atmospheric condition

requires high energy, unlike experiments at an elevated pressure where breakdown might happen at an energy lower than that needed to ignite the mixture.

Kopecek *et al.* [75] evaluated the characteristic of laser ignition using a Nd:YAG laser at 1064 nm with a quality factor less than 2, and a maximum output energy of 40 mJ. A sapphire window with a surface reflectivity of 7% was used, and the losses were considered in the minimum ignition energy calculation. In their experiments, 30 bar and 200°C were chosen as initial conditions to simulate a reciprocating engine environment. It has been noticed that the required energy dropped dramatically compared to tests at atmospheric condition. Also, the lean limit increased from Φ = 0.55 to 0.46 by increasing the pulse energy from 4 to 40 mJ. The analysis showed that the transmitted energy was found to be only in the range of 2 to 6 mJ because of the losses associated with windows and shockwave formation. Also, the time required to reach 5% of the maximum pressure during the combustion event increased by four times with a leaner mixture (comparing Φ = 1.0 to 0.5).

Gupta *et al.* [76] compared combustion parameters such as pressure rise, ignition delay, and lean limits by employing laser and spark ignition systems. Nd:YAG at the second harmonic was used to generate a laser pulse for 7 ns while a capacitor ignition system was utilized for SI. In regards to pressure rise and ignition delay, no difference was observed between the two ignition systems [76]. However, Gupta *et al.* found that the absorbed energy within the plasma increases as the laser pulse energy increases. Namely, higher energy rises the absorption and provides a larger plasma kernel. Also, a higher energy absorption was recorded with shorter focal length. They concluded that the laser ignitor was capable of initiating the combustion process efficiently for mixtures with an initial pressure of 20 bar, unlike the conventional system that was limited to 15 bar.

The effect of focal length, wavelength, pulse duration, and equivalence ratio on the MIE was investigated in Ternel *et al.* [77] study. Nd:YAG laser at two wavelengths (1064 and 532 nm), and two focal lenses (25 to 200 mm) were used to ignite propane/air and iso-octane/air mixtures. It has been noticed that optical breakdown requires more energy at 1064nm, and a higher ignition energy was needed as the focal length increases. This observation agrees with the optical geometry guidelines explained earlier; longer focal length or wavelength provides a bigger focal volume [77], hence, decreases the laser intensity. In their experiments, MIE was always greater than the energy required for the optical breakdown in air. That is mainly because of the necessary energy to sustain combustion process after the optical breakdown. Furthermore, MIE was almost constant in the range of Φ (1-1.3) and increases dramatically for lean mixtures. Ternel *et al.* [77] found that more intensive irradiance can be delivered as the pulse duration decreases because of the inverse proportionality between focal volume intensity and pulse duration, see equation (2.9).

Similarly, Kopecek *et al.* [78] investigated the effect of pressure, focal length, wavelength, and equivalence ratio on the MIE for methane/air mixtures. A sapphire window with 13 mm thickness was utilized to withstand 300 atm design pressure; several convex lenses were employed to provide focal lengths in the range of (50 to 300 mm). They observed a similar trend; MIE decreases by increasing the chamber pressure and utilizing shorter focal length. Also, Kopecek *et al.* realized that the lean flammability limit could be extended by using laser ignition system, however, MIE increases dramatically near the lean limit. Also, MIE increases with wavelength especially with longer focal length 300 mm [78].

In another study, Xu *et al.* [69] studied the wavelength dependence on MIE of gasoline mixture, by considering the absorbed energy in the plasma rather than the laser incident energy in other studies, using Nd:YAG laser. 1064 and 532 nm wavelength are employed with a 500 mm focusing

lens. They noticed that significant energy loss is associated with the absorbance of quartz windows. Also, a higher absorbance was observed with 1064 nm pulse. Xu *et al.* [69] found that the same ignition probability can be achieved at all equivalence ratios by utilizing only half of the incident energy with 523 nm. However, the absorbed energy within the plasma will be identical. This observation was attributed to the wavelength dependence for initial free electrons that is crucial for plasma formations not energy absorbance. The general u-shaped for minimum ignition energy was determined by using laser and spark ignition systems. Even though MIE was defined as absorbed energy with laser systems, it is still higher than that required for conventional spark ignition system.

From the literature review, it is clear that laser ignition improved the combustion process in general. It extended the lean limit and was capable of igniting mixtures at very high pressure, two crucial aspects of lean combustion natural gas reciprocating engine operation. It is noticed that laser ignition requires higher energies relative to the standard ignition system because of the losses associated with optics and shockwave. However, in most combustion applications the ignition is initiated at high pressure, which results in acceptable laser pulse energy. Also, the effect of beam quality factor, wavelength, focal length, and beam diameter was found to match the trend suggested from geometrical optics in equation (2.9). Higher intensities can be achieved by utilizing shorter wavelength, focal length, pulse duration and larger initial beam diameter.

2.1.2.2 Plasma Formation and Flame Kernel Propagation

Though laser ignition has been researched since 1960's, recent studies have brought new insights into the processes associated with laser ignition [70, 79-83] and the picture that emerges can be summarized as follows:

(i) When a high power laser pulse is focused in a gaseous medium, high field gradients are introduced at the focal volume, which result in stripping of the electrons from the local molecules via a multi-photon ionization process. A similar result is attained with cascade ionization if one seed free electron exists because of impurities in the medium. These free electrons, in turn, absorb laser energy via inverse bremsstrahlung absorption, accelerate, and result in the release of more electrons when they collide with other gas molecules. This results in a cascade breakdown leading to the electron concentration increasing almost exponentially with time.

(ii) The resulting plasma kernel is opaque and absorbs the remaining incoming photons. A tear-drop shaped plasma kernel forms that extends towards the incoming laser. As the resulting high-temperatures (~ 50,000 K) and high-pressures (~ 100 atm.) are localized close to the focal spot position, a blast wave develops and propagates into the surrounding gas. This shock wave, though tear drop shaped initially, expands into an elongated ellipsoid before forming a spherical wave as it expands into the surrounding gas. In parallel, the plasma core collapses and fluid elements move from the front of the plasma kernel in a direction opposite to laser propagation. This results in a roll-up leading to an expanding toroid.

(iii) Following the shock wave propagation, energy is transferred to the surrounding fuel-air mixture primarily through advection. In the immediate vicinity where temperatures reach 2000-3000 K, combustion reactions commence and a flame front develops. The energy released in this thin flame region helps sustain an expanding flame that results in “successful ignition.”

The next few paragraphs deliver a literature review on LI plasma formations and flame propagation to the reader in order to understand the reasons leading to an efficient ignition system. Chen *et al.* [84] investigated the spatial and temporal profiles of LI plasma formation in atmospheric pressure. The Nd:YAG laser was operated at the fundamental wavelength with a pulse energy in the order of 100 mJ and 6.5 ns pulse width to develop a plasma in air. The 6 mm laser beam diameter expanded to 2 cm before focusing it with 10 cm focal length lens. The plasma emission was captured with the help of neutral density filter and CCD camera. In general, the laser plasma is smaller by volume, has a spatial symmetry along the beam axis, and quicker than the spark ignition plasma. The uncertainty of absorption (developing plasma) depends on the laser power, if the power is near by the threshold value, the uncertainty increases and the difference in initiation time can be as high as half of the pulse width. Namely, the probability of plasma formation decreases nearby the threshold laser intensity. On the other hand, higher energy reaches the threshold value earlier which increases the absorption time and hence provides a significant reduction in the uncertainty of plasma formation [84].

Several pulses of energy (16-80 mJ) were used to evaluate the absorbed energy within the plasma, the maximum absorption was detected for a pulse energy of 45 mJ. Laser pulses lower or higher than 45 mJ reduced the absorbance because of shorter initiation time, and plasma saturation respectively. The optimum pulse energy was found to be approximately three times the threshold value (16 mJ). Chen *et al.* [84] attributed the lower degree of plasma saturation to the expansion in size. Also, if the pulse energy is higher than the threshold value, plasma might form before the focal point and expands opposite the laser beam.

In another study, Yalcin *et al.* [85] studied the effect of ambient condition on plasma properties such as electron density and temperature by using a focused laser in atmospheric air. It is believed

that the local thermodynamic equilibrium can be achieved in the plasma because the electron density and temperature are high enough to generate collision rate much faster than the radiative rate. A new approach based on Saha and Boltzmann equations was developed and used to estimate the electron density and temperature [85]. Nd:YAG laser at 532 nm, pulse width (10-13 ns), and a pulse energy in the range of 40-150 mJ was focused by 10 cm lens to create the plasma. Also, a spectrometer was employed to analyze the light emission.

They found that the change of plasma temperature and electron density was within 5% by changing the incident laser energy from 4 to 150 mJ, which is within the uncertainty of the experimental setup. However, the expansion velocity increases as the laser energy increase which results in a longer plasma at the same temperature [85]. This study suggests that by increasing the laser energy, the plasma becomes bigger instead of denser or hotter. A similar observation was seen in Strozzi *et al.* [31] experiments; the absorbed energy tend to stabilize at high laser pulse where saturation occurs (around 150 mJ). Any further increase in pulse energy will increase the plasma size, not the temperature or the density.

In Almansour *et al.* laser ignition tests [86, 87], an elongated ellipsoid shockwave was observed by the high-speed camera. Figure 2.4 presents two frames of CH_4/air mixture diluted with carbon dioxide at atmospheric pressure and room temperature. The pulse energy was just above the required to create a plasma in air. The reader is advised to read Appendix A for more details about the experimental setup and Appendix B for effect of CO_2 diluted mixture on LBV measurements. Due to the fact that the flame speed was captured at 20000 fps, the shockwave was seen in only two frames 50 μs apart. One notices that the shape of the shockwave transformed from elongated ellipsoid in the first frame to a perfect sphere after 50 μs (see the black arrows). Also, it is clear that shockwave has a slightly bigger end on the left side, this observation attributed to the fact that

the laser was coming from the left side, where higher absorption occurs as suggested by Endo *et al.* study [81].

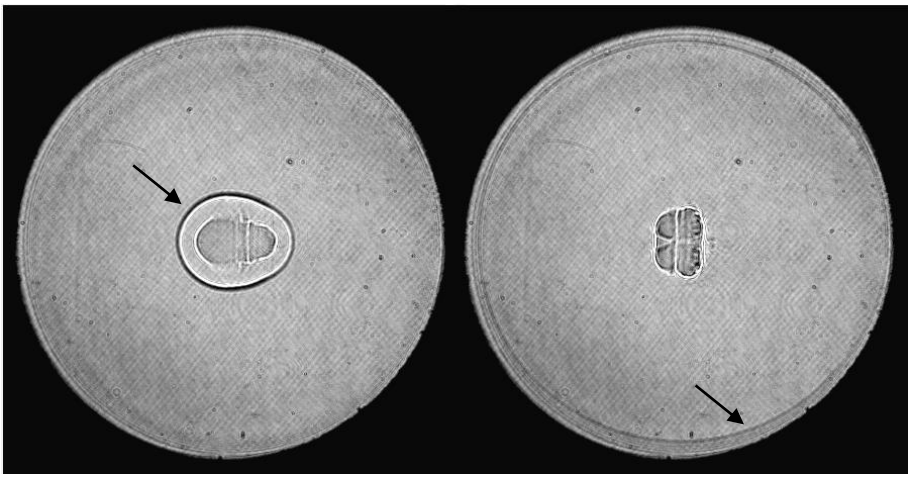

t = 0 t = 50 µs

Figure 2.4. Shockwave formation in methane mixture diluted with carbon dioxide at atmospheric pressure, room temperature, and an equivalence ratio 0.8. Nd:YAG laser at 1064 nm is incident from left side.

Since the behavior of plasma and shockwave formations is not dependent on the mixture composition, further experiments were carried out by using atmospheric air. The high-speed camera setting was altered to a smaller observable window focused on the plasma location. Because of that, the high-speed camera was capable of recording at 67000 fps. The result is shown in Figure 2.5 where the shockwave appears in three frames. It is clear that the elongated ellipsoid shockwave still exists after 14.9 µs, however, after approximately 30 µs small sections of a circular shockwave were observed (see the white arrows). Unfortunately, plasma formation could not be captured even with the 67000 fps; a faster camera is required to study that phenomenon. However, the author believes that plasma forms as tear drop shaped, this explains the shape of the shockwave in the early stage before developing to a perfect sphere.

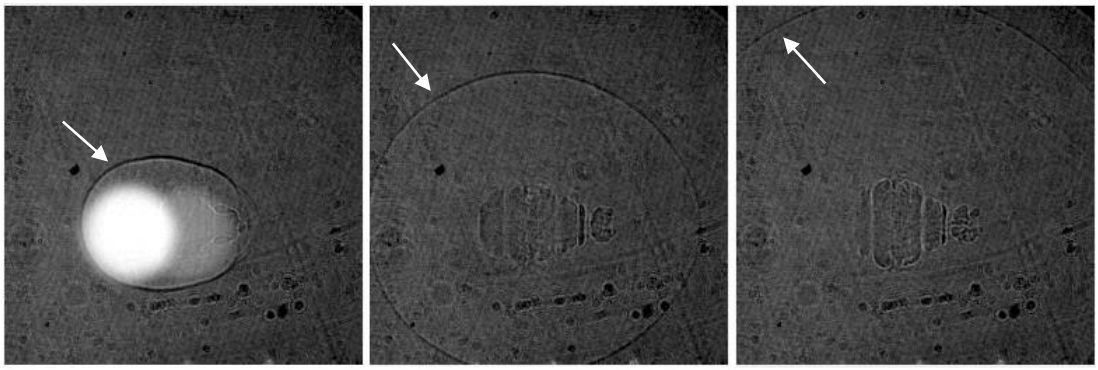

t = 0 t = 14.9 µs t = 29.8 µs

Figure 2.5. Shockwave formation in air at atmospheric pressure and room temperature. Nd:YAG laser at 1064 nm is incident from left side.

Regarding the flame shape, a toroidal flame kernel and propagation has been observed in several laser ignition studies [18, 21, 28, 88, 89]. Two-stage toroidal flame propagation, in the first stage, the flame propagates in a faster rate toward the incoming laser. After developing the toroidal shape, the flame propagates at the same speed in all directions. Figure 2.6 illustrates flame kernel formation and propagation of methane mixture along the first 900 µs of combustion process (frames are 100 µs apart). Several explanations of this toroidal behavior were proposed in the literature; like preheating process by the focused laser beam (ionized gas absorb more laser energy) [28, 81], and the initial flow field due to the radiation laser beam [81, 89, 90]. This flame shape enhances the combustion process by introducing unburned gases to the initial flame kernel (black arrow in third frame of Figure 2.6).

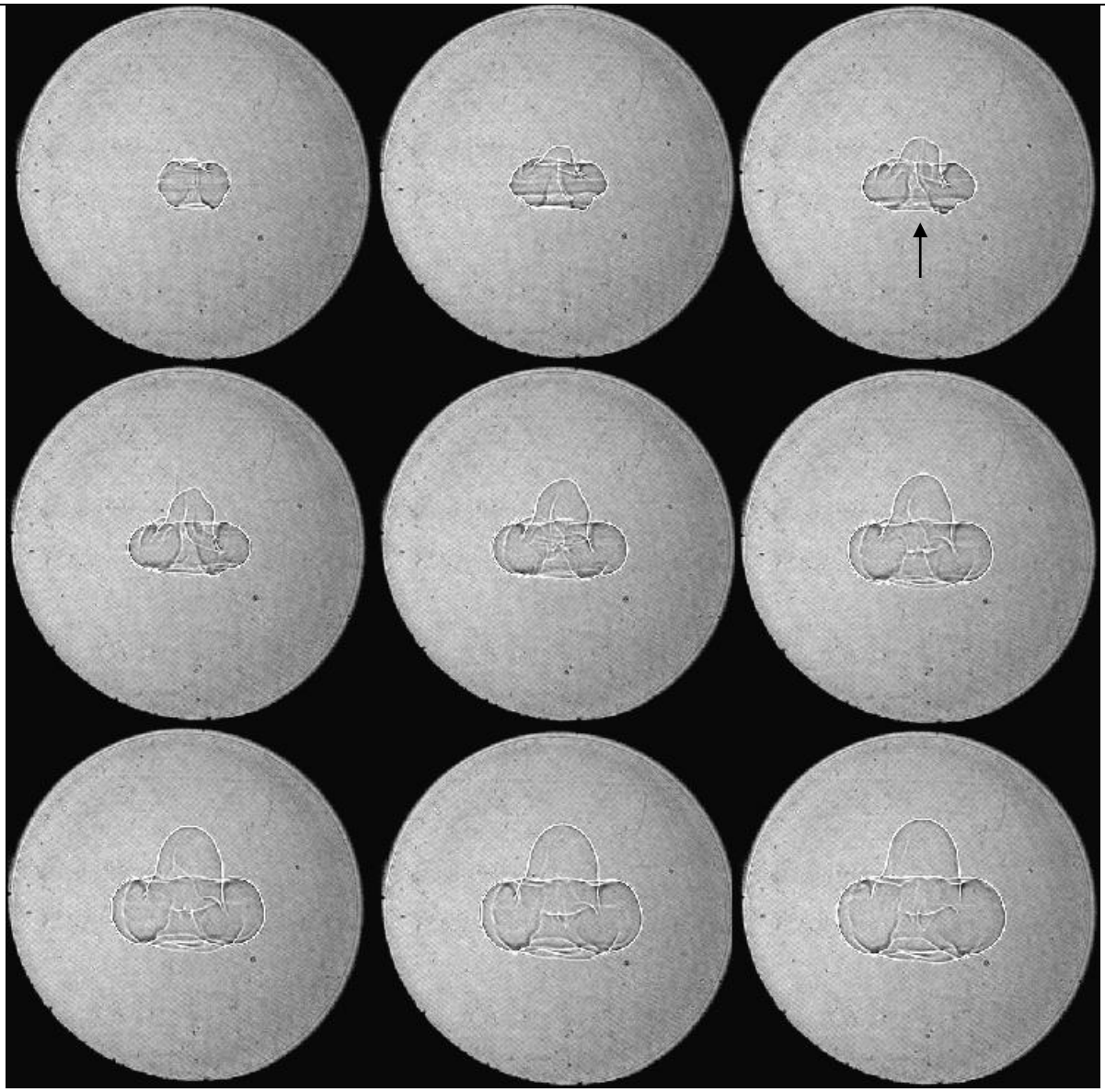

Figure 2.6. Flame kernel formation and propagation of methane mixture diluted with carbon dioxide at atmospheric pressure, room temperature, and an equivalence ratio 0.8. Nd:YAG laser at 1064 nm is incident from top, a toroidal flame is shown (frames are 100 µs apart).

Bradley *et al.* [89] examined the flame propagation of a LI system under quiescent and turbulent environment. Nd:YAG laser at the fundamental wavelength was used to generate pulse energy of 200 mJ for 15 ns to ignite the iso-octane mixture. An elongated ellipsoid shape was noticed for the plasma with the major axis along the laser beam. They attributed the shape to the exponential decay of the absorbed energy with respect to the focal point. Flame propagates after several

hundred μs with a generation of a third lobe which explained by the effect of gas dynamics [89]. Endo *et al.* [81] gave a similar justification for the flame shape, except that a cylindrical plasma was assumed in their analysis. Additionally, Morsy and Chung [88] simulated the initial flame kernel development numerically using a lean methane mixture. A cylindrical plasma was assumed with a symmetric absorption in the direction of laser beam. The kernel shape was attributed to the vortical motion generated by the interaction of pressure field and flow (hydrodynamic effects). It is worth noting that the gas dynamics effects occur in both reacting and non-reacting mixtures.

Recently, Endo *et al.* [81] compared the ignition ability of laser and spark ignition in a quiescent lean-fuel propane/air mixture at atmospheric conditions. Several laser configurations as well as spark ignition system were employed to examine ignition probability, pressure trace, and flame kernel size. One of the laser configurations was with a dummy electrode to provide a setup that has conduction losses such as those exist in SI system. Following a rigorous analysis, Endo *et al.* [81] concluded that improved ignitability of a laser-induced spark is not only due to the avoidance of heat loss to the electrodes, but also due to the initial flame kernel enhancement as its apparent energy is augmented by the rapid heat release from the combustible mixture drawn into the kernel by a non-spherical inward flow which is created by the laser-induced spark.

2.1.2.3 Advanced Laser Ignition Concepts

Multi-point ignition provides spatially separated plasmas that minimizes flame travel path. Radial and longitudinal separation can be used by employing prisms/diffractive lens and multi focal length lenses, respectively. In the literature, up to 4 μlasers were used in a single plug to improve combustion in reciprocating engines. However, the complexity of this concept comes from fitting several optics within a small volume as well as maintaining a good seal on the

combustion chamber. Ronney [64] suggested that the heat transfer losses through combustion chamber wall can be decreased significantly by employing a laminar flow field combustion. In that case, multi-point ignition can be employed to enhance the combustion process where turbulent burning velocity decreases because of a lower gas velocity.

Phuoc [91] evaluated the benefits of multi-point laser ignition in a constant volume combustion chamber for CH_4 and H_2 fuels. Three ignition strategies were tested: (i) a single point near by the wall; (ii) a single point at the center of the combustion chamber; and (iii) two points 37.5 mm apart. Two Nd:YAG laser with a pulse duration of 5.5 ns were used, the pulse energy was fixed to 18.5 mJ for the single pulse tests, and 9.25 mJ per pulse for the two-point ignition. Results showed that the multi-point ignition concept reduces the combustion duration and increases the maximum pressure. Phuoc [91] attributed this observation to the shorter flame path which reduces the time for complete combustion and heat transfer losses to the wall. Also, the effect of multi-point ignition was most prevalent in lean and rich mixtures, due to a lower flame speed. For example, combustion duration of a methane mixture with $\Phi = 0.77$ was reduced from 115 to 75 ms by utilizing the multi-point ignition. In another study, Herdin *et al.* [23] demonstrated similar benefits of multi-point laser ignition, faster and higher heat release was observed in a constant volume chamber. A laboratory scale laser was used to initiate combustion after directing the beam by mirrors and a diffractive lens. Four plasmas were generated from a single laser beam (6 mm), but the plasmas gap was limited to only 5 mm. This is a limiting factor for multi-point laser ignition because the effectiveness of this approach is more evident with a significant plasma separation.

Conversely, laser ignition can also be improved by utilizing several pulses in a single location which is usually referred as multi-pulse or train of pulses laser ignition system. Several studies employed this approach because lasers can be operated at high repetition rate to deliver multi-

pulse without any additional component on the ignition setup, a train of pulses up to 20 has been used [29]. Boker and Bruggemann [92] examined the benefits of multiple laser pulses in hydrogen mixtures, and investigated the wall heat transfer losses relative to the spark ignition system. The experiments were carried out in a constant volume combustion chamber with initial conditions similar to a reciprocating engine, 3 to 25 atm and 420 K. It has been noticed that the multi-pulse laser ignition enlarged the overall flame front with the help of gas velocity. Also, the heat transfer to the wall can be reduced because of the ability to choose the plasma location.

Tsunekane *et al.* [65] conducted tests on a constant volume chamber to evaluate a new design of high-brightness solid state laser (Nd:YAG/Cr:YAG). A pulse energy of 3 mJ was employed in a series of pulses up to 5, in order to ignite a lean mixture after focusing the beam by 10 mm focal length lens. Tsunekane *et al.* [65] proved that multi-pulse laser ignition offers 100% ignition probability by using five pulses for a mixture with equivalence ratio 0.88; spark ignition system, for comparison, doesn't provide 100% ignition probability even at Φ =0.97 [65].

Endo *et al.* [81, 93] evaluated the capability of redirecting laser beams in a constant volume combustion chamber. A corner cube was employed to reorient the laser pulse toward the combustion chamber after developing the first plasma. This concept utilizes a waste energy by forming a secondary plasma that increases laser absorption and enhances the ignition process. The Endo *et al.* concept also delivered consistently higher pressure rise and a bigger flame kernel compared with standard LI system at the same pulse energy (50 mJ). It is worth noting here that increasing the pulse energy with a standard LI system to 64 mj, gave a result similar to the 50 mJ with a corner cube. This behavior was attributed to the fact that the absorbed energy in those cases were identical.

In another approach, Morsy *et al.* [94] and Ryu *et al.* [95] proposed a laser-induced cavity ignition, where the laser is directed into a conical cavity that absorbs and reflects the laser beam toward the apex. Several cavity geometries were assessed, and 40-55 mJ of pulse energy was enough to initiate combustion. A hot gas jet similar to plasma ignition was observed by utilizing a lower ignition energy. Shorter combustion duration and higher maximum pressure were noticed with the laser-induced cavity compared to regular laser ignition system.

2.1.3 Laser Ignition in Reciprocating Engines

The first laser ignition study on reciprocating engines was conducted by Dale *et al.* [96] in 1978. A four-stroke single cylinder engine running at 1000 RPM was employed to investigate the effectiveness of laser ignition on combustion performance under several conditions (equivalence ratio, ignition timing, pulse energy, and plasma location). A CO_2 laser at 10.6 μm wavelength, 300 ns pulse duration, and 300 mJ pulse energy was utilized to ignite the mixture through a window located on the side of the combustion chamber. A higher maximum pressure and a faster pressure rise were noticed but the NO_x emission also increased with the LI system. Dale *et al.* [96] noticed a minimal effect of plasma location except the case where plasma location was very close to the cylinder. The benefit of EGR on reducing the NO_x emission was evaluated by using up to 16% EGR; a lower NO_x emission was achieved. A brake specific fuel consumption (BSFC) vs. NO_x emission map showed that there is a good operating range for laser ignition where lower BSFC can be attained under the same NO_x emission level [96].

After the promising results of Dale *et al.* [96] experiments, several studies [22, 23, 97-99] conducted to assess laser parameters such as focal length and pulse energy on reciprocating engines. While others [75, 100-102] examined the capability of laser ignition to extend the lean

limit of gasoline and natural gas engines. On the other hand, some researchers utilized laser ignition in an advanced combustion concept like direct injection [67] and prechamber ignition systems [103]. A lower brake specific emissions and higher brake thermal efficiency observed in most studies, however, the size of a laboratory laser prohibited the use of such a system in the automotive industry. The µlaser development brought back the attention of laser ignition because of its reasonable size that can be attached directly to the combustion head. This section of the dissertation shows the attractive results of laser ignition experiments with both laboratory and µlasers before discussing some of its limitation and concerns in reciprocating engines.

2.1.3.1 Effect of Laser Parameters

Srivastava *et al.* [22] examined the: (i) heat release; (ii) coefficient of variation in term of indicated mean effective pressure (COV_IMEP); and (iii) engine emissions of a compressed natural gas (CNG) reciprocating engine. A laboratory Nd:YAG laser at the fundamental wavelength with 6-9 ns pulse duration was focused by a 30 mm focal length lens. A sapphire window with a diameter of 12.5 mm and 3 mm thickness was utilized to isolate the focusing lens from the harsh engine environment. The plasma location was adjusted to be exactly in the same position as the spark ignition system. Tests were conducted on a single cylinder engine at 1500 RPM with a spark timing of 25 degrees before top dead center (BTDC). Srivastava *et al.* found that the minimum ignition energy was only 8.5 mJ, however, ignition energies in the range of 9.7 to 24 mJ were tested. It is worth mentioning that the 24 mJ ignition energy (2.82 of threshold value) coincides with the optimum pulse energy suggested by Chen *et al.* [84] for maximum absorption.

The maximum rate of heat release increased by using higher energy pulses, while the trend of the heat released shifted closer to the TDC. This trend was attributed to a higher irradiance by increasing the pulse energy that enhances the combustion process by providing a bigger volume of plasma. However, according to Chen *et al.* [84] study, plasma expands after reaching the saturation level which was defined as three times the threshold value for plasma breakdown. In either event it is clear that the increase of ignition energy improved the combustion process. In addition, Srivastava *et al.* [22] noticed a decrease in the COV_IMEP by increasing the pulse energy. The NO_x emission was constant for a stoichiometric mixture, however, for lean mixtures the NO_x emission increased by utilizing a higher pulse energy. This trend is reasonable because in a stoichiometric mixture, the reaction is fast and a small change in the plasma size produces a negligible difference, unlike the lean mixture that exhibits slow turbulent burning velocity.

In the same experimental setup, Srivastava and Agarwal [100] continued the laser and spark ignition investigation at wide open throttle position for a range of air to fuel ratio and spark timing. LI provided a higher maximum pressure, a faster pressure rise, and a higher rate of combustion. This improvement was attributed to an earlier combustion 1-4° crank angle with laser ignition via changes in ignition delay, time from the laser signal to the start of the combustion compared to the spark process. Such advancement in timing may be attributed to LI provides ignition energy in ~ns time scale, unlike spark ignition system where energy deposition takes ~ 1μs [100]. Lower COV_IMEP, BSFC, CO emissions were observed with laser ignition system. Also, higher brake power and NO_x emission were found, Srivastava and Agarwal [100] believed that the higher NO_x is due to a faster ignition process that results in spark advancement with laser ignition.

In a different study, Srivastava and Agarwal [98] studied the effect of plasma location on the combustion performance. A laser spark plug consisting of two parts (window and lens holders)

was designed to allow 14 mm plasma movement inside the combustion chamber. Figure 2.3B shows a similar configuration were plasma location can be adjusted by changing the spacer width. Nd:YAG laser at 1064 nm with 6-9 ns pulse duration and 15 mJ pulse energy was focused via a 50 mm focal length lens. The evaluation of plasma location was conducted every 2 mm starting from the location of spark ignition system. The effect of plasma position was minimal in terms of brake mean effective pressure (BMEP) and thermal efficiency. However, BSFC decreased to a minimum value by lowing the plasma location 6 mm from the location of the spark plug, beyond which the BSFC increased. Similarly, a faster mass fraction burned was noticed at the 6 mm plasma position. Srivastava and Agarwal [98] attributed this behavior to a lower propagation distance and a reduction in the heat transfer losses. Also, a higher NO_x emission was measured at 6 mm plasma location due to a higher heat release rate.

Mullett *et al.* [97] investigated the effect of focal length (15-36 mm), beam quality and pulse energy by using a laboratory laser on a gasoline reciprocating engine. A flash lamp pumped Q-switched Nd:YAG laser was used at 1064 nm wavelength with different laser cavity apertures 1.3, 2, and 3 mm. The optical plug utilizes a 6 mm diameter, uncoated BK7 plano-convex lens with a 5 mm diameter and 1 mm thick sapphire window. It was noticed that a larger cavity aperture allows higher energies but with lower beam quality [97]. Also, the MIE increases with focal length. This result consistent with the constant volume experiments, because of a bigger focused volume that reduces the maximum intensisty.

It was also noted that the MIE is less than the required for optical breakdown in air because of the increase in both pressure and temperature during the compression stroke. Unlike the study performed by Srivastava *et al.* [22], the combustion performance and stability increases with higher laser pulses until a threshold level, any further increase in laser pulse energy doesn't affect

the combustion process. The reason behind this difference is the small range of ignition energy used in Srivastava *et al.* experiments, where the ignition energy was always lower than the saturation energy. However, Mullett *et al.* [97] found that the pulse-to-pulse variation increases with pulse energy, and elevates the cyclic variation in reciprocating engines. The most successful configuration was with the 15 mm focal length, 3 mm laser cavity, and a 24 mJ pulse energy. Alternatively, the 4 mJ MIE was acheived with a different configuration 15 mm focal length, and 1.3 mm laser cavity. It is worth noting here that the inspection of the laser window after tests revealed that the thermal ablation of CCD on the window maintained a clear laser path. This issue will be discussed in detail in the next sections.

McMillian *et al.* [101] tested the lean and knock limits of a natural gas reciprocating engine by employing SI and LI systems. 68 mJ and >50 mJ ignition energies were used for spark and laser ignition system, respectively. The losses due to window reflection absorption were considered in the calculation of minimum ignition energy, however, the losses in spark ignition were not determined. Due to the fact that the laser plug geometry is different than the regular spark plug, the clearance volume was increased by 1% resulting in a reduction of compression ratio from 13.3 to 13.2. A Ricardo four stroke engine, running at 1800 RPM was employed at several ignition timing, equivalence ratio, and BMEP. In general, laser ignition was capable of igniting leaner mixtures. However, the knock limit was also reduced. Similar to Srivastava and Agarwal [100], McMillian *et al.* [101] found that the combustion starts earlier in LI, ~2° crank angle, at the tested engine speed. Even after compensating for the 2° difference in spark ignition, the spark ignition provided better knock limit.

The lean combustion limit was investigated in Kopecek *et al.* [75] research by using laser ignition on a one cylinder 1 MW reciprocating natural gas engine. A 200 mm focal lens and a

laboratory Nd:YAG laser at 1064 nm with a maximum pulse energy of 150 mJ, and 5 ns pulse duration were used while the reciprocating engine was running at 1500 RPM with several equivelance ratios. It was observed that 15 mJ was enough to ignite the mixture if the pressure is above 10 bar for $\Phi = 0.55$. Also, Kopecek *et al.* [75] noticed an increase in the mean and maximum pressure by increasing the pulse energy from 15 to 60 mJ. Even though 60 mJ pulse energy is above the optimum value suggested by Chen *et al.* for maximum absorption [84], Kopecek *et al.* saw combustion improvement. The lean limit was near to $\Phi = 0.48$, and the lowest NO_x formation was 0.22 g/kWh recorded at $\Phi = 0.49$.

Ahrens *et al.* [99] developed an open path laser plug where plasma location can be changed for two stroke natural gas engines. A laboratory laser with series of mirrors were used to direct the laser toward the optical plug. Four plasma locations were tested, it was found the central geometric spot doesn't give the fastest rate of fuel consumption. This is attributed to the gas turbulence and the variation of equivalence ratio within the combustion chamber. Ahrens *et al.* [99] proved that higher peak pressure and lower cyclic variation could be attained by changing the plasma position compared to the SI system.

Furthermore, Liedl *et al.* [67] showed the benefits of laser ignition in gasoline direct injection by conducting experiments on a single cylinder research engine. The concerns of exposing spark plug electrodes to fuel spray may cause erosion; and the effect of flow velocity within the vicinity of the electrodes are cleared out by LI. A cylindrical mount was designed to change the 50 mm focusing lens position, and a laboratory Nd:YAG laser used with two wavelengths (1064 and 532 nm). Wavelength dependence was not noticed during the experiment, however, there was a reduction of fuel consumption and exhaust gas emission by using laser ignition. The best result was achieved by focusing the laser beam within the fuel spray which is not possible with spark

ignition system [67]. A similar observation has been made by a Graf *et al.* [104] study, in which igniting the gasoline mixture within the spray volume provided the optimum fuel consumption and lowest unburned hydrocarbons in direct injection reciprocating engines.

Herdin *et al.* [23] not only demonstrated a benefit of LI in terms of lower COV_IMEP but also for NO_x emission on a single cylinder reciprocating engine. A laboratory scale laser was used to initiate the combustion after directing the beam by mirrors and a lens. Single plasma laser ignitor provided a faster and higher rate of heat release compared to SI system. Since LI extends the lean limit, a lower NO_x emission was recorded relative to SI and diesel pilot injection ignition systems.

Richardson *et al.* [102] investigated the effect of hydrogen enrichment to reduce the cyclic variations in a lean natural gas engine. It is well known that laser ignition extends the lean operating mode, however, the COV_IMEP increases beyond the manufacturer limits 5% in some cases. Since hydrogen has a higher flame speed than natural gas, it is valid to expect lower COV_IMEP by using hydrogen. A laboratory Nd:YAG laser was used at the fundamental wavelength to generate a 50 mJ, 5 ns pulse that has been directed to an optical plug. A Ricardo single cylinder engine with a compression ratio of 13.3 was used with the help of SI and LI systems, offering approximately the same deposited energy. Tests were conducted at 1800 RPM, by igniting the mixture at a fixed timing 28° BTDC under several equivalence ratios and hydrogen enrichments (0 – 40%).

Richardson *et al.* [102] observed that under the same ignition system and equivalence ratio, the addition of hydrogen increases the NO_x emission. This is inductive of a faster combustion process which in turn increases the in-cylinder temperature and leads to higher NO_x formation. It has been noticed that laser ignition provides a wider operation range in comparison with the conventional spark ignition system. Also, at the same equivalence ratio, same NO_x emission can be achieved by

utilized lower hydrogen enrichment with laser ignition system. On the other hand, the effect of ignition system decreases as the percentage of hydrogen in the mixture increases [102].

Joshi *et al.* [103] investigated three ignition systems on one cylinder of 16 cylinder caterpillar engine at 1723 kW and 1800 RPM. Laser ignition focused in the main chamber, laser ignition with plasma in the middle of a prechamber, and spark ignition with a spark at the end of the prechamber were tested. A laboratory scale Nd:YAG laser was operated at the fundamental wavelength providing 34 mJ at 10 ns pulse duration. A 9 mm focal lens with a sapphire window between two copper rings were utilized to focus the beam either at the prechamber or the main chamber. Even though 100% ignition was observed by depositing plasma in the main chamber, COV_IMEP was higher. This observation is reasonable because prechambers provide partially combusted jets that reduce the combustion duration dramatically. In addition, the results of laser ignition prechamber gave a slight increase of COV_IMEP compared to the spark prechamber. This difference can be attributed to the prechamber volume with laser ignition, it was 18% smaller, and the intensity of the jets are directly correlated to the prechamber volume. Furthermore, the location of the plasma might affect the early flame propagation; turbulent intensity and flow field near by the kernel must be evaluated to understand the increase of COV_IMEP.

2.1.3.2 Multi-Cylinder Engine Operation by Laser Ignitions

Mullett *et al.* [105] ran a multi cylinder engine by employing only lasers and series of mirrors. Two laboratory scale Nd:YAG lasers were used for a four cylinder, four stroke gasoline engine. Two laser pulses at the end of compression and exhaust strokes were utilized in each cycle; the second laser pulse removes window deposits by thermal ablation in order to provide better laser transmission for the subsequent ignition process. Uncoated sapphire windows with 1 mm thickness

and an uncoated BK7 lens were used for optical plugs with the resulting transmission loss found to be nearly 30%. A lower cyclic variation was noticed with LI in comparison with an engine running with regular SI system which suggests enhanced combustion [105].

Bihari *et al.* [106] employed laser ignition system on a six cylinder stationary natural gas engine running at 900 RPM and 15 bar BMEP to extend the lean limit and to enhance engine performance. Instead of directing/mounting a laser ignitor on each cylinder, a single laser can be multiplexed to deliver pulses for all six cylinders. This concept minimizes heat and vibration concerns by keeping the laser away from the engine harsh environment. However, the optical fiber used to deliver laser pulses doesn't maintain the beam quality. Bihari *et al.* [106] utilized a laboratory Nd:YAG laser at the second harmonic wavelength to generate intensity > 200 GW/cm^2. Experiments proved that the lean limit was extended from $\Phi = 0.55$ to 0.52 for spark and laser ignition systems respectively with a COV_IMEP of 15%. Bihari *et al.* [106] concluded that since laser ignition delivers lower COV_IMEP, then higher thermal efficiency can be achieved for the same NO_x emission value but by utilizing a leaner mixture.

Similarly, transmission of the high power laser output using optical fibers has been attempted by Yalin *et al.* [107, 108], however, proved extremely challenging considering the fact that the required peak laser powers were close to the material breakdown thresholds. Alternately, researchers in Japan primarily led by efforts at the Institute of Molecular Science, have devised a scheme wherein the long pulse from a pump laser is transmitted via conventional optical fibers and temporally compressed closer to the spark plug well [109]. Gupta *et al.* [110], have even evaluated the use of free-space transmission and mechanically multiplexing the pulsed laser output among various cylinders of the engine. However, variation in the time-response of electro-mechanical actuators limited the use of this approach to engine speeds lower than 1200 RPM.

Recently, Almansour *et al.* [71] operated a six-cylinder natural gas engine by using µlaser ignitors attached directly on all cylinders. To the author's knowledge, this is the first study in the literature that utilizes only µlaser ignitors to run an engine. More details about the laser ignitors and experimental setup are presented in section 2.3. Engine tests revealed that two consecutive pulses of Nd:YAG laser on each cylinder lowered the cyclic variation, provided a higher average pressure, and a faster heat release. Also, laser ignition extended the lean limit of natural gas engines and provided higher thermal efficiencies under identical NO_x emission levels.

2.1.3.3 µLasers Mounted Directly on Engine Head

µLasers have been designed, tested, and used in several reciprocating engine studies [65, 71, 111-113]. Unlike laboratory lasers that need a special arrangement to direct the laser toward the combustion chamber, µlasers can be mounted directly on the cylinder head. This approach minimized the beam travel distance, enabling less beam divergence, and offered a direct replacement with traditional spark plugs. The simple, inexpensive µlaser designs raised the interest in laser ignition for reciprocating engines, especially with high-pressure applications were spark ignition system does not maintain successful combustion. The only concern in this approach is the effect of temperature on the laser crystal and ignition timing. The literature review shows several proposed designs to overcome the temperature limitation of laser ignition systems as detailed here.

Kroupa *et al.* [112] developed a solid state Nd:YAG laser plug which can be mounted directly on the cylinder head. A side-pumped configuration directly coupled to the laser rod was chosen to create a compact design. The laser provided 25 mJ with 3 ns pulse duration that generates a plasma even with 80 mm focal length. To minimize the heat transfer to the laser, a ceramic spacer was used as insulating material. Tests showed that the laser works properly within a range of +-10°C

from the optimum crystal temperature, this range can be achieved effortlessly with a cooling system. Kroupa *et al.* [112] experiments were conducted for a homogenous and a stratified charge on a reciprocating engine with a blend of iso-octane and n heptane to simulate the gasoline with octane rating 95. The laser extended the lean operating limit from λ 1.3 to 1.5. However, it was noticed that the stratified combustion mode requires more energy to sustain flame propagation. Therefore, the minimum ignition energy was found to be 5 and 10 mJ for homogeneous and stratified combustion mode respectively.

In another study, Myers *et al.* [113] designed a longer life span laser ignition system which has been called high-efficiency side pump (HCEP) laser. The diode pump solid state lasers are sensitive to the changes of temperature, a wavelength centerline drift of 0.25 nm/°C was observed. Since the absorbance of pump band Nd:YAG is narrow, there will be a significant impact on the laser performance. However, Mayer *et al.* used Nd:Glass crystal that delivers excellent absorbance over a wider temperature range. In addition, a new conduction cooled package was installed to minimize the thermal effects. Experiments revealed that the HCEP was running properly even after 43 million shots, which provides ~700 hours of continuous operation. This concept offers an economical solution for reciprocating engines.

Similarly, Tsunekane *et al.* [65] conducted tests on reciprocating engines to validate a new design of high-brightness solid state laser (Nd:YAG/Cr:YAG). The results showed that the laser delay time is not dependent on the pump duration, however, both number of pulses and pump duration strongly affect the jitter of the delay time on the magnitude of 0.5%. The effect of temperature was tested by using a thermo-electric heater attached to the laser. The output energy of a standard Nd:YAG laser decreased by increasing the temperature from 25° to 150°C. On the other hand, the addition of Cr:YAG provided a stable and a higher output energy even at 150°C

crystal temperature, making such a technology feisalbe for automotive applications which have an engine temperature coolant maintined near 100°C.

The reciprocating engine tests were conducted using a commercial Toyota gasoline direct injection, 2 liter, and 4 cylinder engine in the Tsunekane *et al.* study [65]. Engine operation was stable, and no misfire was detected during several minutes of operation with a stoichiometric mixture. The initial LI flame propagates faster and moves freely, unlike SI where the flame propagation is impeded by the electrodes. However, the new laser couldn't ignite lean mixtures on the reciprocating engine because of the limited pulse energy in their design.

Recently, Almansour *et al.* [111] investigated the benefit of laser ignition by using two mounting techniques, directly on the cylinder head and within a prechamber. Initial experiments showed that the laser pulse retards from the intended ignition timing as the temperature of µlaser increases. However, this issue can be circumvented by utilizing a water cooling system to maintain consistent ignition timing. After attaining a tight temperature control, the ignition timing was consistent, and higher thermal efficiencies were observed. The distributive ignition jets minimize the dependence on flame speed, and hence, delivered a faster combustion even with very lean mixtures. Several prechamber geometries were tested at 10 bar BMEP and 1800 RPM. The new approach provided a stable combustion with an increase in brake thermal efficiency of 2.1% while maintaining the EPA limit and industrial standard.

It is clear that several crystals and cooling techniques can be used to provide reliable laser ignition systems for reciprocating engines. Hence, leaner mixtures at higher pressure can be ignited to deliver higher engine efficiencies. Alternatively, as technology proceeds, more efficient optical fibers will be designed to provide higher pulse energy and quality. In that case, a multiplexed

technique similar to the one proposed by Bihari *et al.* [106] study can be employed to place the laser unit away from the high-temperature environment.

2.1.3.4 Window Fouling

In laser ignition systems, the laser ignitor is located outside the combustion chamber, which requires a window for laser beam transmission. The window has to withstand the harsh engine environment, and also provide a long-term operation with minimal reduction of pulse energy [21]. Window fouling is a phenomenon that occurs if combustion chamber deposit (CCD) formed on the window/lens surface. This is a critical topic for laser ignition system because CCD reduces window transmission and ultimately loss of plasma formation in severe cases. Several studies in the literature discussed window fouling [66, 67, 71, 73, 97-99, 101, 102, 104, 105, 111, 112, 114-116], some suggested laser ablation as a solution while other focused on window material or mounting configurations.

The ability of laser pulse to remove CCD depends on the intensity of the pulse at the window inner surface, and the rate of CCD formation. Pulse energy, focal length among other parameters discussed in the optical geometry section 2.1.1 reflect the intensity on that surface. While laser intensity calculation is a straightforward procedure, the estimation of CCD formation rate is complicated and highly dependent on several factors including the operating condition as will be shown. For example, heavy hydrocarbons generate CCD at a higher rate relative to natural gas; and lubricating oil is a primary source of deposits. Some studies proposed a train of pulses while other suggested a pulse at the end of exhaust stroke to ensure a clear path for the ignition pulse [105]. Also, Dearden and Shenton [66] recommended a longer pulse duration to overcome the optical damage that might occur due to the required laser intensity for ablation process. Since the

experimental setup varies from one study to another (test duration, pulse energy, optics, and fuel), the studies that did not encounter window fouling will be shown first. After that, proposed strategies to overcome window fouling will be addressed later.

Since natural gas has several promising characteristics (for lean combustion mode) such as high octane number and relatively clean fuel compared to heavy hydrocarbons, different test durations were investigated in the literature. Inspection of transmission optics after those tests showed that laser ablated deposits and maintained excellent transmission rate. For example, Richardson *et al.* [102] ran an engine for 10 hours; the window withstands the harsh environment without damage or degradation. Similarly, Srivastava and Agarwal [98] did not observe window fouling during 50 hours of natural gas engine operation. McMillian *et al.* [101] used the Ricardo four stroke natural gas engine with several ignition timing, equivalence ratio, and brake mean effective pressure. A clear window was seen after running experiments for approximately 100 hours. Moreover, Almansour *et al.* [71, 111] carried out tests near the lean limit of natural gas reciprocating engines for weeks (>120 hours). The inspection of the plano-convex lens revealed a transparent surface even at the edges.

For liquid fuel, the rate of CCD formation is expected to be higher because of condensation, inhomogeneity, among other variations which are observable in practice but not easily replicable in the lab. Mullett *et al.* [97] employed a Q-switched Nd:YAG laboratory laser to ignite gasoline/air mixture, on one cylinder of the four cylinder engine. Window inspection after operation tests revealed that CCD formed only on the sides where laser does not pass, the laser thermal ablation (self-cleaning) maintained a clear laser path.

Liedl *et al.* [67] tested the ability of laser ignition to remove combustion chamber deposits after running an engine with SI system and attaching a window on the combustion head for 20 hours. A

dark layer of CCD was observed; however, laser ignition ran the engine successfully from a cold start (even with the dark layer). They concluded that the laser pulse clears the laser path, a higher laser pulse was recommended for the first few cycles to ensure the removal of deposits [67]. Liedl *et al.* also suggested multi-pulse laser, the first pulse will be used to remove window deposits while the other one ignites the mixture if the first one did not.

Griffith *et al.* [114] investigated the removal of combustion chamber deposits by altering plasma positions relative to the window. Nd:YAG laser at 532nm wavelength, 200 mm focal length, and borosilicate window covered with a graphite spray (0.15 mm) were used in a constant volume chamber. The intensity within the inner window surface was changed by moving the chamber. Also, single and two pulses techniques were employed with the same total pulse energy.

Griffith *et al.* found that if the window placed 10 mm before the plasma location, only a 7 mJ pulse is needed to remove the carbon layer. That is attributed to the fact that laser intensity decreases exponentially with distance from the focal point; this energy is even lower than that required to create a plasma in air [114]. Furthermore, it has been noticed that to ensure 100% removal of the graphite layer by using a total energy of 15 mJ, the window must be placed 25 mm and 50 mm from the focal point for single and two pulses respectively. Even though each pulse in the two pulses technique is half the energy, the two pulses provided substantial removal of the deposited layer and offered wider range of ignition energy.

Griffith *et al.* believed that there are two mechanisms for removing CCD, vaporization, and impact; impact removal occurs when a significant amount of the deposited layer is displaced from the pulse [114]. Therefore, employing multiple pulses improves the laser ablation process. The two-pulse technique was recommended because it offers a broader operation range in terms of laser energy and mounting position in comparison with a single pulse ignition system. It is obvious

that maintaining a clear laser path was accomplished by employing multiple pulses or shorter focal length lens with lower laser energy. This finding is crucial for laser plugs where optical damages might occur in some designs because localized heating causes a thermally induced local stress. The unconstrained expansion will enable the transfer of shear stresses into the surrounding area of the optical window which in turn enables relatively easy fracture of the window.

Ahrens *et al.* [99] investigated the effect of optical substrate on window fouling, BK7, and fused silica lenses were used on a two-stroke engine. Two stroke natural gas engines are expected to generate higher rate of CCD formation because, large quantities of lubricating oil are burned during tests. The engine stopped after running 12 hours with the BK7, however, the fused silica maintained proper ignition without misfire for 21 hours. It is evident that the optical substrate influences combustion chamber deposit formation due to the change in thermal properties and the surface layer interactions with the adjacent gas phase.

In another investigation, Graf *et al.* [104] examined optics contamination and self-cleaning effect of laser ignition on gasoline engine. Two optics configurations, separated and combined optics (explained earlier in section 2.1.1) were tested on a two-cylinder engine for 200 hours. The combined optics provided ignition at a lower pulse energy, however, the separated optics offered better self-cleaning and longer test duration. This is attributed to the laser intensity at window inner surface that can be increased by focusing the laser beam from a longer distance in the separated optics configuration.

Several laser energies (40 mJ, 45 mJ, and 50 mJ) were utilized in Graf *et al.* study [104]. Misfire was noticed after 7 and 31 hours for a pulse energy of 40 mJ and 45 mJ respectively. On the other hand, 50 mJ pulse was successful without misfire for 200 hours of continuous operation. Indicating a significantly higher laser power is used, though at 200 hours that would correspond to ~12k miles

on the highway which is approaching a reasonable service limit. In addition, 50 mJ pulse was able to clean windows that had CCD from earlier tests (40 mJ and 45 mJ) and provide continuous operation. It seems that in this study the 50 mJ provided intensity just below the required for complete laser ablation. Furthermore, the transparency of the window was checked by using spectra-photometric measurements, which consisted of an incoherent light source, beam collecting optics, and a photodetector. carbon, silicon, zinc, and phosphor were found in the CCD formation after analyzing it which suggests that those deposits generated from lubricating oil and combustion residue.

Similarly, Kroupa *et al.* [112] inspected the laser plug after running homogeneous and stratified charge gasoline combustion. CCD were covering only the outer lens area where laser light does not pass. They concluded that three to five pulses cleared the window and sustained the combustion process [112]. The conclusion of this study agrees with Griffith *et al.* [114] recommendation, multi-pulse laser ignition is more efficient strategy for laser ablation than a single pulse with higher energy.

In another approach, Ranner *et al.* [115] investigated the laser ablation mechanism on a reciprocating engine running with spark ignition. A small gasoline engine that has a high gasoline and lubricating oil consumption was modified and used as a testbed. Running the engine for 1 hour generated a thick layer of CCD which estimated to be a worst-case scenario for regular gasoline engines. Nd:YAG laser at 1064 nm with a pulse energy in the range of 80 mJ and 5 ns pulse duration was used to remove the contamination on ALON window. The location of the focal lens was changed to provide a range of laser intensity on the inner surface.

Ranner *et al.* [115] determined that 10 mJ/mm^2 energy density is needed to remove carbonaceous and mineral deposits. Optical microscopy, secondary scanning electron microscopy,

and energy dispersive x-ray spectroscopy diagnostic tools were used for the windows. The element spectrum of a new ALNO window was compared with the tested windows before and after the cleaning mechanism (laser). The ablation process removed zinc, phosphorus, calcium, and sulfur. A small trace of carbon was still detected after their cleaning mechanism, however, the detected quantity (1 μm) will not disturb the ignition process.

Since laser diagnostic techniques provide valuable information such as temperature, species concentration, and equivalence ratio, Alfier *et al.* [116] examined window transmission. Errors in spectroscopy diagnostic techniques (SDT) which may arise because of window contaminations that lower laser transmission and correspond to underestimation of electron density and temperature. The fundamental wavelength of a Nd:YAG laser with energy pulses of 25-330 mJ was utilized to remove windows contamination. Since the laser pulses were delivered through an optical fiber, the threshold power that provides effective cleaning without damaging the optical fiber was determined by varying the input laser power. After that, the irradiance of the beam was changed by moving two lenses with respect to the windows (fused silica).

Alfier *et al.* [116] noticed that 40 mJ is required to clean window in an open laser path, however, experiments where laser transmitted through an optical fiber, 80 to 100 mJ was needed to compensate for transmission losses. Before cleaning windows, the transmission was measured to be in the range of (5-30%) in compression to (60-80%) for new windows. The single pulse 40 mJ, 8 ns with an average energy density of 8 mJ/mm^2 was capable of recovering 90-97% of the initial transmission. Unlike other investigations, Alfier *et al.* [116] found that a lower energy doesn't recover the loss of transmission even with multiple pulses. At an average density of 4 mJ/mm^2, only a small section in the center recovers 90% of the transmission while remaining area recovered only 60%. That is mainly because the intensity changes with radius based on the beam profile. The

threshold value was estimated to be in the range of 0.6-1.2 MW/mm^2 [116]. This observation is opposite to what Griffith *et al.* found in [114] where two low energy pulses delivered better laser ablation. The difference can be attributed to the fact that in Griffith *et al.* study [114] even the low energy pulse may produced an intensity higher than the threshold value for removing CCD.

2.2 Laser Characterization and Measurements of Methane LBV Under Spark and Laser Ignition Systems

In this section, laser and spark ignition systems are evaluated in a constant volume chamber under several initial conditions in order to understand the reasons leading to an efficient combustion. Laminar burning velocities of CH_4/air are obtained by using the University of Central Florida (UCF) spherical combustion chamber and utilizing the constant volume approach. High-speed shadowgraph photography is utilized to present the flame development and propagation in select cases. First, the lean flammability limit of CH_4/air mixtures is studied by using a Nd:YAG laser ignition system. Pressure traces as well as flame images are presented near the flammability limit. Additionally, three LI energies are used to evaluate their effect on the pressure trance as well as the LBV. CH_4/air mixtures are evaluated for an initial temperature of 297 and 393 K, equivalence ratio range 0.7-1.4 and an initial pressure of 1 and 3 atm. It is noticed that the maximum burning velocity for CH_4/air occurs at an equivalence ratio of 1.05. LBV values obtained using spark ignition (SI) system are compared against those determined by LI system. It is found that the spark ignition provides a higher maximum pressure, and the two ignition systems offer laminar burning velocity values within 2.7%. The results are compared with the laminar burning velocity in the literature and the predicted values obtained by CHEMKIN PRO [33] software using GRI-Mech 3.0 [34] and ARAMCO-Mech 1.3 [56] mechanisms.

Since the spherical combustion chamber is a new facility, validation experiments were conducted to assess the consistency, uncertainty, and feasibility of the experimental setup. The reader is advised to review Appendix A for a detailed description of the spherical combustion chamber and its utilities; design limitations, measurements accuracies, and experimental procedure are also stated. The LBV of CH_4/air mixtures has been studied extensively in the literature, which

makes the fuel a good candidate for calibration of post-processing. Easy mixture preparation at room temperature, Lewis number ~ unity, and linear relationship between the propagation speed and stretch rate are important factors in obtaining accurate LBV measurements. CH_4/air mixture possesses all those excellent combustion properties, and considered a promising fuel for lean combustion mode as explained in Chapter 1.

2.2.1 Methane LBV Studies

Recently, Tahtouh *et al.* [117] obtained the laminar burning velocity of the CH_4/air mixture at room temperature and atmospheric pressure by using a linear extrapolation method. A novel method was introduced to minimize the amplification of experimental noise on the LBV by obtaining an exact solution of the flame radius via a first-order non-linear ordinary differential equation (3.18) [117]. Miao and Liu [118] determined the effect of nitrogen concentration on the laminar burning velocity of the CH_4/air mixture. Both linear and nonlinear extrapolation methods were used in the analysis of LBV, results show that the stretch model effect is insignificant in the case of CH_4 as both models give similar results [118]. However, the Markstein lengths obtained by using linear method are slightly higher than those from the nonlinear approach, especially at rich mixtures. Miao found that the LBV decreases and the flame stability increases by increasing the N_2 concentration [118]. This reasonable observation can be attributed to the variation of Lewis number with N_2 concentration as shown in Figure 2.7.

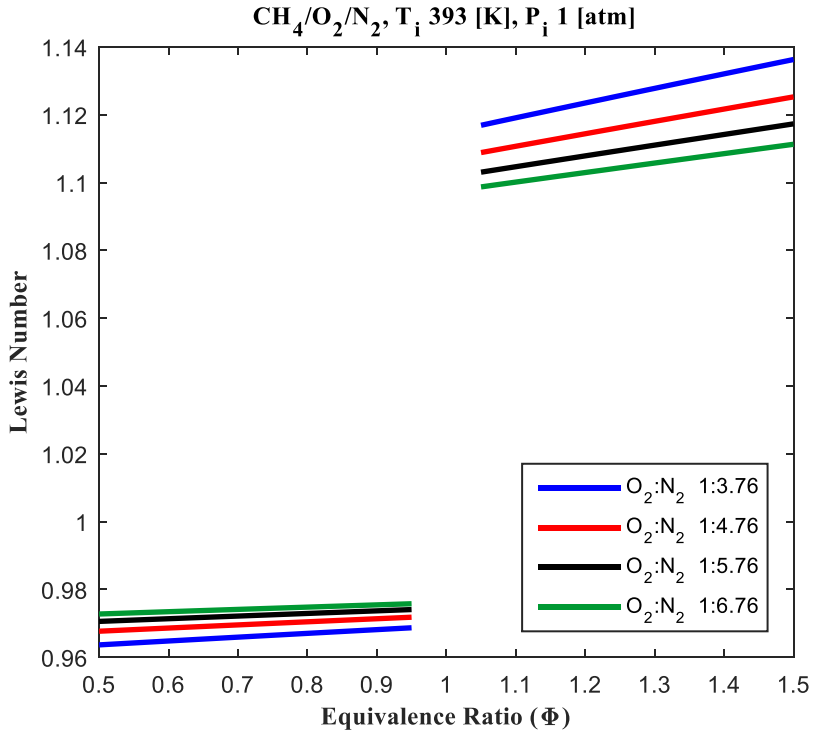

Figure 2.7. Lewis number variation for methane mixture diluted with several nitrogen proportionalities.

The above figure demonstrates the change of Lewis number versus equivalence ratio at 393 K and 1 atm. Four N_2 concentrations in the range of (3.76 to 6.76) were assessed, it is evident that the deviation from unity Lewis number decreases as N_2 concentration increases. This fact suppressed the diffusional-thermal instability for lean mixtures. In contrast, the density difference between burned and unburned gases promotes hydrodynamic instability. This matter was not crucial in Miao and Liu's [118] study as the early part of the combustion process was utilized for the constant pressure approach. However, the increase of density difference along one isentrope during the combustion process promotes hydrodynamic instability in the constant volume approach. LBV decreases because of the cooling effect of diluent as its proportionality increases in the mixture. Namely, N_2 reduces the adiabatic flame temperature which has a direct effect on mixture reactivity and LBV. At high N_2 concentrations, care must be taken in the evaluation of

LBV because body forces and heat transfer losses will dominate and must be considered in the combustion model.

Bradley *et al.* [119] carried out a numerical investigation based on spherical flame propagation where explosion, implosion, and stationary flames are studied. They found that ignition energy effects are negligible on LBVs if the flame radius is bigger than 6 mm. Additionally, the effect of strain rate and flame curvature on stretch rate were examined. Recently, Jayachandran *et al.* [120] considered the molecular transport and thermal radiation loss in the assessment of LBV data by using a one-dimensional direct numerical simulation. In general, a mixture with Le≠1 or a mixture with a noticeable difference between fuel and O_2 diffusivity results in a bigger extrapolation error. Also, Jayachandran found that for heavy hydrocarbons, the sign of the Markstein number changes from positive to negative for lean and rich mixtures respectively. In addition, the effect of stretch on the flame of rich and lean mixtures are characterized by the differential diffusion and Lewis number respectively [120]. Also, the result of radiation runs shows that the cooling of burned gases increases away from the stoichiometric condition due to a longer combustion event which results in a systematic underprediction of the LBV values.

Several values of methane flammability limits were reported in the literature. Tahtouh *et al.* [117] ignited CH_4/air mixtures at $\Phi = 0.55$ with spark ignition system; the minimum ignition was noticed to increase with lean mixtures. In Wang *et al.* [121] investigation, the LBV of CH_4/air mixture near the lean flammability limit was studied under microgravity condition; they successfully ignited a mixture with an equivalence ratio of 0.512. Alternatively, Dumitrache *et al.* [122] initiated methane combustion at $\Phi = 0.4$ by utilizing rapid compression machine (RCM) and a laser ignition system. RCM compressed the test mixture to an extent below the auto-ignition (782 K and 39.7 atm) just before forming the laser plasma.

Farrell *et al.* [123] obtained the laminar burning velocities of 45 hydrocarbons by using an experimental setup similar to the one used in this study. Farrell utilized the constant volume approach and Metghalchi and Keck [124] model to obtain LBVs by LI and SI systems; negligible differences was found in LBV measurements using these two ignition methods. Also, Bradley *et al.* compared the laminar burning velocity of laser and spark ignition system by tracking the flame position with respect to time which is referred to as the constant pressure approach [125]. The study concluded that, if the spark ignition energy is just enough to initiate flame, the LBV obtained with laser ignition system is only higher at the beginning of the combustion process. The main reason for that difference is the conduction losses in spark ignition experiment; after a radius of 36 mm (larger radius), the flame speed of the spark ignition system was close to that obtained by laser ignition system [125].

In this section, laser and spark ignition systems are employed to investigate several combustion properties of the CH_4/air mixture. The laser characteristics are shown before discussing the experimental uncertainty. The validation of methane experiments, flammability limits, and the effects of ignition energy are presented in the result section. The LBV of CH_4/air mixture at several equivalence ratios and initial conditions are studied by utilizing two ignition systems are presented next. Finally, the laminar burning velocity is compared with recent experimental results and numerical predictions from the literature.

2.2.2 Combustion Model

In this work, LBV has been calculated by using the constant volume method, which requires evident pressure change during the analysis which occurs after the flame has grown to a large size. A detailed discussion on LBV theory and thermodynamic models is given in Chapter 3. The

original Metghalchi and Keck model [124] was used for this section. The burned and unburned mixture properties (specific heat ratio and enthalpy) are found from NASA polynomials (taken from GRI-Mech 3.0 [34] thermo file); the highest thirteen species are utilized to reflect the burned gas properties.

Detailed description of the UCF spherical combustion chamber facility including ignition systems, pressure measurements, shadowgraph imaging system, and fuel/oxidizer mixture preparation are provided in Appendix A. The schematic representation of the experimental setup with laser ignition (LI) system is shown in Figure 2.8. The ignition setup consists of the 1064 nm laser pulse passing through a simple bi-convex lens with the focal plane centered in the spherical combustion chamber. The laser pulse passes through a focusing lens and two quartz windows before it reaches the ignition point; windows thicknesses were 3.175 mm and 12.7 mm for the oven and sphere respectively. Since the primary aim of this effort was not investigation of minimum ignition energy, reflection and absorption losses were neglected for simplicity. The reported values were measured using an energy meter (Coherent J-50MB-YAG) and a beam splitter; therefore, it is a pulse energy rather than absorbed ignition energy. In the tests presented here, a pulse energy of 155 mJ was used which was just above the minimum threshold energy for plasma formation. In addition, two pulse energies 227 mJ and 356 mJ were employed to investigate the effect of pulse energy on LBV.

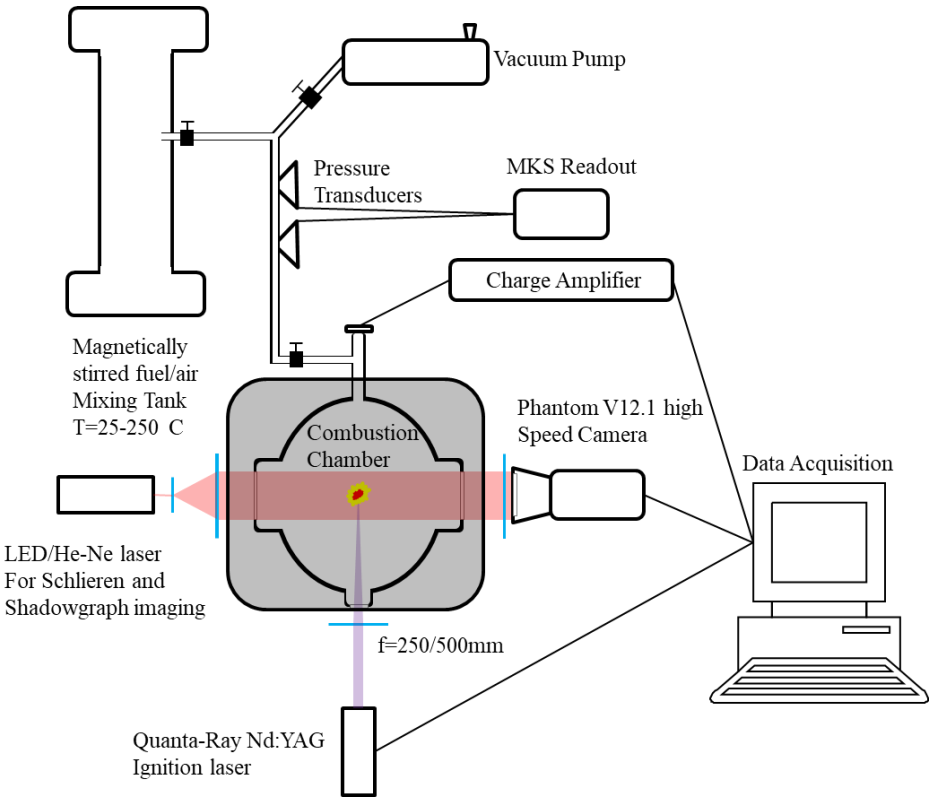

Figure 2.8. Schematic representation for the experimental setup with laser ignition system.

2.2.3 Laser Characterization and Stability

Laser beam profile and characterization is imperative in understanding the initial plasma development and consequently the ignition process. Non-ideal beam profiles lead to excess energy requirements and can influence plasma development. As the focus of this study is centered on flame propagation as opposed to plasma formation characteristics, only a rudimentary characterization of the laser was conducted. The minimum pulse energy required for the formation of plasma via optical breakdown was approximately 155 mJ. This reported pulse energy is higher than the range of values reported by other authors (15 mJ to 100 mJ) [21, 126]. One reason for this comes from the geometry of the optical ignition setup. The diameter of the focal waist size is directly proportional to the laser wavelength and lens focal length; and indirectly proportional to

the initial beam diameter (before the focal lens). An approximate expression for the diameter of the focal waist has been given in section 2.1.1 (see equation (2.8)).

Here, relatively long focal length lenses (500/250 mm) were used because the chamber placed in an oven, as well as an unexpanded input laser beam into the lens leading to a reduction in the energy density at the focal plane. A second justification for the high pulse energies reported comes from the laser operational energy. It is known that Nd:YAG lasers typically experience a reduction in beam quality when operated below their maximum power. Since the laboratory laser was operated at roughly 15% of its full range, it is reasonable to expect a reduction of beam quality, hence, higher pulse energy was required to achieve the energy density required for plasma formation. Figure 2.9 shows the probability of plasma formation as a function of the laser pulse energy as well as the shot to shot energy fluctuation. The probability of plasma formation increases to approximately 70% at the energy level of 155 mJ used in this study.

50 shot sample of the inherent shot-to-shot energy fluctuations were recorded for a mean energy level slightly above the plasma formation threshold. Shot to shot energy fluctuations were characterized using a Coherent J-50MB-YAG detector, where the beam was found to have a standard deviation of 5 mJ yielding a pulse uncertainty of 10 mJ at 95% confidence. The pulse energy is of importance in affecting the kernel formation and the beginning of combustion process. However, energy fluctuations of 5-10% will have virtually no impact on the burning velocity as will be shown later. Therefore, despite small laser flaws, the pulse quality was sufficiently high to provide an ignition source which would yield reliable data for propagation studies.

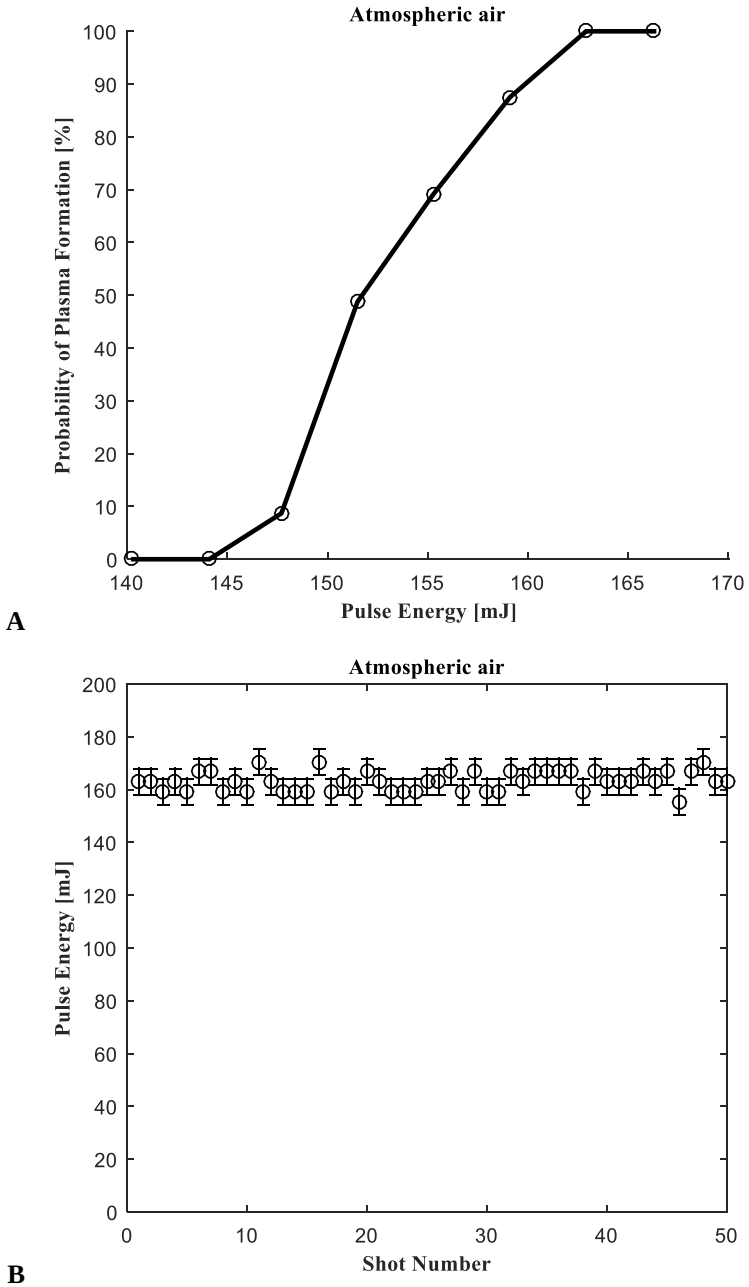

Figure 2.9. Laser characterization for quanta-Ray Lab 190 Q-switched Nd:Yag, probability of Plasma formation (a), and energy fluctuations (b).

2.2.4 Consistency and Uncertainty

Consistency analysis is a crucial part of experimental investigations. Since the pressure is recorded during the combustion event, the author decided to present the inconsistency in terms of

the variation of pressure traces during the combustion process. Several experiments carried out for CH_4/air utilizing both SI and LI systems at different initial conditions; the comparison of pressure traces of all tests showed consistent results. It is evident in Figure 2.10 that the three runs are virtually identical with a negligible difference in run #2. The maximum difference found to be less than 0.01 atm between runs 1 and 3 in the utilized region for LBV measurements.

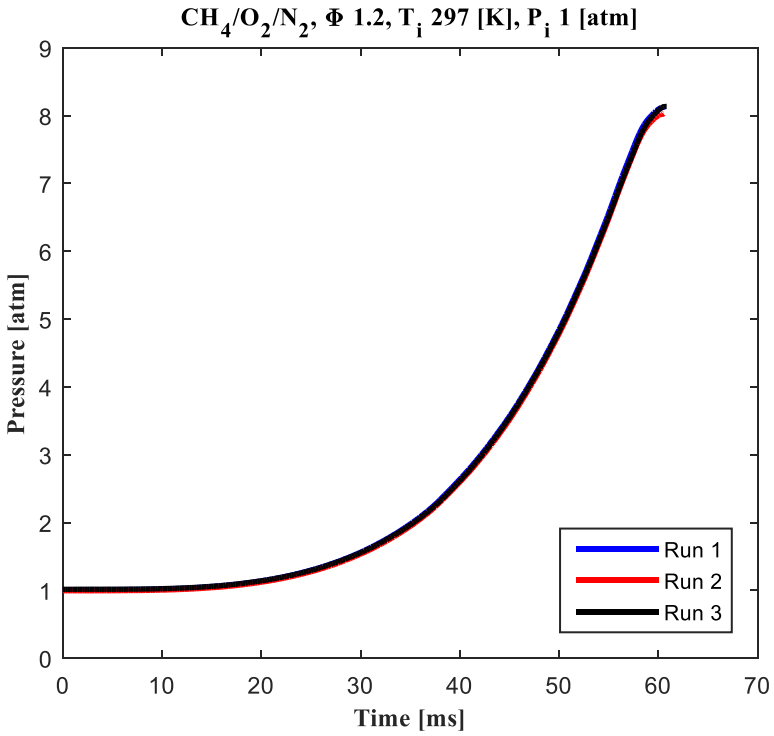

Figure 2.10. Pressure traces of CH_4/air mixture ignited by a spark ignition system at an equivalence ratio of 1.2.

The uncertainty of experimental measurements depends on several factors such as environment condition, sensors accuracies, and experiment/analysis procedure. For example, the contributions of fuel preparation and mixing process occur from the entrance of atmospheric air into the system, chamber vacuum limit, and accuracy of 628 and E27 MKS Baratrons. Also, the accuracy of 603B1 Kistler dynamic pressure transducer and thermocouples are possible causes of measurement uncertainty. Additionally, LBV calculation and extrapolation methods (filtering and curve fitting)

also have a direct effect on LBV values. Therefore, all those factors must be considered in the uncertainty analysis. Since two ignition systems were used in this study, uncertainty analysis was performed for laser and spark ignition systems to evaluate their influence. Table 2.2 provides the result of each parameter for CH_4/air mixture at Φ 1; the total uncertainty in current experiments is around 5.8% and 3.8% for laser and spark ignition systems respectively.

Table 2.2. Uncertainty analysis for CH_4/air at Φ = 1.

Uncertainty source	**Laser ignition**	**Spark ignition**
Initial pressure	(+-) 0.84%	(+-) 0.74%
Initial temperature	(+-) 0.54%	(+-) 0.18%
Mixture composition	(+) 1.8%, (-) 3.82%	(+) 1.8%, (-) 2.3 %
LBV curve fitting	(+-) 3.11%	(+-) 2.1%
Random error for 3 experiments	(+-) 3%	(+-) 2%
Overall uncertainty	5.80%	3.8%

2.2.5 CH_4/air LBV Results and Comparisons

The general trend of LBV was observed were CH_4/air mixture burning velocity increases and decreases by increasing the initial temperature and pressure respectively. For the first sets of experiments conducted by LI at room temperature, the equivalence ratio was changed from 0.9 – 1.3 in steps of 0.2 in addition to stoichiometric ratio. The laminar burning velocity changes from 29.51 cm/s at Φ = 0.9 to 36.58 cm/s at Φ = 1. The second sets of experiments carried out at an initial temperature of 393 K for four equivalence ratios (0.8 – 1.4) in steps of 0.2. This result is presented in Figure 2.11 (pressure traces) and Figure 2.13 (LBV), it is obvious that the fastest burning velocity was noticed for a stoichiometric mixture, as the 1.05 equivalence position was skipped. A similar conclusion can be made from the pressure traces figure (faster pressure rise relative to other Φ's). Also, the laminar burning velocity increased from 24.79 cm/s to 57.02 cm/s

by varying the equivalence ratio from 1.4 to 1 respectively. The observed maximum burning velocity occurs at an equivalence ratio of 1 for the two sets of experiments with laser ignition. However, the trend of data points suggests that a maximum value for a slightly rich mixture similar to the one obtained by numerical prediction.

Figure 2.12 presents the flame propagation of CH_4/air mixture with LI system at $\Phi = 1$ and initial temperature of 393 K. It is clearly that an elongated ellipsoid flame (vertical to the laser beam) was formed up to 1 ms due to the laser ignition effects. This shape is attributed to gas dynamics near the plasma as described in Bradley *et al.* [89] study. However, flame grows toward a spherical shape as illustrated in the figure after 4.5 ms. Also, the LBV model requires an evident pressure change which does not happen while the flame propagates within the observable window. This fact increases the model feasibility of utilizing a nearly spherical flame spread. It is worth mentioning that the window diameter is only 47.24 mm, and the figure shows the early flame propagation 4.5 ms from a combustion event that lasts 36.3 ms. Additionally, tests at different initial pressures were also conducted at room temperature, and the author found that the LBV at $\Phi = 1$ decreased from 36.58 to 24.97 cm/s by increasing the initial pressure from 1 to 3 atm.

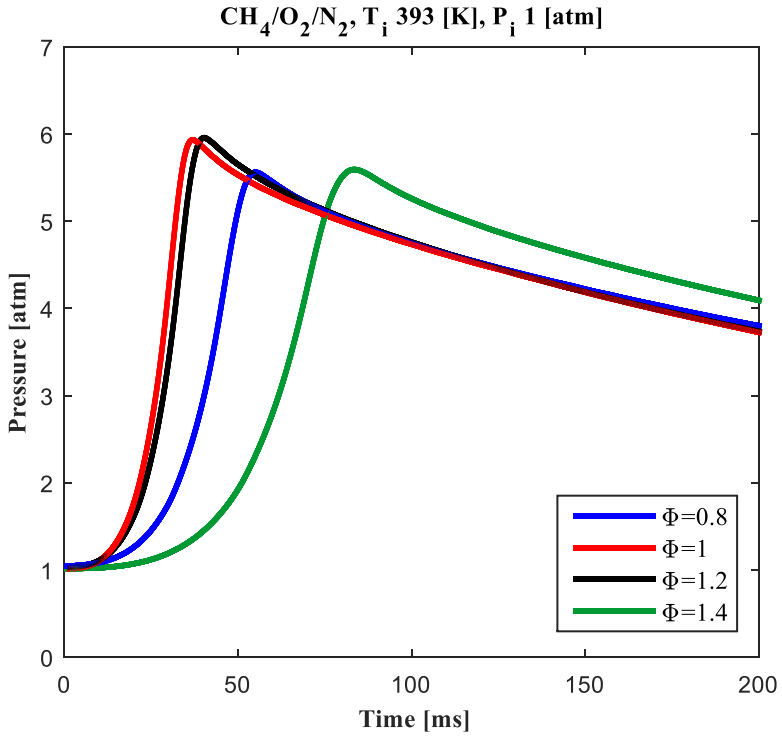

Figure 2.11. Pressure traces of CH_4/air mixture at an initial temperature of 393 K and 1 atm initial pressure.

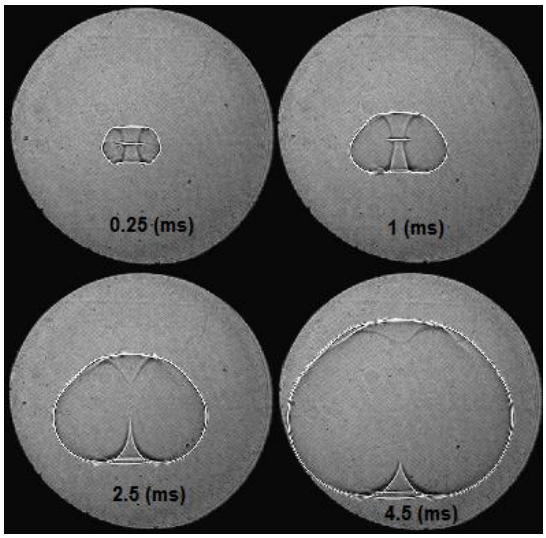

Figure 2.12. Flame propagation of CH_4/air mixture at equivalence ratio 1, 393 K initial temperature and 1 atm initial pressure. Laser enters from top.

CH_4/air LBV data at 297 K and 1 atm are compared with experimental and numerical studies in the literature [117-120]. A good agreement is illustrated in Figure 2.13 between all studies, especially in the range of Φ = 0.9 to 1.2. However, there is a noticeable deviation at an equivalence

ratio of 1.3. The numerical data points obtained by Bradley *et al.* [119] is much slower than the experimental values in this work and those determined by Tahtouh *et al.* [117]. This difference reveals the importance of using advanced chemical kinetic mechanisms for numerical simulation. Conversely, Jayachandran *et al.* numerical simulation provided good agreement at $\Phi = 1.3$. Bradly *et al.* [119] and Jayachandran *et al.* [120] numerical prediction of LBV are slightly higher than the experimental data near the stoichiometric region; such variation is inductive to heat transfer losses encountered in experimental setup. A similar deviation between numerical and experimental results has been noticed in this study after obtaining the LBV by using the one-dimensional premixed flame model in CHEMKIN PRO [33] (shown later).

The variation between our experimental values and Tahtouh *et al.* results were 4.8 and -2.9% for $\Phi = 1$ and $\Phi = 1.3$ respectively. This is attributed to the experimental method (constant pressure or volume approach), and thermodynamic model (Metghalchi and Keck) used in the analysis. The reader is advised to review chapter 3 for better exposure on thermodynamics models (multilayer models provide accurate LBV values).

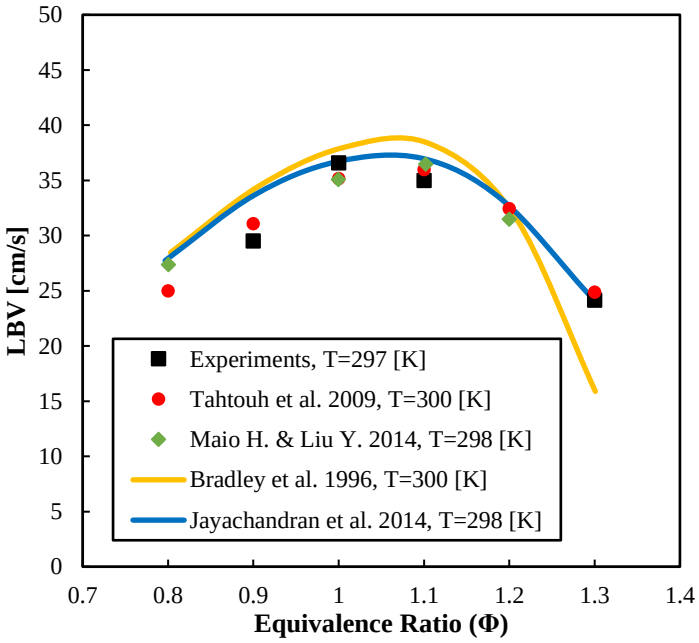

Figure 2.13. The laminar burning velocity for CH_4/air mixture at 297 K and 1 atm initial pressure are illustrated with those from Tahtouh et al. [117], Maio H. & Liu Y. literature [118], Bradley et al. [119]and Jayachandran et al. [120].

The author determined the laminar burning velocity by using CHEMKIN PRO [33] software as a second reference to validate the spherical combustion chamber. Both GRI-Mech 3.0 [34] and ARAMCO-Mech 1.3 [56] chemical kinetic mechanisms have been used for different initial conditions and equivalence ratios. These two mechanisms are discussed in detail in chapter 3; number of species, chemical reactions, and validation range are presented in Table 3.2. Figure 2.14 compares the CH_4/air experimental values at two initial temperatures with CHEMKIN PRO numerical prediction. ARAMCO-Mech 1.3 provides LBV values closer to the experimental results for lean mixtures, while GRI-Mech 3.0 gives a better estimation for rich mixtures. The LBV trend, as well as location of maximum value using SI system has a better agreement with the GRI-Mech 3.0 mechanism. Even though the experimental data are very close to the predicted results, the numerical values are slightly above the experimental values. That is mainly because of the simplified kinetics used in the simulation, and heat transfer losses during experiments.

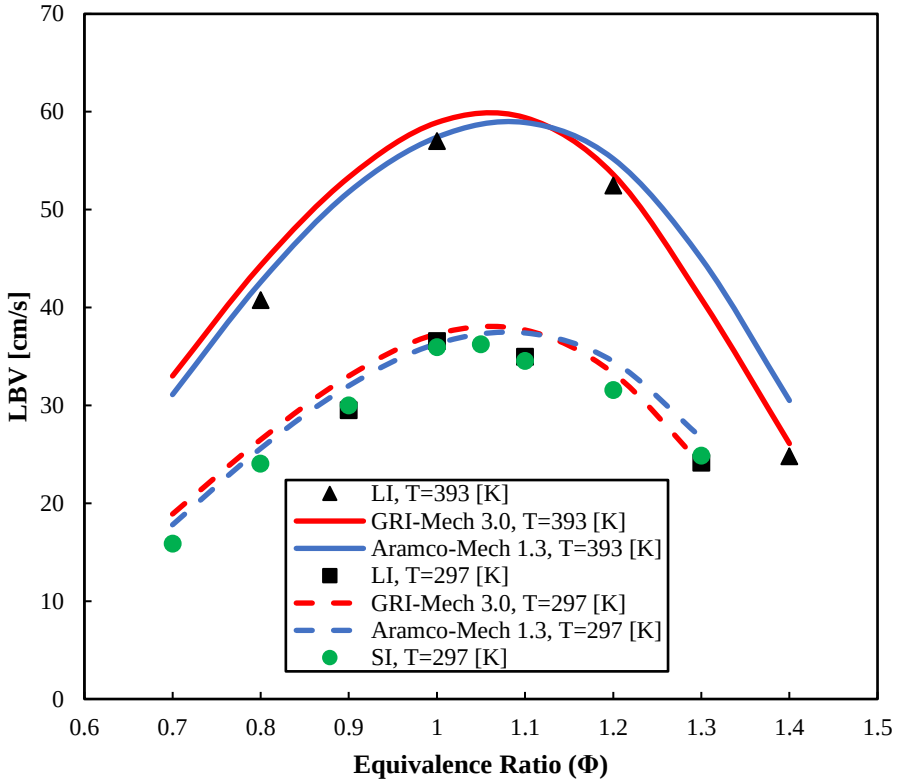

Figure 2.14. The laminar burning velocity for CH_4/air mixture at two initial temperatures and 1 atm initial pressure are illustrated. The black squares and triangles show the LI experimental values for 297 and 393 K initial temperature respectively. Red and blue lines present the CHEMKIN PRO results for GRI-Mech 3.0 and ARAMCO-Mech 1.3 mechanisms, while green circles shows SI values.

2.2.5.1 Ignition Energy

The author carried out tests to evaluate the effect of ignition energy on the laminar burning velocity, and Figure 2.15 illustrates the results of pressure traces. Utilizing higher energy is predicted to increase the reaction rate at the beginning of the combustion process due to bigger volume of plasma formation. Experimental results agree with this prediction, as it is apparent in Figure 2.15 the pressure increases at a fixed time during the combustion process by using higher pulse energy. This is an intuitive behavior because pressure rise is directly proportional to the burned gas volume, which increases due to higher pulse energy.

Instead of achieving higher energy density plasma by increasing the pulse energy, the plasma tends to expand in size as suggested by [84]. The author believes this expansion (bigger flame kernel) is the reason behind the differences of pressure traces. Despite the increase in pressure with ignition energy, variations in the pressure rate of change are virtually nonexistent. Since the laminar burning velocity is a function of the rate of change of pressure, the obtained laminar burning velocity values are almost identical, the deviation is less than uncertainties of the experimental setup.

The result is presented in Table 2.3 (LBV) and Figure 2.15 (pressure traces), the difference in laminar burning velocities between 356 mJ and 158 mJ is only 1.6% compared with an experimental uncertainty of 5.8%. Others suggested that a stronger shockwave may result in a better compression of the unburned mixture, hence, higher unburned gas temperature, and LBV's are expected. However, the author did not notice an increase in laminar burning velocity or the effect is very small relative to experimental uncertainties in the test range of pulse energy.

Table 2.3. Laminar burning velocities of CH_4/air mixture are presented for the different ignition energies.

Ignition energy [mJ]	Laminar burning velocity [cm/s]
158	36.58
227	36.71
356	37.16

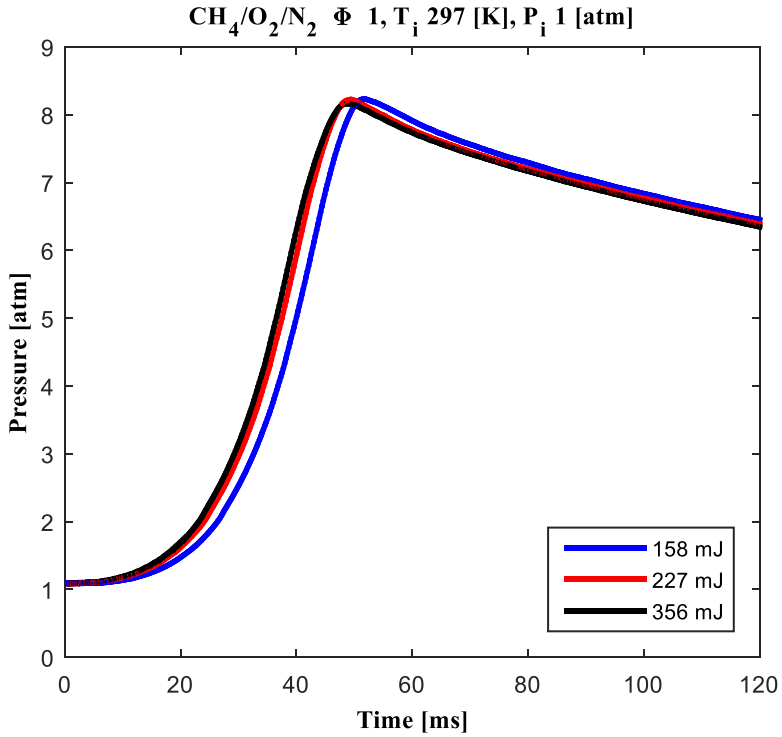

Figure 2.15. Pressure traces of CH_4/air mixture at atmospheric conditions and stoichiometric ratio, three ignition energies 158 mJ, 227 mJ, and 356 mJ were chosen.

2.2.5.2 Methane Flammability Limit

Although there is little use for experiments near the flammability limits in reciprocating engines, those data are valuable for safety applications, and there is interest in examining laser ability in that region. The flammability limits of premixed fuel using spark ignition (SI) system are well defined in the literature. However, there is a need to understand the limits when an advanced ignition system is employed. In a SI system, the electrodes provide a venue of energy dissipation which tends to absorb energy from the ignition point and therefore increase the required fuel concentration in a mixture for successful ignition. Conversely, there is no similar energy dissipation with LI, hence, a leaner mixture can be ignited. This is a growing industrial concern as powerful lasers are finding their way into an increasing amount of applications were combustible gases might coexist.

In the flammability limit regime, the thermodynamic losses approximately balance the energy release of the flame; quenching of the flame occurs if the heat release is less than the losses. Although the flammability limit can be classified as a regime as opposed to a specific point, it is significant to note that in this regime small changes in equivalence ratio can lead to significant variation in combustion processes. Pressure traces near the flammability limit are shown in Figure 2.16 at an initial temperature and pressure of 297 K and 1 atm. One notices that the peak pressure location is not a well-defined point compared to other pressure traces shown earlier, however, a region of the maximum value is illustrated (due to slow combustion). Also, pressure traces reveal that the flame quenches earlier, and correspondingly lower peak pressure is achieved as the equivalence ratio decreases. The combustion timescale is significantly bigger compared to the previous runs; the maximum pressure is attained around 500 ms compared to less than 50 ms with stochiometric mixture (see Figure 2.15).

The maximum recorded pressure for the case of $\Phi = 0.51$ and $\Phi = 0.5$ are only 1.34 atm and 1.09 atm respectively. It is evident that the flammability limit obtained in this study by LI is less than those values suggested by Tahtouh *et al.* [117] and Wang *et al.* [121] for spark ignition systems. Figure 2.17 presents the flame propagation of a methane mixture at $\Phi = 0.53$. The laser enters from the left, and a clear toroidal flame shape (propagating toward the laser) is forming up to 2 ms. After that the flame shape deviates randomly; even after 20 ms the flame still exists within the observable window (shown in a black arrow).

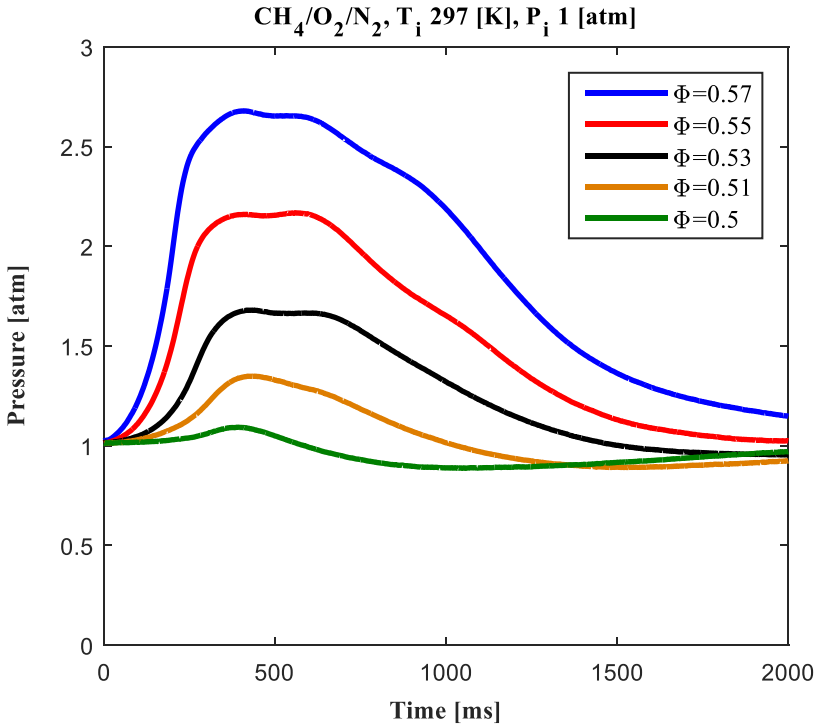

Figure 2.16. Pressure traces of the ignition process near the flammability limit for CH_4/air mixture.

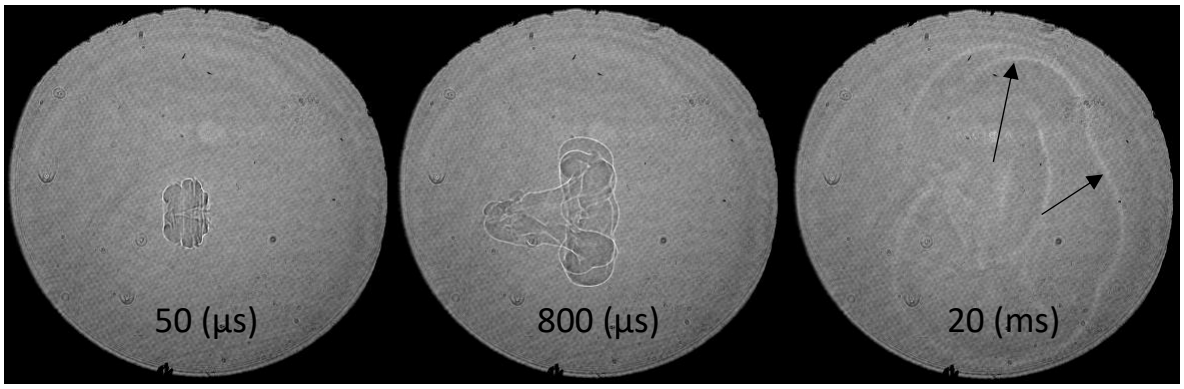

Figure 2.17. Shadowgraph images of the flame propagation for Φ = 0.53, which is near the flammability limit. Laser enters from left side.

2.2.5.3 Laser Vs Spark Ignition Systems

Experiments with SI system are carried out for a range of equivalence ratio (0.7-1.3) to assess and compare LBV values obtained by LI system. A Lucas ignition circuit is assembled [127], and controlled by LabVIEW software to provide the ignition energy (details in Appendix A). Also, a spark plug was modified by welding two tungsten electrodes (1 mm) to produce a spark at the

center of the combustion chamber. Figure 2.18 presents spherical flame propagation for methane mixture at room temperature and atmospheric pressure for Φ = 1.05. For that case, the flame left the observable window after 10 ms when the recorded pressured was 1.06 atm.

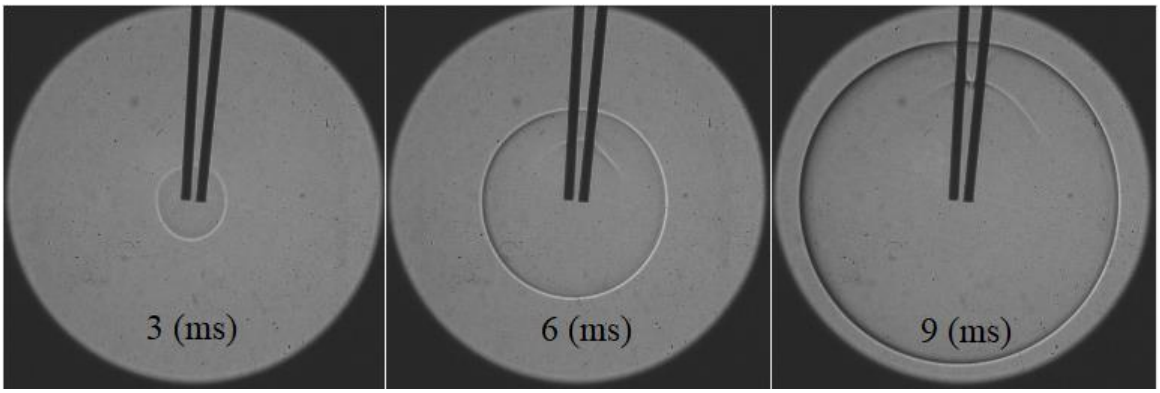

Figure 2.18. Schlieren imaging of methane flame propagation at 297 K and 1 atm initial conditions for Φ = 1.2, spark ignition system is used to ignite the mixture.

In terms of pressure traces, the laser ignition system gives a faster pressure rise (shorter combustion duration) than spark ignition system. That is mainly because of the conduction heat transfer losses associated with the two electrodes which lower fuel reactivity, particularly at an early stage. The figure above presents a small flame after 3 ms by SI, while flames cover approximately half of the observable window with LI system. However, the laser ignition system provides a lower maximum pressure; this might be attributed to flame distortion from the spherical shape which creates more unburned mixture zones. Although there is a difference in the pressure traces, the LBV values are very close (the pressure rate of change was almost identical) with a maximum difference of 2.8% for the case of Φ = 1.3. Table 2.4 shows the LBV values of laser and spark ignition systems for four equivalence ratios. The results in term of LBV vs equivalence ratio is presented in Figure 2.14 for comparison. It is obvious that in spark ignition experiments the maximum LBV is obtained at 1.05 which matches the numerical prediction [33]. Farrell *et al.* [123] observed a similar trend between laser and spark ignition systems, the laminar burning

velocities obtained for 45 hydrocarbons with negligible differences. Therefore, it is valid to conclude that laser ignition system provides accurate LBV values even with initial toroidal flame propagation; because flame tends toward spherical propagation as it expands.

Table 2.4. Laminar burning velocities (cm/s) of CH_4/air mixtures are presented for the different ignition systems.

Φ	LI	SP	Difference [%]
0.9	29.51	30	-1.63
1	36.58	35.95	1.75
1.1	34.98	34.53	1.30
1.3	24.16	24.85	-2.78

2.2.6 Conclusion of LI experiments in a constant chamber

Although the Nd:YAG laser profile is not a Gaussian profile and long focal length lenses were employed, the laser was capable of igniting the mixture consistently and the energy density is similar to the value found in the literature. The laminar burning velocity increases and decreases with initial temperature and pressure respectively. Also, LBV values are not a function of ignition energy; even though the maximum pressure occurs earlier with higher ignition energy, the difference between LBV values were negligible. The higher maximum pressure is attributed to a larger flame kernel. Toroidal and spherical flame propagations have been noticed during the experiments, more investigation is required to justify the flame shape after the ignition process. Laser and spark ignition systems are compared, the LBV values are almost identical with a maximum difference of 2.8% for the rich mixture (Φ = 1.3). The maximum laminar burning velocity occurs at an equivalence ratio of 1.05 for the CH_4/air mixture. Also, the highest recorded LBV value was 57.02 cm/s for stoichiometric mixture at initial conditions of 1 atm and 393 K.

2.3 Performance of a Laser Ignited Multi-Cylinder Lean Burn Natural Gas Engine

In this section, laser and spark ignition systems are evaluated in a six-cylinder natural gas engine to illustrate the benefit of LI near the lean limit. The engine was operated at high-load (298 kW) and rated speed (1800 RPM) conditions. Ignition timing sweeps and excess air ratio (λ) sweeps were performed while keeping the NO_x emissions below the EPA regulated value ($BSNO_x < 1.34$ g/kW-hr), and while maintaining ignition stability at industry acceptable values (COV_IMEP < 5%). Through such engine tests, the relative merits of (i) standard electrical ignition system, and (ii) laser ignition system were determined. A rigorous combustion data analysis was performed and the main reasons leading to improved performance in the case of laser ignition were identified. The work provided in this chapter has been published in the Journal of Engineering for Gas Turbines and Power NOVEMBER 2017, Vol. 139 / 111501.

2.3.1 The Laser Igniters

Recent advancements in laser materials and laser pumping schemes have resulted in µlasers having sufficient laser pulse energies to be able to create sparks when focused [109, 128-130]. While such designs are still evolving, we report here the results from ignition tests conducted using one such state-of-the art µlaser design. Schematic representation of the µlaser along with a photograph is shown in Figure 2.19. It consists of a water cooled high power Vertical Cavity Surface Emitting Laser (VCSEL) pump whose output is focused using a single positive lens to end-pump a Nd:YAG rod having appropriate anti-reflection coatings. At the other end of the Nd:YAG rod is a Cr4+:YAG saturable absorber that acts as a passive Q-switch. This type of laser is known for less beam divergence and bigger beam diameter. The pump VCSEL is operated up to 500 µs resulting in an output comprising of two 1064 nm pulses, approximately 190 µs apart,

each with 14.5-16.5 mJ and 4.72 ns pulse width at FWHM. On account of various advanced design features of this µlaser, it had a wall-plug efficiency of 2.22%, which amounts to the requirement of a mere 1.35 J of electrical energy per combustion cycle for laser operation. Considering the fact that these are passively Q-switched lasers (as opposed to actively Q-switched lasers) they are also known as PQLs in the literature [82]. Table 2.5 presents some of the advantages of VCSEL over edge emitters lasers.

Table 2.5. Advantages of vertical cavity surface emitting laser.

	VCSEL	**Edge Emitter laser**
Beam quality	Circular simpler optical train	Elliptical with high aspect ratio
Reliability FIT number of failures in billions of hours of operation time	10^{-3} p-n junctions do not intersect the surface	≈500 p-n junction intersects the facet mirrors, facet coatings are prone to catastrophic optical damage
Efficiency (at room temperature 25°C)	55%	50-65%
Efficiency (at room temperature 60°C)	>50%	≈35%

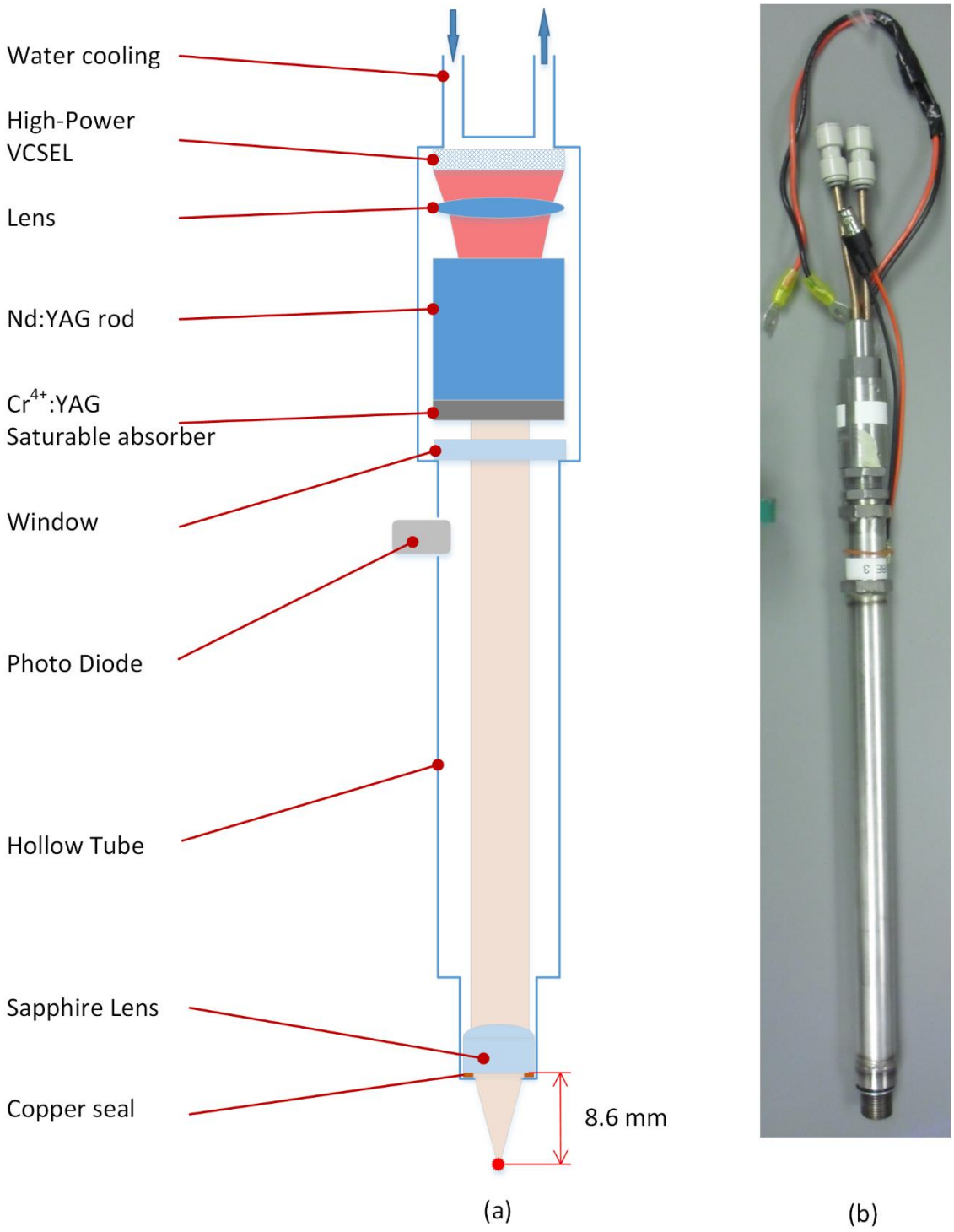

Figure 2.19. Schematic (a) and photograph (b) representation of the laser igniter equipped with water-cooled VCSEL pumped µlaser [71].

The µlaser of above design was placed at the distal end of a hollow tube. The 1064 nm pulsed output was focused into the combustion chamber using a single sapphire lens having a back focal length of 8.6 mm. The focusing lens has a thickness of 6.35 mm that is capable to with stand to a maximum pressure of 100 bar and a safety factor 4 according to equation (2.10). While the beam quality was not measured, it was sufficient to successfully create sparks in 1 atm. air when the laser beam of 2 mm diameter was focused using the sapphire lens. Copper seals placed beneath the sapphire lens prevent the leakage of hot combustion gases into the hollow tube. Overall, the arrangement shown in Figure 2.19 had the same footprint as a standard spark plug and would fit in the spark plug well without any interference.

Initial tests performed on the engine by placing the laser igniter in the cylinder with the hottest environment showed that the µlasers on these igniters would attain temperatures as high as 72°C under full load conditions. Furthermore, a thermal analysis performed using temperatures measured at various points on the igniter showed an overall heat flux of 25 Watts, which could be removed by circulating cooled water. With the passive Q-switching used here, a pump laser operating at a slightly higher temperature results in delayed emission of the laser pulses from the rising edge of the trigger pulse. This, in turn, translates to delayed ignition timing (IT) in the engine. To improve the accuracy of IT, the cooling water temperature was tightly controlled to be 22 ± 1°C, and further the timing was monitored using a photodiode installed on the walls of the laser igniter (see Figure 2.19).

2.3.2 The 6-Cylinder Engine Test Platform

A Cummins QSK19G, turbocharged, inline 6-cylinder, 350 kW, lean-burn natural gas fueled stationary engine was used as the test platform. Further specifications of the test engine are

provided in Table 2.6. This engine was coupled to a 465 kW AC dynamometer to facilitate engine tests at controlled engine load and speed. Individual cylinders were instrumented with pressure transducers (Kistler 6067C) and in-cylinder pressure data was recorded using an AVL indicom system after signal amplification using Kistler 5010B charge amplifiers. Cummins supplied Calterm-II software enabled control of various engine operational parameters.

Table 2.6. Specifications of the Cummins QSK19G engine.

Engine	**Cummins QSK19G 6-Cylinder,4-Stroke, SI**
Bore [mm]	159
Stroke [mm]	159
Comp. Ratio	11:1
Displacement [L]	19
Power [kW/hp]	350/469
Speed [RPM]	1800
Ignition System	CDI / Laser
Lube oil	35 gal.
Dynamometer	623 hp AC drive

The standard Capacitance Discharge Ignition (CDI) system on the engine was replaced with six laser igniters to perform the laser ignition tests (see Figure 2.20). The engine control system used a UEGO sensor in conjunction with a Woodward throttle actuator to allow variation of the λ value. A National Instruments FPGA based control system that used signals from an encoder mounted on the crankshaft enabled changing the IT. The intake airflow and fuel flow were measured using appropriately sized laminar flow meter and a Coriolis flow meter. Emission measurements were performed using a Horiba 7100D emissions bench. Subsequently, the measured emission values were processed per the procedure given in the SAE J1003 standard.

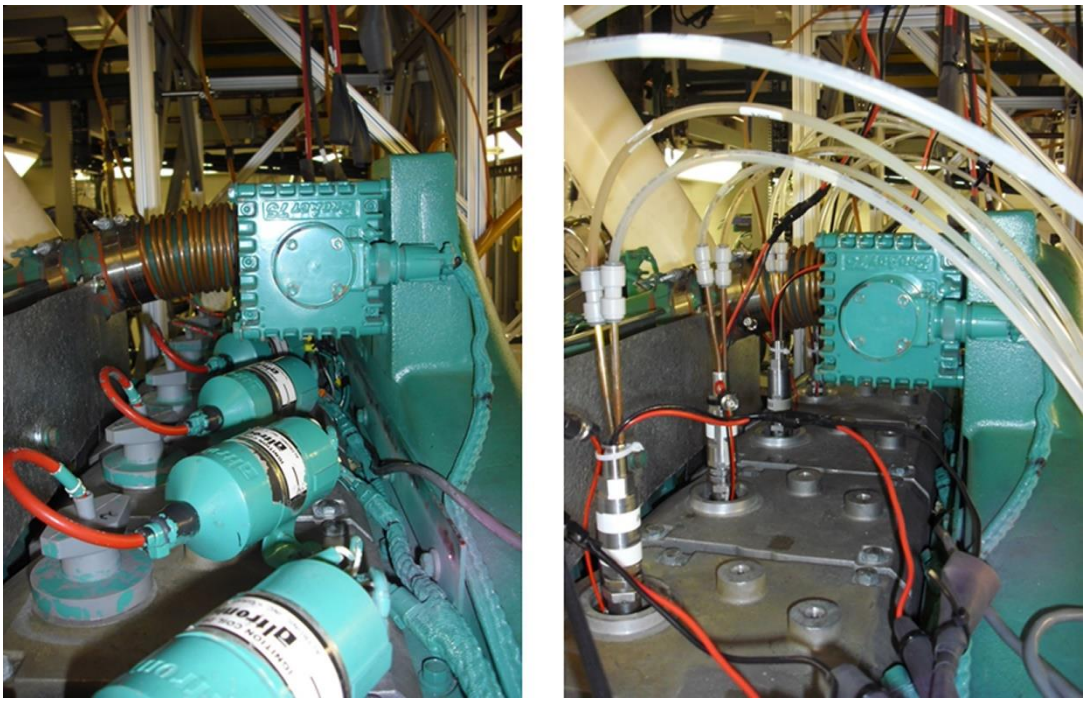

Figure 2.20. View of standard spark ignition systems (left), and laser ignition system (right) as seen from cylinder#1 of the engine at Argonne National Lab.

2.3.3 Results and Discussion

For an ideal Otto cycle one can represent the cycle efficiency by equation (2.11) where, CR is the compression ratio and $\gamma = (C_p/C_v)$, the ratio of specific heats. In lean fuel-air mixtures γ value increases and as a result efficiency increases. However, in leaner mixtures the flame speed decreases leading to lower efficiencies. In addition to these two counteracting phenomena, efficiency strongly varies with IT. All of these manifest themselves in the trends shown in Figure 2.21. For the remainder of this section, the term efficiency, η, is used to represent Brake Thermal Efficiency = (dyno power/ fuel energy rate).

$$\eta_{cycle} = 1 - \frac{1}{CR^{(\gamma-1)}} \tag{2.11}$$

In these set of tests, for a given excess air ratio, λ, the IT was varied between 13° and 40° CA BTDC. However, the actual test points closely confirmed to the two limitations corresponding to $BSNO_x$ < 1.34 g/kW-hr, and COV_IMEP < 5%, that are marked by horizontal red lines in Figure 2.21B, C, E, and F. As shown in the case of λ = 1.68 in Figure 2.21B, COV_IMEP decreases with initial IT advance, however, it starts increasing at larger IT advance as the number of partial burns and misfires increase. Such a convex-up trend is not shown in some of the curves in Figure 2.21B and E, especially those corresponding to richer mixtures at advanced ignition timing, as the test points with $BSNO_x$ significantly higher than 1.34 g/kW-hr. were excluded from the test matrix.

In a typical Otto cycle engine, with IT advance efficiency increases but eventually decreases after the MBT timing is exceeded. Within the range of IT variation used here (see Figure 2.21A and D), the engine efficiency monotonically increases with IT advancement. Figure 2.21C and F show a similar trend for $BSNO_x$ variation with ignition timing. Additionally, noticing the trends for 2P-LI in Figure 2.21E and D, one notices that for a given ignition timing (say, 30° CA BTDC), COV_IMEP increases with increasing λ, whereas, efficiency shows the opposite trend.

In the case of 2P-LI, extension of the lean ignition limit up to λ = 1.7 is possible, however, the reduction in apparent flame speeds under lean-burn conditions appear to offset any efficiency gains due to increased γ values. As a result, identification of the optimal engine operating condition having high efficiency, low NO_x emissions and low COV_IMEP requires variation of both ignition timing and excess air ratio.

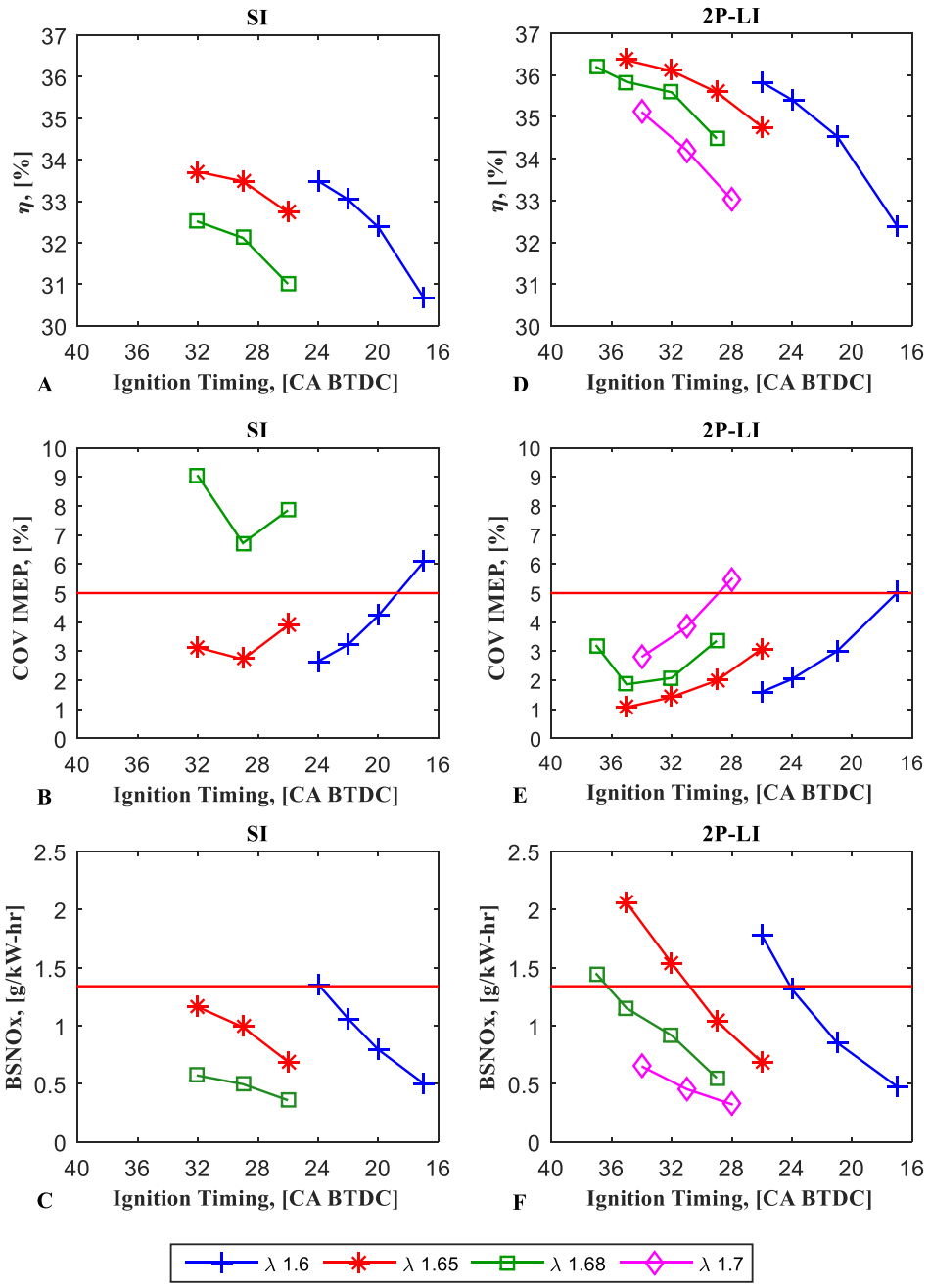

Figure 2.21. Efficiency, COV_IMEP and $BSNO_x$ variation with ignition timing.

The measured values of COV_IMEP, $BSNO_x$ for the above two ignition strategies are shown as a function of engine efficiency in Figure 2.22. The current EPA emission regulation for $BSNO_x$ of 1.34 g/kW-hr is marked by a horizontal red line. The industry accepted value for ignition

stability, i.e., COV_IMEP = 5% is shown similarly marked by a horizontal red line. Confirming to these two limitations, one notices by taking the baseline SI point to correspond to $\lambda = 1.6$ and IT = 24° CA BTDC and the 2P-LI optimal operational point as that corresponding to $\lambda = 1.68$ and IT = 36° CA BTDC, an efficiency gain of 2.6% points is possible. This efficiency gain may not be attributable only to the fact that an ignition advance of 12° CA is facilitated by improved ignition with the use of 2P-LI. As one shifts from $\lambda = 1.6$ to $\lambda = 1.68$, the transition of ignition kernel into a sustained flame front and the subsequent combustion of in-cylinder charge are slower necessitating optimal ignition phasing. To gain further insight into the associated combustion processes, in-cylinder pressure data was processed to compare ignition delays and combustion durations.

Due to the design of the cooling passages in the inline 6-cylinder engine used here, Cyl#1 is the coolest and Cyl#6 is the hottest in operation. To capture the trends midway between these extremes, cylinder pressure data corresponding to cyl#4 were processed and shown in Figure 2.23 and Figure 2.24. In actuality, the trends presented in these figures are observable in all 6 cylinders.

Figure 2.23A shows the rate of heat release (ROHR) ensemble averaged over 500 cycles for $\lambda = 1.68$ and IT = 29° CA BTDC. The corresponding ROHR plots for individual combustion cycles are shown in light color in the background. In spite of the cyclic variations that are typical of lean burn combustion, the ensemble averaged curve is representative of the overall combustion process. Similar plots for 2P-LI, as shown in Figure 2.23B, show a narrower spread about the ensemble average indicating smaller cyclic variation. Both of these plots were merged in Figure 2.23C to compare combustion performance in SI and 2P-LI. As noticed, the ensemble averaged ROHR for 2P-LI shows earlier ignition and further accelerated combustion, which is representative of the

trends in individual cycles. For the remainder of the discussion, values derived from individual, as well as, ensemble averaged ROHR curves were used.

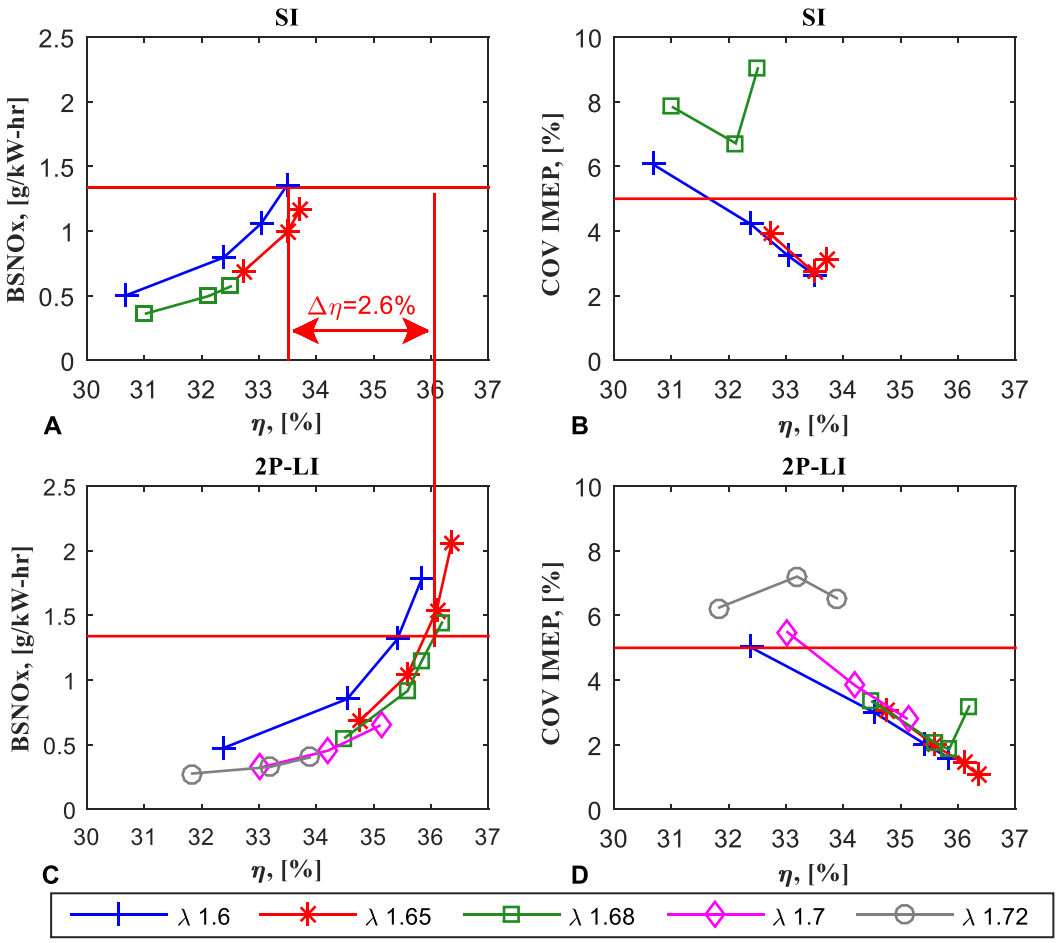

Figure 2.22. $BSNO_x$ vs. Brake Thermal Efficiency tradeoff (left), COV_IMEP vs. Brake Thermal Efficiency (right). Allowable limits for NO_x emissions and ignition stability are marked with horizontal red arrows.

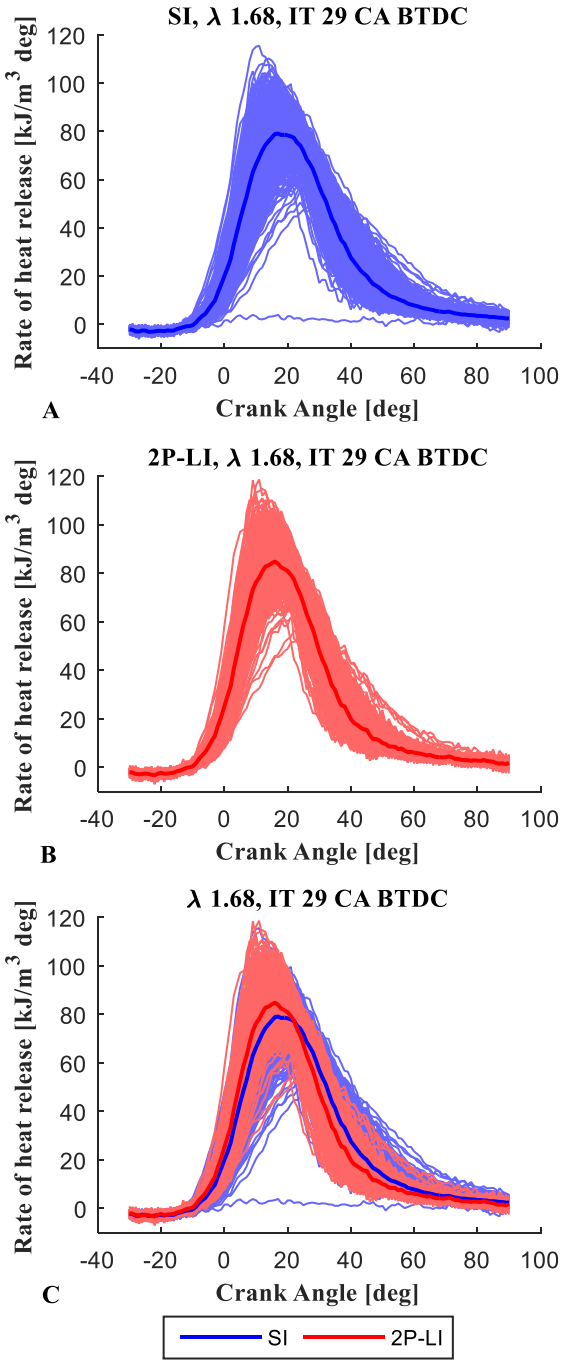

Figure 2.23. Rate of heat release in cylinder#4 for SI and 2P-LI.

For the purposes of discussion, we will define "ignition delay" to correspond to the time period between ignition timing and that corresponding to 10% mass fraction burned. In the case of SI and 2P-LI, this definition somewhat coincides with Sjoberg and Zeng's "inflammation time" [131],

wherein the flame kernel survives its nascent laminar state and transitions to a fully developed turbulent deflagration. During this time scale, especially in lean mixtures, the stochastic variations in temperature, velocity, and turbulence could influence the fragile flame kernel to result in significant cycle-to-cycle variations.

In a similar manner, we will define "combustion duration" to correspond to the time interval between 10% and 90% mass fraction burned. This time period corresponds to most of the fuel chemical energy being converted to mechanical energy in the form of high-pressure combustion gases. A short combustion duration that is phased appropriately results in a major fraction of the heat release to occur at the top dead center, i.e., leading to constant volume combustion, which in turn leads to higher thermal efficiency.

These values corresponding to cylinder#4 with a spread of ±standard deviation are shown in Figure 2.24. As noticed, 2P-LI always results in shorter ignition delays and shorter combustion durations, with these effects more pronounced under leaner conditions. Additionally, reduction in cyclical variations with laser ignition, especially under lean mixtures conditions, is clearly illustrated. For example, by comparing values of MFB50% of SI and 2P-LI at $\lambda = 1.68$, one notices considerably less spread in the case of 2P-LI. Similarly, a closer observation of the standard deviation values of MFB 0-10%, MFB 10-90% and MFB 50% at the optimal points with baseline SI ($\lambda = 1.6$ and IT = 24° CA BTDC) and 2P-LI ($\lambda = 1.68$ and IT = 36° CA BTDC), shown with continuous line circles and dashed line circles in Figure 2.24, reveals that combustion not only occurs earlier and faster but is also more stable with 2P-LI.

An important point to note is that for the baseline SI case an ignition delay of 29° CA leads to a combustion start at 5.5° CA ATDC. Whereas, for the 2P-LI optimal point an ignition delay of 37° CA leads to combustion start at 0.8° CA ATDC. With combustion durations being similar (see

Figure 2.24B), this results in combustion phasing, i.e., MFB 50%, in the case of 2P-LI to precede that of baseline SI by 5° CA (see Figure 2.24C).

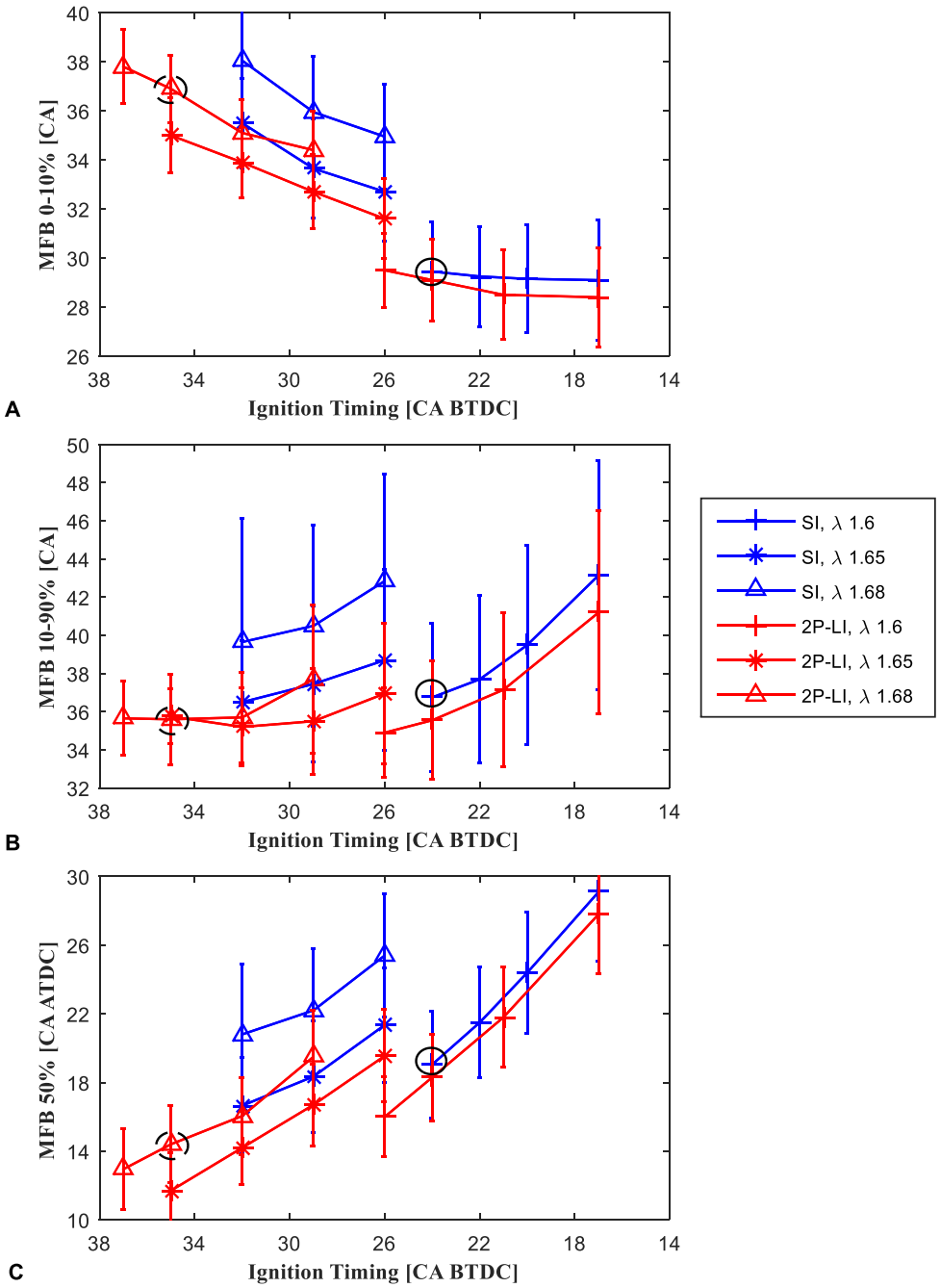

Figure 2.24. Ignition delay (A), combustion duration (B), and MFB50% (C) in cylinder#4 for SI and 2P-LI systems.

Recently, Sjoberg and Wei [131], in their tests using a gasoline engine have reported a mixed mode of combustion, wherein the end gas auto ignites following a brief period of deflagration. For the 2P-LI optimal point, a graph similar to the ones shown in Figure 2.23. is plotted in Figure 2.25. Due to the absence of a bimodal distribution in the ROHR curves, both in individual as well as ensemble averaged ones, we can rule out the possibility of such a mixed mode of combustion. Indeed, it is difficult to auto ignite natural gas which has an octane number ≥ 110 as compared to gasoline which has octane number in the range 87 to 93.

From the above discussion, the observed net benefit of $\Delta\eta$ = 2.6% points for 2P-LI optimal point over SI baseline case is attributable to two effects: First, laser ignition improves ignition stability to enable highly advanced ignition timing. Second, laser ignition enables ignition of leaner fuel-air mixtures. Improved efficiency from the former effect overcomes the loss in efficiency resulting from the latter to result in a net benefit of $\Delta\eta$ = 2.6% points.

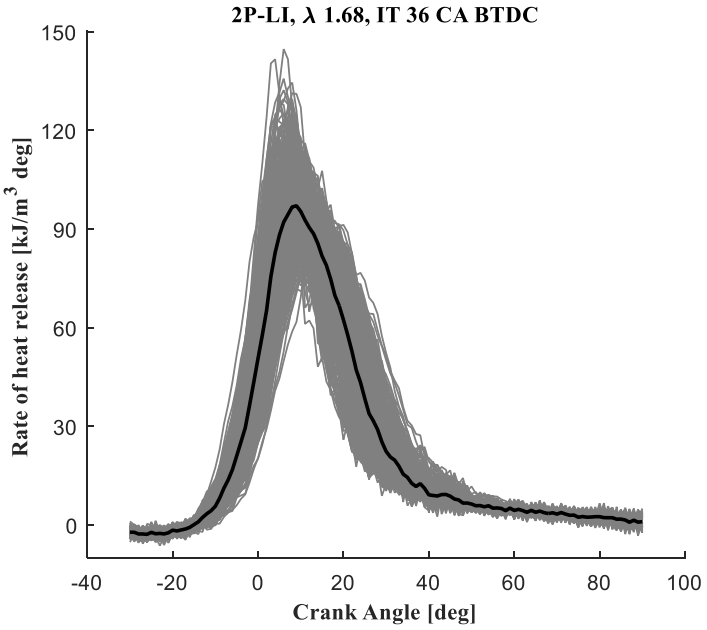

Figure 2.25. Rate of heat release plots for the optimal operational point with the use of 2P-LI.

Measured values of brake specific unburnt hydrocarbons (BSHC) and brake specific carbon monoxide (BSCO) emissions are shown in Figure 2.26 for the optimal operating conditions under SI and 2P-LI. As noticed, the difference in these emission levels is very small for optimal conditions using either ignition system to have a noticeable impact on combustion efficiency.

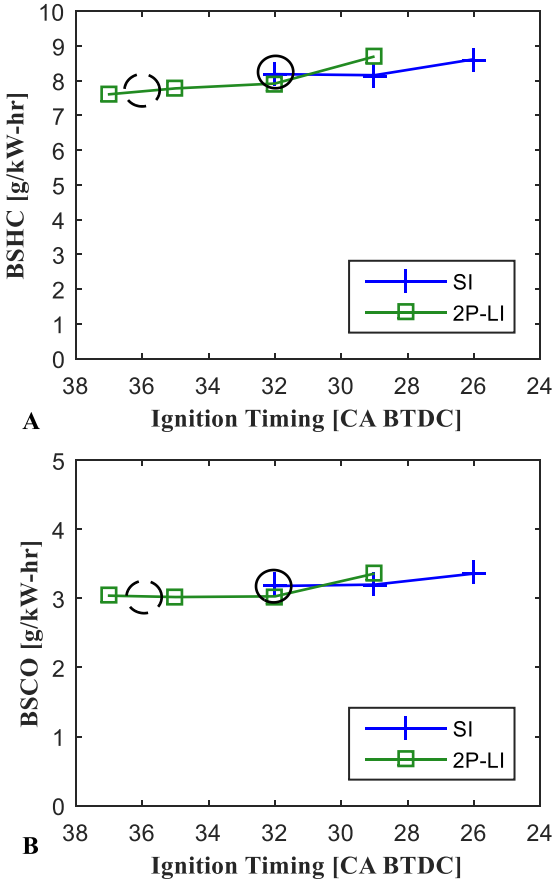

Figure 2.26. BSCO and BSHC emissions for SI (λ = 1.6) and 2P-LI (λ = 1.68). Circles mark the ideal conditions for either ignition system.

2.3.4 6-Cylinder Engine Study Conclusions

The 6-cylinder natural gas engine was successfully operated at rated speed and high load conditions with µlasers igniting all 6 cylinders. To the best of the knowledge, this is the first time that this has ever been performed in the world. Ignition timing sweeps and excess air ratio sweeps were performed and the engine performance was compared for the cases of SI and 2P-LI. A brake

thermal efficiency improvement of 2.6% points was observed with the use of 2P-LI. A detailed analysis shows that laser ignition leads to significantly improved ignition under advanced ignition timings, which, in turn, enables optimal phasing to result in efficiency improvements. Further efficiency gains can be envisioned as strategies promoting multi-point ignition or "volumetric ignition" can be devised using laser ignition.

2.4 Prechamber Equipped Laser Ignition (PCLI) for Improved Performance in Natural Gas Engines

In this section, the optimal geometry of prechamber was identified through several tests in a single-cylinder engine as a compromise between autoignition, NO_x and soot formation within the prechamber. Lean-burn operation of stationary natural gas engines offers lower NO_x emissions and improved efficiency. However, under lean conditions, flame speed reduces thereby offsetting any efficiency gains resulting from the higher ratio of specific heats. The reduced flame speeds, in turn, can be compensated with the use of a prechamber to result in volumetric ignition, and thereby lead to faster combustion. Tests were conducted in a single-cylinder natural gas engine comparing the performance of three ignition systems: SI, 2P-LI, and prechamber equipped laser ignition (PCLI). Out of the three, the performance of PCLI was far superior compared to the other two. Efficiency gain of 2.1% points could be achieved while complying with EPA regulation and the industry standard for ignition stability. Test results and data analysis are presented identifying the combustion mechanisms leading to the improved performance. The work provided in this chapter has been published in the Journal of Engineering for Gas Turbines and Power OCTOBER 2017, Vol. 139 / 101501, and was presented in Proceedings of the ASME 2017 Internal Combustion Fall Technical Conference.

2.4.1 The Argonne Single Cylinder Engine Test Platform

A single cylinder natural gas engine (RSi-130Q) in Argonne National laboratory was utilized in this study. Engine specification and schematic representation are shown in Table 2.7 and Figure 2.27 respectively. It is known that the single cylinder engine suffers from high cyclic variation due to the pulsation in the intake and exhaust manifolds. Because of that two surge tanks were

employed to dampen the flow pulsation (see Figure 2.28). Also, with the help of two electronic valves, the surge tanks were used to simulate the turbocharger condition. An intake pressure in the range of 5 to 24 psi gauge was used to achieve the required brake mean effective pressure (BMEP) for each excess air ratio (λ 1.54, 1.58, 1.65, 1.67, 1.7 and 1.75). The engine is coupled to a 111 kW AC dynamometer to facilitate ignition testing. Also, an external lubrication oil and coolant systems were employed to supply the required lubricant oil at 85°C and maintain the optimum engine temperature at 90°C respectively.

Table 2.7. Cummins engine specification (RSi-130Q).

Engine	**Single cylinder, four stroke**
Bore (mm)	130
Stroke (mm)	140
Displacement (L)	1.857
Compression ratio	11
Power (kW)	33
Speed (RPM)	1800

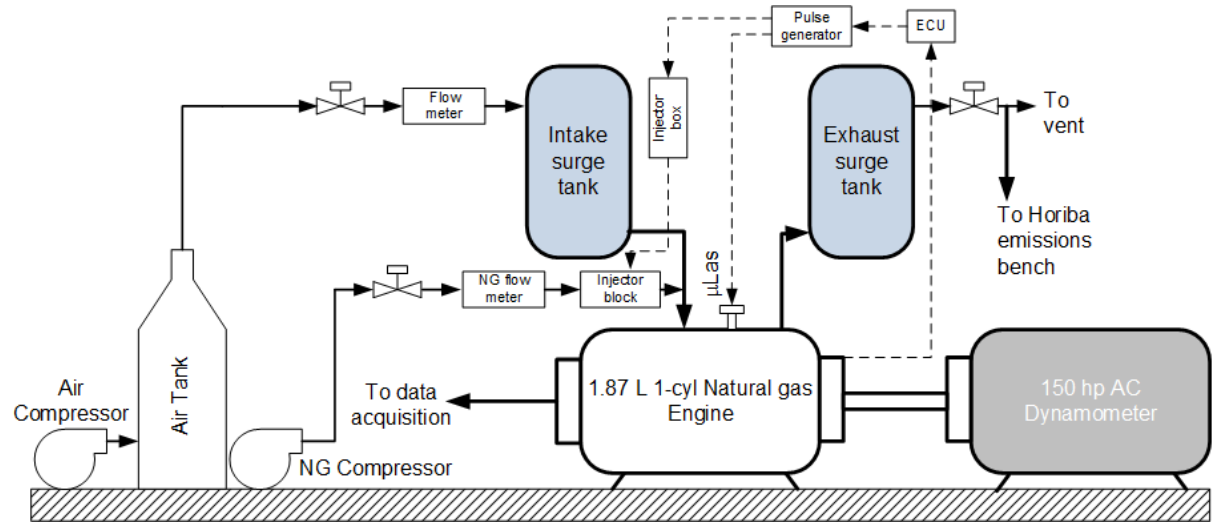

Figure 2.27. Schematic of the engine test setup.

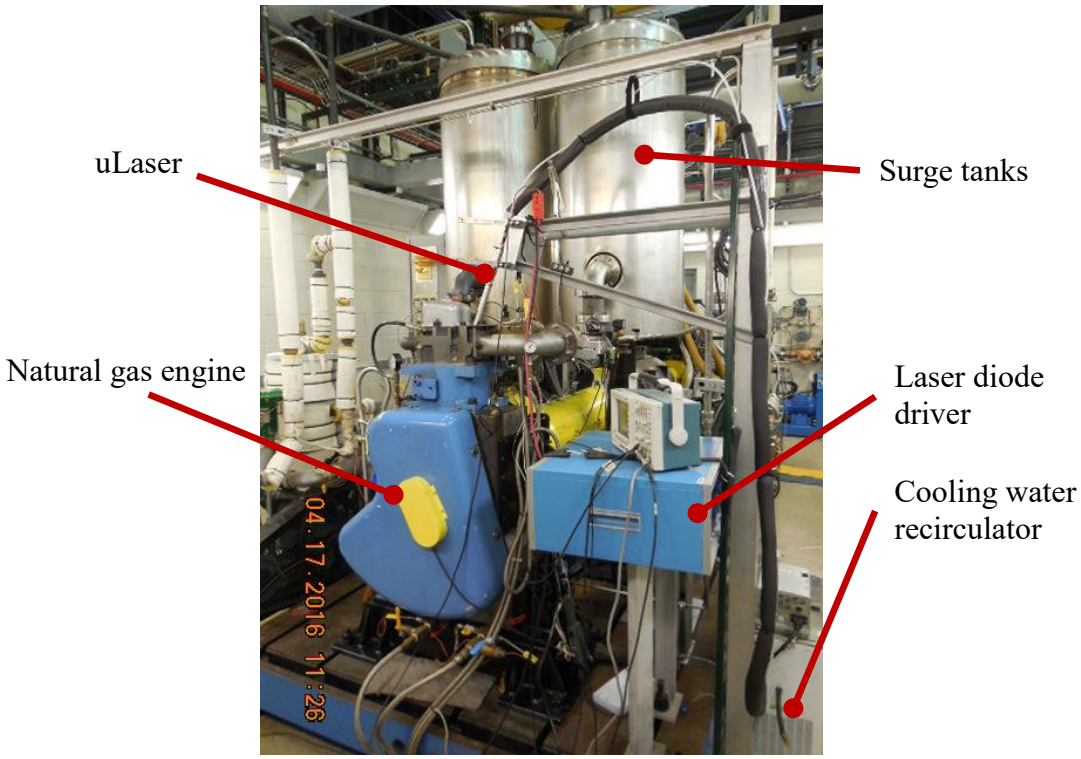

Figure 2.28. View of Cummins research engine (RSi-130Q) at Argonne National Lab

Pipeline natural gas (PLNG) was used during the experiments. The composition of the natural gas changes slightly on a daily basis, however, a gas chromatography analysis was carried out to evaluate the composition over several days. The stoichiometric air to fuel ratio was found to be 16.39; the composition of one of the tests is presented in Table 2.8. The natural gas was compressed from 5 to 130 psi gauge by using a CompAire natural gas compressor before directing it to the injector block. The PLNG flow measurement was obtained by utilizing a Micro Motion Coriolis flow meter downstream of the compressor. While fuel was injected into the intake manifold with the help of two electronically controlled natural gas injectors (CAP Inc.). Additionally, Horiba MEXA-7100D emission bench was used to measure the composition of exhaust gases (CO, CO_2, NO_x, UHC, and O_2). In each test case data were recorded over three minutes and average values utilized for subsequent analysis.

Table 2.8. Composition of pipeline natural gas (PLNG).

Gas	Molar [%]
Nitrogen	1.08
Carbon dioxide	0.7
Methane	94.53
Ethane	3.43
Propane	0.21
C4-C6	0.04

The in-cylinder pressure was recorded by using a piezoelectric pressure transducer (Kistler 6013B) mounted on the cylinder head. Also, a charge amplifier (Kistler 5010) was employed to convert the charge into a voltage signal. The transducer records at 100 kHz which gives approximately 10 data points every crank angle at 1800 RPM. Kistler 2614A optical shaft encoder was coupled with the engine crankshaft to determine the exact piston location. The data was recorded with a high-speed data acquisition system (AVL indicom) to perform the thermodynamics analysis. 500 consecutive cycles were recorded for each test after reaching a steady state engine condition, to minimize the cyclic variation, an average pressure was utilized to perform the heat release analysis using AVL Concerto software.

2.4.2 Ignition Systems

Following ignition systems were used:

1) Spark Ignition (SI): A standard Capacitance Discharge Ignition system (Altronic CD200) was used in tandem with a standard 18 mm J-style spark plug (Altronic L1863ip). The system was capable of generating up to 30 kV pulses across the gap with an average energy of 35 mJ/strike.

2) Laser Ignition (2P-LI): The laser igniter was identical to the one used in the 6-cylinder engine study and described earlier in section 2.3.1. Further details of the laser igniter are given in the author previous publications [71, 111].
3) Prechamber equipped laser ignition (PCLI): The PCLI was similar to the laser igniter in all respects, except that a prechamber was affixed to its distal end. A schematic representation of the three ignitors is shown in Figure 2.29. As previous studies by Roethlisberger and Favrat [37, 132] show prechamber geometry such as, volume, number of nozzle holes, nozzle diameters and their placement has a profound impact on ignition performance, and the formation of NO_x, CO and unburnt hydrocarbons. Using the basic frame work laid out by these researchers, optimization of the prechamber that can be used with a laser ignitor entails:
   (i) Avoiding soot formation within the prechamber;
   (ii) Minimizing NO_x formation both in the prechamber as well as in the jets;
   (iii) Avoiding autoignition within the prechamber [35] – occurrence of one such event in the prechamber imparts a fast rising pressure pulse that often leads to failure of the window/ lens material.

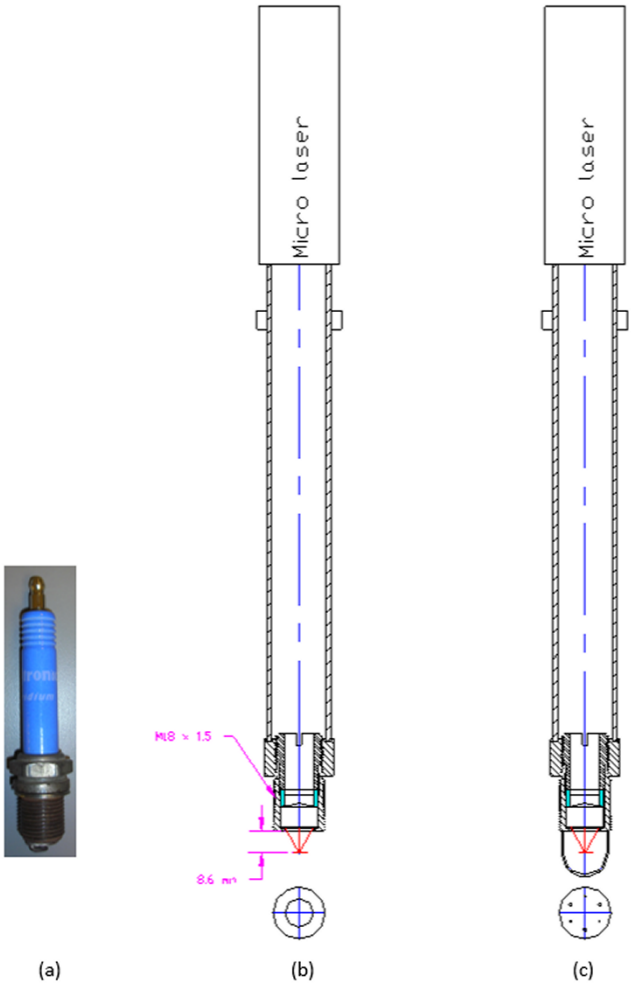

Figure 2.29. Ignition geometries that were tested: (a) Spark Ignition (SI), (b) single-point laser ignition (2P-LI), and (c) prechamber laser Ignition (PCLI).

2.4.3 Test Matrix

The engine tests were performed at a fixed speed of 1800 RPM, and a load of 10 bar BMEP. For gradually decreasing values of λ, IT sweeps were performed. Other researchers [14], especially those working with gasoline engines, have used optimal combustion phasing to correspond to MFB 50% coinciding with a fixed value of 5° ATDC. However, to accurately identify the optimal IT for the slow burning natural gas fuel that was used here, for a given λ, IT was varied between ignition advance corresponding to the EPA emissions regulation ($BSNO_x$ <1.34 g/kW-hr.) and

ignition retard corresponding to the limit for ignition stability (COV_IMEP < 5%) as accepted in the industry. This approach illustrates how engine efficiency is compromised with some ignition systems, and provide guidance toward higher brake thermal efficiency.

2.4.4 General Trend of Spark Ignition System

In a reciprocating engine, the optimum point of spark timing is obtained by swiping the ignition timing to achieve the maximum brake torque (MBT) at a fixed operating condition. In general, this point is attained if the maximum pressure and mass fraction burned 50% happen to be around 15° and 5°-10° CA ATDC respectively. However, engine knock and emission requirements might limit the use of such IT. If the spark advanced beyond that timing without encountering engine knock, the negative compression work increases and results in a lower engine torque. Figure 2.30 shows a relative engine torque with respect to IT where the MBT occurred by igniting the mixture at 33° CA BTDC.

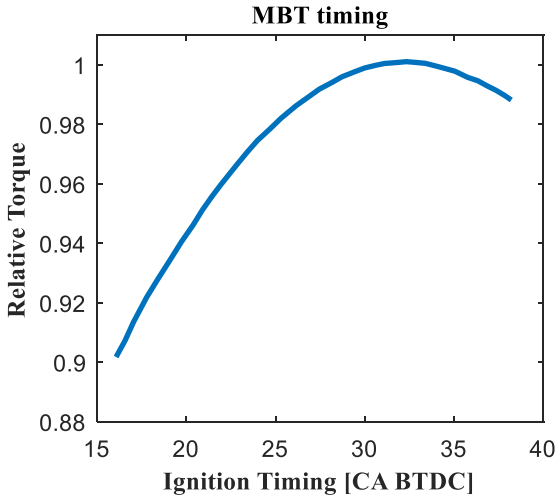

Figure 2.30. Engine relative torque versus ignition timing. The maximum brake torque timing happens at IT 33° CA BTDC.

Recently, Zhu *et al.* [133] developed a closed loop control system based on the highest acceleration of mass fraction burned to maintain optimal IT with engine aging and operational

conditions. It was found that the MBT timing is reached on all operation conditions if the maximum acceleration of heat release is just after TDC. It is obvious that the optimum IT is a function of all engine parameters such as load, speed, turbulence, ignition system, and the air to fuel ratio. Also, since combustion duration is a function of turbulent burning velocity, it can be minimized by increasing the turbulence or by burning a mixture with higher LBV. Though with lean combustion mode other strategies must be employed to minimize the combustion duration.

In the beginning, the SI experiments are discussed to evaluate the general trend of a single cylinder research engine. As mentioned earlier, this engine suffers from high cyclic variation. Even though that two surge tanks were utilized to minimize the pulsation in intake and exhaust manifold, the cyclic variations were incomparable to the 6-cylinder engine study (presented earlier in section 2.3). In fact, the main reason for observing a lower engine efficiency gain with LI in the single cylinder engine is attributed to the cyclic variation.

Previous studies [134-136] have shown the inflammation phase, i.e., the transformation of the ignition system generated plasma kernel into a self-sustaining flame front, is highly tenuous and depends upon the local equivalence ratio, flow field, as well as, turbulent intensities. Once the flame propagates to a sufficiently large radius, the cycle-to-cycle variation decreases dramatically. Several cyclic variation metrics have been proposed in the literature to understand this phenomena which is prominently enhanced under lean or highly diluted mixture conditions [135]. Here, the assessment was performed based on IMEP, location of maximum pressure (LOMP), and value of maximum pressure (MP).

Figure 2.31 shows the cyclic variation for $\lambda = 1.58$ at several IT. In this example, it is evident that the cyclic variation decreases with ignition timing advance from 15° to 21° CA BTDC. This is inductive of a shorter combustion duration as the IT approaches the MBT timing. However,

exhaust gas emission forbids the advance ignition timing 19° and 21° CA BTDC as will be shown later. Also, a comparison of cyclic variation metrics under fixed ignition timing showed that the intensity increases as we go leaner because of the reasons discussed earlier. One notices that the intensity of cyclic variation is more pronounced with the location and value of maximum pressure (see Table 2.9), which is in agreement with the results of Reyes et al. study [136]. The high fluctuations in LOMP is a markedly pronounced indicator of the performance limit of an ignition system, and is consistently observed before exceeding the acceptable industrial COV_IMEP value.

Table 2.9. Coefficient of variation for SI system at $\lambda = 1.58$.

IT [° CA BTDC]	**15**	**17**	**19**	**21**
COV_IMEP [%]	5.33	4.13	4.12	3.09
COV_MP [%]	10.4	9.9	10	8.5
COV_LOMP [%]	38.63	13.47	10.69	9.18

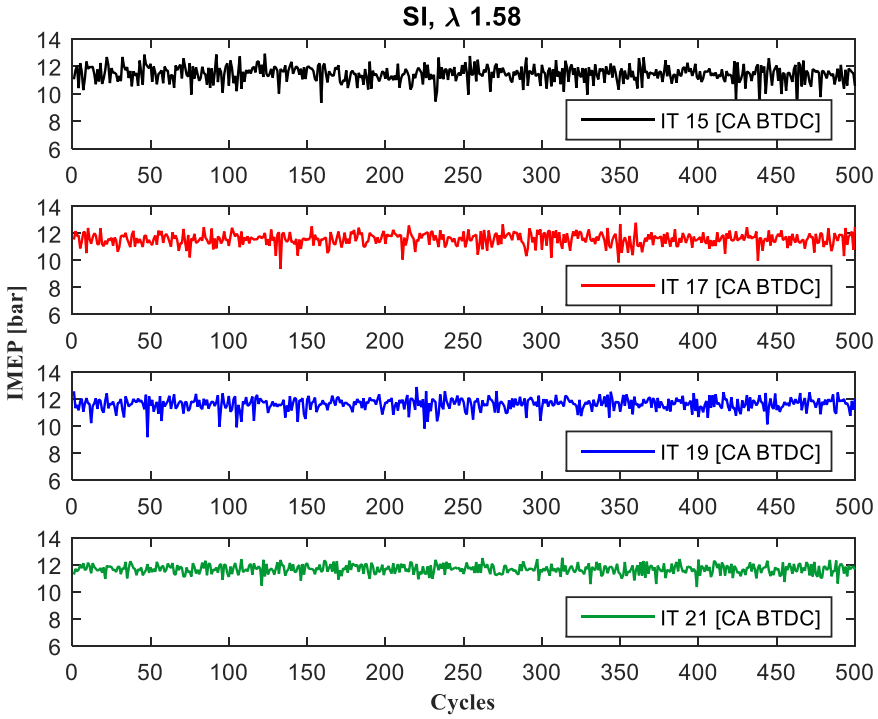

(A) Indicated mean effective pressure

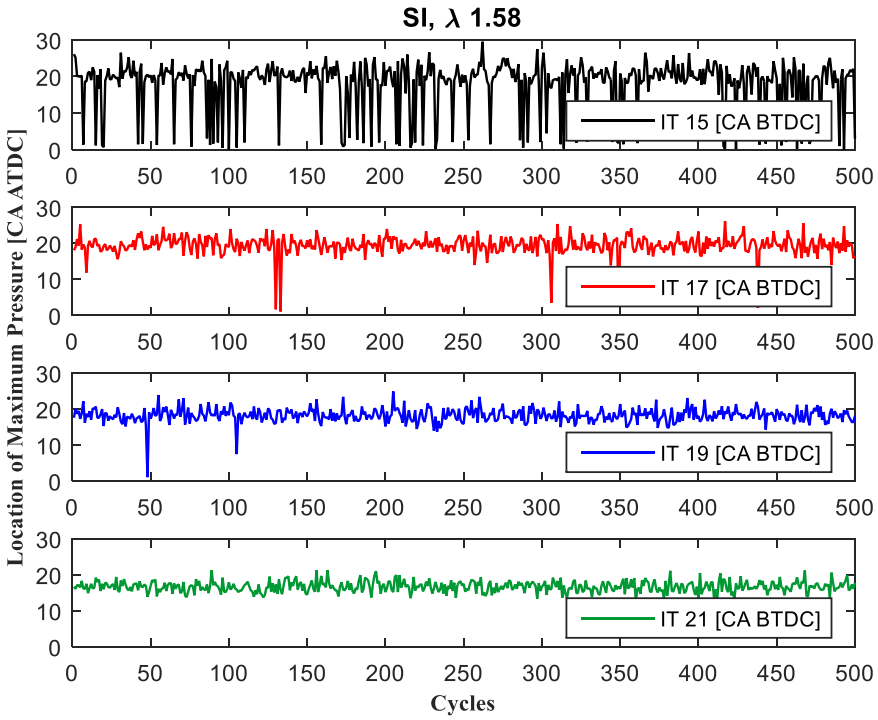

(B) Location of maximum pressure

Figure 2.31. Cyclic variation of a single cylinder engine ignited with spark ignition system at λ = 1.58 and several IT.

Analyzing individual cycles is a tedious procedure especially if a full map of IT and λ is carried out. Also, sometimes the result might not be conclusive because of high cyclic variations associated with the single cylinder research engines. Ensemble averaged pressure trace based on 500 consecutive cycles are used in most studies to deliver a general combustion trend. This methodology has been adapted in this section to compare pressure and heat release traces.

Figure 2.32 shows pressure traces for three different λ values at fixed ignition timing 19° CA BTDC. As expected the peak pressure decreases, and the location of the peak pressure shifts away from the TDC as λ increases. This is an inductive of the reduction in LBV which is directly related to the combustion duration. However, IT can be advanced to compensate for the increase in combustion duration.

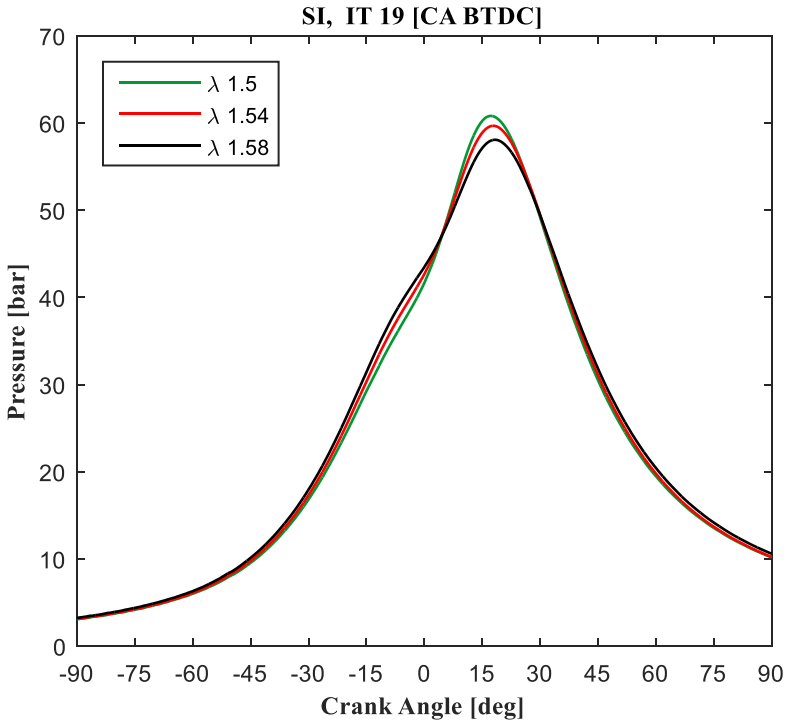

Figure 2.32 Pressure traces of natural gas reciprocating engine operated with spark ignition at a fixed ignition timing and several air to fuel ratios.

Figure 2.33 illustrates the pressure traces for four experiments at fixed λ and different IT. One notices that the maximum pressure increases with IT advance from 15° to 21° CA BTDC due to a higher rate of heat release (see Figure 2.34). Although the mixture temperature decreases with spark advancement (lowers the LBV at fixed λ), the volume at which the charge is burnt decreases and improves the overall combustion process.

Pressure traces shown in Figure 2.33 at λ = 1.58 illustrate a clear example of SI system limitation with lean combustion mode. Thermodynamic analysis revealed that the maximum pressure, MFB 50%, and maximum accelerations of heat release at IT 21° CA BTDC, occurred at 16.8°, 14.8°, and 3° CA ATDC respectively. Even though the MBT timing was not attained at IT 21° CA BTDC, the NO_x exhaust emission exceeded the allowable EPA limit (more details given later).

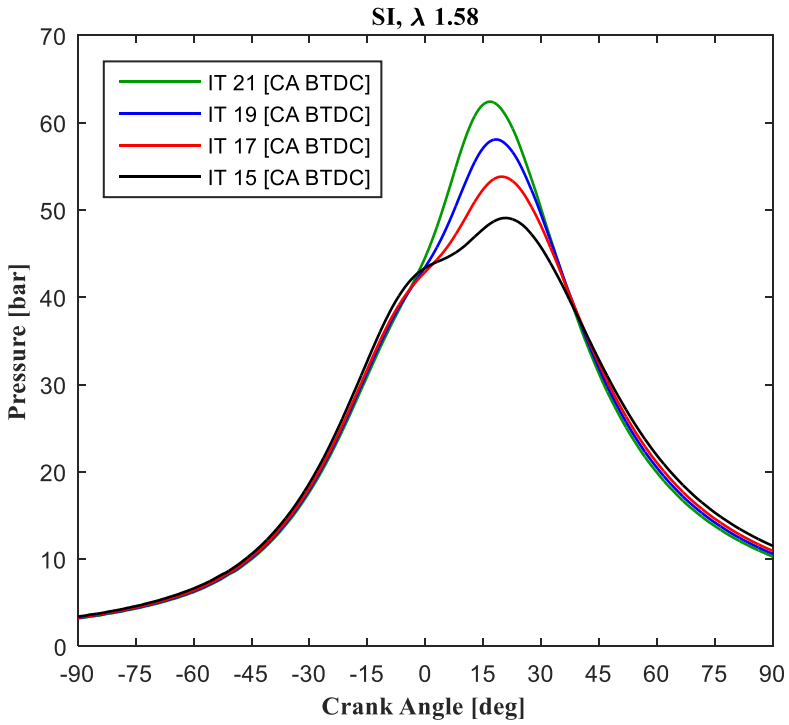

Figure 2.33. Pressure traces of a natural gas reciprocating engine operated with spark ignition at λ = 1.58 and several ignition timing.

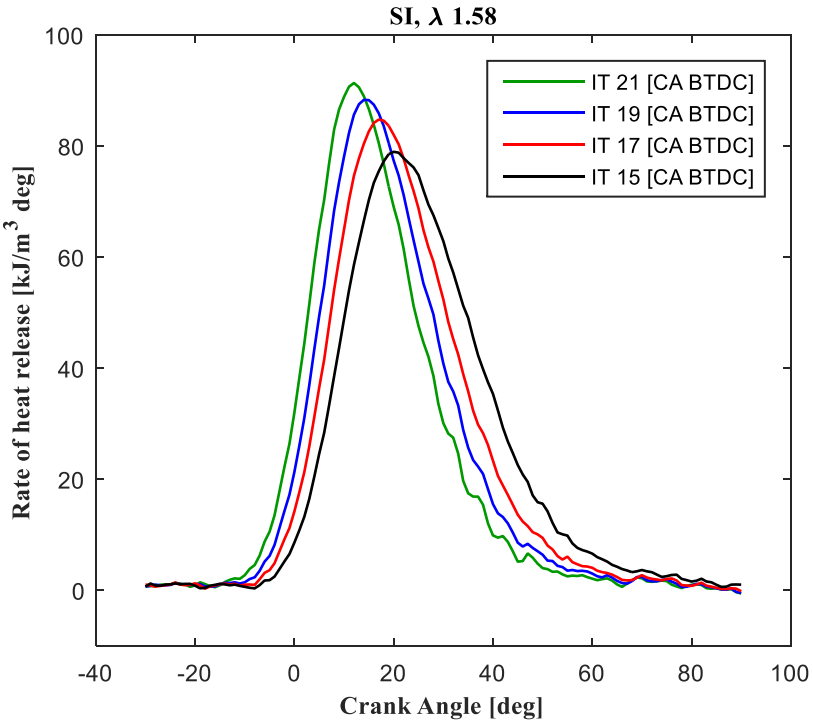

Figure 2.34. Rate of heat release of a natural gas reciprocating engine operated with spark ignition at λ = 1.58 and several ignition timings.

The acceptable operating points can be found after mapping $BSNO_x$ emission and COV_IMEP versus brake thermal efficiency. Figure 2.35 shows the two parameters mapped for several λ and IT. The EPA allowable $BSNO_x$ limit and the industrial accepted COV_IMEP value are shown as red lines; only data points below those lines can be employed in stationary natural gas engines. Since NO_x emissions are proportional to the temperature, the $BSNO_x$ increases as air to fuel ratio decreases for lean mixtures. Similarly, under fixed λ, engine efficiency increases with spark advancement (see Figure 2.35), however, the limiting factor the is $BSNO_x$ emission. It is apparent that for λ = 1.5, no data point can be used because of a high NO_x emission. Since the NO_x emission is expected to be even higher with more advanced ignition system due to shorter combustion duration and lower heat transfer losses, tests at λ = 1.5 were neglected with 2P-LI and PCLI ignition systems.

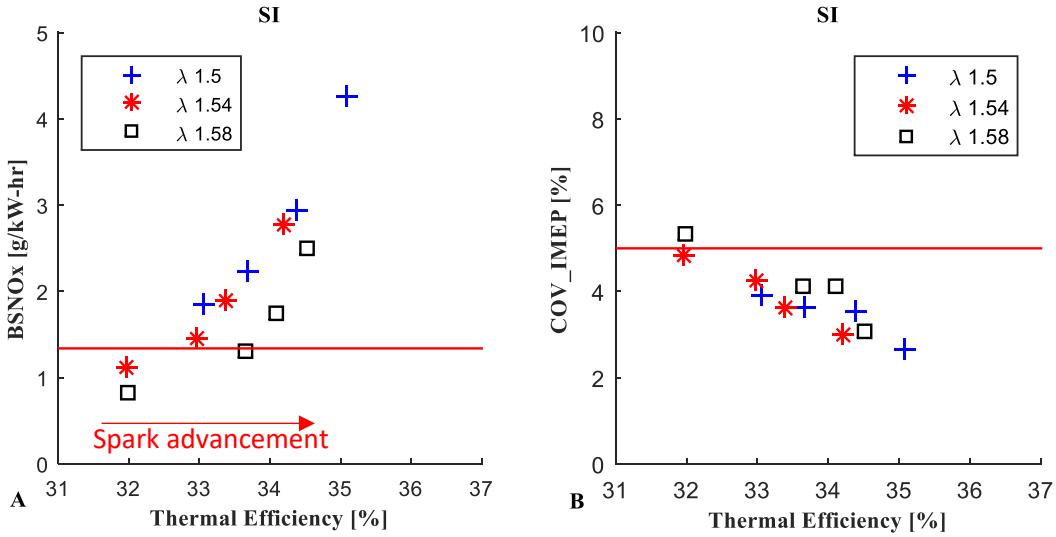

Figure 2.35. Brake specific NO_x emission and COV_IMEP for spark ignition system at several operating conditions.

Out of the 12 operating conditions shown in Figure 2.35 with SI system, only three points maintained the EPA regulated value of $BSNO_x$, and provide acceptable COV_IMEP. The optimum operating point found to be for λ = 1.58, and IT 17° CA BTDC that delivered brake thermal efficiency of 33.65%. Conversely, the COV_IMEP shows an opposite trend in the tested range of SI experiments; a lower COV_IMEP can be attained by utilizing richer mixture and advancing the IT. For lean mixtures, the LBV increases as λ decreases; as a result, a faster combustion process occurs which in turn leads to lower COV_IMEP. Utilizing a mixture leaner than λ = 1.58 with SI system was not an option because the COV_IMEP increases dramatically to values close to 10% due to partial combustions and some misfire events. It is concluded that SI system is not sufficient to ignite a mixture leaner than λ = 1.58 under 10 bar BMEP engine load.

Unlike NO_x emission, other emission gasses like carbon monoxide and unburnt hydrocarbon can be oxidized easily by employing after treatment system. Experiments with SI system showed that the IT has a minimal effect on BSCO and no evident trend with BSHC. The range of BSCO was within 2 – 3.7 g/kW-hr for all tested mixtures and IT. Similarly, the BSHC was in between 4

– 6 g/kW-hr. In contrast, the trend of both emissions was clear as a function of λ, BSHC and BSCO increase by utilizing leaner mixtures. That is mainly because of the reduction of adiabatic flame temperature, and hence the increase of oxidation time which in turn leads to higher emission if the tests are conducted at constant engine speed.

2.4.5 Laser Ignition

The results of SI system showed that advancing the IT while utilizing a leaner mixture can promote the system toward higher engine efficiency. However, igniting a mixture leaner than λ = 1.58 was not possible because of the sudden rise of COV_IMEP. This is attributed to the increase of breakdown voltage with higher boost pressure that is needed to compensate for the reduction of available charge energy. On the other hand, laser absorption increases with pressure and promotes its utilization for lean combustion mode. However, before demonstrating how higher engine efficiency can be achieved with 2P-LI, it behooves us to examine the COV_IMEP and COV_LOMP for identical cases with SI and 2P-LI systems.

Figure 2.36 shows two comparison cases between SI and 2P-LI system where λ = 1.58 and IT = 15° and 17° CA BTDC. One notices that laser ignition minimizes the COV_IMEP from 5.33% to 4.01% for IT 15° CA BTDC. Similarly, the reduction of COV_IMEP at IT 17° CA BTDC was from 4.13% to 3.17% (compare Table 2.9 and Table 2.10 for other cyclic variation metrics). The reduction of cyclic variation is more noticeable for the LOMP; 2P-LI eliminated the variation compared to SI under identical operating conditions. Even if spark ignition system were to be compared with a retarded laser ignition case, the 2P-LI leads to a more stable operation. For example, the COV_LOMP with SI at IT 17° CA BTDC was 13.47% while COV_LOMP for 2P-

LI at IT 15° CA BTDC was only 8.4%. Since cyclic variation decreases by spark advancement (see Figure 2.35B), this observation demonstrates the capabilities of 2P-LI with lean mixtures.

Table 2.10. Coefficient of variation for 2P-LI system at λ = 1.58.

IT [° CA BTDC]	**13**	**15**	**17**
COV_IMEP [%]	4.19	4.01	3.17
COV_MP [%]	9.71	10.3	8.8
COV_LOMP [%]	17.88	8.4	8.2

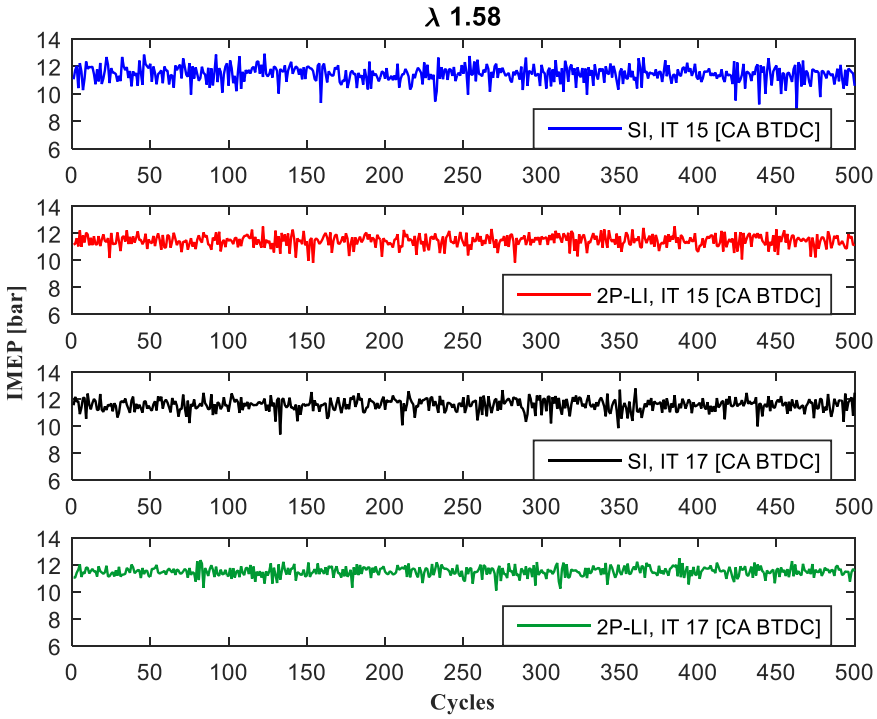

(A) Indicated mean effective pressure

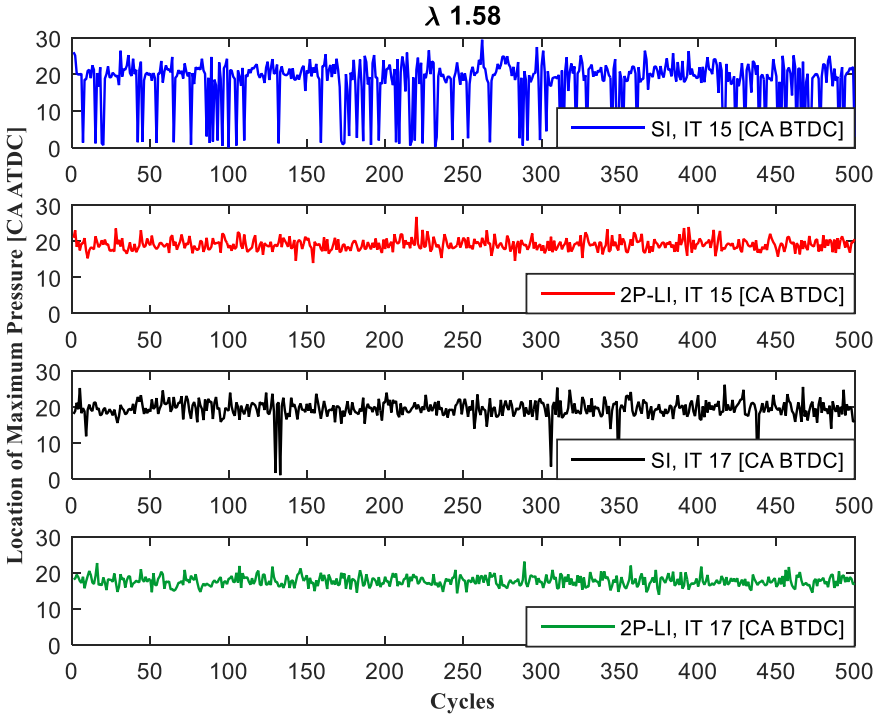

(B) Location of maximum pressure

Figure 2.36. Comparison of cyclic variation of a single cylinder engine ignited with SI and 2P-LI systems at λ = 1.58 and IT 15° and 17° CA BTDC.

Also, the benefit of laser ignition can be visualized by comparing the averaged pressure traces. Figure 2.37 presents pressure traces of laser and spark ignition systems in red and blue colors respectively for λ = 1.58 at IT 15° CA BTDC. As noticed, the pressure trace of 2P-LI system is narrower and higher than the SI system. This is attributed to a shorter combustion process which in turn leads to higher engine efficiency. Similarly, the rate of heat release analysis revealed a faster and higher values with 2P-LI (shown in Appendix C). The reader is advised to check Figure 2.51 for other examples with λ = 1.58 at IT 15° CA BTDC, and λ = 1.54 at IT 13° CA BTDC, similar trends were observed.

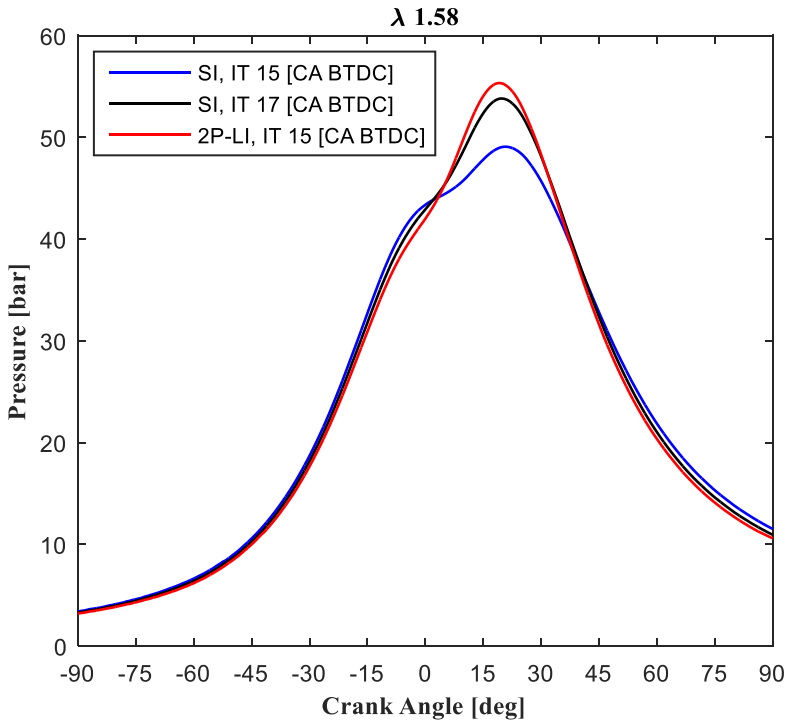

Figure 2.37. Comparison of spark and two pulse laser ignition pressure traces at λ = 1.58 and two ignition timing 15° and 17° [CA BTDC].

In the literature, there are some speculations about laser ignition benefits which suggests that lasers provide only a spark advancement in reciprocating engines. To eliminate this concern, the SI system was advanced 2° CA and compared with the 2P-LI. The solid black line shows the result

of SI at IT 17° CA BTDC; even after advancing IT, 2P-LI provided a faster combustion process. This result proves that the laser ignition improves combustion process in general by providing lower heat transfer losses, shorter ignition delay, and combustion duration as will be shown later. In addition, a similar advantage of 2P-LI can be noticed by comparing cyclic variation metrics (see Table 2.9 and Table 2.10 for SI and 2P-LI systems respectively). The COV_IMEP of 2P-LI for λ = 1.58 at IT 15° CA BTDC was 4.01% while SI system provided 5.33% and 4.13% for IT 15° and 17° CA BTDC respectively. It is worth noting here that engine operation under identical conditions, i.e., same IT and λ, leads to 2P-LI exhibiting higher BSNOx values than SI, which may be attributed to the resulting accelerated combustion.

The author explained earlier the limitation of lean combustion mode in section 2.3; where the LBV reduction offsets the gain from higher specific heat ratios and lower heat transfer losses. This limit exists because of the increase in combustion duration which in turn leads to higher cyclic variations. It has been noticed that the limit varies from engine to engine, based on the number of cylinders as well as the general design of the combustion chamber. In the 6-cylinder engine study, the engine successfully operated at λ = 1.68, however, the single-cylinder engine faced high cyclic variation. Even though that 2P-LI can ignite the lean mixture, the stable engine operation point was shifted to λ = 1.65. This trend is reasonable because single-cylinder engines suffer from high cyclic variations due to the pulsations in intake and exhaust manifolds. However, extending the lean limit from λ = 1.58 in SI to λ = 1.65 with 2P-LI, and using advance IT increased the brake engine efficiency.

Figure 2.38 presents ensemble averaged pressure traces with 2P-LI at λ = 1.65 and several IT. One notices that the IT shifted to more advance values compared with other λ to compensate for the reduction of turbulent burning velocity. The general trend of pressure traces with 2P-LI system

matches those obtained with SI system, an improved combustion process with IT advancement. Also, the rate of heat release analysis given in Figure 2.39 shows a higher rate of heat release. Since a leaner mixture was used in the case of 2P-LI system, the NO_x production met the EPA limit with IT 21° CA BTDC.

Only for IT 23° CA BTDC the $BSNO_x$ emission surpassed the EPA limit of 1.34 g/kW-hr (see Figure 2.54). In that case, represented by an orange line in the pressure trace and rate of heat release analysis figures (see Figure 2.38 and Figure 2.39), the maximum pressure was 66.28 bar at 15° CA ATDC while the highest rate of heat release was 88.43 kJ/m^3deg at 9° CA ATDC. Subsequent thermodynamic analysis revealed that the MFB 50% occurred at 12.7° CA ATDC. Likewise, the location of maximum acceleration of heat release occurred at the TDC which is the optimum point of operation according to Zhu *et al.* study [133]. To conclude, IT 23° CA BTDC was the MBT timing at $\lambda = 1.65$, but due to the fact that the engine was running without a catalytic converter, the EPA limit could not be met. Therefore, the IT 21° CA BTDC was used for further analysis during the comparison of SI, 2P-LI, and PCLI ignition systems. The optimum points for SI, 2P-LI, and PCLI system will be discussed in detail in section 2.4.7.

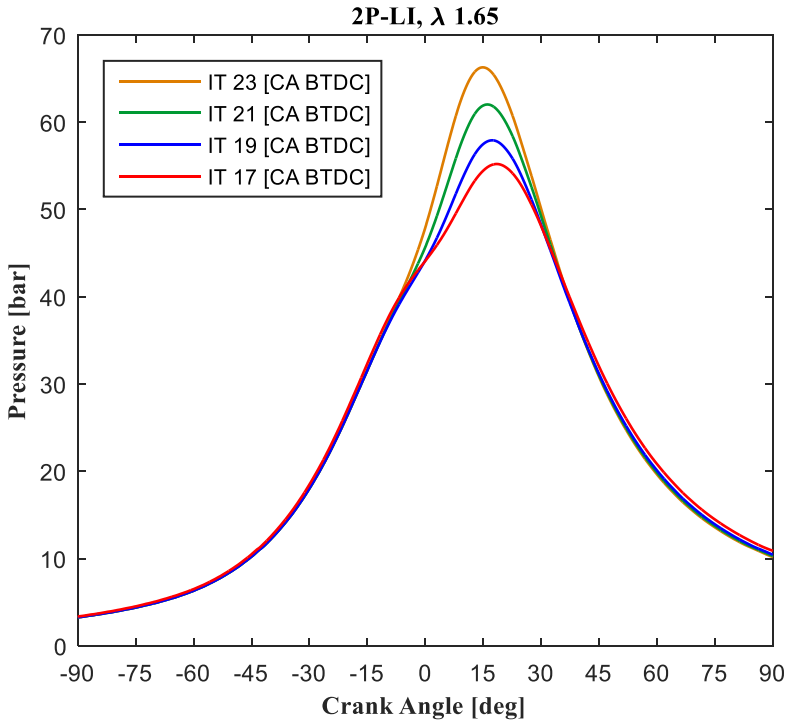

Figure 2.38. Pressure traces of natural gas reciprocating engine operated with 2 pulse laser ignition at λ = 1.65 and several ignition timing.

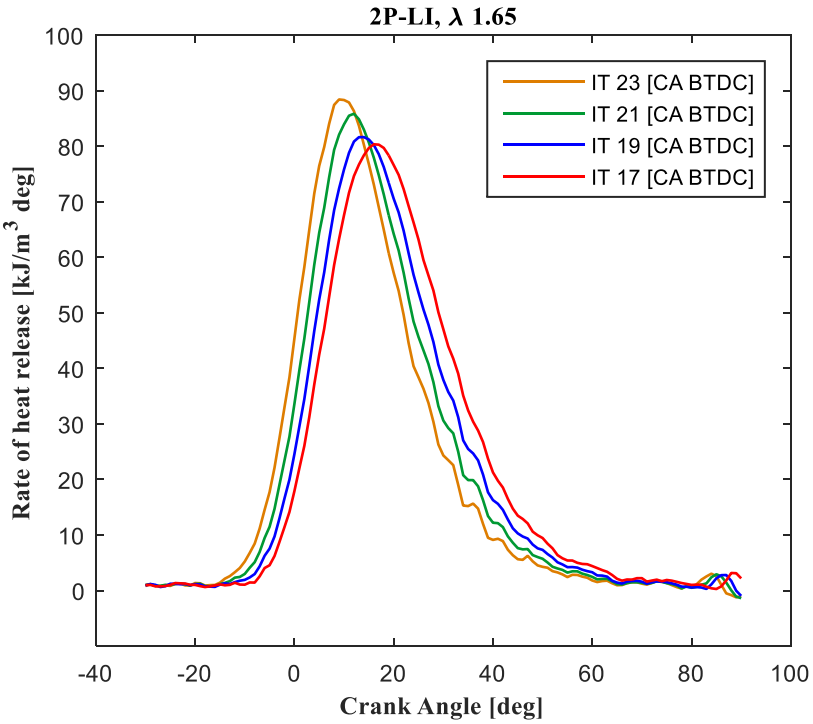

Figure 2.39. Rate of heat release of a natural gas reciprocating engine operated with two pulse laser ignition at λ = 1.65 and several ignition timing.

The cyclic variation in terms of IMEP and LOMP are shown for 2P-LI system in Figure 2.40 at $\lambda = 1.65$ and several IT. Also, several COV metrics are given in Table 2.11. It is evident that the cyclic variation reduces by advancing the IT, due to the shift of operating condition toward the MBT timing that is known for a stable combustion. Comparing Figure 2.40 for 2P-LI at $\lambda = 1.65$ and Figure 2.31 for SI at $\lambda = 1.58$; one notices that even though a leaner mixture was used with 2P-LI the LOMP was more stable. For instance, at IT 19° CA BTDC, COV_LOMP were 9.63% and 10.69% for 2P-LI and SI system respectively. Similarly, COV_IMEP was almost identical 4.14% and 4.12% for 2P-LI and SI systems at the same point.

Table 2.11. Coefficient of variation for 2P-LI system at $\lambda = 1.65$.

IT [° CA BTDC]	**17**	**19**	**21**	**23**
COV_IMEP [%]	4.34	4.14	3.91	3.44
COV_LOMP [%]	12.07	9.63	9.46	9.51
COV_MP [%]	9.53	9.53	9.82	9.02

Unlike the result of COV_LOMP at identical IT and different λ (discussed above), the COV_IMEP and COV_MP show benefits for SI system in some cases. This is attributed to the change of air to fuel ratio, and its direct effect on combustion rate. As noticed, COV_IMEP and COV_MP were slightly lower with SI at $\lambda = 1.58$ relative to 2P-LI at $\lambda = 1.65$ under fixed IT (see IT 21° CA BTDC in Table 2.9 and Table 2.11). Therefore, it is valid to speculate that λ is more dominant factor than the ignition system. However, EPA regulations limit the range of operating points which in turn leads to a different conclusion. As explained earlier, IT cannot be advanced beyond 17° CA BTDC with SI at $\lambda = 1.58$, unlike 2P-LI that offers acceptable $BSNO_x$ emission at 21° CA BTDC with $\lambda = 1.65$. Comparing cyclic variation metrics of those points revealed the importance of ignition systems. All cyclic variation metrics are reduced with 2P-LI system due to the shift of operating point toward MBT timing.

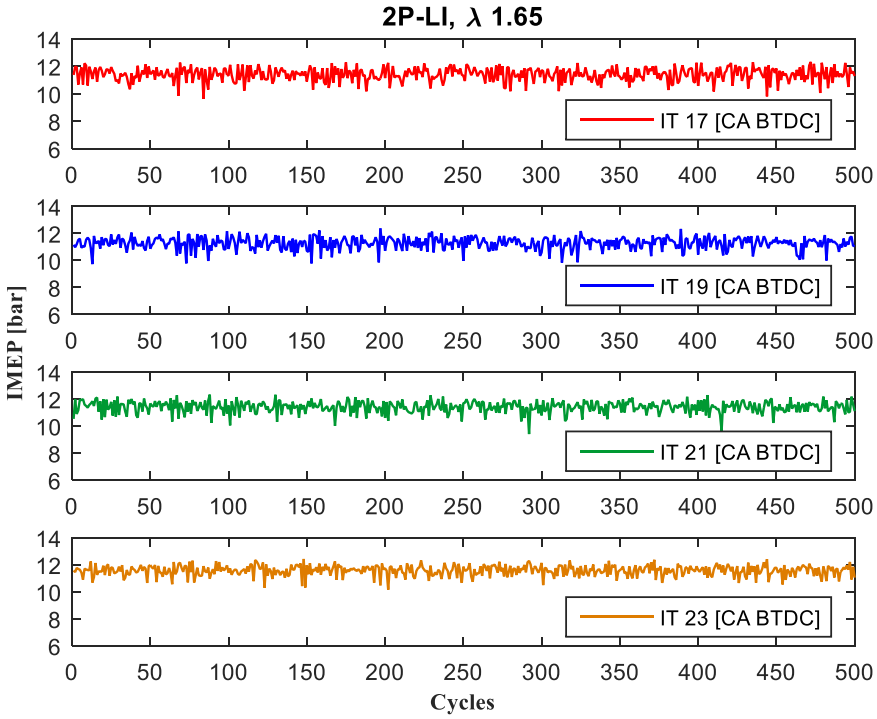

(A) Indicated mean effective pressure

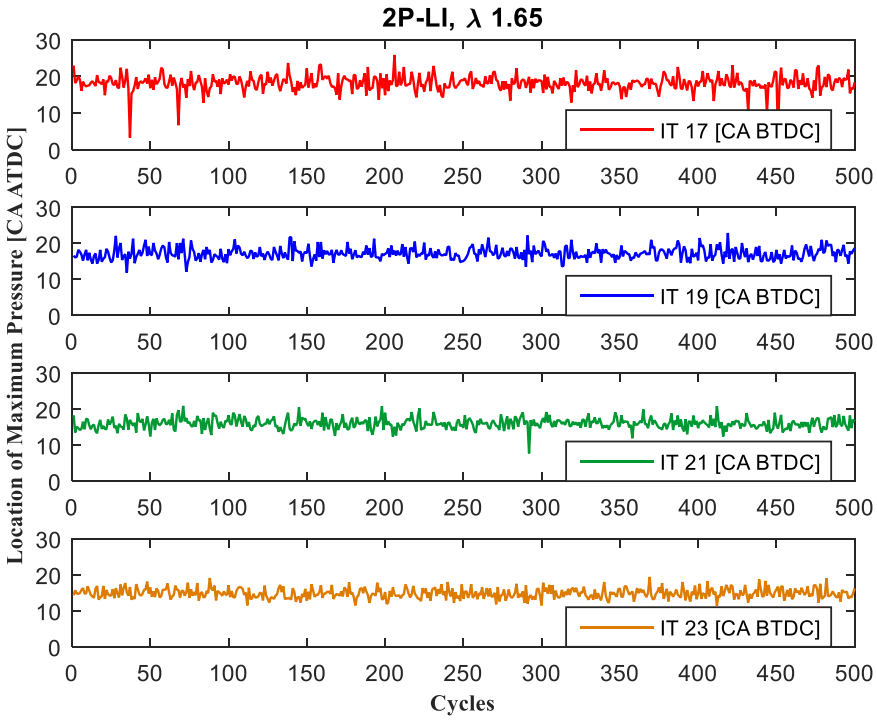

(B) Location of maximum pressure

Figure 2.40. Cyclic variation of a single cylinder engine ignited with 2 pulse laser ignition system at λ = 1.65 *and several IT*.

2.4.6 Prechamber Optimization

In our efforts, the prechamber volume was kept constant at 1600 mm^3 corresponding to 0.08% of the combustion chamber clearance volume, and four different designs were tested. Table 2.12 presents the diameter, number of holes, and the surface area of each design, while a schematic representation is shown in Figure 2.41. Designs D1 and D3 have the same total nozzle cross-sectional area. Designs D2, D3, and D4 have the same configuration, except for the fact that hole sizes were different. Only few tests conducted with D4, three holes 2 mm diameter, but they provided a result similar to those attained by D3. Hence, the fourth design has been neglected in this evaluation.

Table 2.12. Prechamber geometries.

Design	Number of holes	Diameter of holes [mm]	Total surface area [mm^2]
D1	6	2 & 1	11.78
D2	3	1.6	6.03
D3	3	2.23	11.72
D4	3	2	9.42

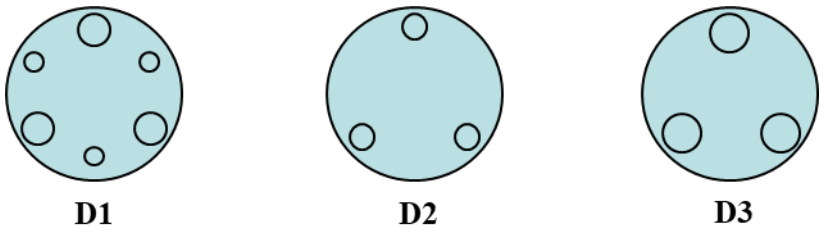

Figure 2.41. Schematic representation of three prechamber geometries.

Even though that the optimum IT might be different for each ignition system or prechamber configuration, here a first comparison was made under fixed IT and λ to understand the benefit of spatial distribution and nozzle diameter. After that, the full analysis is shown for the most promising design. Figure 2.42 and Figure 2.43 present the pressure traces and rate of heat release for λ = 1.58 with two IT. It is evident that D1 which has six holes in staggered configuration gave

the best performance, higher and faster pressure rise. The rate of heat release also provided the same conclusion with the most rapid combustion in D1 compared to D2 and D3 (Figure 2.43 illustrates faster rate of heat release with D1, shown in red color).

Design 2 which has three holes, 1.6 mm diameter, gave a slightly higher rate of heat release (maximum value) because of its optimum IT in that case. The full thermodynamic analysis of D1 revealed that the IT was advanced beyond the MBT timing as shown in Table 2.13. Alternatively, D2 at IT 15° CA BTDC and D3 at IT 14° CA BTDC attained the MBT timing according to the maximum acceleration of heat release criterion.

Table 2.13. Combustion parameters for the three prechamber designs at λ = 1.58.

Design	**D1**	**D2**	**D3**
Maximum pressure [bar]	75.07	71.44	68.84
Location of Max. pressure [CA ATDC]	13.4°	14°	14.7°
Mass fraction burned 50% [CA ATDC]	8.5°	9.65°	10.6°
Maximum acceleration of heat release [CA ATDC]	-3°	0	0

The cross-sectional area of D1 and D3 are the same, but the spatial distribution of flame jets (six compared to three) in D1 provided a shorter ignition delay and combustion duration (see Figure 2.44). Similarly, comparing D2 and D3 that has the same hole configuration but with different diameters reveals a definite advantage. D2 provided shorter combustion duration because the flame jets velocity increases as the nozzle diameter decreases, thereby, deeper penetration and better spatial distribution were accomplished. However, the ignition delay shown in Figure 2.44 increased slightly in D2 because of higher flow restriction. In that design, engine knock was detected for $\lambda \geq 1.65$ after reaching the target engine load (10 bar BMEP). Hence, D2 was tested only at $\lambda = 1.58$, and the full range was evaluated for D1 and D3. In case of engine knock, the weakest spot is the focusing lens that cracks after few knocking cycles.

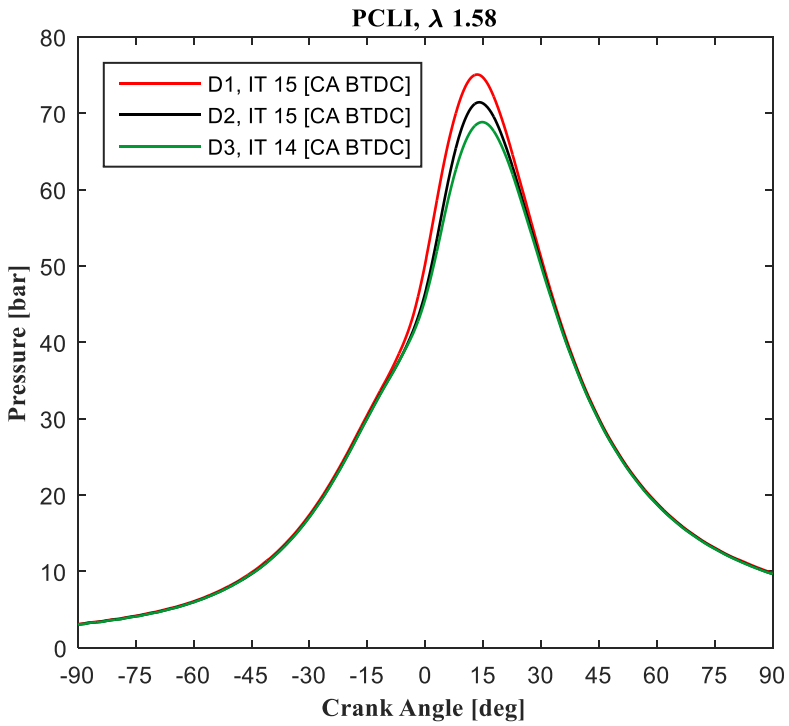

Figure 2.42. Pressure traces of natural gas reciprocating engine equipped with several designs of PCLI at λ = 1.58 and 10 bar BMEP.

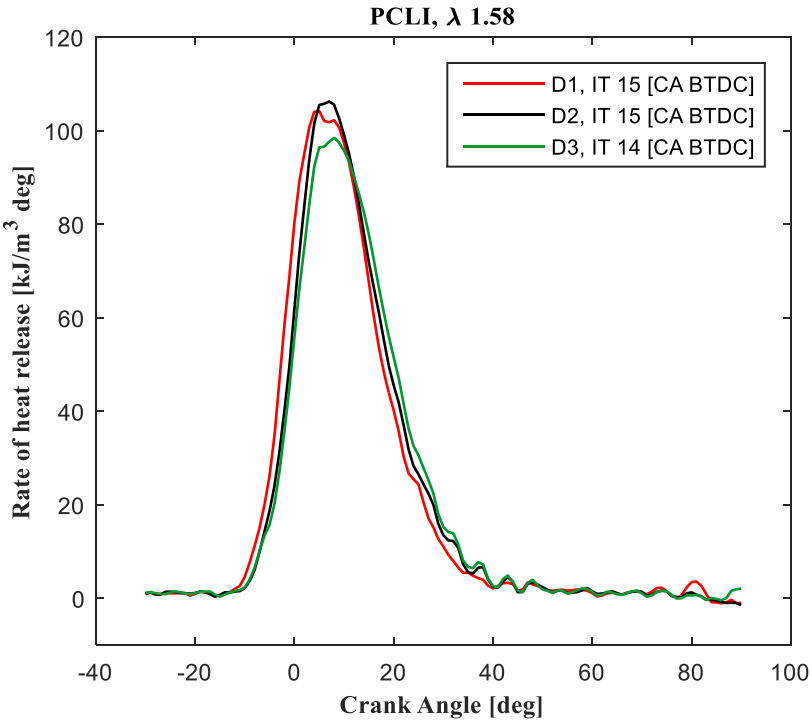

Figure 2.43. Rate of heat release of natural gas reciprocating engine equipped with several designs of PCLI at λ = 1.58 and 10 bar BMEP.

In lean combustion mode, the spatial distribution of jets has a dominant effect by minimizing the flame travel path which in turn leads to faster combustion. Therefore, instead of advancing IT with lean mixtures, IT was retarded in PCLI relative to SI and 2P-LI systems. Ignition delay and combustion durations for the three geometries at λ = 1.58 are shown in Figure 2.44. It is obvious that D1 provided a shorter ignition delay, the difference was approximately 1-1.5° CA compared with the other designs. The MFB 10% was almost constant with IT, however, the MFB 10-90% decreases as the IT advanced because of a better charge utilization. As seen, the combustion durations are somewhat similar at λ = 1.58.

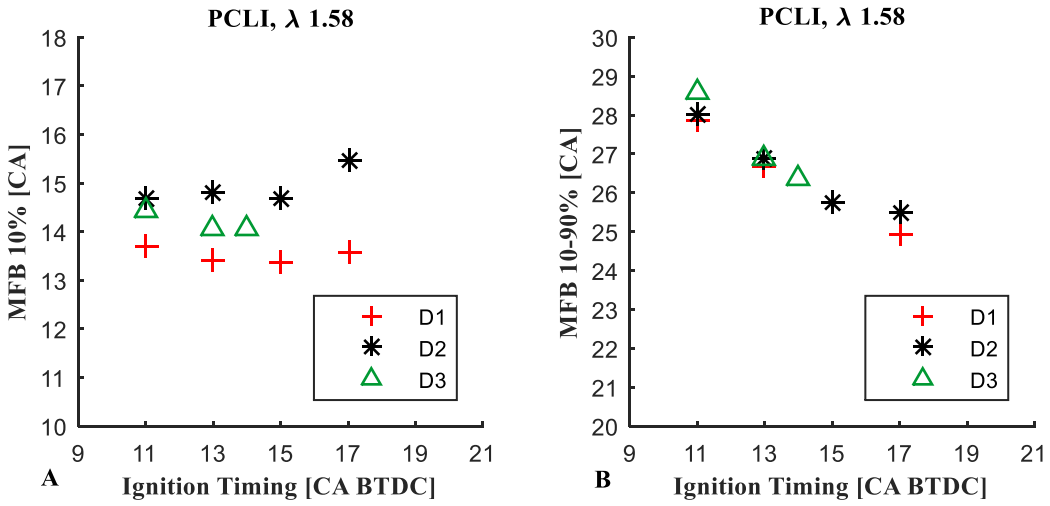

Figure 2.44. (A) Ignition delay and (B) combustion duration for the three prechamber geometries for λ = 1.58.

Subsequent tests comparing D1 and D3 (see Figure 2.45) showed that both ignition delay and combustion duration were lower with D1. It has been noticed that the benefit of D1 is more noticeable with a leaner mixture. For example, the difference in ignition delay between D1 and D3 at IT 13° CA BTDC for λ = 1.58 was only 0.65° CA while the difference increases to 1.7° CA at λ = 1.7. Similarly, at the same conditions, the difference in combustion duration was almost negligible for λ = 1.58 while it was 3.1° CA with λ = 1.7. This observation shows how crucial is

the spatial distribution with very lean mixture combustion. Additionally, there was no incidence of autoignition in the case of D1 even with a very lean mixture (λ = 1.75). The superior performance of D1 is attributable to the fact that it uses 2 and 1 mm diameter holes in a staggered fashion, which in addition to the spatial separation, leads to temporally separated issuance of jets from the larger and smaller holes.

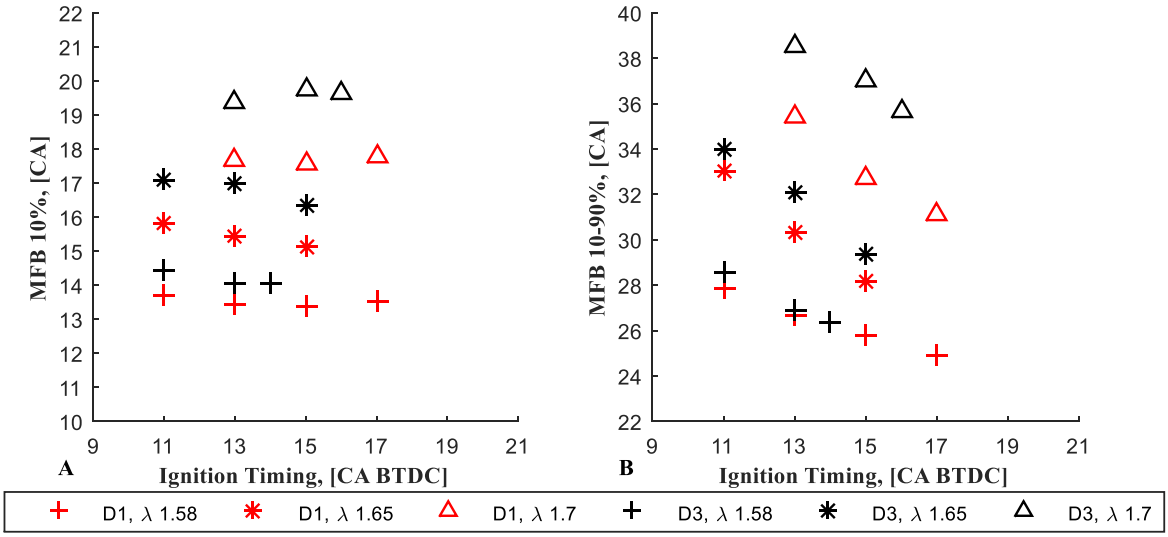

Figure 2.45. (A) Ignition delay and (B) combustion duration for D1 and D3.

Overall design D1 - prechamber volume 1600 mm^3, 3 holes 2 mm Dia. and 3 holes 1 mm Dia. at 45° to the igniter axis - was the optimal geometry that would offer low NO_x emissions and at the same time avoid autoignition and soot formation. This prechamber geometry was used in PCLI for subsequent tests comparing the three ignition systems shown in the next section.

A wide range of IT 11-21° CA BTDC, and λ 1.54-1.75 were used for the PCLI D1 to evaluate its performance, and compare it with SI and 2P-LI. The trend of pressure traces and rate of heat release with IT was identical to the results presented earlier with SI and 2P-LI systems; a faster combustion with spark advancement. Figure 2.46 shows the rate of heat release for PCLI D1, λ = 1.58, and several IT. The maximum acceleration of heat release analysis revealed that IT 15° and 17° CA BTDC were advanced beyond the MBT timing. Even though the engine was stable,

running at those conditions results in a lower brake thermal efficiency due to the negative work against the compression stroke. The reduction of brake thermal efficiency was observed clearly with λ = 1.54 where the value reduced from 36.13% to 35.95% by advancing the IT from 15° to 17° CA BTDC. It is worth mentioning that running the engine with PCLI at λ ≤ 1.58 generates high $BSNO_x$ emission, but the author carried out those tests in order to compare the PCLI with SI system at identical conditions IT and λ.

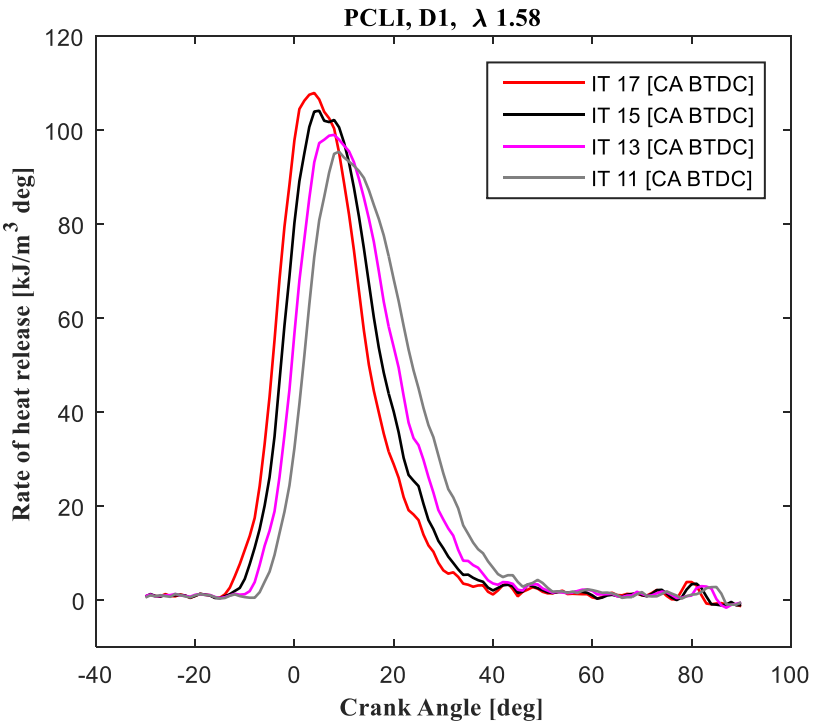

Figure 2.46. Rate of heat release of natural gas reciprocating engine equipped with PCLI D1 at λ = 1.58, several ignition timings, and 10 bar BMEP.

Since the cyclic variations were presented under fixed air to fuel ratio and several IT with SI and 2P-LI systems, the author intended to show the effect of λ for the PCLI system. This illustration does not only demonstrate the capability of PCLI system but also emphasize the effect of λ on cyclic variation Figure 2.47 compares the cyclic variation at IT 15° CA BTDC and a range of 1.58 ≤ λ ≤ 1.7. Also, the COV_IMEP, COV_LOMP, and COV_MP are presented in Table 2.14.

It is clear that under fixed IT all cyclic variation metrics increases by using leaner mixtures because of the reduction in turbulent burning velocity. The COV_IMEP was within the acceptable industrial value for all tests except at $\lambda = 1.75$ where a sudden jump of COV_IMEP was noticed as will be shown later. Similarly, the COV_MP increased but at a relatively higher rate. This is an inductive of COV_MP sensitivity to λ which has a drastic effect on combustion duration. The COV_LOMP was almost constant for $1.54 \leq \lambda \leq 1.7$ (see Table 2.14), and it was very small compared to SI 38.6% and 2P-LI 8.4% at identical operation condition. Overall, PCLI system improved engine cyclic variation by distributing the ignition sites and minimizing the dependence of flame speed. This feature is crucial for stationary large bore natural gas engines because brake thermal efficiency can be improved by using a lean mixture if the cyclic variation can be maintained within acceptable values.

Table 2.14. Cyclic variation of PCLI D1 system at IT 15° CA BTDC and several λ.

λ	**1.58**	**1.65**	**1.68**	**1.7**
COV_IMEP [%]	2.21	2.7	3.01	3.7
COV_LOMP [%]	6.15	6.15	6.23	6.71
COV_MP [%]	4.95	6.51	6.75	7.52

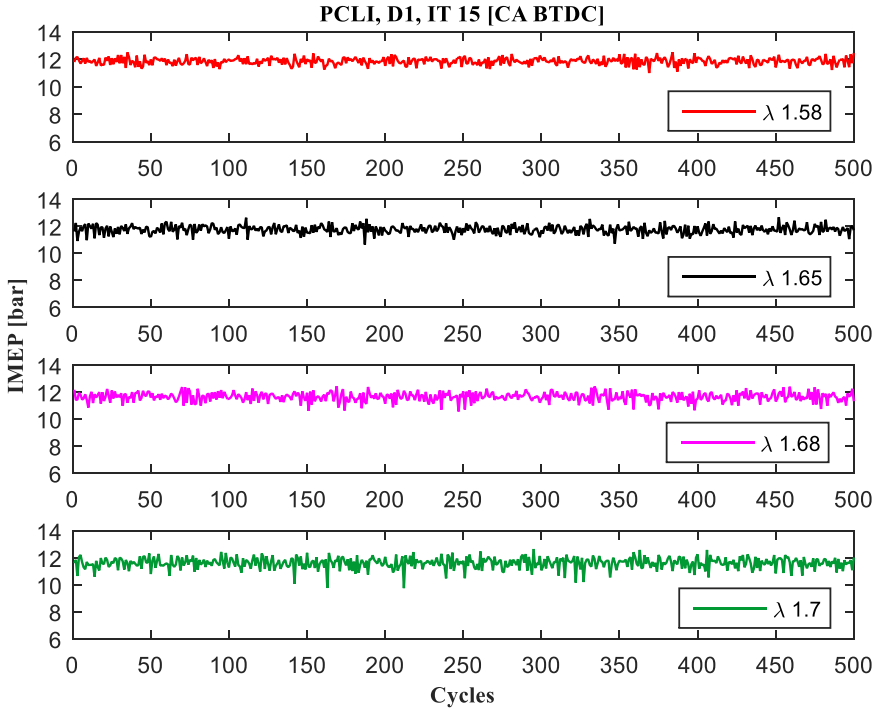

(A) Indicated mean effective pressure

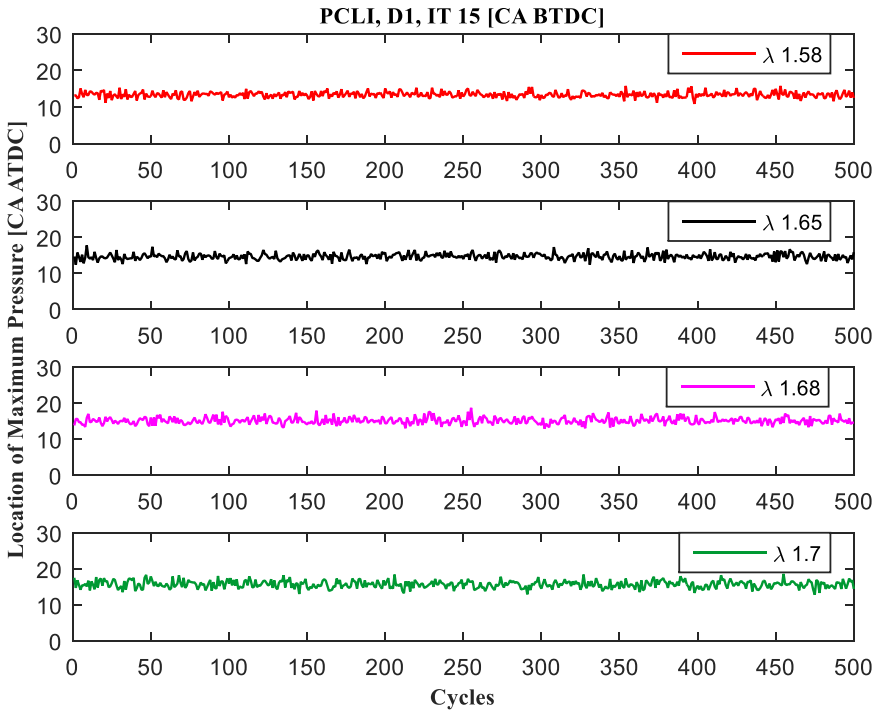

(B) Location of maximum pressure

Figure 2.47. Cyclic variation of a single cylinder engine ignited with prechamber D1 at IT of 15° CA BTDC and several air to fuel ratios.

The average pressure traces for 500 consecutive cycles are illustrated in Figure 2.48 at IT 15° CA BTDC. The maximum pressure increases and shifts toward the TDC by utilizing richer mixtures due to the increase in combustion rate. However, at IT 15° CA BTDC, only $\lambda \geq 1.68$ provides acceptable $BSNO_x$ emission with PCLI because of the rapid combustion process.

Mass fraction burned analysis is shown in Figure 2.49 under several IT and λ. One notices that the ignition delay was almost constant with spark advancement, only at $\lambda = 1.75$, the ignition delay was increasing with IT. Conversely, the ignition delay was increasing with λ; for instance, the MFB 10% increased 1.35° CA by increasing λ from 1.68 to 1.7 at IT 15° CA BTDC. The general trend for all data points was an increase in the range of 0.8-1.8° CA in between the considered λ. Only at $\lambda = 1.75$, the increase was 3.65° CA compared to $\lambda = 1.7$ at IT 17° CA BTDC. This sudden rise is attributed to the high cyclic variation encountered during those tests which revealed the limit of PCLI system.

The trend of combustion duration with the excess air ratio was identical to the ignition delay. The MFB 10-90% increased 2.8° CA by increasing λ from 1.68 to 1.7 at IT 15° CA BTDC. However, the combustion duration decreases with IT as illustrated in Figure 2.49B. This is indicative of burning the charge in a smaller volume which in turn leads to a faster combustion process. For the cases at $\lambda = 1.75$ and IT 17-21° CA BTDC, no clear trend was observed due to high cyclic variation as stated earlier.

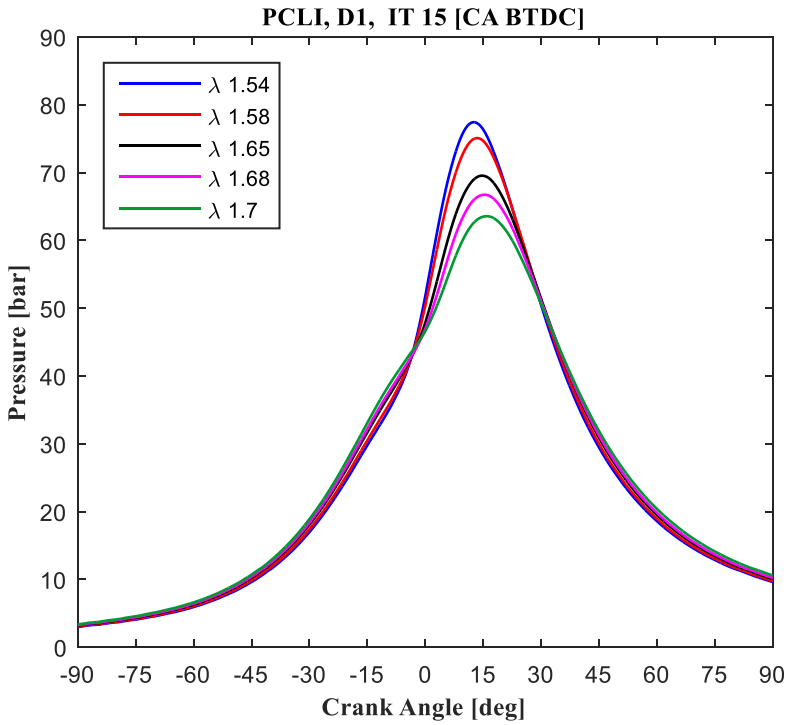

Figure 2.48. Pressure traces of natural gas reciprocating engine equipped with PCLI D1 at IT 15° CA BTDC, several excess air ratio, and 10 bar BMEP.

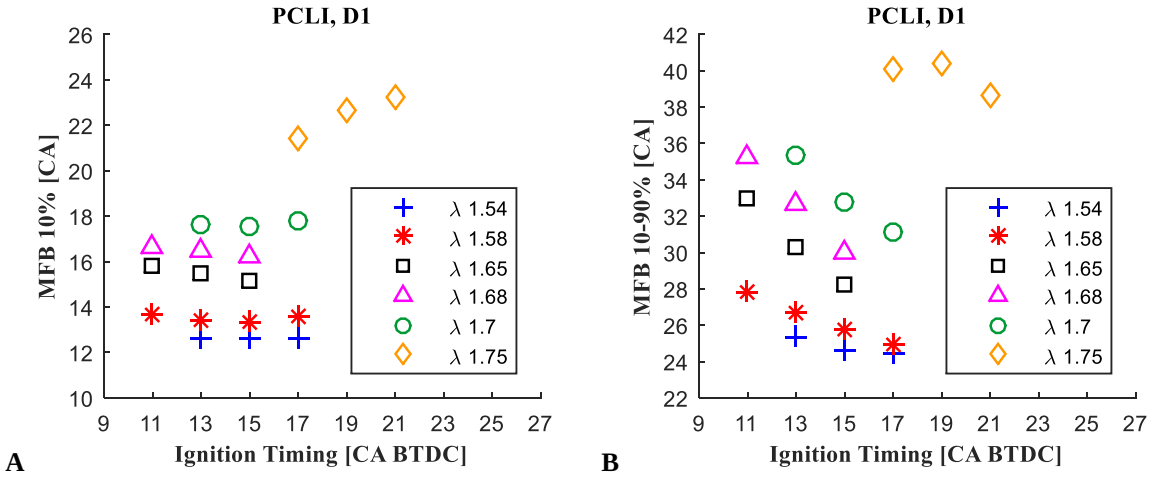

Figure 2.49. (A) Ignition delay and (B) combustion duration for PCLI D1.

Figure 2.50 shows $BSNO_x$ emission as well as COV_IMEP for all the data points taken by PCLI D1. The scale of y-axis was increased to accommodate the wide range of engine operating conditions taken with PCLI. The $BSNO_x$ emission increases while the COV_IMEP decreases with spark advancement. One notices that all data points taken with $\lambda = 1.54$ and 1.58 provide $BSNO_x$

emission higher than 1.34 g\kW-hr (EPA limit). Also for λ = 1.65, only one data point can be employed with PCLI at IT 11° CA BTDC.

Likewise, all data points taken with λ = 1.75 offers COV_IMEP higher than the industrial accepted value. The sudden rise of COV_IMEP was noticed for all ignition systems but at a different λ. For the case of PCLI system, the COV_IMEP increased from the range of 3.7-5.11% at λ = 1.7 to 10.24-13.82% at λ = 1.75. Since those data points do not comply with EPA regulation and the industrial accepted COV value, they were disregarded. Therefore, the PCLI system operating range was limited to $1.65 \leq \lambda \leq 1.7$ and IT 11°-17° CA BTDC.

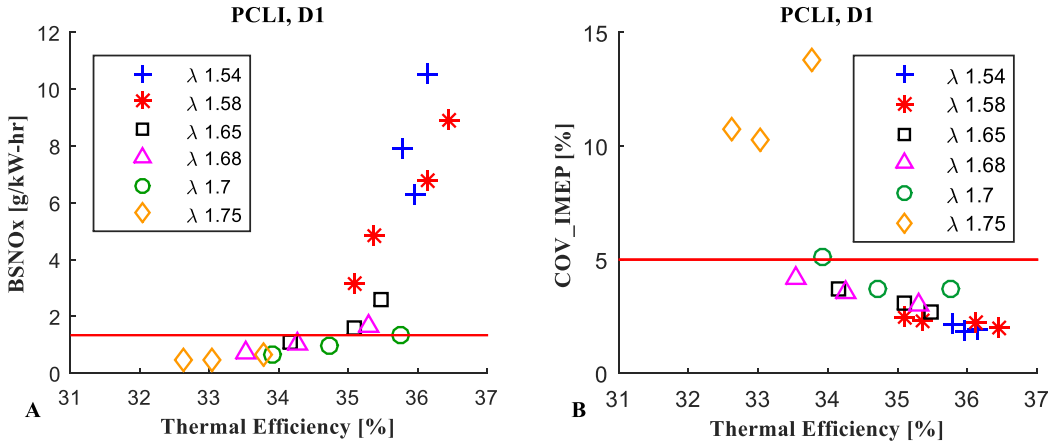

Figure 2.50. Brake specific NO_x emission and COV_IMEP for PCLI system at several air to fuel ratio.

2.4.7 Results and Discussion of the Three Ignition Systems

The averaged pressure curves for the three ignition systems, for two different test conditions IT 13 at λ 1.54, and IT 17 at λ 1.58 are shown in Figure 2.51A and C respectively. One notices that in both conditions, 2P-LI leads to faster combustion that results in a higher peak pressure value as compared to SI. As evident from the rates of heat release shown in Figure 2.51B and D, LI also leads to shorter ignition delay. This may be attributed to larger flame kernel developed in the case of LI, which gets further amplified by heat released from combustion gases entrained from the

surroundings [81]. The net effect is accelerated combustion leading to higher peak pressures and stable engine operation.

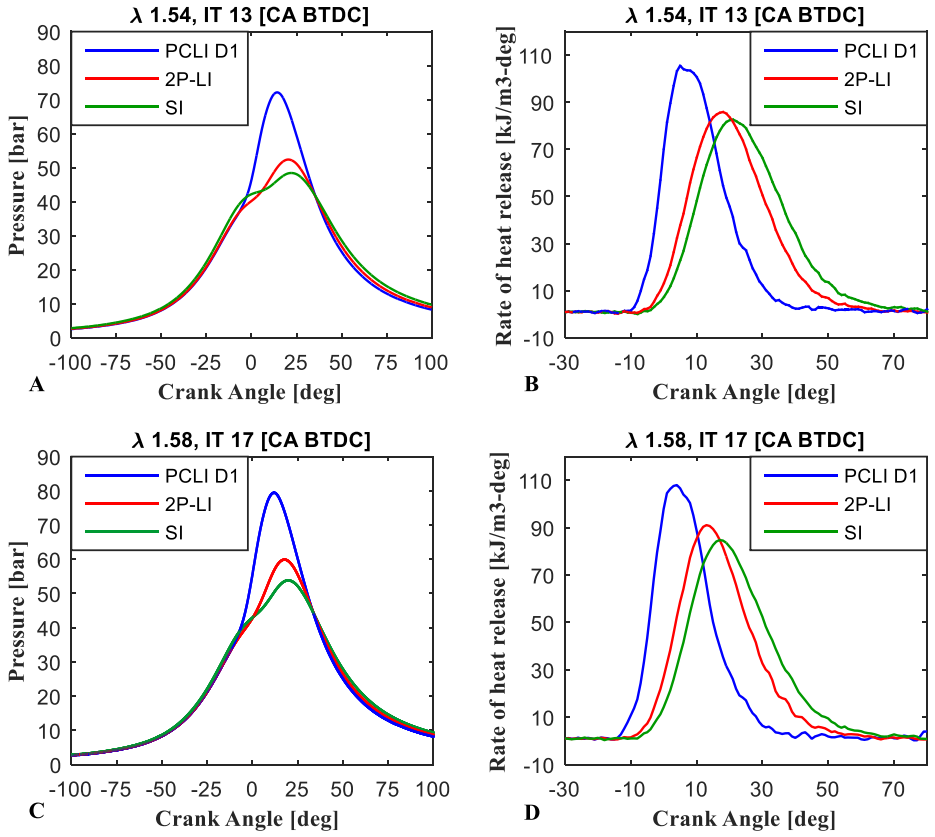

Figure 2.51. Pressure traces and heat release rates.

Similarly, in the case of PCLI D1, the partially combusted jets issuing from the prechamber introduce spatially distributed ignition sites at multiple locations, especially at the jet head vortices [137], leading to earlier and much faster combustion. This results in peak cylinder pressures approximately 20 bar higher than in SI or 2P-LI. These trends are further evident when one compares ignition delays (see Figure 2.52) and combustion durations (see Figure 2.53) for the three ignition systems. Ignition delays for prechamber ignition system are approximately 10° CA shorter than those corresponding to SI. Similarly, the difference was about 6.8° CA compared with the laser ignition. Combustion durations are reduced on an average by 8° CA in the case of PCLI

D1. Such trends warrant delayed ignition phasing in the case of 2P-LI and PCLI D1 for optimal engine operation.

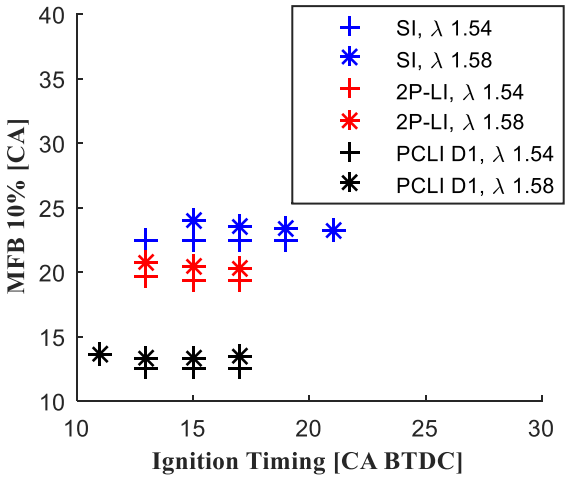

Figure 2.52. Ignition delay for the three ignition systems.

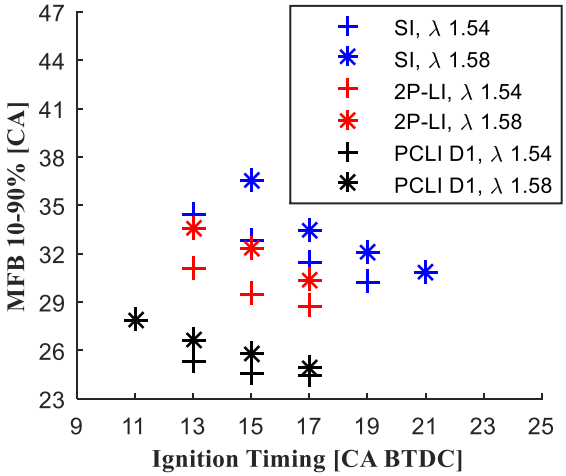

Figure 2.53. Ignition duration for the three ignition systems.

The $BSNO_x$ vs. brake thermal efficiency and the corresponding COV_IMEP vs. brake thermal efficiency plots for the three ignition systems are presented in Figure 2.54. Also shown in this figure with red horizontal lines are the allowable levels for $BSNO_x$ per EPA regulation (1.34 g/kW-hr) and the acceptable industry value for ignition stability (COV_IMEP = 5%). Only data points close to those limits are shown for each ignition system (the full range was illustrated earlier). One notices that for all three ignition systems, for a given λ value, NO_x emissions increase with increase

in brake thermal efficiency (resulting from spark advancement), whereas COV_IMEP decreases (i.e., combustion stability improves). This behavior was captured for all ignition systems before reaching their lean limits, after that, a sudden jump in the order of an additional 5-7% COV_IMEP were recorded.

Laser ignition (2P-LI) extends lean operation to λ 1.65, whereas PCLI extends it even further to λ 1.7. As a result, the optimal operating point for a given ignition system was chosen as the λ and IT combination that offers the maximum brake thermal efficiency. This results in 2P-LI exhibiting an incremental efficiency improvement of $\Delta\eta$ = 1.3%, whereas PCLI performs even better with an improvement of $\Delta\eta$ = 2.1% (see Figure 2.54A, C, and E). As mentioned before, this is primarily attributed to the spatially distributed ignition sites facilitated by PCLI, which lead to faster combustion and close to the top dead center. It is believed that the PCLI system will provide even higher efficiency improvement on the 6-cylinder engine due to its stable operation.

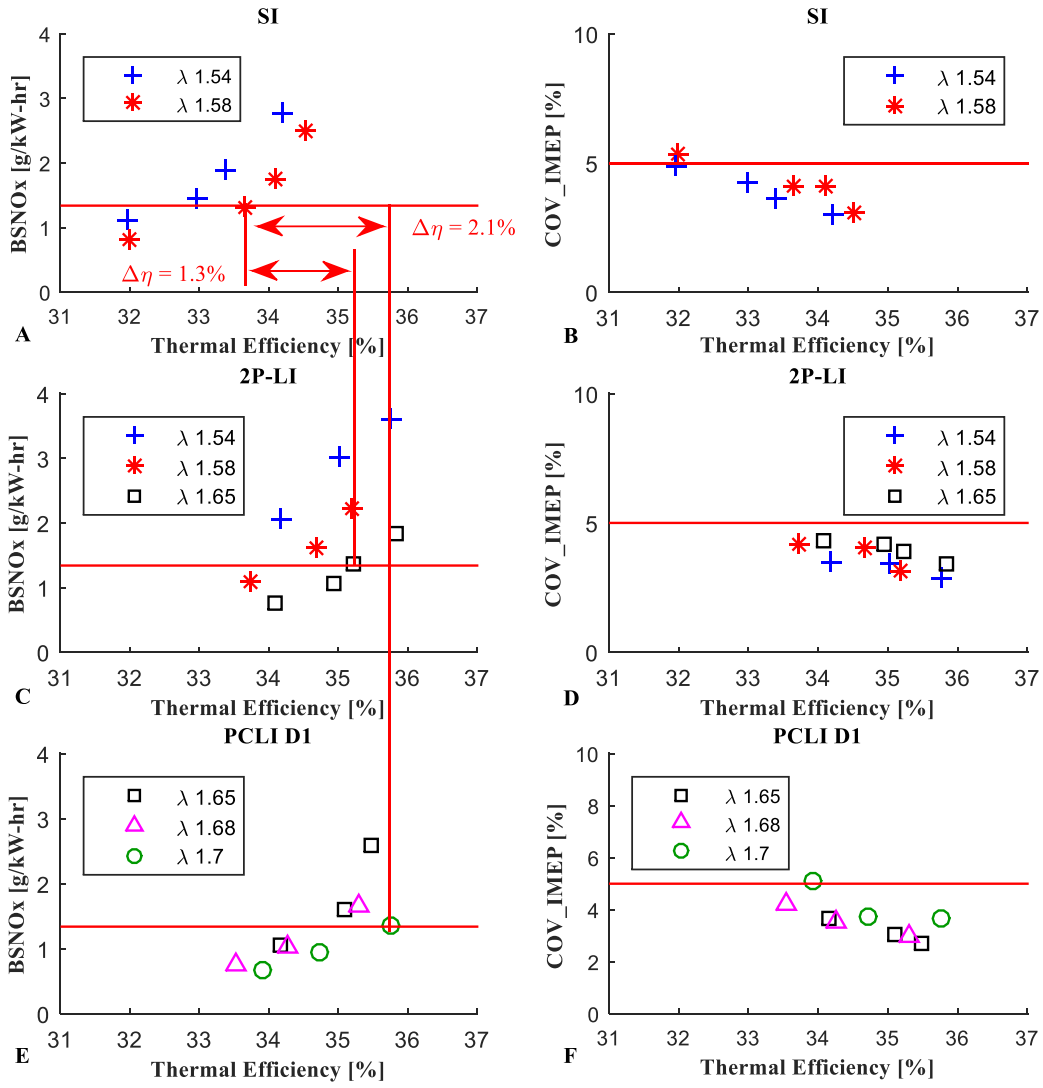

Figure 2.54. Relative performance of SI, LI and PCLI.

As the performance of each of the ignition systems is governed by different physical processes, the optimal operational point for each one of them, i.e., λ and IT were different. For example, the optimum SI point happened to be with λ = 1.58 at IT 17° CA BTDC. Similarly, the 2P-LI optimum point occurred with λ = 1.65 and IT 21° CA BTDC, whereas for PCLI, λ = 1.7 and IT 17° CA BTDC yielded the highest efficiency.

Figure 2.55 shows the average pressure trace for the optimal operating points in each ignition system. Arrows and diamond marks were used to present the IT and the time for mass fraction burned 90% respectively. Orange arrow was used for IT 17° CA BTDC because both SI and PCLI-D1 share that point. One notices that the time required for achieving 90% MFB decreases by using advance ignition systems such as 2P-LI or PCLI. This reflects efficient combustion process as shown in the rate of heat release figure. Also, it is evident that the peak pressure was increasing in the order of SI, 2P-LI, and PCLI while the location of peak pressure was shifting toward the top dead center. A similar observation was noticed for the rate of heat release, but the values were very close. Table 2.15 compares several combustion parameters for spark, laser, and prechamber ignition systems at optimal operating conditions.

Table 2.15. Combustion parameters for the three ignition systems at optimal operation condition.

Ignition system	**SI**	**2P-LI**	**PCLI D1**
Maximum pressure [bar]	53.8	62	67.1
Location of Max. pressure [CA ATDC]	19.8°	16.1°	14.7°
Maximum rate of heat release [kJ/m^3-deg]	84.8	85.9	87.6
Location of Max rate of heat release [CA ATDC]	17°	12°	9°
Mass fraction burned 50% [CA ATDC]	20.3°	14.95°	13°
Maximum acceleration of heat release [CA BTDC]	7°	3°	0 (@TDC)

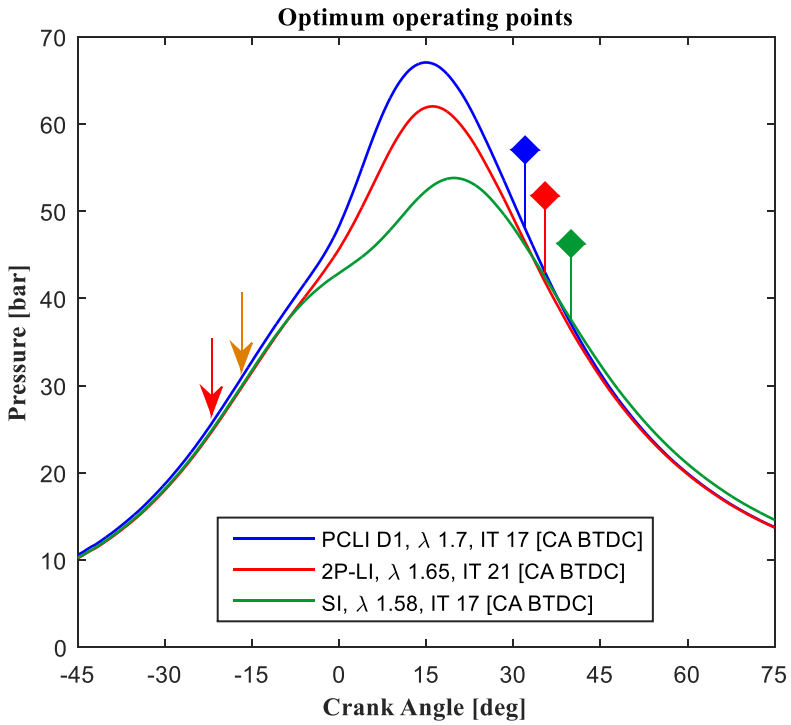

Figure 2.55. Pressure traces of optimal operating points on natural gas reciprocating engine equipped with several ignition systems at 10 bar BMEP.

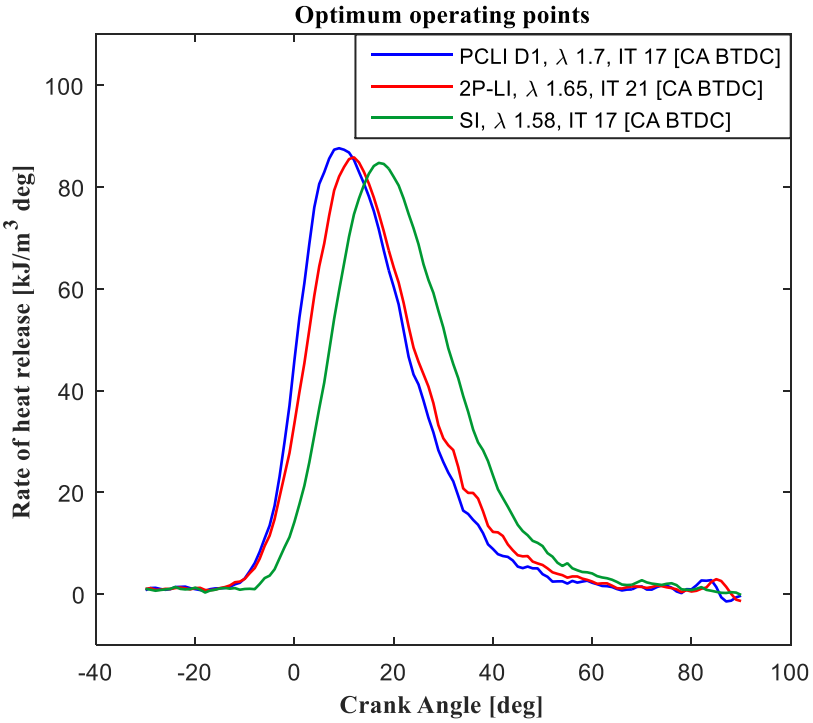

Figure 2.56. Rate of heat release of optimal operating points on natural gas reciprocating engine equipped with several ignition systems at 10 bar BMEP.

Subsequent thermodynamic analysis revealed that the angle at which MFB 50% is attained shifted from 20.3° CA ATDC with SI to 14.95 and 13° CA ATDC by using 2P-LI and PCLI respectively. An observation worthy of mention is the fact that maximum acceleration of heat release gradually moves towards the TDC, and in the case of PCLI occurs at TDC. As argued earlier, it might be a better metric for optimal combustion phasing as compared to others. It is evident that the SI was running with at retarded point relative to the MBT timing. That is mainly because $BSNO_x$ emission exceeds the EPA limit with advance IT at $\lambda = 1.58$. On the other hand, 2P-LI was very close to the MBT timing with a difference of only 1.1° CA for LOMP and 5° CA for MFB 50% criteria. The engine was running exactly on the MBT timing with PCLI system as shown in several combustion parameters in Table 2.15. To conclude, PCLI system was stable enough to reduce λ to an extent where MBT was achieved without compromising $BSNO_x$ emission or cyclic variation; an operating condition that cannot be fulfilled with SI and 2P-LI systems.

Figure 2.57 shows the cyclic variation in terms of IMEP and LOMP for the optimum operating points. It is evident that the PCLI system reduced the cyclic variation even though it was running with a leaner mixture. The reduction of cyclic variation can also be seen in Table 2.16 that compares the COV of several metrics. A reduction of COV_IMEP was observed from 4.13% with SI to 3.68% using PCLI. Similarly, there was a huge reduction of COV_LOMP from 13.46%with SI to 7.05% by PCLI. Also, the sensitivity of combustion instability is more noticeable with the LOMP metric; a similar observation was made earlier with SI and 2P-LI under different IT. The reduction of cyclic variation is primarily attributed to the multiple partially combusted turbulent flame jets issuing from the prechamber, because of their spatial distribution, lead to volumetric and faster ignition.

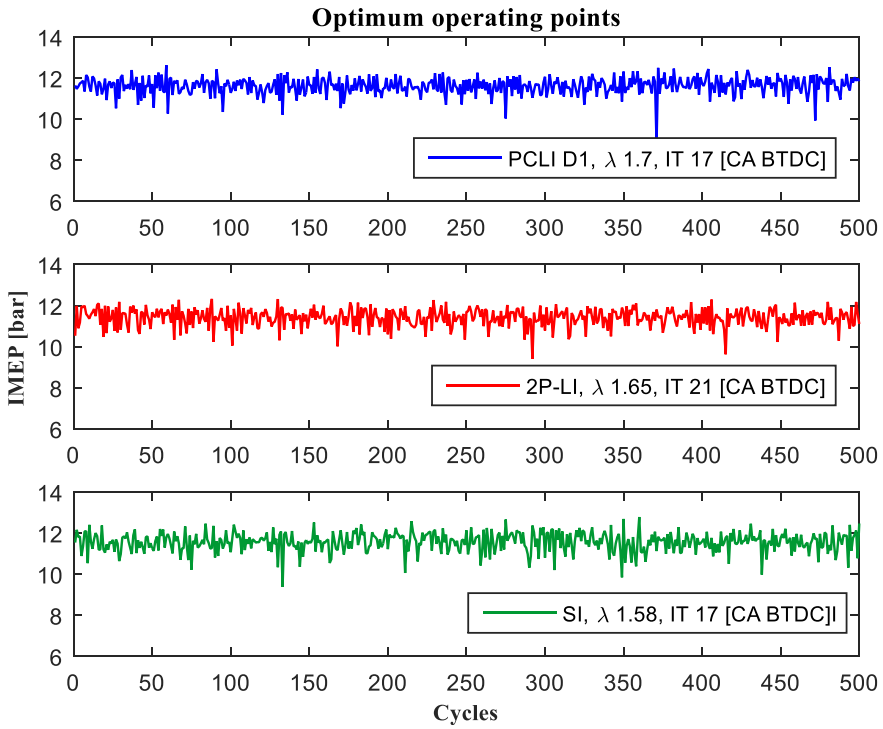

(A) Indicated mean effective pressure

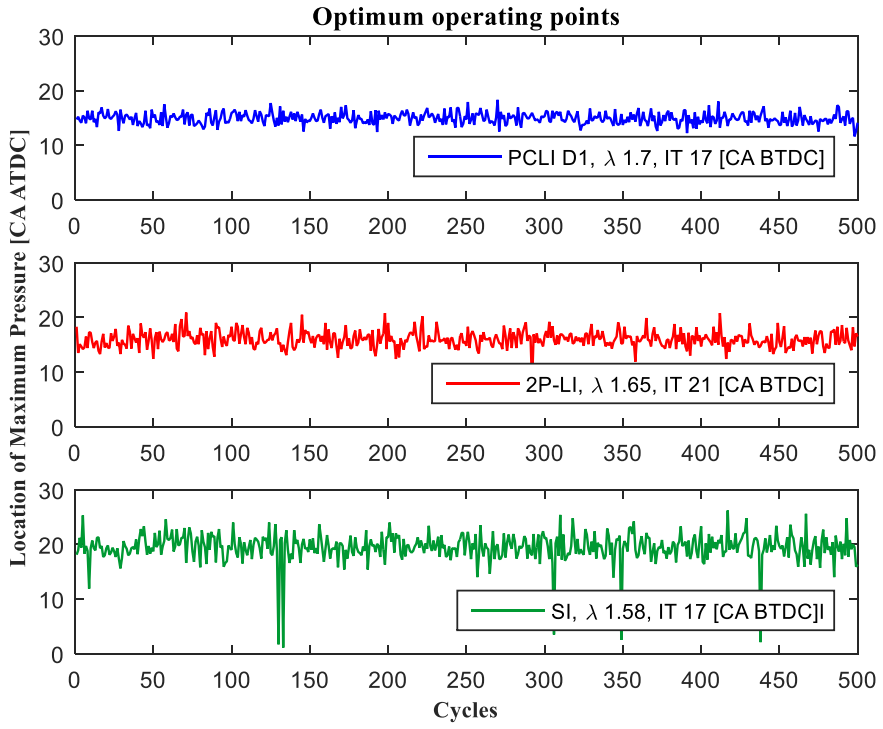

(B) Location of maximum pressure

Figure 2.57. Cyclic variation of a single cylinder engine ignited with several ignition systems at the optimum operational condition.

Table 2.16. Cyclic variation at optimal operating points of each ignition system at ignition timing 15° CA BTDC and several λ.

	SI	**2P-LI**	**PCLI D1**
COV_IMEP [%]	4.13	3.91	3.68
COV_LOMP [%]	13.46	9.46	7.05
COV_MP [%]	9.87	9.82	8.33

BSHC and BSCO emissions are compared in Figure 2.58; the optimal operating points are shown as black circles. One notices that there is a small rise in the BSHC emission from 5.47 g/kW-hr using SI to 6.7 g/kW-hr with PCLI. This behavior is attributed to the lower adiabatic flame temperature as λ increases which in turn leads to slower chemical reactions. However, the unburned hydrocarbon can be tackled easily using post cylinder oxidation strategies. As noticed, the BSHC decreases with spark advancement for all ignition system. This is inductive of the increase of available time to convert fuel molecule to products with spark advancement.

Conversely, BSCO emissions were very close in all ignition systems around 2.36 g/kW-hr. The value remains constant with PCLI D1 tests conditions while it shows slightly increase with spark advancement in 2P-LI and SI systems. This behavior might seem counterintuitive for 2P-LI and SI, however, a reduction of BSHC was seen with spark advancement which results in more combustion products such as CO. It is believed that the BSCO remain constant during PCLI tests because of utilizing leaner mixture that requires longer oxidation time.

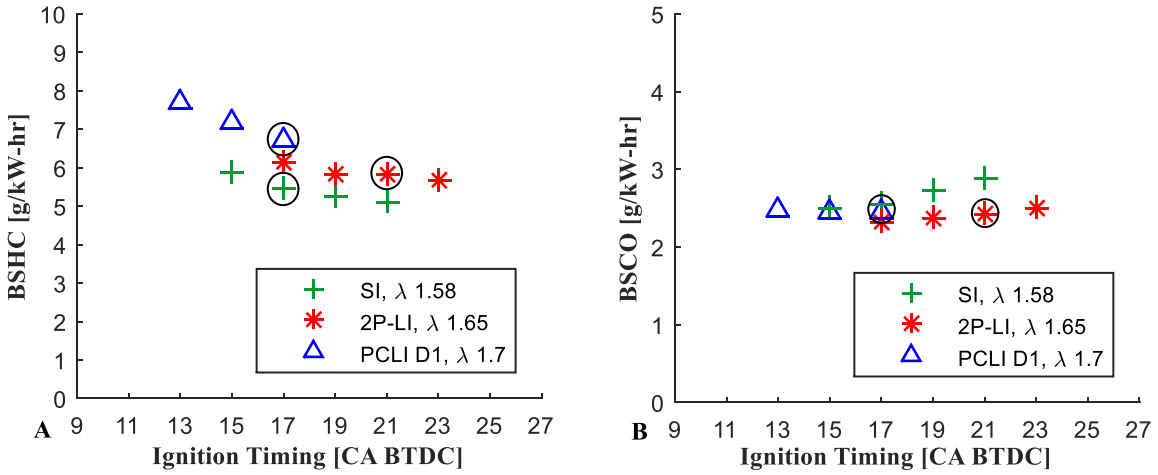

Figure 2.58. Unburned hydrocarbon and carbon monoxide emission of the optimum operational points.

2.4.8 Prechamber Study Conclusions

The main objective of this task was to evaluate the efficacy of using a prechamber in offsetting the reduction in efficiency that results from lower flame velocities under extreme lean burn conditions facilitated by laser ignition. Towards this direction, through a series of systematic tests performed on a single-cylinder natural gas engine, prechamber geometry was optimized for use with laser ignition. In the process, using a unique prechamber geometry, the primary concern for integrity of laser delivery optics, i.e., auto-ignition within the prechamber, was avoided. Subsequently, tests were conducted comparing the performance of three ignition systems: SI, 2P-LI and PCLI. Out of the three, PCLI proved to have the best performance as it not only led to extension of the lean ignition limit, but also shortened ignition delay and combustion duration significantly. As a result, within the bounds of EPA emissions limits and industry accepted ignition instability limits, an overall efficiency improvement of 2.1% points was observed.

CHAPTER 3: IGNITION AND LAMINAR BURNING VELOCITY MEASUREMENTS

3.1 Theory of Laminar Burning Velocity

The Laminar burning velocity (LBV) is defined as the velocity at which unburned gases move through the combustion wave in the direction normal to the wave surface [54, 58, 138-141]. It is an important fundamental property of a fuel/air mixture for engine applications, and it depends on the composition, temperature, and pressure. At specified initial conditions, there is a single LBV value in a 1 D stretch-free flame that provides information about mixture exothermicity, diffusivity, and reactivity. Therefore, the LBV is not only crucial in understanding several aspects of combustion in spark ignition engines, and fuel comparatives; it is commonly used to validate the chemical kinetic mechanisms [54, 55, 58, 138-141] that are used for numerical studies. Since the planar, adiabatic, and stationary flame is difficult to attain, significant amounts of studies in literature focused on multiple approaches for evaluating the LBV. In a recent literature review, Egolfopoulos *et al.* [142] described difficulties, limitation, and uncertainties associated with several LBV measurement approaches.

There are many methods used for determining the LBV, for both stationary and non-stationary flames [55, 58, 138, 139]. A stationary flame is achieved by feeding a burner with a constant velocity fuel and air mixture in order to establish a standing flame. Common stationary flame examples are Bunsen burner, counterflow burner, and stagnation flow burner. Each of these burners has its difficulties in obtaining the LBV. For example, in a Bunsen burner, the LBV can be calculated after evaluating the surface area of the cone and measuring the flow rate. However, it should be noted that the Bunsen burner is controlled by complicated physics involving the

negative stretch from the burner base to its main surface, the strong curvature at the tip, and a nonuniform flame speed over the flame surface [142, 143].

As the name implies, the non-stationary flame is a flame that propagates along a path. The simplest example is a flame propagating down a length of the tube; however, this approach suffers from difficulties in evaluating the heat transfer losses to the wall during combustion. The outwardly propagating spherical flame is the most favorable method for obtaining LBV at relevant engine conditions according to Metghalchi [141]. A spherical flame develops from the ignition kernel at the center of the combustion chamber, and propagates toward the unburned mixture.

The outwardly propagating flame can be analyzed by either constant pressure or constant volume methods. In the constant pressure method, the flame speed is found from the measurement of flame radius with respect to time by schlieren/shadowgraph photography [125]. This approach utilizes the early stage of the combustion process where the pressure can be assumed constant, which limits the useful part of experiments. However, a dynamic pressure transducer is utilized in the constant volume method to record the chamber pressure during the combustion process. After which, a thermodynamic model is employed to determine the LBV after reaching an evident pressure change. Even though that each method uses a different stage of the combustion process, the obtained LBV values between the two methods are very close. Accounting for stretch effect and determining several data point from one test are the advantages of constant pressure and constant volume approaches respectively.

3.1.1 Constant Pressure Method

In this work, the spherically expanding flame was used to obtain the laminar burning velocity. The fundamental parameters of the constant pressure approach will be discussed to enlighten the

reader on their importance before explaining the constant volume method which has been used in this work. The flame radius and its rate of change, S_b, can be obtained using a high-speed shadowgraph imaging. Flame visualization is not only vital to ensure spherical flame but also used to eliminate experiments with flame instability: hydrodynamic, diffusional-thermal, and body forces [58]. Also, since the pressure and temperature of the unburned mixture are almost constant in the early part of the combustion process, the flame speed is only a function of stretch [143], due to strain rate and flame curvature, and a stretch-free LBV can be estimated using an extrapolation method.

The intensity of the stretch is represented by the stretch rate K, which is defined to be the rate of change of flame area divided by the flame area [58]. The equations below show the stretched flame speed and stretch rate for a spherical coordinate.

$$S_b = \frac{dR_f}{dt} \tag{3.1}$$

$$K = \frac{1}{A_f}\frac{dA_f}{dt} = \frac{2}{R_f}\frac{dR_f}{dt} \tag{3.2}$$

The stretch free flame speed can be obtained by using linear or nonlinear extrapolating methods suggested in the literature [117, 120, 142-151]. The linear extrapolation is developed by Markstein [152] for a weak stretched flame and considered the most used method because of its simplicity. Markstein, expanded the stretch sensitivity expression via a Taylor's series and utilized only the first order term to determine a simple equation for the stretch-free flame speed [140]. The expression is shown in equation (3.3); Markstein length, L_b, and stretch-free flame speed, S_b^o, are found by a linear regression after plotting the stretched flame speed versus the stretch rate. Here, Markstein length reflects the flame sensitivity to stretch, however, parameters such as Markstein

Number and Karlovitz number (normalizing with respect to flame thickness and S_u^o) are also commonly used in the literature to describe the effect of stretch on the flame.

Ronny and Sivashinksy [153] and Kelley and Law [58, 154] suggested a nonlinear extrapolation approach for mixtures that deviates from unity Lewis number (Le), see equation (3.4). However, Chen [150] found that the suggested nonlinear model accuracy is limited for mixtures with Lewis number > 1 which lead Kelley *et al.* [155] to propose a generalized nonlinear model (3.5). According to the continuity equation, the density ratio can be used to determine the laminar burning velocity S_u^o after evaluating the stretch-free flame speed.

$$S_b = S_b^o - L_b K \tag{3.3}$$

$$ln(S_b) = ln(S_b^o) - S_b^o L_b \frac{2}{R_f S_b} \tag{3.4}$$

$$\left(\frac{S_b}{S_b^o}\right)^2 ln\left(\frac{S_b}{S_b^o}\right)^2 = \left(\frac{2L_b}{S_b^o}\right)\left(\frac{dS_b}{dR_f} - K\right) \tag{3.5}$$

The above analysis assumes that the velocity of burned mixture is zero. However, as the combustion develops, the compression induced flow (thermal expansion) reduces the accuracy of laminar burning velocity significantly as illustrated in [143]. Peter [156] demonstrated the behavior of burned and unburned mixture velocities in the continuity equation by defining the positive velocity in the outward direction. In such a reference frame, the continuity equation is shown in (3.6) by assuming infinitely thin flame where the difference in flame area can be neglected. ρ and U are used for the density and velocity respectively, while the subscripts *u* and *b* represent the unburned and burned mixture. It is obvious that in this expression the flame speed differs by the velocity of burned mixture.

$$\rho_u \left(U_u - \frac{dR_f}{dt} \right) = \rho_b \left(\frac{dR_f}{dt} - U_b \right) \tag{3.6}$$

$$S_b = \frac{dR_f}{dt} - U_b \tag{3.7}$$

Rearranging the continuity equation in the above expression gives the stretch laminar burning velocity. Similarly, Markstein linear expression for weak stretch can be developed based on continuity equation. Therefore, an accurate value can be achieved when there is a pressure change,. however, several studies in the literature utilize the constant pressure segment of the combustion process, and good stretch laminar burning velocity can be found by neglecting the second term.

$$S_u = (\frac{\rho_b}{\rho_u}) \frac{dR_f}{dt} - (\frac{\rho_b}{\rho_u}) U_b \tag{3.8}$$

$$S_u = S_u^o - (\frac{\rho_b}{\rho_u}) L_b K \tag{3.9}$$

The constant pressure method provides a simple way of evaluating LBVs without calculating the instantaneous properties of reactants and products. However, the author noticed that the method is highly sensitive to the numerical approximation that is used to obtain the rate of change of flame radius. Also, Farzan *et al.* [157] developed a theoretical model based on geometrical optics for flame tracking; their analysis showed that the sudden change of light intensity does not coincide with the flame edge in schlieren photography if the flame thickness is not negligible. Others [125] defined two laminar burning velocities; one for the propagation of flame front and the other one is based on the formation of products. Those two definitions converge to a single value as the flame expands to a large radius where stretch effects are minimal. It is evident from the three stated reasons that there are several sources of discrepancies associated with the constant pressure method.

3.1.2 Constant Volume Method

In this study, the laminar burning velocity is calculated by using the constant volume approach which requires evident pressure change during the analysis. By definition, the LBV is proportional to the instantaneous mass of burned gases m_b passing through the area of the flame A_f [141] (see equation (3.10)). Fiock *et al.* [158] developed the first laminar burning velocity expression in 1940. However, due to difficulties in evaluating some parameters such as the instantaneous flame position and thickness, the expression was not used in the literature. Also, it has been noticed that the errors associated with the measurement of flame radius and thickness magnify the error in LBV measurements [159]. On the other hand, Lewis and Von Elbe [138] employed burned gas assumptions such as adiabatic compression, and a constant average specific heat ratio in 1961 to develop a LBV formula that is a function of mass fraction burned and pressure. Relatively accurate values of LBV were found because their expression does not require complex measurements like those in Fiock *et al.* [158] equation.

$$\rho_u S_u^o = \frac{1}{A_f}\frac{dm_b}{dt} \tag{3.10}$$

O'Donovan and Rallis [159], Bradley and Mitcheson [160], and Takizawa *et al.* [68] among others presented the expressions for the flame radius and LBV by dividing the control volume into burned and unburned regions, assuming the isentropic compression, spherical flame, and spatially uniform pressure. The derivation of the flame radius R_f and its inclusion in the definition of LBV expression are described in the literature [68, 138, 159-161] and presented here for the reader. In this derivation we define m_b and m_u as the mass of products and reactants respectively, X as the mass fraction burned, V as the chamber volume, M is the total mass inside the combustion

chamber, v_b & v_u are the specific volumes of burned and unburned mixtures respectively. According to the continuity equation, the reactant and product mass fractions can be presented as:

$$M = m_b + m_u \tag{3.11}$$

$$X = \frac{m_b}{M} \tag{3.12}$$

$$\frac{m_u}{M} = 1 - X \tag{3.13}$$

The total volume is conserved and accordingly:

$$V = XMv_b + (1 - X)Mv_u \tag{3.14}$$

Assuming a spherical flame and that the unburned mixture is compressed isentropically during combustion, we have:

$$V = \frac{4}{3}\pi R^3 \tag{3.15}$$

$$XMv_b = \frac{4}{3}\pi R_f^3 \tag{3.16}$$

$$v_u = v_{u0}\left(\frac{P_i}{P}\right)^{1/\gamma_u} \tag{3.17}$$

Here, R and R_f is the combustion chamber and flame radii respectively, γ is the specific heat ratio, and the subscript, *i*, denotes initial condition. Substituting back to the conservation of volume provides the flame radius expression as a function of mass fraction burned and pressure as shown in equation (3.18) [138].

$$R_f = R\left[1 - (1 - X)\left(\frac{P_i}{P}\right)^{1/\gamma_u}\right]^{\frac{1}{3}} \tag{3.18}$$

Replacing those equations in the LBV definition, utilizing the specific volume of the unburned mixture, and the surface area of a sphere. Also, the burned mass can be obtained by using the mass fraction burned gives:

$$m_b = XM = X\frac{V}{v_{u0}} = X\frac{4\pi R^3}{3v_{u0}} \tag{3.19}$$

$$S_u = \frac{R^3}{3R_f^2}\left(\frac{P_i}{P}\right)^{1/\gamma_u}\frac{dX}{dt} \tag{3.20}$$

Substituting the flame radius in the above equation leads to the LBV expression:

$$S_u = \frac{R}{3}\left[1-(1-X)\left(\frac{P_i}{P}\right)^{1/\gamma_u}\right]^{-2/3}\left(\frac{P_i}{P}\right)^{1/\gamma_u}\frac{dX}{dt} \tag{3.21}$$

Above, R indicates the vessel radius, while P_i and P represent initial and instantaneous pressures. S_u is the laminar burning velocity, γ_u is the specific heat ratio of unburned mixture, and X is used for the mass fraction burned. During the combustion event, temperature of unburned mixture increases according to the isentropic compression assumption, and the value of specific heat ratio varies. Similarly, along one isentrope LBV increases due to the change in unburned mixture properties. Unlike the constant pressure approach, one experiment in the constant volume approach provides a range of useful laminar burning velocity data points along one isentrope [54, 141, 162]. However, solving this equation requires knowledge of the variation of X with time. Therefore, several models are proposed in the literature, Linear model [138], Metghalchi and Keck's model [124], and the Multilayer model [54, 163] for evaluating the mass fraction burned. A detail discussion based on accuracy and limitation of each model is presented in section 3.1.3.

In a different approach, Lewis and Von Elbe [138], and Bradley and Mitcheson [160] differentiated the conservation of mass to evaluate the LBV. They assumed that the burned mixture

behaved as an ideal gas and compressed isentropically during combustion. Solving the equation based on the fact that the rate of reduction of reactant is proportional to mass flow rate toward the reaction layer gave the second expression of S_u.

$$\frac{dm_u}{dt} = -\frac{dm_b}{dt} \tag{3.22}$$

$$\frac{dm_u}{dt} = -4\pi R_f^2 \rho_u S_u \tag{3.23}$$

$$m_b = V_b \rho_b = \frac{4\pi}{3} R_f^3 \rho_b \tag{3.24}$$

$$\frac{d\rho_b}{dt}\frac{1}{\rho_b} = \frac{dP}{dt}\frac{1}{\gamma_b P} \tag{3.25}$$

$$S_u = \frac{\rho_b}{\rho_u}\left[\frac{dR_f}{dt} + \frac{R_f}{3\gamma_b P}\frac{dP}{dt}\right] \tag{3.26}$$

The second expression of laminar burning velocity requires the density ratio, specific heat ratio of burned mixture, and the flame radius as a function of time. The density ratio (density jump) can be calculated using the isentropic compression of reactant and equilibrating the unburned mixture at constant enthalpy and pressure along one isentrope. Similarly, the flame radius and its rate of change can be evaluated from expression shown earlier after utilizing a thermodynamic model (Linear, Metghalchi and Keck's, or Multilayer models).

Errors associated with evaluating mass fraction burned exist for both LBV expressions. However, in the second expression, the error magnifies due to the specific heat ratio of burned mixture; which is a function of the temperature that varies inside the combustion chamber based on the flame radius and time. Namely, the first burned layer exists at a higher temperature due to the isentropic compression as the combustion proceeds. The specific heat ratio of burned mixture can be evaluated using an average burned gas temperature, like the one obtained in Metghalchi

and Keck's model [124]. However, this assumption simplifies the combustion process dramatically because large temperature gradient has been determined with the Multilayer model. It is worth mentioning here that the second expression of laminar burning velocity looks identical to the one derived by the constant pressure method with compression induced flow in equation (3.7). The reader can get the parameters of burned gas velocity U_b by comparing the two expressions.

One of the assumptions of this method is the spherical flame propagation which might be compromised due to gravity (or buoyant) force. The flame surface area alters from the spherical shape if the LBV is slow. Takizawa *et al.* [68] showed the deviation of the flame shape for fluorinated compounds with 5.4 cm/s LBV. Freefall experiments illustrate that the buoyancy effect can be neglected if the laminar burning velocity is higher than 15 cm/s [164]. In general, hydrocarbons LBV's are in the range of 40 cm/s at standard initial conditions; and higher values will be attained during the compression process. Therefore, it is valid to assume that, in most cases, gravity distortion can be ignored and the flame propagates spherically.

3.1.2.1 Linear Model

As stated earlier, X can be calculated using several models. The Linear model is the most widely used thermodynamic model for the constant volume method because of its simplicity. Lewis and Von Elbe [138] assumed that the mass fraction burned is linearly proportional to the pressure rise during the combustion event in 1961. Two problematic assumptions arose in the derivation of the Linear model, constant unburned gas temperature and constant equilibrium temperature for the burned gases [165]. Even though those assumptions are not reasonable as will be shown in the Multilayer model, Several studies [143] showed a slight overestimation of LBV values using this method. Under the Linear model, the mass fraction burned, flame radius, and laminar burning

velocity can be obtained directly from the pressure trace without calculating properties of burned and unburned mixtures. Replacing mass fraction burned in the flame radius and LBV equations provide:

$$X = \frac{P - P_i}{P_e - P_i} \tag{3.27}$$

$$R_f = R\left[1 - (1 - \frac{P - P_i}{P_e - P_i})\left(\frac{P_i}{P}\right)^{1/\gamma_u}\right]^{\frac{1}{3}} \tag{3.28}$$

$$S_u = \frac{R}{3}\left[1 - (1 - \frac{P - P_i}{P_e - P_i})\left(\frac{P_i}{P}\right)^{1/\gamma_u}\right]^{-2/3} \frac{1}{P_e - P_i}\left(\frac{P_i}{P}\right)^{1/\gamma_u}\frac{dP}{dt} \tag{3.29}$$

Above, P_e is the theoretical maximum pressure during the combustion event which can be evaluated using a chemical equilibrium at constant internal energy and volume. Since the maximum pressure depends on the used chemical kinetic mechanism in simulation, there are discrepancies in reported LBV values. This is the paramount limitation of the Linear model, because mechanisms predict different maximum pressure values. As a result of using simple approximation for mass fraction burned, the Linear model overestimates the LBV in comparison with more advanced models as will be shown in section 3.1.3.

The laminar burning velocity obtained using the constant volume method is usually treated as an unstretched value because the approach requires evident pressure change that happened when the flame expands to a large radius. This is a valid assumption because as combustion proceeds the rate of change of flame radius and flame surface area decreases and increases respectively; two factors minimize the stretch effect in the outwardly propagating spherical flame [55]. It has been reported [147] that if the pressure rise is bigger than $1.2P_i$, a stretch free LBV can be obtained accurately by using the constant volume approach. Furthermore, Moghaddas *et al.* [166] examined

the stretch effect in a constant volume chamber by conducting experiments at different initial conditions but along one isentrope. Each experiment gives a LBV value at different stretch rates; negligible differences were observed which suggest that an accurate stretch free LBV is determined with the constant volume method.

However, other researchers like Chen *et al.* [143] raised the importance of stretch effect in constant volume method for mixtures that deviates from unity Lewis number. Since the Markstein length is a function of unburned gas temperature, the stretch rate must be considered only in the early part of combustion process where the temperature can be assumed constant. Chen *et al.* [143] used the region where the pressure varies between the initial pressure P_i and $1.05(P_i)$ in their calculation.

The analysis was based on linear extrapolation of a weak flame stretch proposed by Markstein [152]. Chen *et al.* [143] differentiated the flame radius equation with respect to time and employed the definition of the stretch rate given in equation (3.2) to obtain the stretch rate expression (3.31). The zeroeth order approximation was used for a hydrogen/air mixture, and the calculation revealed that the effect of stretch on flame speed is more than 10% when the pressure is below $1.2P_i$. Keep in mind that this significant variation is due to the used fuel (hydrogen) that has a highly deviated Lewis number. It is worth noting here that this analysis requires accurate pressure measurements because small fluctuations in that stage of combustion process might have a drastic effect the final value.

$$\frac{dR_f}{dt} = \frac{R^3}{3R_f^2}\left(\frac{P_i}{P}\right)^{1/\gamma_u} \frac{1}{P_e - P_i}\left[1 + \frac{P_e - P}{\gamma_u P}\right]\frac{dP}{dt} \tag{3.30}$$

$$K = \frac{2R^3}{3R_f^3}\left(\frac{P_i}{P}\right)^{1/\gamma_u} \frac{1}{P_e - P_i}\left[1 + \frac{P_e - P}{\gamma_u P}\right]\frac{dP}{dt} \tag{3.31}$$

$$\frac{S_u^o - S_u}{S_u^o} \approx \frac{KL_u}{S_u} \tag{3.32}$$

3.1.2.2 Metghalchi and Keck's Model

Instead of using the linear assumption for the mass fraction burned, Metghalchi and Keck [124, 141] developed a thermodynamic model in 1976. They noticed that the equations for conservation of energy and volume can be solved iteratively using the Newton-Raphson method. A rigorous explanation was given in [124, 141], followed by other studies [68, 161-163, 167, 168] that gave a simplified description and eliminated some of the assumptions in the model. In addition to the previously stated assumption for spherical expanding flame, the model divides the gases into two regions, burned and unburned mixture. The model also assumed that there is no heat or mass transfer between the two regions, and the dissociation products are in chemical equilibrium. Under those assumptions, the substitution of the ideal gas equation into the conservation of energy and volume provides two equations with only two unknowns X and T_b.

$$V/M = Xv_b + (1 - X)v_u \tag{3.33}$$

$$E/M = Xe_b + (1 - X)e_u \tag{3.34}$$

Above, v and e represent the specific volume and internal energy respectively, while b and u indicate burned and unburned mixtures. Also, E is the total internal energy that can be evaluated at the initial conditions. In this model, the burned species fraction is constant during the analysis, determined by the chemical equilibrium at constant volume and internal energy. This is one of the limitations of this approach because combustion process is not instantaneous and properties (temperature and pressure) vary as the flame travels inside the combustion chamber. In addition, there is a variation in species mole fraction of burned gases due to the isentropic compression

which has been neglected in this model. Only ideal combustion where all unburned mixture is utilized instantaneously delivers the mole fraction, temperature, and pressure of constant UV equilibrium. It is clear that errors exist in this method because of the simple adaptation of constant UV species mole fractions.

X, and T_b are found by dividing the chamber into two regions. The combustion event at two-time steps are illustrated in Figure 3.1A and B. The yellow and green colors indicate burned and unburned mixtures respectively, while a darker color was used to represent higher temperature. Also, a Multilayer model representation is shown for comparison in the same figure. Unburned mixture temperature increases due to the isentropic compression, and the model determines the variation of burned gas temperature as combustion proceeds. There is a temperature distribution within the burned gases, however, the model solves for an average value. The properties of burned and unburned mixture are evaluated at each time step based on NASA polynomials (3.35) and (3.36). Since the properties of burned mixture depends on the temperature, NASA polynomials must be included in the Newton-Raphson iterative method to reflect the change of properties in the conservation equations. On the other hand, A Multilayer model gives a better description of the complicated physics in this problem where the temperature of the inner layer exists at a higher temperature as shown in Figure 3.1C and D due to compression process.

$$\frac{C_{pk}}{R} = a_{1k} + a_{2k}T_k + a_{3k}T_k^2 + a_{4k}T_k^3 + a_{5k}T_k^4 \tag{3.35}$$

$$\frac{H_k}{RT_k} = a_{1k} + \frac{a_{2k}T_k}{2} + \frac{a_{3k}T_k^2}{3} + \frac{a_{4k}T_k^3}{4} + \frac{a_{5k}T_k^4}{5} + \frac{a_{6k}}{T_k} \tag{3.36}$$

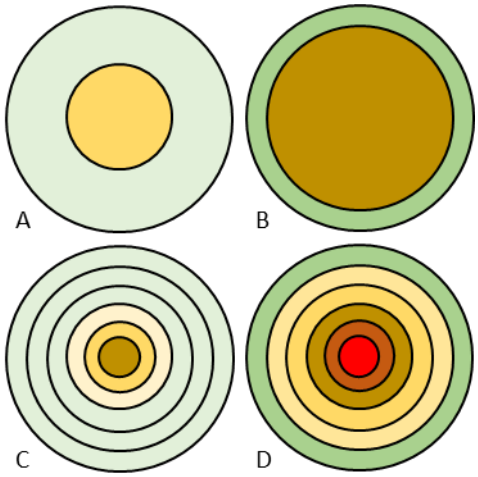

Figure 3.1. Two zones and multilayer representation of a combustion chamber that shows temperature distribution. Colors represent temperature of each layer from red to green (highest to lowest).

3.1.2.3 Mulilayer Model

The Multilayer model separates the burned region into multiple layers; each layer is at identical pressure but different temperature. Also, the unburned mixture is treated as a single layer at an increasing temperature with time. This is considered one of the limitations of the Multilayer model; there is a small thickness of the unburned mixture that has a constant temperature due to the close proximity to the chamber wall (wall quench layer). Studies suggested that this layer does not burn at the end of combustion process as will be discussed in the next section.

The second problematic physical aspect of this model is the sudden jump from burned to unburned gas temperature; there is a flame preheat zone that exists between the reaction layer and unburned mixture. For simplicity, those layers (wall quench and preheat), mass, and thermal diffusion have been neglected in the Multilayer model. Elia *et al.* [163] among others updated Metghalchi and Keck model by providing multiple burned gas layers. A gradient of temperature in the burned gas region was captured in their analysis of CH_4/air mixture. Under the previously stated assumption the conservation and energy and volume can be written as:

$$\frac{V}{M} = xv_b + \left(1 - \sum_{i=1}^{n-1} x_i - x\right) v_u - \sum_{i=1}^{n-1} x_i v_i \tag{3.37}$$

$$\frac{E}{M} = xe_b + \left(1 - \sum_{i=1}^{n-1} x_i - x\right) e_u - \sum_{i=1}^{n-1} x_i e_i \tag{3.38}$$

$$X = \sum_{i=1}^{n} x_i \tag{3.39}$$

The definitions of all symbols are presented in the Abbreviations section. It is worth noting here that the small x_i is the mass fraction burned of a specific layer burned earlier. While the x is the mass fraction burned of a layer that is solved during the iterative process. In this model, the properties of burned layers at the next time steps must be calculated before the iterative process. The accumulative mass fraction burned can be found by summing all values of the layers as shown in equation (3.39). Figure 3.1 illustrates the combustion chamber divided in into six layers, at two-time steps after burning three layers C and five layers D. There is an increase in both burned and unburned gas temperatures due to the compression process.

Instead of assuming a single species more fractions for the burned mixture, Saeed and Stone [54] determined the burned mole fractions based on adiabatic combustion at constant pressure. The pressure rise is due to the expansion of burned gases, and each layer has a different mole fraction. Since $T_b > 1600$ K, the assumption of frozen chemistry during compression process is not valid and therefore, solving for new species mole fraction during isentropic compression is needed [54, 162]. Namely, if a frozen chemistry assumption is used for each burned layer, the burned layer temperature and internal energy will be overestimated. An equilibrium calculation under constant entropy and pressure minimizes Gibbs energy at each time step and reflects the correct thermodynamic properties of each layer [54].

In the Multilayer model, the optimum number of layers must be good enough to represent a reliable LBV trend, i.e., if very small or large number of layers are used, the LBV slope might be compromised due to a limited number of data points or fluctuation in the LBV trend respectively. Both flame speed and flame thickness change during the combustion event in a constant volume chamber. A simple calculation based on averaged values for C_8H_{18}/air mixture at atmospheric pressure and 400 K showed that the time step must be larger than 0.16 ms to maintain a layer bigger than the flame thickness. Also, the mass and heat diffusion effects dominate and cannot be neglected as the layer thickness decreases. In this study, we divided the combustion chamber based on a fixed time step, roughly the number of the layers varied from 90 to 150.

All parameters in equation (3.21) can be found after determining the two unknowns (T_b and X) using Metghalchi and Keck's or Multilayer models. The rate of change of mass fraction burned with respect to time can be evaluated numerically using a central difference scheme with 4^{th} order of accuracy. Even though the variation of specific heat ratio of the unburned mixture is small, an accurate solution can be achieved by including the changes during the isentropic compression. NASA polynomials or chemical equilibrium codes like Cantera software [169] can be used to evaluate the properties of burned and unburned mixtures. After that, the LBV is usually plotted against the temperature of unburned mixture, and a linear regression is employed to extrapolate the values to the initial temperature.

If the flame is stable, LBV increases linearly from the initial temperature until it reaches a maximum value. After that, there is a sudden reduction at the end of the combustion process. In some cases, LBV trace shows a sudden discontinuity because of the change in the flame area; which is attributed to flame hydrodynamic instability. The properties of flame change as combustion proceeds due to the variation of unburned mixture properties. For example, the flame

thickness and density jump decrease and increases receptively along one isentrope. It has been observed that the increase of density jump coincides with the increase of density difference between unburned and burned gases. Those factors trigger flame instability, and flame develops a cellular structure which limits the useful range of data points [55]. Further discussion on flame instability is presented in the numerical comparison section.

The stretch effect is found here for the nonlinear models, where the mass fraction burned is calculated based on Metghalchi and Keck's model [124], or the Multilayer model [54, 163]. The author differentiated the flame radius equation with respect to time by incorporating the variation of reactant specific heat ratio during the compression process. Substituting the differential equation (3.40) in the stretch rate expression (3.2) gives the stretch rate nonlinear models formula (3.41). Similar to the mass fraction burned, the rate of change of specific heat ratios with respect to time can be evaluated numerically.

$$\frac{dR_f}{dt} = \frac{R^3}{3R_f^2}\left(\frac{P_i}{P}\right)^{1/\gamma_u}\left[\frac{dX}{dt} - \frac{(X-1)}{\gamma_u P}\frac{dP}{dt} - \frac{(X-1)}{\gamma_u^2} ln\left(\frac{P_o}{P}\right)\frac{d\gamma_u}{dt}\right] \tag{3.40}$$

$$K = \frac{2R^3}{3R_f^3}\left(\frac{P_i}{P}\right)^{1/\gamma_u}\left[\frac{dX}{dt} - \frac{(X-1)}{\gamma_u P}\frac{dP}{dt} - \frac{(X-1)}{\gamma_u^2} ln\left(\frac{P_o}{P}\right)\frac{d\gamma_u}{dt}\right] \tag{3.41}$$

In a procedure similar to the Linear model, the reader can determine the effect of stretch on the LBV using the above expression. However, the stretch approach should be used for a mixture that highly deviates from unity Lewis number. Moreover, only the early part of pressure trace can be used to minimize the effect of unburned gas temperature variation on the Markstein length.

Recently, Omari and Tartakovsky [165] and Luijten *et al.* [170, 171] reviewed several models for the spherical expanding flame. Luijten *et al.* developed an analytical solution for the mass fraction burned to minimize the complexity and computational cost of nonlinear numerical models

like Metghalchi and Keck's or the Multilayer [170]. The analysis is based on the perfect gas and constant composition assumptions for burned and unburned mixtures. A stoichiometric CH_4/air mixture was used to evaluate Linear, 2 zones, and Multi-zone analytical models. Their model gave a better estimation for the mass fraction burned compared to the Linear model; the maximum difference was noticed to be around X = 40%. They found that the analytical model and Linear model overpredicts LBV values by 4 and 8% respectively [171].

Askari *et al.* [172, 173] developed a novel differential based multi-shell model for laminar burning velocity calculation in a constant volume approach. The differential equations were solved by using CVODE solver from sundials package. In their model, the energy exchange between the burned layers was considered in the conservation equation. Also, thermal boundary layer and displacement thickness concept were employed for evaluating the heat losses to the electrodes and chamber wall.

3.1.3 Comparison of Different Models

The results of Linear, Metghalchi and Keck's, and Multilayer models are compared using CH_4/air mixture. The comparison provides insight into the effect of the model on the mass fraction burned, flame radius, and laminar burning velocity. The stoichiometric CH_4/air mixture was chosen because of its excellent properties such as a Lewis number close to unity that minimizes the stretch effect. The initial conditions selected to be atmospheric pressure and room temperature to match the analytical solution of [170] in order to compare the new suggested method with the Multilayer model.

Before discussing the differences between three mass fraction burned models, the author presented a solution based on the Multilayer model to explain the physics behind combustion

process in a constant volume chamber. The Multilayer model was chosen because of its capability to capture the radial variation of burned gas temperature. All combustion parameters are normalized to their maximum value during the combustion event to illustrate their behavior in one figure. Traces of normalized pressure, reactant temperature, mass fraction burned, product temperature, flame radius, and laminar burning velocity versus the normalized time are presented in Figure 3.2. It is worth noting that the early part of the combustion process is not shown because the constant volume method requires an evident pressure change. The range of data points from a normalized time 0 to 0.05 are neglected as can be seen in the figure, because of a high fluctuation in the pressure trace. The inclusion of such data points does not allow the code to converge due to the reduction of pressure which is against the physics of a constant volume combustion.

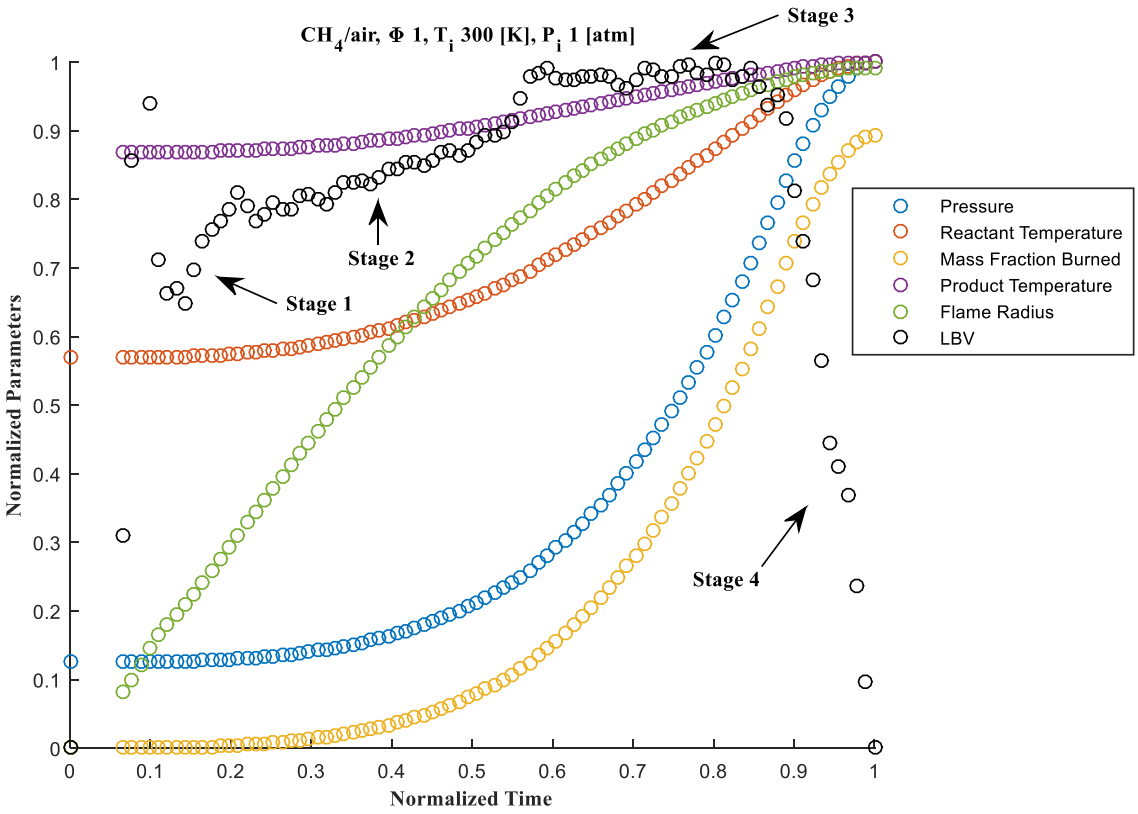

Figure 3.2. Normalized combustion parameters for stoichiometric CH_4/air mixture at an initial temperature 300 [K] and initial pressure of 1 [atm]. The solution is based on the Multilayer model.

The dynamic pressure is the only measured parameter during the combustion event; all other parameters are evaluated based on the previously stated assumption and models. However, before solving for the laminar burning velocity, a 1-D MATLAB smoothing function [174] was used to minimize the pressure fluctuation. The smoothed trace was compared to the original signal at each experiment to ensure that the mean value of the pressure fluctuations was captured. After that, the reactant temperature is evaluated based on the isentropic compression before solving for the two unknowns in combustion models.

The mass fraction burned increases as combustion proceeds until it reaches the maximum value at the end of the combustion event. In this case, the maximum value was 0.89; a full charge

utilization is not a reasonable solution because of heat transfer losses and wall boundary layer where mixture does not react. In the Multilayer model, the radial variation of burned gas temperature is obtained, however, the author presented in Figure 3.2 a mass average temperature that increases with time. The temperature distribution within the burned region will be addressed later in a separate figure.

Next, the flame radius can be obtained using equation (3.18). The figure clearly illustrates two phases of flame development. The normalized flame radius in the range of 0.1 to 0.7 increases linearly with time from the beginning until approximately half of the combustion event. After that, a big reduction in the rate of change in the flame radius is noticed due to top compression effects in the later stage of combustion.

LBV is shown in black circles based on the 1st expression of LBV which is commonly used in the literature. The author divided the trace of LBV to four stages (see Figure 3.2) based on the normalized time (0, 0.16, 0.54, 0.84, and 1) to simplify the physics for the reader. In the first part, there is a high fluctuation in the LBV associated with the small changes in the pressure trace. The optimum stage to capture the LBV is the second stage where the values increase almost linearly with time. Next, flame instability is the reason behind the sudden discontinuity and the variation of LBV slope in stage 3. The last stage is where the laminar burning velocity decreases dramatically to zero.

3.1.3.1 Mass Fraction Burned Models

The mass fraction burned was solved by Linear (X_{Linear}), Metghalchi ($X_{Metghalchi}$), and Multilayer ($X_{Multilayer}$) models. Green, blue and red colors are reserved for Linear, Metghalchi, and Multilayer models respectively in the next figures. The GRI-Mech 3.0 [34] kinetic mechanisms was used in

the analysis below to calculate the properties and species mole fractions of the mixture. The differences of mass fraction burned between the three models cannot be visualized properly by directly plotting the results as a function of time. Instead, the author presented the difference of a model relative to the Linear model solution in the y-axis versus the Linear model value in the x-axis. This approach illustrates the differences between those models and indicates the time at which the maximum difference occurs. Also, this representation allows for the comparison with the new analytical model developed by Luijten *et al.* [171].

Figure 3.3 illustrates the discrepancy between the used models. Both Linear and Metghalchi models overestimate the mass fraction burned relative to the Multilayer model. The difference between two numerical models relative to the linear model increases during combustion until it reaches a maximum value, then it decreases until flame extinction. The maximum difference for Metghalchi model was -0.013, happened to be at X_{Linear} 0.39. Similarly, the maximum difference for Multilayer model was -0.017 occurred at X_{Linear} 0.37. Keep in mind that flame instability limits the range of useful data points; for instance, X_{Linear} was limited to 0.11 in the given case (see Figure 3.2). Even though the differences are small between those models, the Linear model overestimates the LBV by 11% compared with the Multilayer model.

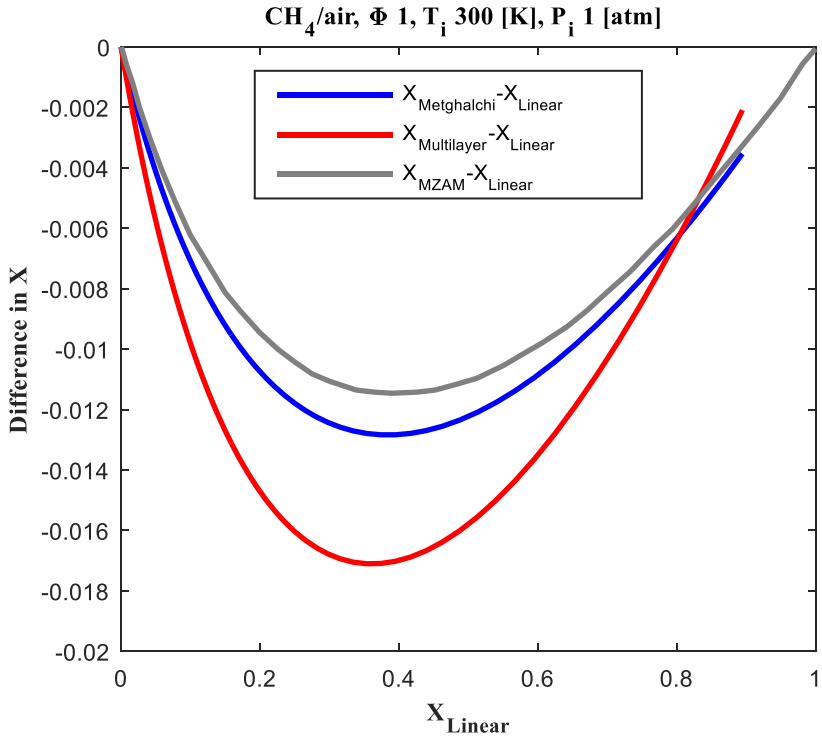

Figure 3.3. Models comparison based on the difference of mass fraction burned for stoichiometric CH_4/air mixture at an initial temperature 300 [K] and initial pressure of 1 [atm].

Luijten *et al.* [170, 171] developed an analytical solution for the mass fraction burned in a spherically expanding flame to minimize the complexity associated with nonlinear numerical models. Their multi-zone analytical model (X_{MZAM}) was presented in gray color in Figure 3.3. The maximum difference for the multi-zone analytical model compared with the Linear model was -0.011, occurred at X_{Linear} 0.4. In general, the new analytical solution provides a better estimate than the Linear model (close to Metghalchi's model solution); and it is a good step toward achieving accurate values without the complexity of numerical solutions. However, the difference is still significant compared with the Multilayer models. As stated earlier, the point at which the maximum difference occurred is shifted to a lower value in the numerical Multilayer model. Therfore, this trend increases the error in all reported models relative to the Multilayer model. It

is obvious that validation studies for chemical kinetic mechanism must be performed using the most accurate model.

The burned gas temperature differs in the radial direction due to the compression process that occurs to layers ahead of the burned one. This physical aspect of the combustion process is only captured in the Multilayer model. Hence, the comparison of the three models is shown based on the mass average burned gas temperature in Figure 3.4. The temperature of burned gases is shown in green for the Linear model, where the temperature is constant and equals to the adiabatic temperature under constant internal energy and volume (UV) during the combustion event. This is one of the problematic assumption used in Linear model. Also, the author presented the adiabatic temperature under constant enthalpy and pressure (HP) in the same figure to aid the next discussion.

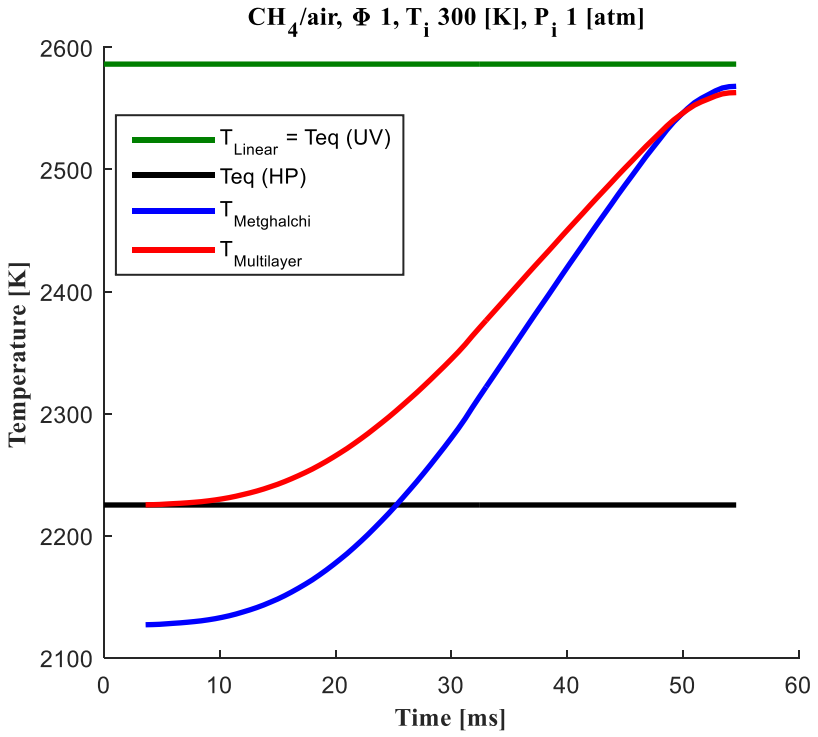

Figure 3.4. Burned gas temperature obtained by Linear, Metghalchi, and Multilayer models for stoichiometric CH_4/air mixture at an initial temperature 300 [K] and initial pressure of 1 [atm].

Blue and red colors are used to demonstrate the temperature of burned gases for Metghalchi and Keck's, and Multilayer models respectively. In both models, the temperature of burned gases increases as combustion proceeds, and the maximum temperature is below the adiabatic temperature at constant UV. The temperatures at the end of combustion process were 2586 K, 2568 K, and 2563 K for Linear, Metghalchi and Keck's, and Multilayer models respectively. It is worth noting here that the questionable assumption of using constant speceis mole fractions in Metghalchi and Keck's model reduced the burned gas temperature at the beginning of combustion process to a value below the equilibrium temperature at constant HP.

Likewise, if species mole fractions are obtained using equilibrium at constant HP, the burned gas temperature starts from the HP value, but exceeds the constant UV temperature (ideal case) at the end of the combustion process. Even though there was a significant temperature deviation between Metghalchi and Multilayer models, the mass fraction burned are very close, and good LBV values can be obtained with the Metghalchi model.

The optimum trend of burned gases temperature is attained using the Multilayer model. Here, the temperature starts from the equilibrium temperature at constant HP and increases to a value below the constant UV equilibrium. Figure 3.5 presents the variation of burned gas temperature for 83 layers at each time step. The x-axis shows the burned layer and y-axis used for temperature, the time increases in the vertical direction as shown in a red arrow for each layer. The combustion process is presented as a sudden jump from reactant to product temperatures. Blue and black lines indicate the temperature distribution for the initial and final time steps also donated as T_O and T_F in the figure. The radial temperature variation can be noticed clearly at the end of the combustion process where the temperature of first and last burned layers were 2902 K and 2396 K.

The isentropic compression process for burned and unburned gases are shown in purple and green ellipses respectively. One notices that the compression process increased the temperature of first burned layer from 2230 K to 2902 K. Similarly, the temperature of unburned mixture was raised from 300 K before ignition to 525 K at the end of combustion. It is evident that the spherical expanding flame has a complex progression where temperature and mole fraction changes continuously, and a simple treatment of constant mole fraction values reduces the accuracy of laminar burning velocity. Species mole fraction variation study was discussed in the liquid fuel experiments for C_8H_{18} and DIPK using Multilayer model (see section 3.2).

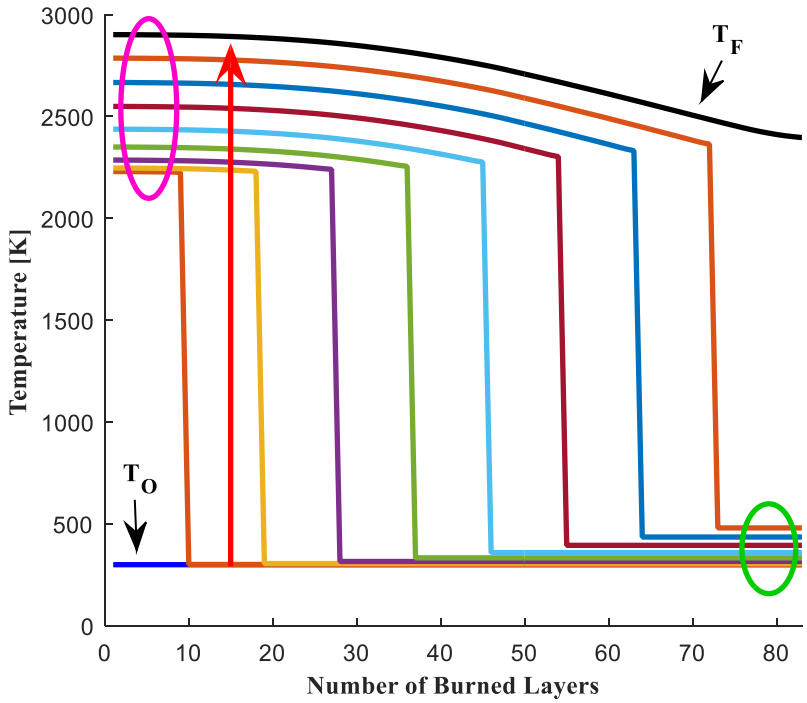

Figure 3.5. Burned gas temperature distribution based on Multilayer model for stoichiometric CH_4/air mixture at an initial temperature 300 [K] and initial pressure of 1 [atm].

The LBV is determined for a stoichiometric CH_4/air mixture by using the three models. As stated earlier, there are four stages in a LBV trace as shown in Figure 3.2, only the 2nd stage was shown in Figure 3.6 where LBV can be extracted without the effect of flame instability and

pressure fluctuations. In that region, the unburned gas temperature and pressure increased to approximately 360 K and 2 atm respectively. It is known from the literature that the LBV increases with temperature and decreases with pressure, along one isentrope with our initial conditions, the temperature is a more dominant factor. Therefore, LBV increases along the isentropic line as shown in the figure. One notices that from one experiment a range of useful data point can be obtained with the constant volume approach, and the values of unburned gas pressure can be found using isentropic compression relation. It is common to plot the LBV against the temperature of the unburned mixture; such a representation provides a linear relationship between the parameters (small range of temperature change). The validity of this approach is shown in the numerical section by using CHEMKIN PRO [33] and ARAMCO-Mech 1.3 [56] kinetic mechanism.

As expected, the Linear model overestimates LBV values and gives a lower slope with respect to unburned gas temperature. Linear regression was used to extrapolate the value to the initial temperature 300 K, Table 3.1 shows LBV value of each model and the percentage difference by using the Multilayer model as the correct value. A significant improvement was noticed using Metghalchi model where the difference decreased from 11% to 3.8% relative to the Multilayer model. All above calculation are based on the GRI-Mech 3.0 [34] kinetic mechanism; the author noticed a small difference in the range of 0.5% based on the used kinetic mechanism, those differences will be discussed in the numerical section 3.1.3.3.

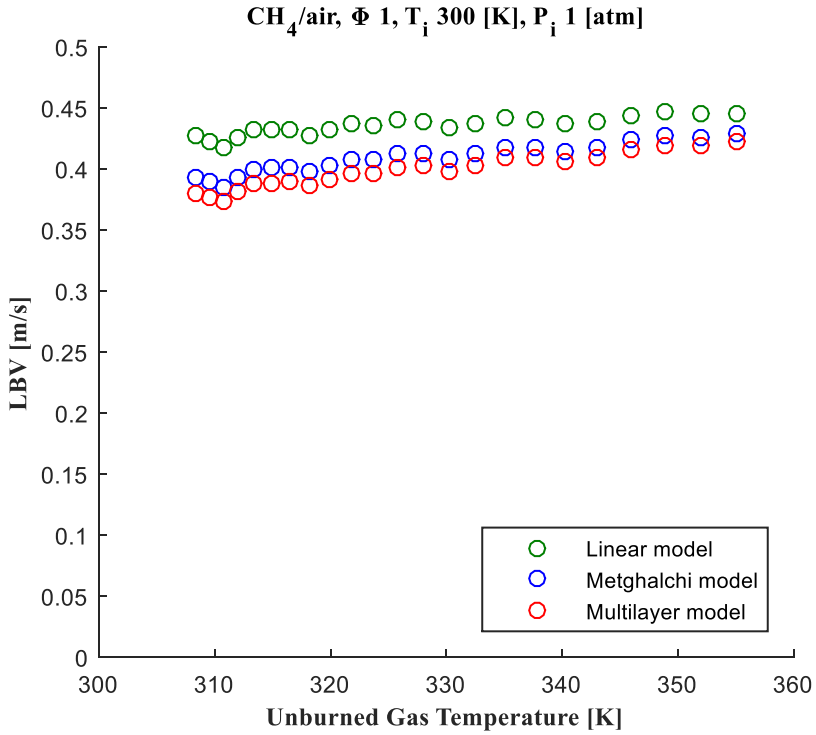

Figure 3.6. Laminar burning velocity comparison for stoichiometric CH_4/air mixture at an initial temperature 300 [K] and initial pressure of 1 [atm].

Table 3.1. Comparison of LBV obtained by several models. Stoichiometric CH_4/air mixture at an initial temperature 300 [K] and initial pressure of 1 [atm].

Model	**LBV [cm/s]**	**Difference [%]**
Linear	42	11
Metghalchi	38.33	3.8
Multilayer	36.93	-

The normalized flame radius and stretch rate are obtained using equations (3.18) and (3.41) respectively for the Multilayer model (shown in Figure 3.7A and B). The author intended to plot those parameters versus the temperature of the unburned mixture to picture the used range of data points. The smooth LBV trace was in between 310-360 K, it is apparent that most of the flame expansion occurred in the early part of combustion process where the temperature of the unburned mixture was 300-360 K. Later, a dramatic reduction of dRf/dt was shown due to the sharp pressure rise inside the combustion chamber.

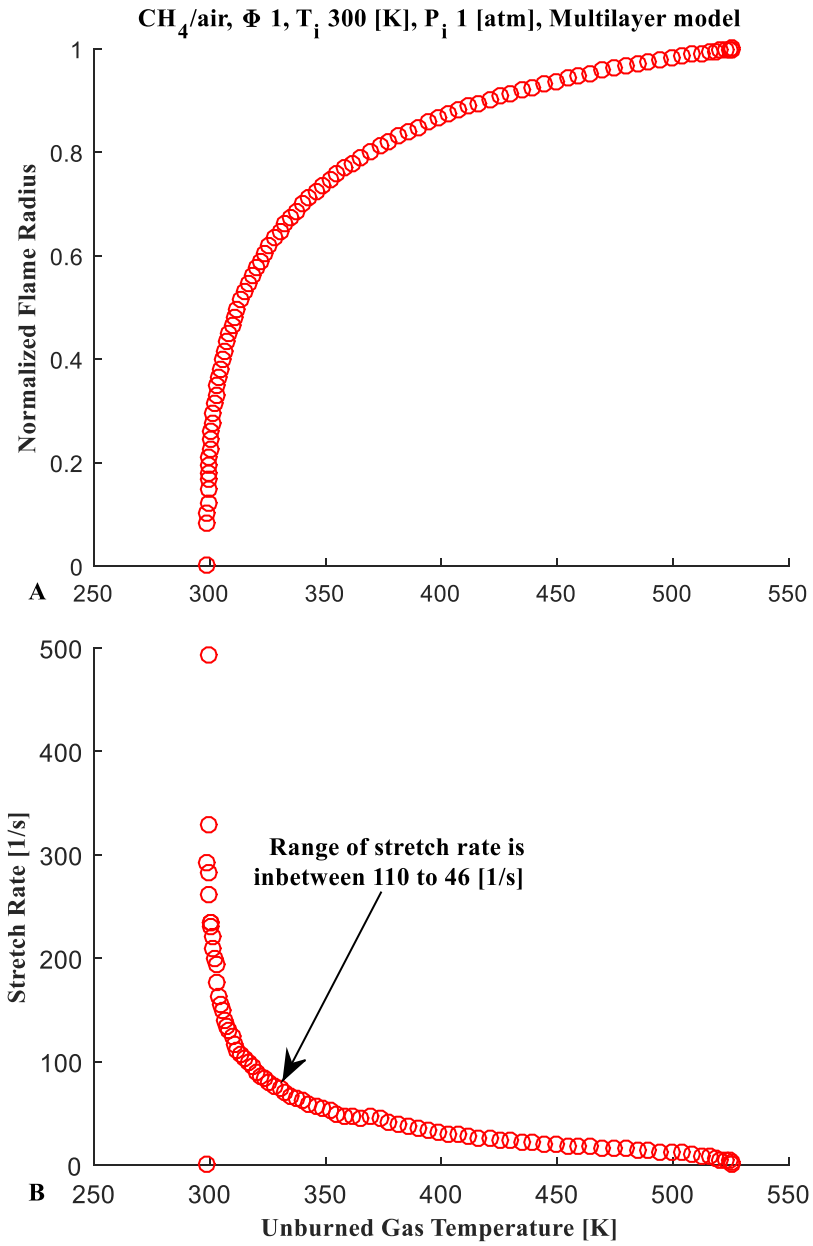

Figure 3.7. Flame radius and stretch rate obtained by the Multilayer models for stoichiometric CH_4/air mixture at an initial temperature 300 [K] and initial pressure of 1 [atm].

In contrast, the stretch rate starts with a high value and decreases to 110-46 1/s in the used range of data points for LBV. Then it drops to almost zero at the end of the combustion process; this is attributed to the inverse proportionality between stretch rate and the flame radius. The range of stretch rate is small in our experiment compared to those obtained by constant pressure method

where stretch rate varies from 500-100 1/s. Most of the constant volume studies assume that the stretch effect is negligible because of that reason. The validation of this assumption was carried out by researchers [166, 175] who examined the effect of the stretch rate by conducting experiments along one isentrope; they concluded that the LBV is almost constant under several stretch rates.

3.1.3.2 Expressions for Laminar Burning Velocity

Two expressions for laminar burning velocity are derived and shown earlier (3.21), (3.26) in the constant volume method section. In this work, the author obtained the LBV by using the first expression because it has fewer input parameters and reflects accurate result. For example, the 2nd expression (3.26) requires the knowledge of the specific heat ratio of burned gases which can not be estimated accurately due to the temperature distribution of the burned gases.

Since the 1st expression requires only the X, it is believed that the errors using this equation is relatively smaller. The specific heat ratio of an ideal gas is a function of the temperature and species mole fractions. It has been shown in Figure 3.4 that the Metghalchi model does not give a correct burned gas temperature particularly in the early part of the combustion process. Hence, the two LBV expressions are compared by using the Multilayer model, and the specific heat ratio is found based on an average mass value. Figure 3.8 presents the full traces of LBVs obtained using the two expressions; the data points of 2nd expression are called LBV2.

The four stages of LBV are shown as a function of unburned gas temperature. One notices that there is a dramatic change in the LBV slope between stage 2 and 3, this is a good illustration of the effect of flame instability on the LBV trace. Since the 2nd stage is used to evaluate the LBV, the comparison of LBV expressions in discussed only for the second stage. The differences

between the two expressions are minimal at the beginning of combustion process. After that, the 2nd expression underestimates the LBV in comparison to the first expression. This contributes to a slightly lower LBV gradient which in turn lead to an underestimation of LBV along the isentrope. In the tested case, the laminar burning velocities at 300 K were identical. As stated earlier, the 2nd expression is only used in Figure 3.8, the analysis of LBV in all experiments was conducted based on the first expression (3.21).

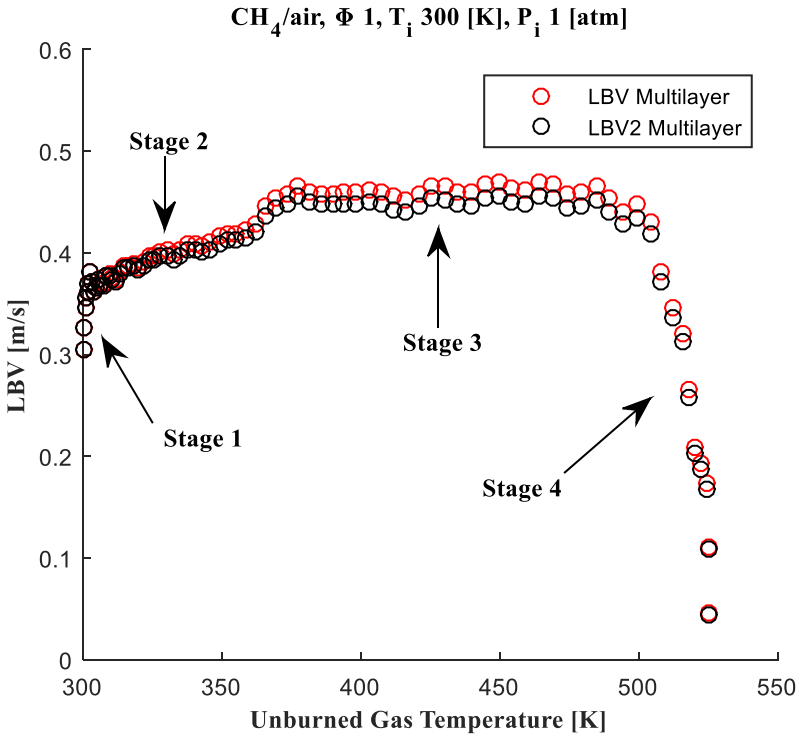

Figure 3.8. Traces of Laminar burning velocity obtained by two expressions.

3.1.3.3 Numerical Comparison

The solution of LBV using numerical models depends on the properties of reactants and products which can be determined using equilibrium codes or NASA polynomials. The author utilized CANTERA software [169] for that purpose because of its simplicity and integrity with MATLAB. Equilibrium codes require a chemical kinetic mechanism that contains the thermal and

transport properties as well as chemical reactions and reaction rate coefficients. Methane kinetic mechanisms developed and validated over the years by several studies [176-178] because of its extensive use in the scientific community. The most known methane kinetic mechanisms are GRI-Mech 3.0 [34] and ARAMCO-Mech 1.3 [56]. Table 3.2 provides the number of species and reactions considered in GRI-Mech 3.0 and ARAMCO-Mech 1.3; also the validated pressure and temperature range are tabulated. Recently, the Combustion Chemistry Centre at NUI Galway introduced an updated version - ARAMCO-Mech 2.0 [179], however, the number of species and reactions increased dramatically which resulted in a significant increase in the computational time. Because of that reason, the author preferred to use ARAMCO-Mech 1.3 in this work.

Table 3.2. Specification of methane chemical kinetic mechanisms used in the dissertation.

	GRI 3.0	**ARAMCO 1.3**
Elements	C, H, O, N, and Ar	C, H, O, N, Ar, and He
Number of species	53	253
Number of chemical reactions	325	1542
Ignition delay pressure validation range [atm]	0.013-10	1.2-260
Ignition delay temperature validation range [K]	1000-2500	1200-2500

All LBV results shown before the Numerical Comparison section was made with the GRI-Mech 3.0 to reduce the computational cost. Figure 3.9 compares the useful range of LBV obtained using the Multilayer model and two chemical kinetic mechanisms. It is evident that the LBV values determined by ARAMCO-Mech 1.3 are slightly lower than those found with GRI-Mech 3.0. However, the difference is insignificant compared to the uncertainties of spherical combustion chamber experiments. In this case, if the value extrapolated linearly to the initial temperature, the LBV of ARAMCO-Mech 1.3 and GRI-Mech 3.0 mechanisms are 36.8 cm/s and 36.95 cm/s. GRI-Mech 3.0 overestimates the value by only 0.4%, an order of magnitude smaller than the

experimental uncertainty. Throughout the dissertation several mechanisms are utilized, the used mechanism will be specified in each section to eliminate any confusion.

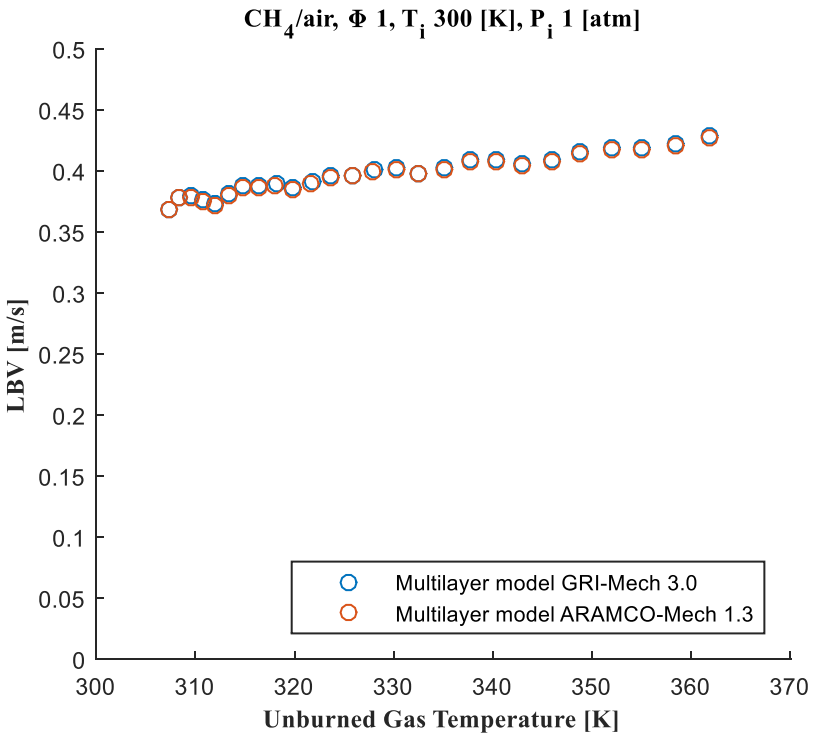

Figure 3.9. Laminar burning velocity comparison based on two chemical kinetic mechanisms for stoichiometric CH_4/air mixture at an initial temperature 300 [K] and initial pressure of 1 [atm].

In the constant volume method, the LBV fluctuates at the beginning of each experiment until an evident pressure change is recorded (see stage 1 in Figure 3.8). The fluctuation disappears approximately after 5 ms. Hence, an extrapolation method is needed to estimate the LBV at the initial condition. The linear extrapolation was validated by using the premixed flame model from CHEMKIN PRO [33] using the ARAMCO-Mech 1.3 [56] mechanism. The initial conditions of each data point are calculated based on the isentropic compression process before solving the premixed flame code. Note that the Soret and multicomponent mass diffusions are considered in the code to provide accurate LBV values. Figure 3.10 illustrates the numerical prediction results versus the unburned gas temperature. It is apparent that the LBV increases linearly with the

unburned gas temperature in the tested range. The least square fit matches the numerical values, and only residuals of 0.0024 was found which might be due to the convergence criterion in the premixed flame model. To conclude, it is valid to extrapolate the LBV trend linearly to the initial condition in order to estimate the LBV value.

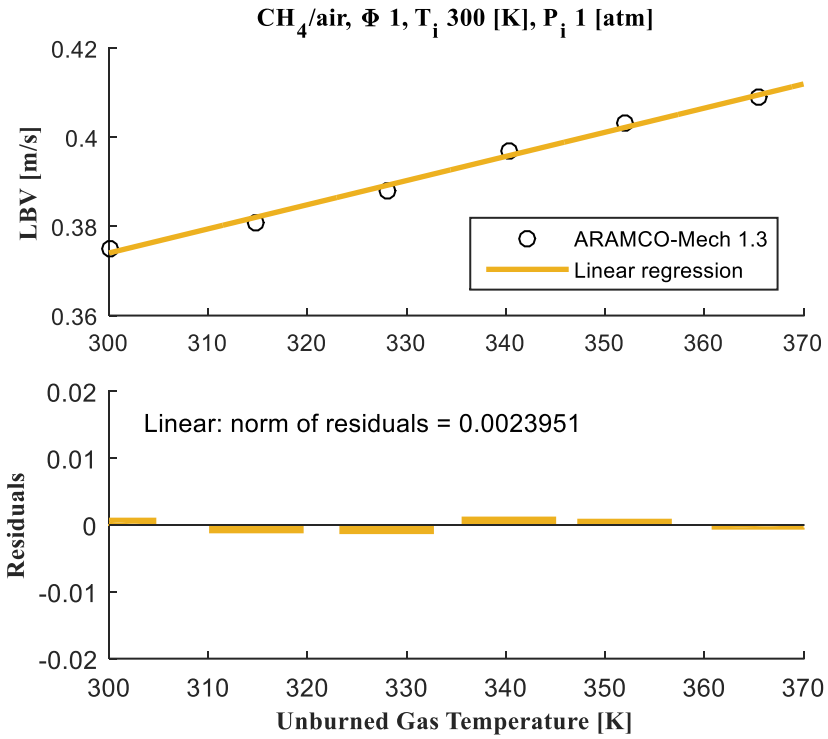

Figure 3.10. Validation of Linear extrapolation by using ARAMCO-Mech 1.3 [56] for stoichiometric CH_4/air mixture at an initial temperature 300 [K] and initial pressure of 1 [atm].

The CHEMKIN PRO [33] solution was extended to study flame properties along one isentrope because of their importance in flame instability studies. The range of data points increased from 1-10 atm to provide a general trend for an experiment that starts with atmospheric pressure and room temperature. Three types of flame instabilities arise in a confined spherically expanding flame, body forces, hydrodynamic, and diffusional-thermal instabilities [58, 173, 180, 181]. The buoyancy effect can be neglected for most hydrocarbon fuels because LBV is higher than 15 cm/s.

However, hydrodynamic and diffusional-thermal instabilities distort flame surface area by developing cracks and cells.

Hydrodynamic instability occurs if the effect of density variation across the flame (density jump) is higher than the stabilization factor. The density jump (σ) is defined as the density ratio between burned to unburned gases as shown in equation (3.42). This ratio increases along one isentrope and coincides with the increase of density difference between burned and unburned gases which in turn promotes flame instability. Conversely, fast expanding flames prevents cells formation if the rate of expansion is higher than the rate of cells formation. Namely, the flame positive curvature stabilizes the expanding spherical flame and reduces cells development [180]. Since the flame curvature is directly related to the flame thickness, thicker flame increases flame stabilization. However, cell development is expected as combustion proceeds due to the reduction of flame thickness along one isentrope.

$$\sigma = \frac{\rho_b}{\rho_u} \tag{3.42}$$

$$\delta_f = \frac{T_{ad} - T_u}{\left\{\frac{dT}{dx}\right\}_{max}} \tag{3.43}$$

Above, δ_f is used for the flame thickness while T_{ad} and T_u are employed for the adiabatic flame temperature and the temperature of unburned mixture respectively. A numerical derivative was used for the flame temperature to provide the maximum value after solving the premixed flame code.

As the name implies, diffusional-thermal instability is caused by the difference between thermal and mass diffusivities. A rigorous discussion has been made in the literature [58, 138-140], they found that the flame will be unstable if the mass diffusion is faster than the thermal diffusion.

Lewis number (Le), defined as the ratio of thermal to mass diffusivity [58, 138]. is usually used to examine the mixture tendency toward diffusional-thermal instability. Since several binary diffusional coefficients exist for a mixture of gases, Lewis number was estimated for a mixture using the thermal diffusivity of the mixture relative to the mass diffusivity of the deficient reactant toward the diluent gas [58]. The diffusional-thermal instability delivers cracks or cells from the initial part of combustion process. Therefore, if no instability behavior was noticed from the beginning (flame visualization), the diffusional-thermal instability can be neglected for the tested mixture.

The variation of flame properties (density jump, flame thickness, and LBV) are shown in Figure 3.11 for CH_4/air mixture. The author decided to plot the flame properties with respect to the pressure along one isentrope to allow for direct comparison with the LBV trend obtained earlier as a function of unburned gas temperature. Keep in mind that the range of data points was increased dramatically from 1-2 atm in Figure 3.10 to 1-10 atm in Figure 3.11 because the aim was to evaluate variation of properties along the entire combustion event. One notices that all obtained parameters vary nonlinearly with pressure. Also, it is evident that the density jump that reflects the difference between reactant and product densities increases along one isentrope. The density jump increased from 0.136 to 0.23 by increasing the equilibrium condition from 1-10 atm. Similarly, the density difference increased from 0.97 kg/m^3 to 4.6 kg/m^3 at those conditions.

The flame thickness was calculated using equation (3.43) after solving the premixed flame model. The domain was kept constant as 0.6 cm with 300 grid points, and adaptive grid curvature and gradient of 0.5 was chosen. Unlike the density jump, it was found that the flame thickness decreases alone one isentrope. The flame thickness of a stoichiometric CH_4/air mixture was found to be 0.375 mm at atmospheric pressure and 0.08 mm at 10 atm. As stated earlier, the stabilization

effect decreases as the flame gets thinner in expanding spherical propagation flame which in turn leads to hydrodynamic flame instability. This is the most important factor for hydrodynamic instabilities in constant volume experiments. Therefore, a stable flame in a confined volume develops flame instabilities as combustion proceeds (an example is shown in Figure 3.2). Care must be taken to eliminate such data points from the LBV fit to ensure reliable values.

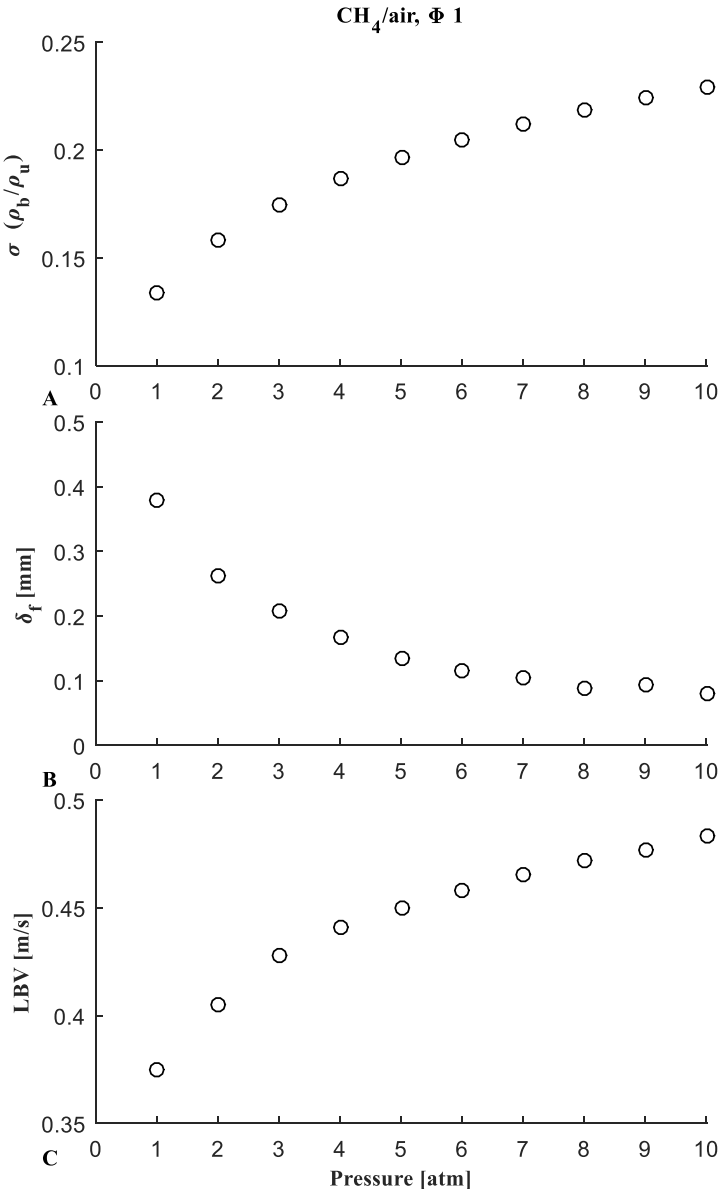

Figure 3.11. Properties of flame along one isentrope obtained using CHEMKIN PRO [33] with the ARAMCO-Mech 1.3 [56] mechanism.

3.2 LBV Measurements of DIPK Mixture

DIPK LBV measurements were conducted under several initial conditions using the UCF spherical chamber. A direct flame visualization was utilized to ensure that the flame is spherical and stable (no cellular structure was observed within the flame) in order to provide reliable results with the constant volume approach. LBV measurements were also performed in iso-octane (C_8H_{18}), a relatively well characterized fuel, in order to validate our facility and measurement technique. The LBV results of C_8H_{18}/air and DIPK/air mixtures are compared with several oxygenated fuels in the literature and numerical values predicted by two chemical kinetic mechanisms. Furthermore, several diluents at two proportionalities were used to mitigate flame instability at high pressure experiment. It was observed that He provided a smooth spherical flame without cellular structure even at a rich equivalence ratio of 1.6, and delivered a wider range of data points compared to Ar diluted mixtures. A similar observation was noticed by increasing the diluent ratio from 3.76 to 5, because of the increase in flame thickness relative to the density jump. Since the constant volume approach is used for determining LBV, many data points can be extracted out of a single experiment (up to 10 atm and 503 K) which brings several validation targets for DIPK chemical kinetic mechanisms. The work provided in this chapter has been published in the SAE Int. J. Fuels Lubr. 10(2):2017, doi:10.4271/2017-01-0863, and was presented in SAE World Congress 2017, SAE Paper No 2017-01-0863 & SAE World Congress 2018, SAE Paper No 2018-01-0921.

3.2.1 DIPK Literature Studies

Recently, Yang and Dec investigated the auto-ignition characteristics of DIPK in both HCCI and SI engines [52]. Experiments were conducted over a wide range of operating conditions to

characterize the fuel reactivity for auto-ignition and its sensitivity to the variations of temperature and pressure. Allen *et al.* carried out an experimental and modeling study on DIPK combustion chemistry [49]. Ignition delay time, pyrolysis, and oxidation measurements were conducted under a wide range of operating conditions. They found that the DIPK ignition delay time is substantially shorter than that of structurally similar hydrocarbons, and their experiments showed a region of negative temperature coefficient behavior in the range of 650 to 750 K [49]. Barari *et al.* [182, 183]. experiments covered a range of initial conditions, 1093-1630 K, 1-6 atm, and equivalence ratios (Φ = 0.5-2.0) using shock tube and laser absorption diagnostics. Also, Barari *et al.* [184] ran a numerical simulation of HCCI engines by using single and multi-zone models. Their single zone model provided reasonable agreement during the compression stage until the onset of ignition, however, it over-predicted the peak pressure after the ignition process.

Allen *et al.* [49] developed a DIPK chemical kinetics mechanism based on the automated reaction mechanism generator (RMG) tool; while Barari *et al.* [182, 183] used the reaction class approach to develop their high temperature mechanism. They achieved better agreement with experimental data points in comparison to the Allen *et al.* mechanism [49]. However, the freely propagating flame model in CHEMKIN PRO [33] does not converge while using the available DIPK chemical kinetic mechanism (even with low convergence criterion) to simulate LBV and flame thickness. Also, there are no laminar burning velocity measurements for DIPK in the literature, therefore our aim in present study is to provide values at several initial conditions.

Several literature studies have evaluated the effect of diluents on the LBV numerically [185-187], and experimentally [151, 186-189]. N_2, CO_2, Ar, H_2O, He, and a combination of diluents which were assessed at various initial conditions and equivalence ratios. It has been found that diluent interact in the combustion process mainly via three mechanisms: (i) dilution effects, (ii)

chemical participation, and (iii) change of thermochemical properties. The laminar burning velocity decreases by increasing the diluent ratio because of the increase in specific heat relative to the released energy; a higher reduction was noticed with a diluent such as CO_2 which has high molar specific heat.

As for the chemical participation effect, both Hu *et al.* [185] and Galmiche *et al.* [186] used fictitious molecules that have the same thermal properties but did not react during combustion and observed that the highest difference was observed with CO_2 (but it was only in the range of 5-6%). Thus they concluded that the chemical participation effect is the smallest relative to other factors, and can be neglected in most diluents especially at high diluent ratios. Conversely, the change in properties, such as specific heat and thermal diffusivity, has a strong effect on the LBV. For example, diluents with lower specific heats cause higher adiabatic flame temperature which will increase fuel reactivity and LBV. Also, the specific heats of Ar and He are identical, higher LBV values were measured with He because of its higher thermal diffusivity. In addition, Galmiche *et al.* [186] evaluated the effect of molecular diffusion by utilizing a fictitious molecule that has the thermal properties of He and the transport properties of Ar, a negligible difference in LBV was noticed which suggested that the molecular diffusion effects can be neglected.

Helium has been used in constant volume chamber experiments to suppress flame instabilities because of its excellent properties - high thermal diffusivity and low specific heat. The high thermal diffusivity increases the Lewis number and eliminates the diffusional-thermal instability, while higher diluent ratio can be used to mitigate the hydrodynamic instability by providing thicker flames and acceptable density jump (further discussion is presented in the numerical result section). Rozenchan *et al.* [188] conducted LBV measurements of stochiometric methane mixture at 60 bar to validate chemical kinetic mechanisms for automotive application. A stable flame with

only few large wrinkles was observed at high pressure by using He at high diluent ratio. Large discrepancies were observed between measurements and numerical predictions using the GRI mechanism [34] for He diluted mixtures.

In another study, Eisazadeh-Far *et al.* [189] evaluated the diluent effect on flame structure and laminar burning velocity of a jet propellant. They found that increasing the initial pressure and equivalence ratio for combustion with air developed flame instabilities. Ar was found to be the most destabilizing inert gas compared with N_2 and He; this was attributed to its lower thermal diffusivity. On the other hand, He provided a stable flame even at high initial pressure conditions, a wider range of data points along one isentrope were extracted. The LBVs determined using He as a diluent was much higher than those obtained in the case of N_2. The authors justified the trend by noting that the mixture had a very high adiabatic flame temperature and thermal diffusivity compared to N_2 diluted mixture.

Since laminar burning velocity values of DIPK are not available in the literature, this work provides measurements with several diluents at a wider range of initial conditions. This study was performed to provide fundamental combustion data needed for developing DIPK kinetics mechanisms at high initials condition and enable engine designers to assess the suitability of DIPK as a fuel. In the beginning, a numerical investigation is conducted to estimate mixture properties by using different diluents. Properties such as density jump, Lewis number, thermal diffusivity, specific heat, adiabatic flame temperature and pressure were obtained to understand the benefit of He for combustion studies. Numerical predictions of LBV and flame thickness were investigated using C_8H_{18} with several diluents because iso-octane is a widely studied and well-characterized reference fuel [144, 190] with several validated mechanisms in the literature.

After that, LBVs are determined in $C_8H_{18}/O_2/N_2$ mixtures as a validation of our liquid fuel experimental strategy. Comparisons with numerical predictions and literature data are presented to assess the advantages of Multilayer model relative to Metghalchi and Linear models. Also, flame propagation by schlieren imaging was used to ensure a stable flame; and to compare the sudden discontinuity of LBV trace with the start of cellular formations. DIPK LBV was measured at various equivalence ratios (Φ = 0.8-1.6) at a temperature range 403-503 K and pressure range of 5-10 atm. In addition, experiments with N_2 and Ar diluents were conducted to assess the fuel reactivity dependence on different diluents.

3.2.2 Experimental Setup

Details of the UCF spherical combustion chamber facility including fuel/oxidizer mixture preparation, ignition systems, pressure measurements, shadowgraph/schlieren imaging system, and experimental procedure are provided in Appendix A. 2,4-Dimethyl-3-pentanone (DIPK) and iso-octane (C_8H_{18}) were supplied by Fisher Scientific; Table 3.3 presents their properties and purities. Research grade (purity > 99.999%) O_2 (Praxair), N_2 (Air Liquide), Ar (Nexair), and He (Nexair) were utilized to create oxidants. The oxidant term is used in this study for oxygen and diluent mixture, and the diluent ratio (D) is the ratio of diluent to oxygen.

Table 3.3. Physical and chemical properties for C_8H_{18} and DIPK fuels.

	Isooctane	**DIPK**
Molecular Formula	C_8H_{18}	$C_7H_{14}O$
Density, [g/mL]	0.692	0.8
Molecular Weight, [g/mol]	114.23	114.19
Boiling Point, [°C]	98-99	124-125
Vapor Pressure, [mbar @ 20°C]	51	5
Flash Point, [°C]	-12	15
Assay (Purity), [%]	≥99	≥98

The test matrix was chosen based on the capabilities of our ignition system, the range of MKS E27 Baratron, and the limit where diffusional-thermal instability was observed. Two initial temperature were used 393 K and 403 K for C_8H_{18} and DIPK, respectively, while three initial pressures were studied (1, 3, and 5 atm). According to the stated constraints, experiments at high pressure with diluent ratio D = 3.76 gave an equivalence ratio range of 0.7-1 (with N_2), limited by the ignition energy in the lean limit and flame instability at the stoichiometric ratio. While He experiments with diluent ratio D = 5 results in a wider range of equivalence ratio 0.7-1.6 (limited by the MKS Baratron range).

3.2.3 Combustion Model

Solving the LBV equation requires knowledge of X with time. Instead of employing a Linear model, the Multilayer and Metghalchi and Keck's [124] models are used to obtain the mass fraction burned. The model's assumptions and validation tests were presented in section 3.1.and 3.1.2. respectively. In this study, we divided the combustion chamber based on a fixed time step, roughly the number of the layers varied from 80 to 150. The properties of burned and unburned mixtures (e.g., specific heat ratio, entropy, and internal energy) are calculated by using Cantera software [169] along with Blanquart *et al.* [191] (C_8H_{18}) and Barari *et al.*[184] (DIPK) mechanisms. All species in both mechanisms are utilized to represent reliable properties of burned mixtures. Table 3.4 shows the number of species and chemical reactions considered in each used model.

Table 3.4. Specifications of used chemical kinetic mechanisms in combustion models.

Fuel	**C_8H_{18}**	**C_8H_{18}**	**DIPK**
Chemical kinetic mechanism	Blanquart *et al. Combustion and Flame, 2009*	Chaos *et al.* 5th US com. meeting, 2007	Barari *et al. Fuel*, 2016
Species	148	107	267
Chemical reactions	928	723	1602

For every equivalence ratio, a minimum of 3 experiments were conducted (to minimize random errors) and the overall uncertainty of LBV was found to be in the range of 4.4-5.63%. Uncertainty analysis was performed based on several parameters for two diluents (N_2 and He) at various initial conditions. Table 3.5 presents the result at an equivalence ratio of 0.9 using C_8H_{18} and DIPK fuels at 1 atm and 393 K; while Table 3.6 illustrates the effect of diluent proportionalities for DIPK at 5 atm and 403 K. The highest uncertainty source was the random errors that contributed to a difference in the range of 0.32-4.06%. The random error is obtained by assessing the variation of LBV in three tests at identical initial conditions. The author is not certain what is the reason behind those variations.

Table 3.5. LBV uncertainty analysis for C_8H_{18} and DIPK fuels at atmospheric pressure, 393 [K] and $\Phi = 0.9$.

Uncertainty Source	**$C_8H_{18}/O_2/N_2$ (3.76)**	**DIPK/O_2/N_2 (3.76)**
Initial pressure (+- 0.02 atm)	+- 0.02%	+- 0.02%
Initial temperature (+- 1 K)	+0.06%, -0.32%	+0.31%, -0.14%
Equivalence ratio (+- 0.05)	+2.4%, -3.24%	+2.57%, -3.2%
Number of layers (+- 30)	+0.67%, -0.16%	+0.1%, -0.07%
LBV fitting parameters	+0.89%, -2.13%	+0.73%, -2.98%
Random error	+1%, -4.06%	+1.4%, -2.76%
Overall uncertainty	*+2.8%, -5.63%*	*+3.1%, -5.22%*

Table 3.6. LBV uncertainty analysis for DIPK with two diluents at 5 atm, 403 [K], and $\Phi = 0.9$.

Uncertainty Source	**DIPK/O_2/N_2 (3.76)**	**DIPK/O_2/He (5)**
Initial pressure (+- 0.02 atm)	+0.13%, -0.05%	+0.14%, -0.13%
Initial temperature (+- 1 K)	+0.29%, -0.1%	+0.12%, -0.12%
Equivalence ratio (+- 0.05)	+4.11%, -3.45%	+2.64%, -2.06%
Number of layers (+- 30)	+0.05%, -0.03%	+0.09%, -0.03%
LBV fitting parameters	+0.23%, -1.78%	+0.2%, -0.92%
Random error	+0.75%, -2.59%	+0.32%, -3.8%
Overall uncertainty	*+4.19%, -4.67%*	*+2.67%, -4.4%*

3.2.4 Numerical Results

The numerical analysis was carried out to investigate the effect of diluent and its proportionality on mixture properties. Again, Cantera software [169] along with the Barari *et al.* [182] mechanism was used to determine mixture properties at various initial conditions. Also, CO_2 was included in the numerical investigation to evaluate a mixture with high molar specific heat. Since both He and Ar have identical specific heats, properties such as adiabatic temperature and density jump were identical (only He results are shown in Figure 3.12A and B). Figure 3.12 illustrates mixture properties with respect to the equivalence ratio. Solid and dashed lines were used to reflect properties with a diluent ratio (D) 3.76 and 5, respectively. It has been found that the adiabatic temperature follows the variation of mixture specific heat at a fixed diluent ratio, mixtures with higher specific heat reduces the maximum temperature. For instance, the maximum adiabatic temperature increases from 1898 K at $\Phi = 1.01$ to 2704 K at $\Phi = 1.11$ by switching the diluent from CO_2 to He as shown in Figure 3.12A.

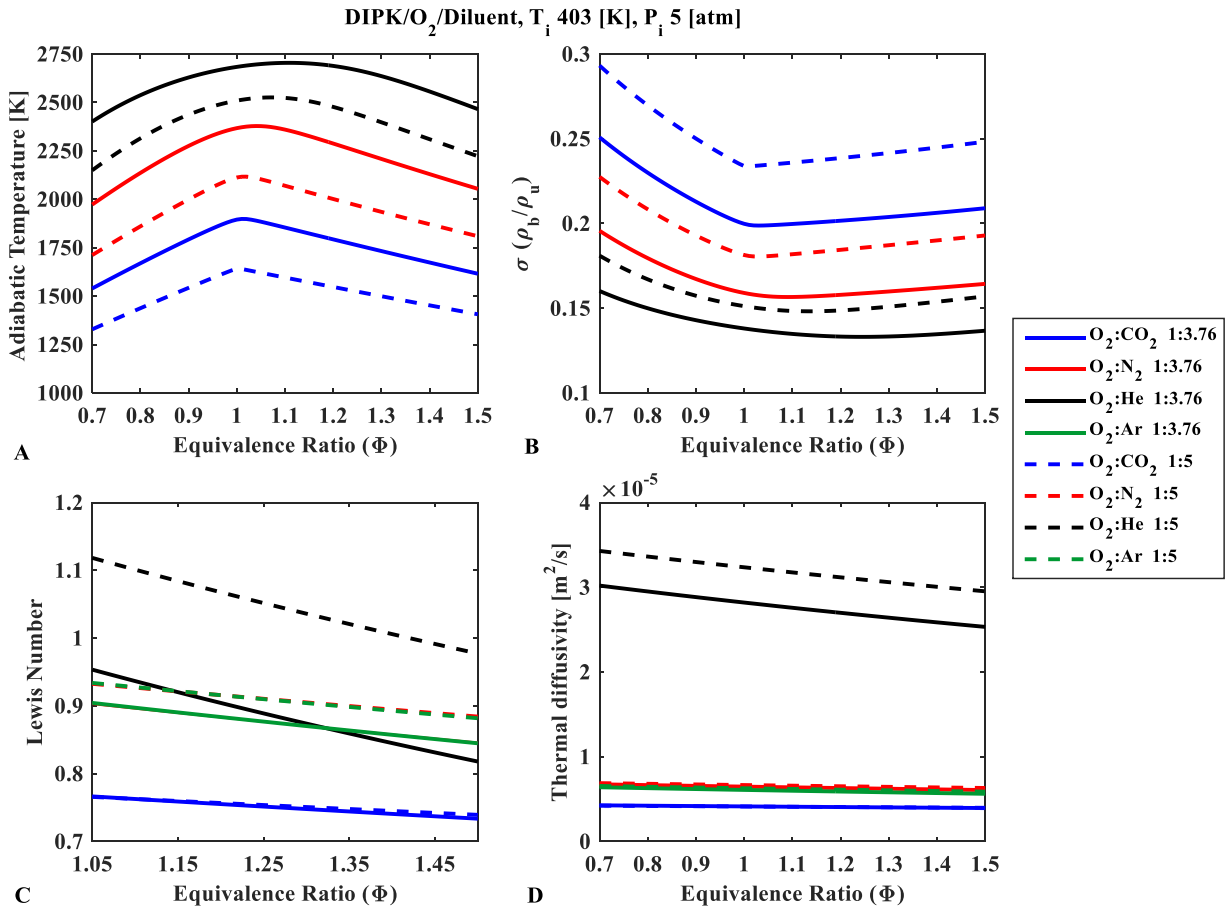

Figure 3.12. Properties of DIPK/O_2/diluent mixtures vs phi at initial T=403 [K] and initial P= 5 [atm]. The blue, red, black, and green colors are used for CO_2, N_2, He, and Ar diluent, respectively. The adiabatic flame temperature at constant enthalpy and pressure is shown in subplot (A), a lower gradient cure is observed with He diluted mixtures. Subplots (B, C, and D) present the variations of density jump, Lewis number, and thermal diffusivity.

Compared to CO_2 and N_2, He does not show a sharp reduction of adiabatic temperature with Φ; its variation is better described as a wide concave down curve (this fact was also noticed with the LBV curve shown in Figure 3.26, that demonstrates the relationship between adiabatic temperature and LBV). This behavior can be attributed to the dissociation effect that increases at higher adiabatic flame temperature and provides a lower temperature gradient with respect to the equivalence ratio. A simple analysis based on a fixed diluent but at different initial temperatures presented identical results. Similarly, the energy released relative to the specific heat decreases as

diluent ratio increases that reduces the adiabatic temperature. For example, the maximum temperature in N_2 diluted mixtures decreased from 2378 K to 2117 K by increasing diluent ratio from 3.76 to 5. An opposite trend was observed in the density jump across the flame (σ), the value increases by increasing the diluent proportionality and was minimum close to the stoichiometric ratio. He offered the smallest density jump relative to N_2 and CO_2. Similarly, He provided the lowest density difference between burned and unburned gases relative to N_2 and CO_2. For instance, the density difference in He and CO_2 diluted mixtures increased from 1.57 kg/m^3 to 5.19 kg/m^3 for $\Phi = 1$ and D = 3.76.

Le is usually used to examine mixture tendency toward diffusional-thermal instability that occurs if Le < 1 [181]. This type of flame instability forms small cracks or cells from the initial stage of the combustion process and can be neglected if a smooth flame is captured within the observable window. It is known that heavy hydrocarbon such as C_8H_{18} and DIPK provides Le > 1 for a lean mixture, for that reason, Lewis number shown in Figure 3.12C presents the rich mixtures side where diffusional-thermal instability occurs. For D = 3.76, all diluents provided Le < 1, but the value increased by using He relative to the other diluents. That is mainly because of He thermal diffusivity (see Figure 3.12D). The difference between Ar and N_2 diluents was negligible in the case of Le, and Ar diluted mixture provided a slightly lower thermal diffusivity. However, utilizing diluent ratio (D) of 5 increased the Le of He diluted mixture substantially. Unlike other diluents, increasing the proportionality of He to D = 5 provided a noticeable increase in mixture thermal diffusivity. Out of the four tested diluents, He is the only gas that can eliminate diffusional-thermal instability by increasing the thermal diffusivity and providing Le > 1.

The hydrodynamic instability is another type of flame instability encountered in constant volume combustion chamber that develops if the effect of density jump across the flame exceeds

the stabilization factor [180, 181]. In general, increasing the diluent proportionality increases both density jump and flame thickness, and the optimum diluent ratio must provide a thicker flame relative to the density jump. In our study, diluent ratio 5 was chosen with He because it provides a density jump close to the N_2 diluted mixture with D = 3.76, and a thicker flame. It is worth noting here that the increase of diluent proportionality lowers the LBV, however, it is necessary to keep LBV higher than the limit where buoyancy effect must be considered. Unfortunately, Chemkin Pro [33] (freely propagating flame model) did not converge while using the available DIPK chemical kinetic mechanism to simulate LBV and flame thickness.

Subsequent analysis with C_8H_{18} fuel using Chaos *et al.* [192] mechanism revealed that the LBV increases substantially by using He. This observation can be attributed to the increase of adiabatic flame temperature and thermal diffusivity as illustrated earlier. Figure 3.13 shows the laminar burning velocity and flame thickness for C_8H_{18} mixture at initial temperature 403 K and initial pressure 5 atm. One notice is that the LBV of N_2 diluted mixture with D = 5 lowers the LBV considerably to the extent that buoyancy effect must be included unlike He or Ar diluted mixtures.

The flame thickness was calculated using the graphical approach [58, 139] after solving the premixed flame code in Chemkin Pro [33]. A numerical derivative was used for the flame temperature domain in order to determine the maximum gradient before evaluating the flame thickness. The results show that the flame thickness decreases by using He or Ar, and increases by increasing the diluent ratio. The thinnest flame was detected for Ar diluted mixtures, even at D = 5, the flame thickness was smaller than those obtained with N_2 diluted mixtures with D = 3.76. It was evident that Ar is not a good candidate to suppress flame instability because thinner flames promote hydrodynamic instabilities as explained earlier in Section 3.1.3. Our conclusions from the numerical analysis can be summarized as follows: mixtures diluted with He at D = 5 suppress

flame instability by providing Le > 1, acceptable density jump, and a slightly thicker flame. However, one needs to keep in mind that mixture properties change during the combustion event (isentropic compression) and triggers hydrodynamic flame instability.

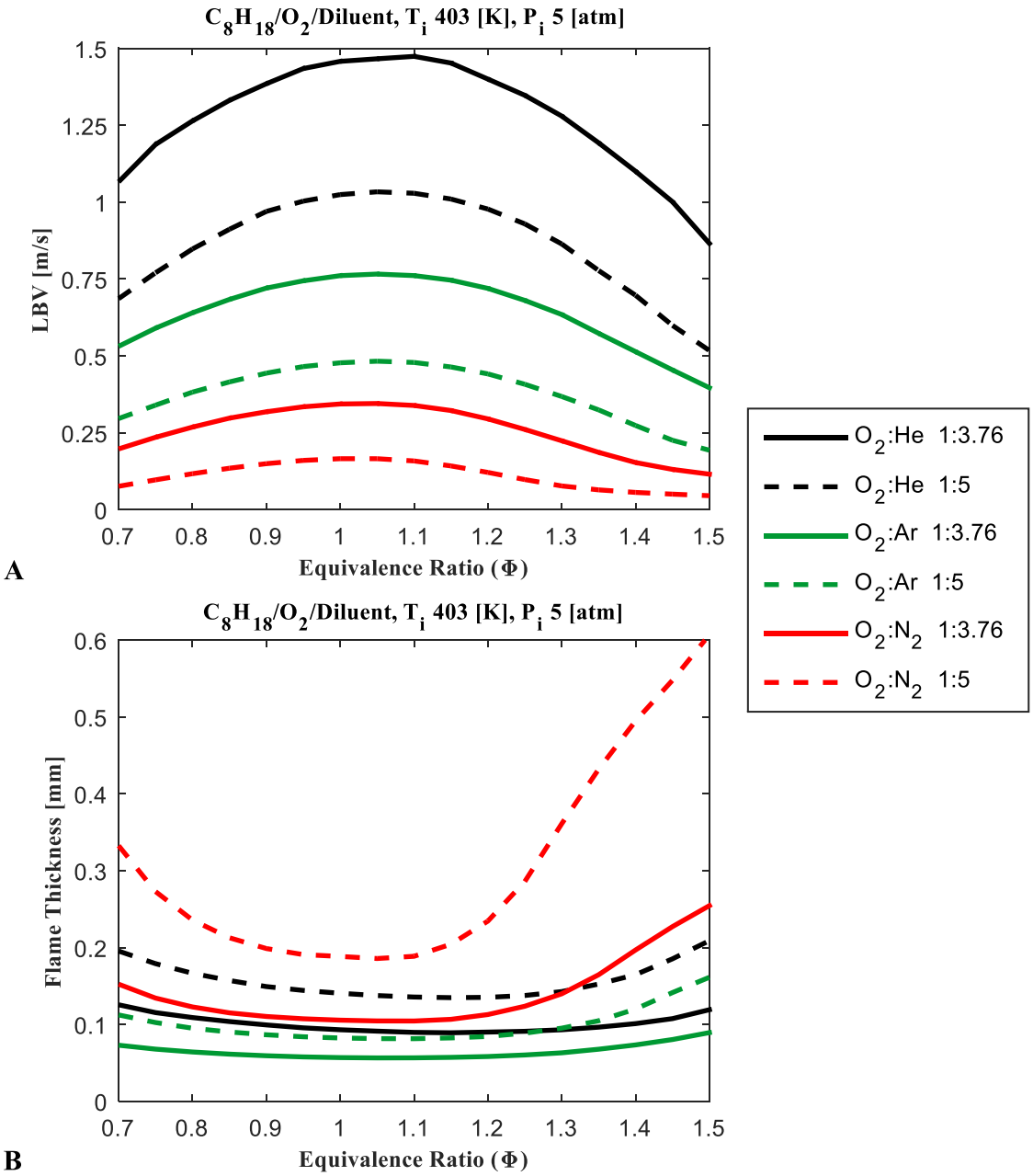

Figure 3.13. Numerical prediction of LBV and flame thickness of C_8H_{18}/O_2/diluent mixtures versus equivalence ratio at initial temperature of 403 [K] and initial pressure of 5 [atm]. The highest LBV was observed with helium at a diluent ratio 1:3.76 while the thinnest flame was predicted for argon at a similar diluent ratio.

3.2.5 Experimental Results of Iso-Octane/Air

Here the discussion is presented for C_8H_{18}/air mixture at an equivalence ratio of 0.9 (a similar trend was noticed for all tested mixtures). A linear relationship between X and the pressure rise inside the combustion chamber is assumed in many combustion studies but was slightly modified by Metghalchi [124, 141]. Figure 3.14 illustrates the difference in mass fraction burned between Linear (X_{Linear}) and Metghalchi ($X_{Metghalchi}$) models, and our Multilayer ($X_{Multilayer}$) approach with respect to the normalized radius. It is evident that the difference is negligible at the beginning of combustion event, however, it increases as the flame grows and reaches its maximum value when the normalized flame radius is approximately 90%. It has been noticed that both Linear and Metghalchi models overestimates X relative to the Multilayer model.

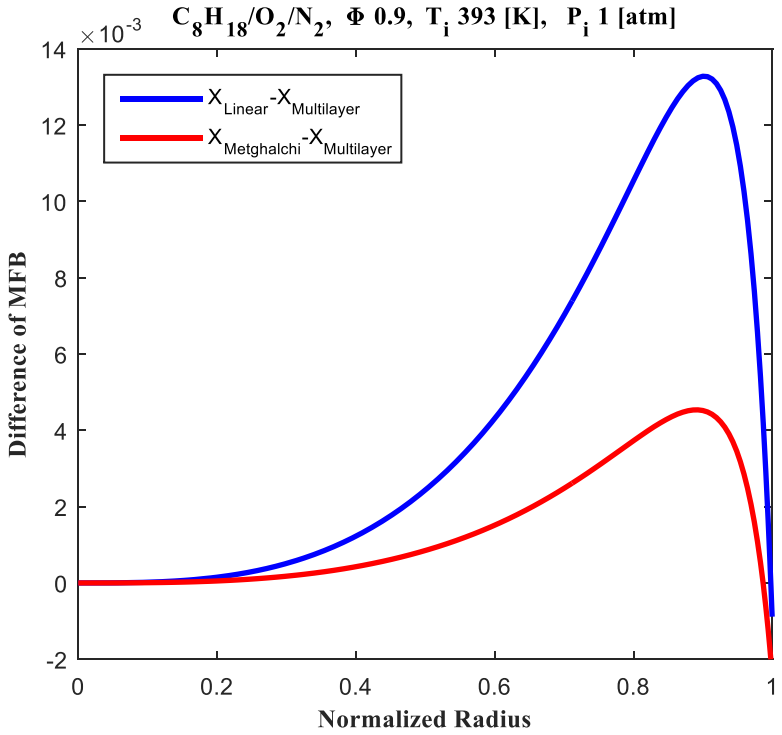

Figure 3.14. Mass fraction burned for C_8H_{18}/air mixture (Φ = 0.9) at initial temperature of 393 [K] and initial pressure of 1 [atm]. The blue line displays the difference between linear and multi-layer models while the red line represents the difference between Metghalchi and multi-layer models.

Our Multilayer model gives the temperature distribution inside the combustion chamber. Figure 3.15 illustrates the change in both burned and unburned gas temperatures versus the number of layers (combustion chamber divided into 93 layers). The straight blue line represents the temperature of initial gases 393 K (before ignition) and the black line on top shows the temperature distribution at the end of the combustion event. It can be noted that the maximum temperature is around 2877 K for the first burned layer, while the last layer is only at 2370 K. All lines in between the blue and black lines, show the history of temperature change and is clear that for both burned and unburned mixtures, temperature increases with time due to compression process. Only ten-time steps are illustrated in Figure 3.15 to visualize the combustion process clearly, however, during the iterative process, all 93 temperature traces are developed.

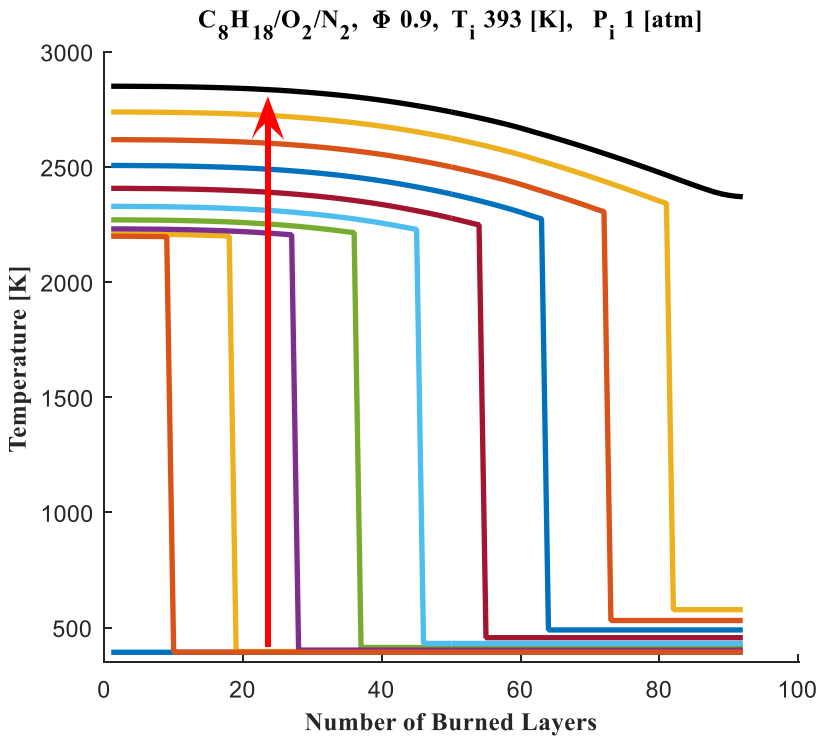

Figure 3.15. Temperature distribution of C_8H_{18}/air mixture (Φ = 0.9) at initial temperature of 393 [K] and initial pressure of 1 [atm]. The time increases in the vertical direction, the intersection of any vertical line with horizontal lines presents the value of temperature at that defined time. For example, the red vertical line shows the temperature time-histories of layer number 23.

Table 3.7. Comparison of temperature and entropy at the end of the combustion process.

	Temperature [K]	**Entropy [J/ kg -K]**
Ideal case (CV)	2601.4	9243.5
Multilayer model	2579.9	9055.5
Metghalchi model	2584.9	9058.2

A second approach to verifying our Multilayer model has been made by using the entropy generation and the average temperature based on X (see Table 3.7). It is found that both entropy trace, as well as the mean temperature, of the Multilayer model tend toward values (slightly underpredicting) obtained by equilibrium at constant volume and internal energy (ideal case, CV). This trend is identical to what has been presented earlier for CH_4/air mixture in section 3.1.3 (see Figure 3.4); here the average temperature was 2579.9 K, approximately 21 K lower than the

adiabatic flame temperature at constant UV. The difference from ideal case is attributed to two reasons; the theoretical pressure is not reached (heat transfer losses), and a small portion of the combustible gases did not burn (especially those near the combustion chamber wall). Note that a similar observation from Metghalchi's model is found in Table 3.7.

In addition to the above comparisons, the author tracked the average species mole fraction during the combustion event by utilizing the Multilayer model. Such an analysis intends to illustrate the limitation of the original Metghalchi model that assumes constant mole fraction. In the Multilayer model, the mole fractions of each layer are found under constant HP equilibrium. Also, the mole fractions change due to the isentropic compression process. Here CO_2 and CO mole fractions are presented in Figure 3.16.

The straight black and red lines in Figure 3.16 show the mole fraction using equilibrium calculation at constant HP and UV respectively. One notices that the mole fraction of each species starts from the value of equilibrium at constant HP, and then approaches the constant UV value. In fact, at the end of the combustion process, the mole fraction of CO_2 is lower than the equilibrium value at constant UV (ideal case). As combustion proceeds, the burned gas temperature of initials layers increases to values beyond 2601.4 K (equilibrium value at constant UV) which in turn promotes higher dissociation of CO_2 molecules (see Figure 3.16). In this case, the maximum temperature was 2877 K; 275 K higher than the ideal case. Even though there are some layers exist at a temperature lower than 2601.4 K, the overall equilibrium provides lower CO_2 mole fraction. The opposite trend was noticed for CO; the mole fraction is higher than the value of equilibrium at constant UV due to the same reason. Similarly, the water molecule and OH radical show identical trend. Higher carbon monoxide and OH radical mole fractions were noticed at the end of combustion process. It is obvious that treating the burned gas with constant mole fractions raises

concerns in regards to burned gas properties that influences the iterative solution. A similar observation has been shown in Section 3.1.3 for the average temperature of burned region.

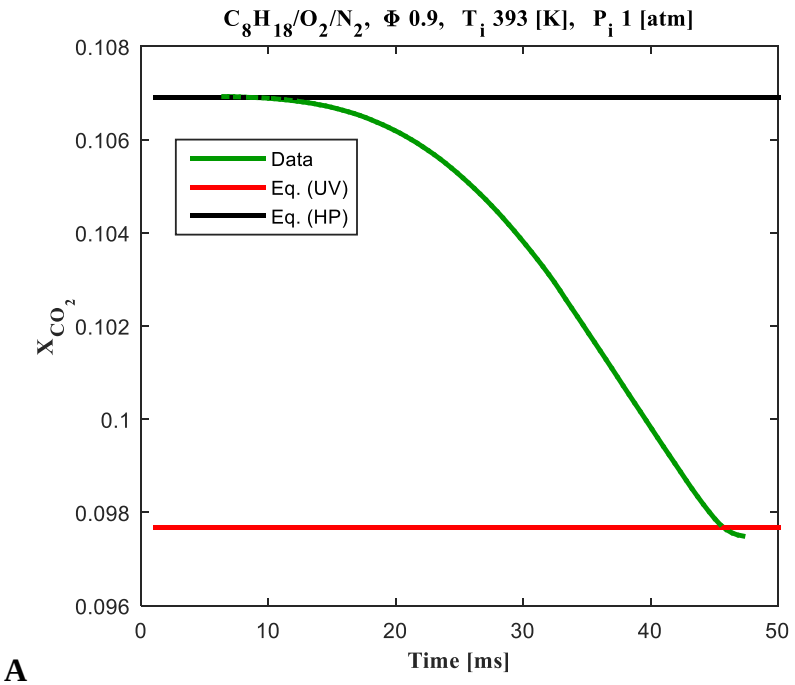

A

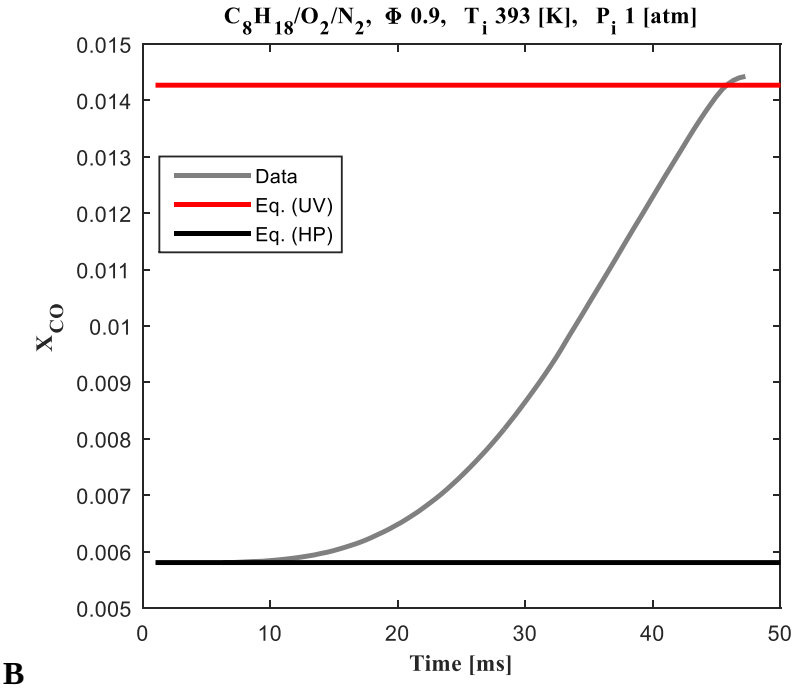

B

Figure 3.16. Mole fraction variation of Carbon Dioxide (A) and Carbon Monoxide (B) during combustion event.

The LBV trend of C_8H_{18}/air mixture at initial temperature of 393 K, the initial pressure of 1 atm, and Φ = 0.9 is shown in Figure 3.17 as a function of the unburned gas temperature. In the constant volume approach, a single experiment gives several LBV data points along one isentrope. A linear regression (least-squares fit, see Figure 3.17) was used to evaluate the LBV value at the initial temperature of 393 K. In general, if the flame is stable, LBV increases as temperature and pressure increase during the combustion event. LBV drops dramatically only near the end of the combustion process.

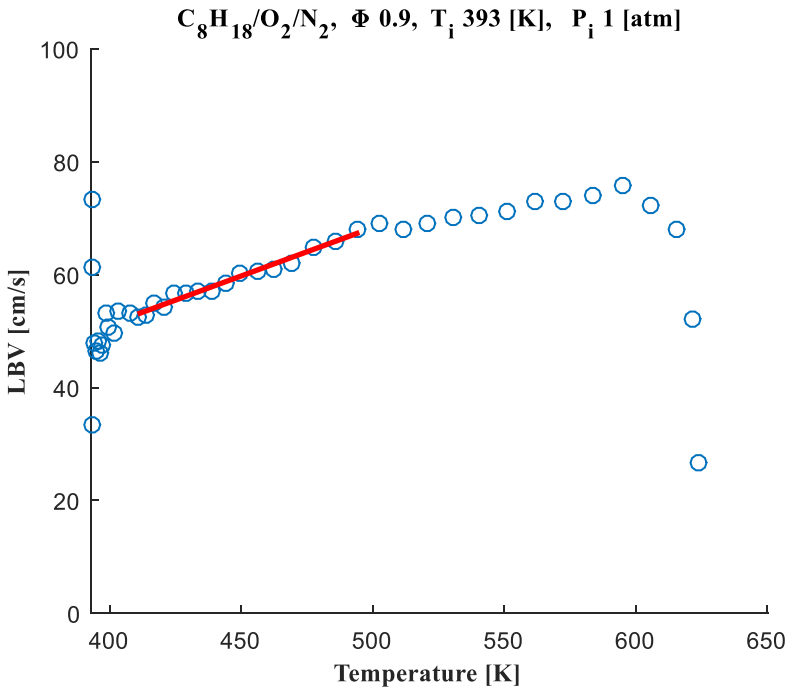

Figure 3.17. Laminar burning velocity [cm/s] of C_8H_{18}/air mixture (Φ = 0.9) at initial temperature of 393 [K] and initial pressure of 1 [atm].

Figure 3.18 presents the LBV as a function of equivalence ratios for C_8H_{18}/air mixtures. The classical trend of LBV vs Φ was observed where the maximum burning velocity occurs slightly after the stoichiometric ratio and drops for both lean and rich mixtures. The fastest (56.14 cm/s)

and lowest (24.75 cm/s) LBV values are recorded for mixtures with equivalence ratio of 1.05 and 1.5, respectively in the range of our current experiments.

Comparisons with literature data (Li *et al.* [193] and Broustail *et al.* [194]) and predictions of mechanisms (Blanquart *et al.* [191] and Chaos *et al.* [192]) are also shown in Figure 3.18. Reasonable agreement was noticed for Φ = 1.1-1.4 with literature data, however, both Li *et al.* [193] and Broustail *et al.* [194] experimental studies are slightly lower than current data in the lean region. The minor differences between various experimental studies are attributed to the test methodology (constant volume versus constant pressure). The CHEMKIN PRO [33] (freely propagating flame model) simulations using two literature (Blanquart *et al.* [191] and Chaos *et al.* [192]) kinetic mechanisms are presented in Figure 3.18. In general, there is very good agreement between current data and those predicted by the Blanquart *et al.* mechanism, though the mechanism underpredicts values for rich mixtures above Φ = 1.35. It is worth mentioning here that even though iso-octane is a relatively well-characterized reference fuel, the disagreement between the two numerical predictions around Φ = 1.1 illustrate the complexity of the kinetics of transportation-relevant liquid fuels.

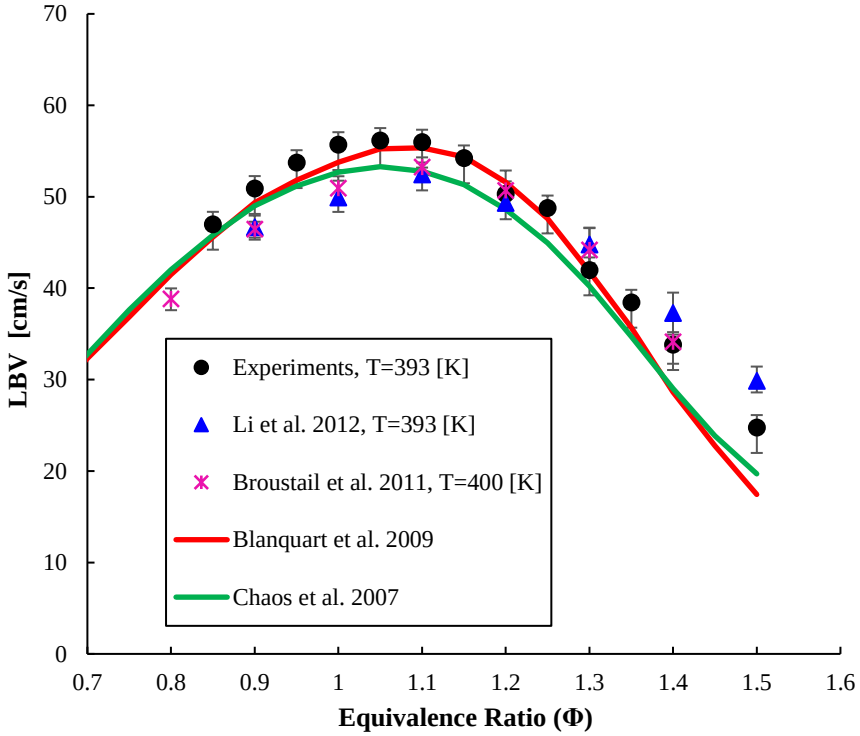

Figure 3.18. Laminar burning velocity [cm/s] vs Φ for C_8H_{18}/air mixture (current study) at initial temperature of 393 K and initial pressure of 1 atm. Comparisons with literature data (Li et al. [193] and Broustail et al. [194]) and predictions of kinetic mechanisms (Blanquart et al. [191] and Chaos et al. [192]) are also shown.

3.2.6 Experimental Results of DIPK/O_2/diluent

Initial experiments were conducted to evaluate the LBV of DIPK/air mixture at 393 K and two initial pressures of 1 and 5 atm. The classical trend of LBV was found for the DIPK/air mixture in the tested equivalence ratios between 0.8 and 1.5 (see Figure 3.19). The maximum LBV (61.4 cm/s) was recorded at even richer mixture (Φ = 1.1) compared to iso-octane (Φ = 1.05). Also shown in Figure 3.19 are LBV values for other oxygenated fuels from literature (ethanol and methanol fuels [46, 48]). The initial pressure was the same (1 atm) for all studies in Figure 3.19, however, the initial temperature varied. It is clearly shown that the LBV of DIPK is slower than the ethanol, however the maximum LBV value occurs at a similar Φ. In the case of Methanol, the maximum LBV is expected to be in between the Φ (1.1-1.2), in all compared fuel the maximum

LBV tend toward a richer mixture compared to gasoline. The author believes that this behavior is attributed to differences in the deviation of the Lewis number from unity, differential diffusion, and the Φ value of maximum adiabatic temperature. As mentioned earlier, the DIPK kinetics mechanisms used by Allen *et al.* [49] and Barari *et al.* [184] are not suitable for simulating LBV and hence not shown in the figure.

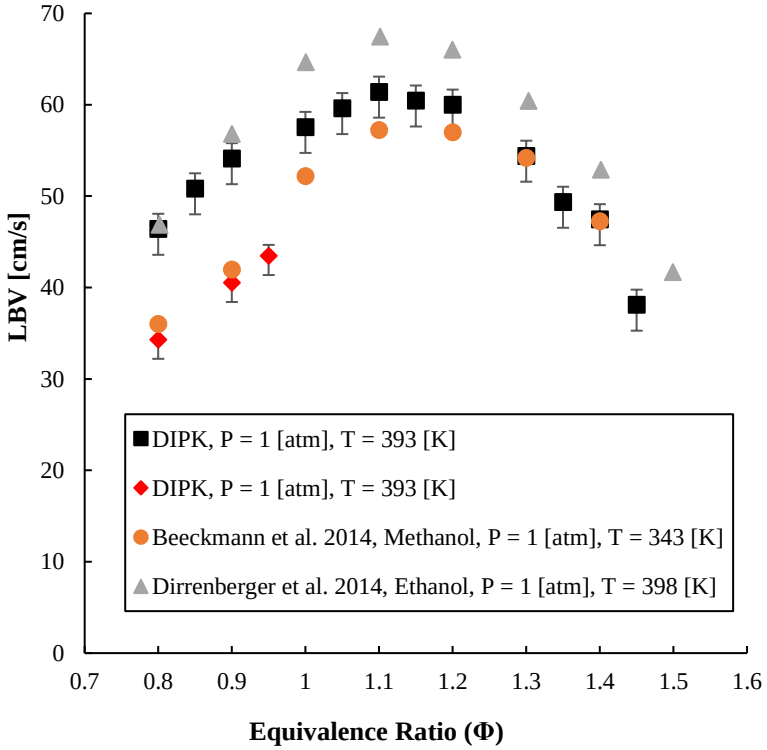

Figure 3.19. Laminar burning velocity [m/s] vs Φ for DIPK/air mixture (current study) at initial conditions of T = 393 [K] and P = 1 and 5 [atm]. Comparisons with ethanol at 398 [K] and 1 [atm] and methanol at 343 [K] and 1 [atm] fuels [46, 48] are also shown.

Experiments at 5 atm initial pressure were limited to only lean mixtures due to flame instability as will be discussed in next section. All documented LBV values (see Figure 3.19) at 5 atm (initial pressure) experiments are based on the early part of the combustion process where the flame was stable. When comparing Figure 3.19 and Table 3.8, the LBV values of DIPK/air mixtures at Φ = 0.8 decreased from 46.4 to 34.3 cm/s when the initial pressure increased from 1 to 5 atm. Similarly,

the reduction was from 54.1 to 40.5 cm/s for Φ = 0.9. It is evident that flame instability at high initial pressure tests limited the range of DIPK LBV values, hence, several diluents were evaluated.

Table 3.8. Laminar burning velocity of DIPK/air mixtures at 393 [K] and 5 [atm].

Φ	**0.8**	**0.9**	**0.95**
LBV [cm/s]	34.3	40.5	43.47

The second sets of experiments were conducted to evaluate the diluent capability to suppress flame instability at initial conditions of 5 atm and 403 K. The initial temperature increased to eliminate any concern in regards to fuel condensation at high initial pressure experiments. Lean mixture diluted with N_2 at D = 3.76 provided a stable, smooth, and spherical flame where LBV can be extracted easily. However, around 2/3rd of the combustion process, the flame develops hydrodynamic instability that results in a sudden discontinuity in the LBV trace; and provide a smaller gradient with respect to unburned gas temperature after the jump (examples are shown as flame propagation in Figure 3.20 and LBV trace in Figure 3.21).

As explained earlier, the reduction of flame thickness and the increase of density jump along one isentrope triggers the hydrodynamic instability. On those experiments, the LBV can be evaluated based on the stable flame region (early part of combustion process). Also, it has been observed that the hydrodynamic flame instability advances as the initial pressure increases and results in a narrower region of useful data points. The sudden discontinuity shifts from an unburned gas temperature 473 K at 3 atm initial pressure to 429 K at 5 atm for DIPK mixture at Φ 0.9. In that case, the appearance of small cells after 29 ms coincides with the shift in LBV trace because of the increase in flame surface area. However, in some experiments, the shift of LBV trace happens to be 1-2 ms before the appearance of the cellular structure. This is attributed to the fact that the observable windows (50.8 mm) show a small section of the flame area during that time, and initial cell formations might occur in a different spot. The hydrodynamic flame instability

problem can be tackled by using different diluent/higher diluent ratio (D) in order to provide a thicker flame relative to the density jump (results are presented later).

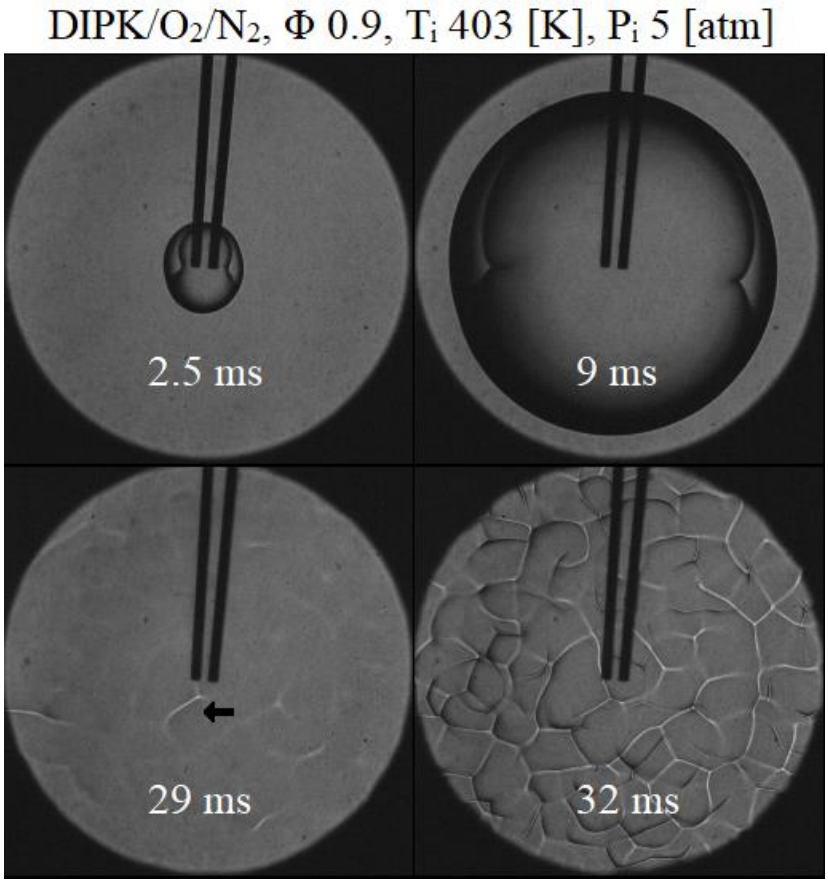

Figure 3.20. Flame propagation of DIPK/O2/N2 at Φ = 0.9, initial T = 403 [K], and P = 5 [atm]. The start of cell formation is shown in after 29 [ms] by a black arrow (only data points before the cellular formation was used to evaluate LBV).

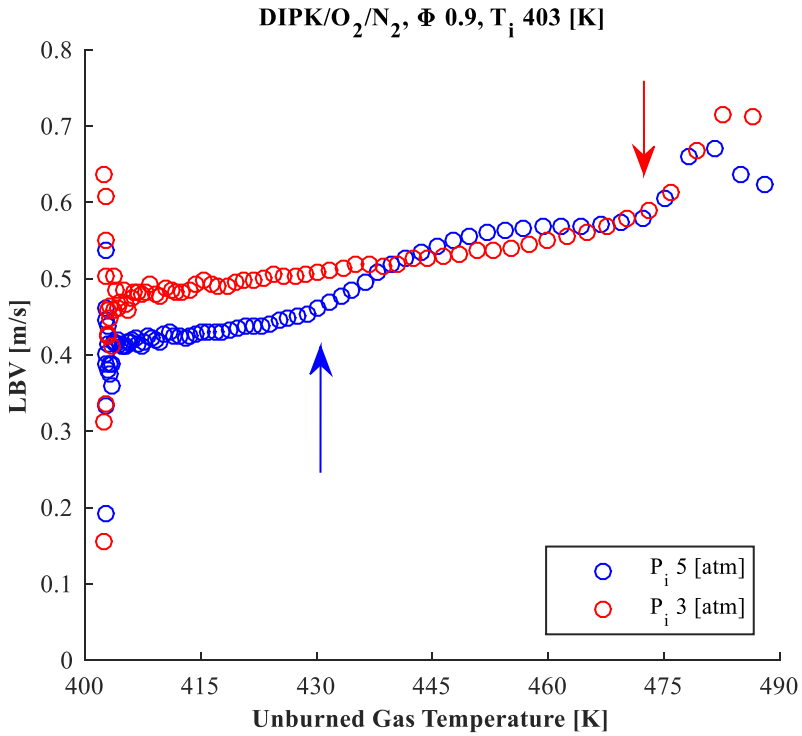

Figure 3.21. LBV vs unburned gas temperature for DIPK/O_2/N_2 at initial conditions of T = 403 [K] and P = 3 and 5 [atm]. Arrows indicate the start of hydrodynamic instability, while red and blue colors are used to illustrate the variation of LBV along two isentropes.

Tests at stoichiometric mixtures demonstrate a different behavior with N_2, even though the flame was smooth and spherical in the initial stage, it develops many cells as the flame approaches the edge of our observable window (50.8 mm). The pressure trace in those experiments cannot be utilized to determine the LBV because most of the data points taken in the analysis happen to be after the flame leaves the observable window where flame cells are already developed with stoichiometric mixtures. Even though, there is an interest in cellular burning velocity [165], this work is intended to produce LBV values that can be used to validated chemical kinetic mechanisms. For that reason, those tests are eliminated from the results in this work.

In a similar manner, the flame instability is more dominant for rich mixtures because of the diffusional-thermal instability (Le < 1). Figure 3.22 shows examples of flame propagation at

several equivalence ratios with different diluents at 5 atm and 403 K. The second column shows flame instability after the ignition process for a DIPK mixture with $\Phi = 1.2$ diluted with N_2 at D = 3.76. It is obvious that after five ms several cellular structures appeared, and around 6.8 ms the flame surface area was covered with cells. Increasing the N_2 diluent ratio to 5 produced very slow flame speed in lean mixtures and did not solve flame instability with rich mixtures (see Figure 3.23). That is mainly because Le < 1 even after increasing the diluent ratio as illustrated in the numerical section. It is believed that the diffusional-thermal instability is the main source of cell formation in both stoichiometric and rich mixtures.

The severity of flame instability was increased by switching the diluent from N_2 to Ar because of its lower thermal diffusivity, and thinner flame thickness. The flame of Ar diluted mixture at D = 3.76 develops cell formation even with lean mixtures (cannot be used for LBV measurements). After increasing the diluent ratio to 5, a stable flame was observed for lean mixtures but with an earlier hydrodynamic instability. This fact reduces the valuable data points along one isentrope. The flame propagation of Ar diluted mixture at $\Phi = 1$ and diluent ratio D = 5 is shown in Figure 3.22. It is apparent that the cell structure forms as the flame approaches the windows edge. This trend was also observed at identical Φ with N_2 at D = 3.76. It is clear that argon is not a good candidate as a diluent in hydrocarbon mixtures for laminar burning velocity measurements, especially with the constant volume approach that depends on evident pressure change which occurs after the disappearance of flame edge.

Helium provided a stable combustion compared to other diluents, especially with those experiments conducted with a diluent ratio of 5. Figure 3.22 presents the result of He diluted mixture at D = 5; a smooth flame propagates spherically at $\Phi = 1.5$. This is attributed to He high

thermal diffusivity that increases Le and provides a stable flame even with rich mixtures. The author did not observe diffusional-thermal instability with He even at an equivalence ratio of 1.6.

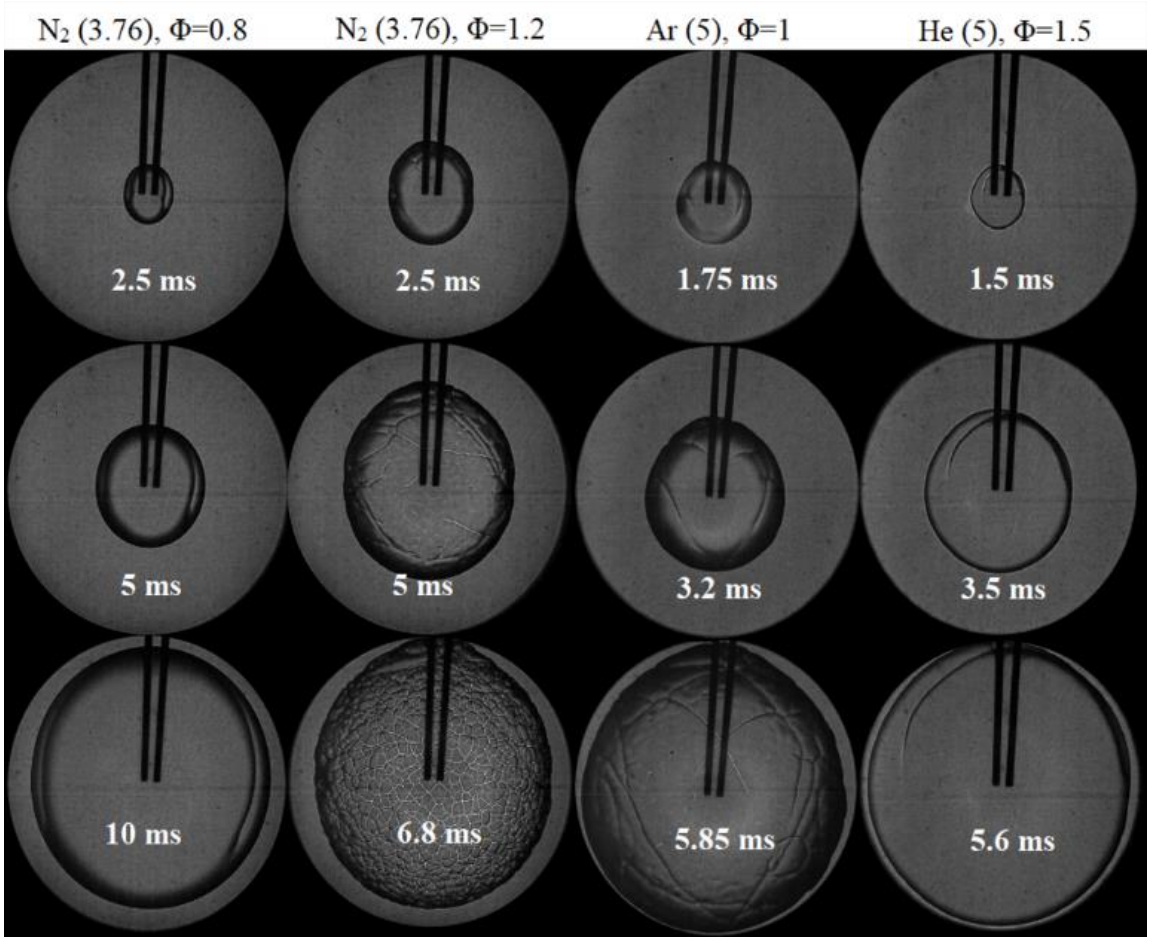

Figure 3.22. Flame propagation of DIPK/O_2/diluent at initial conditions of T = 403 [K], and P = 5 [atm] for several equivalence ratios. Helium is the only diluent that provides a stable combustion in rich mixtures.

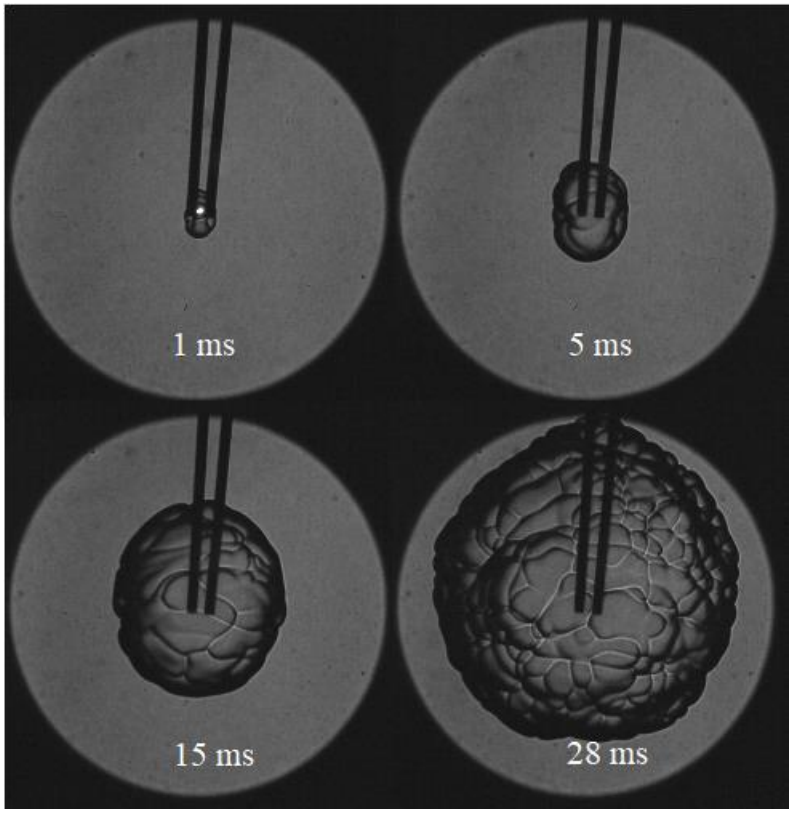

Figure 3.23. Flame propagation of DIPK/O_2/N_2 at initial conditions of T = 403 [K], and P = 5 [atm] for diluent ratio D = 5.

After demonstrating how He at high diluent ratio suppresses diffusional-thermal instability, the investigation was shifted to assess its ability to extend the useful range of data points by delaying the hydrodynamic instability. This can be found by comparing LBV traces as well as the appearance of cell formation within the observable window by using mixtures at identical equivalence ratios and different diluent ratios.

Figure 3.24 illustrates LBV traces for mixtures diluted with He at $\Phi = 0.85$ and two diluent ratios. This equivalence ratio was chosen to eliminate the effect of diffusional-thermal instability which might exaggerate the differences between LBV traces and triggers flame instability earlier. It is apparent that the increase of diluent ratio delayed the discontinuity of LBV trace which results in an increase of the valuable data points along one isentrope. In the given example, the maximum

pressure and temperature increased from 9.15 atm and 487 K to 9.85 atm and 503 K by increasing D from 3.76 to 5. Since the LBV of those mixtures are different, the time of hydrodynamic instability appearance is not a conclusive parameter for comparison. Instead, the authors compared the ratio of hydrodynamic instability appearance to the time at the end of the combustion process. It is noticed that the time ratio increased from 0.63 to 0.68 by increasing the diluent ratio. This observation is seen in all tests, and it is more evident as Φ increases toward the stoichiometric ratio.

A similar comparison was made for a stoichiometric mixture and provided a flame instability delay of 46 K. However, those mixtures might promote flame instability in that region because of Le < 1. Similarly, comparing the LBV traces of He and N_2 diluted mixture at identical diluent ratios showed a huge advantage of He diluted mixtures. Figure 3.21 and Figure 3.24 show LBV traces of mixtures that have similar Φ, but with a different diluent, He delayed flame instability by 58 K that corresponds to an increase of time ratio from 0.48 to 0.63.

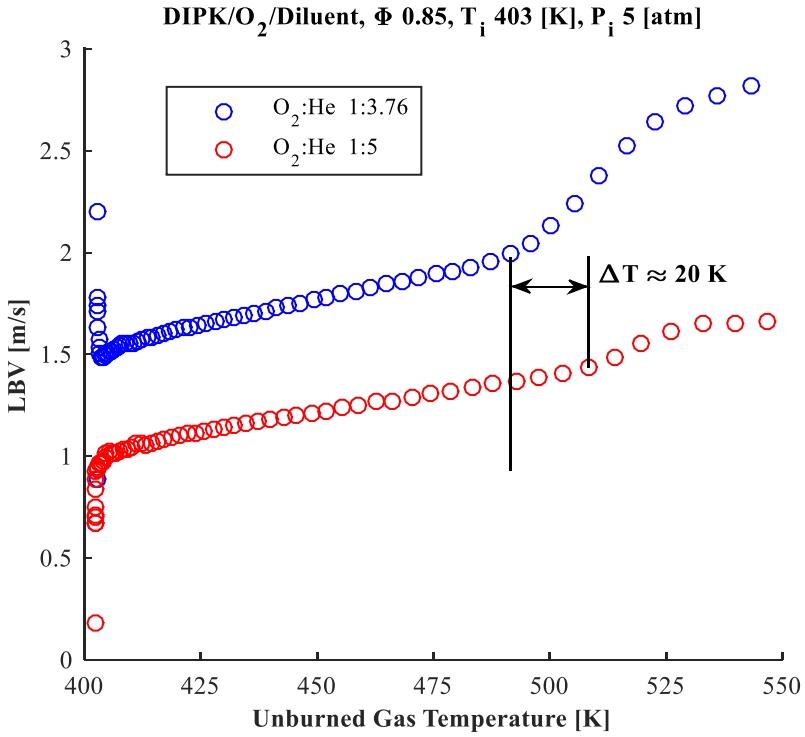

Figure 3.24. Laminar burning velocity versus unburned gas temperature for DIPK fuel diluted with helium using two diluent ratios at initial conditions of T = 403 [K] and P = 5 [atm]. Hydrodynamic instability is suppressed by using higher diluent ratio because of the increase in flame thickness relative to the density jump.

The laminar burning velocities were observed to increase in the order of N_2> Ar > He diluted mixtures. Even after increasing the diluent ratio to 5 with He and Ar, the LBVs are higher than those obtained with N_2 at D = 3.76 diluent ratio. Figure 3.25 presents LBV variation along three isentropes at Φ = 0.85 by using several diluents. One notices that the slope of LBV with respect to unburned gas temperature (in the stable region) increases in a similar order. The slope for N_2, Ar, and He diluted mixtures were 0.12, 0.22, and 0.39 cm/s·K respectively. Identical diluent ratios were used for He and Ar to evaluate the effect of thermal diffusivity on LBV at identical molar specific heat. It is found that LBV increases from 49.95 cm/s to 102.72 cm/s by using He diluted mixture that provides a thermal diffusivity of 3.33 x 10-5 m^2/s. This value is almost one order of magnitude higher than the Ar diluted mixture thermal diffusivity.

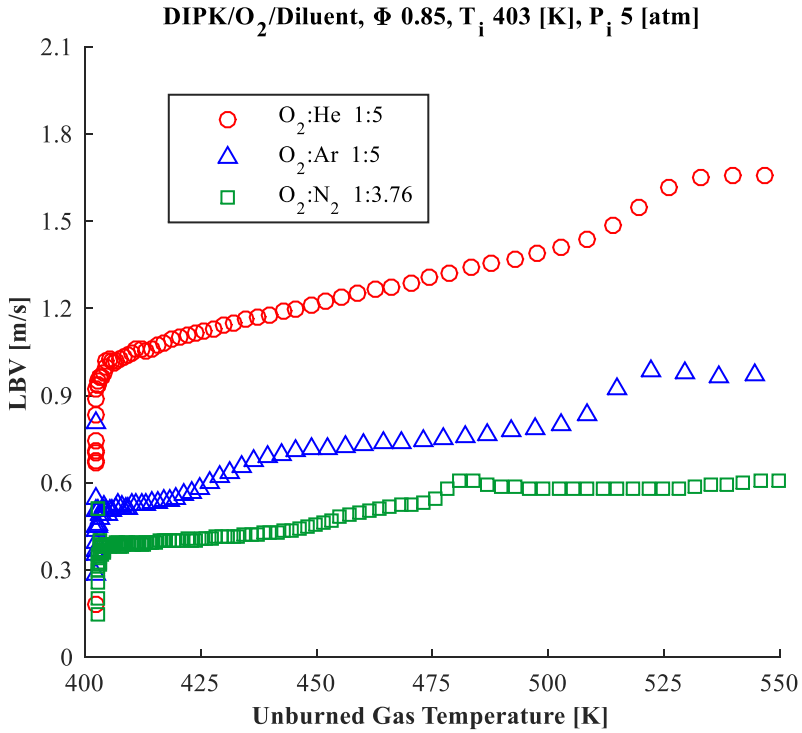

Figure 3.25. Laminar burning velocity along three isentropes for DIPK/O₂/diluent at Φ = 0.85 and initial conditions of T = 403 [K] and P = 5 [atm]. Several diluents/diluent ratios are employed to study the effect of mixture properties on LBV.

Similarly, the effect of mixture specific heat was assessed by comparing Ar and N_2 diluted mixtures at different diluent ratios. Diluent ratios 5 and 3.76 were used for Ar and N_2 mixtures respectively to deliver close thermal diffusivities. The thermal diffusivities were 6.406 x 10-6 m^2/s and 6.6 x 10-6 m^2/s while molar specific heats were 24.94 J/mol·K and 32.6 J/mol·K for Ar and N_2 mixtures at $\Phi = 0.85$, $T_i = 403$ K, and $P_i = 5$ atm. The reduction of LBV from 49.95 cm/s to 38.25 cm/s by using N_2 is attributed to the increase of mixture molar specific heat that has an almost identical ratio of increase. It is worth noting that the flame instabilities with Ar diluent occurs before even the N_2 diluent and results in a narrower region of useful data points as illustrated in the figure.

Regarding N_2 diluted mixtures, the flame was stable for a wider range compared to Ar, but it was almost half the range of He diluted mixture. Also, the increase of diluent ratio did not provide

a stable flame for rich mixtures where deviation of thermal and mass diffusivity triggered flame instability (see Figure 3.23). Finally, it is evident that the flame thickness is the most important factor in hydrodynamic instability because all tested mixtures in Figure 3.22 have a close density jump, however, a considerable difference of stability behavior was observed. That is mainly because of the flame thickness that increases in the order of Ar, N_2, and He diluted mixtures as illustrated in the numerical section.

The classical trend of LBV vs equivalence ratio has been obtained for DIPK mixtures diluted with He at 403 K, 5 atm, and D = 5. The LBV was maximum for slightly rich mixture and decreased for both lean and rich mixtures. This trend is identical to the adiabatic flame temperature obtained earlier in the numerical section. The maximum LBV was 120.8 cm/s at Φ = 1.1, while the minimum measured value was 47.2 cm/s at Φ = 1.6. One notices that the LBV increased from 38.24 cm/s with N_2 to 102.7 cm/s by using He diluent at Φ = 0.85; this increase is more than double the value measured with N_2 mixture. This is attributed to the increase of adiabatic flame temperature, reduction of molar specific heat, and the increase of thermal diffusivity that has a vast influence on LBV. A similar increase of LBV was observed in Rozenchan *et al.* [188] and Eisazadeh-Far *et al.* [189] studies, and shown in the numerical section of this study.

Metghalchi and Keck [124]'s laminar burning velocity correlation is used to estimate the LBV of DIPK mixture diluted with He at D = 5. Power low fit has been employed to estimate the correlation constants by using the least square method. Since the triggering point of hydrodynamic instability is a function of Φ, the LBV correlation has been validated for unburned gas temperature (403-495) K, pressure (5-9.5) atm, and Φ (0.85-1.5). Some mixtures provided a wider range of stable flame, but our intention is to offer a general correlation. Table 3.9 shows correlation constants (a_1, a_2, α, and β) in equation (3.44).

Table 3.9. Power law fit constants for LBV of DIPK/O2/He mixture.

S_{uo} [cm/s]	a_1	a_2	α	β
118.7	-0.288	-2.323	2.402	-0.359

$$S_u = S_{uo} * (1 + a_1(1-\Phi) + a_2(1-\Phi)^2)\left[\frac{T_u}{T_{ui}}\right]^{\alpha}\left[\frac{P}{P_i}\right]^{\beta} \quad (3.44)$$

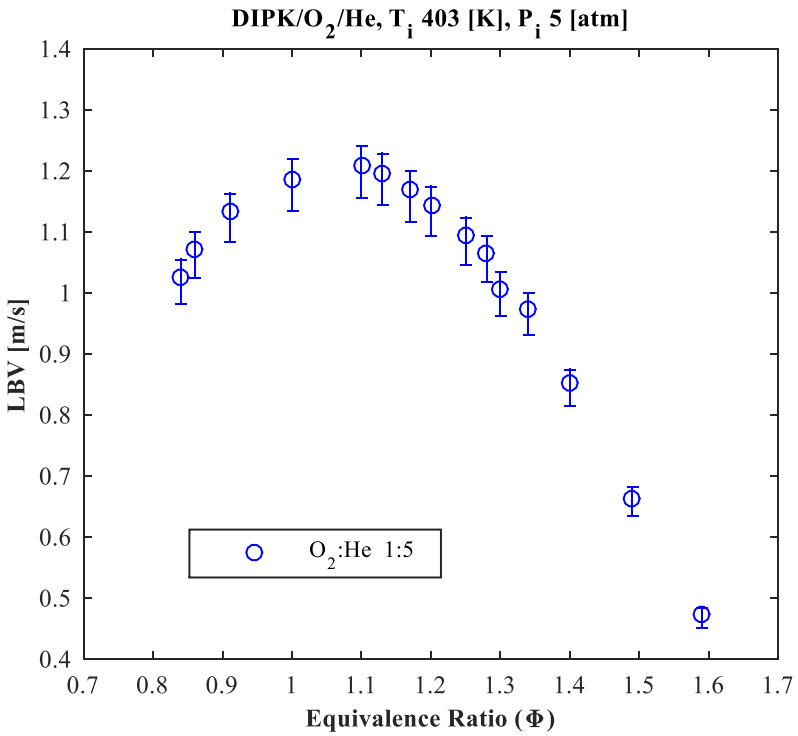

Figure 3.26. LBV vs Φ for DIPK/O2/He at initial temperature of 403 [K] and initial pressure of 5 [atm].

Where S_{uo} is the LBV in cm/s at a reference point (P_i = 5 atm, T_{ui} = 403 K, and Φ = 1), and T_u, P are the unburned gas temperature (K) and pressure (atm) respectively. The laminar burning velocity along four isentropes are shown in Figure 3.27 to deliver a range of useful data points in the literate. Experimental values are shown as circles while solid lines are used to illustrate the LBV obtained using Metghalchi and Keck [124] correlation. The pressure of each data point can be calculated using the isentropic compression assumption, for example, at Φ = 1.35 the range of pressure was from 5 to 9.5 atm (limited because of hydrodynamic instability). It is evident that the

LBV increases along one isentrope because the unburned gas temperature is a dominant factor relative to the increase of pressure during the isentropic compression process, the correlation constants α and β clearly shows that. The Laminar burning velocity of 2,4-Dimethyl-3-pentanone (DIPK) is obtained at high initial condition to provide data points to validate chemical kinetic mechanisms for the automotive application.

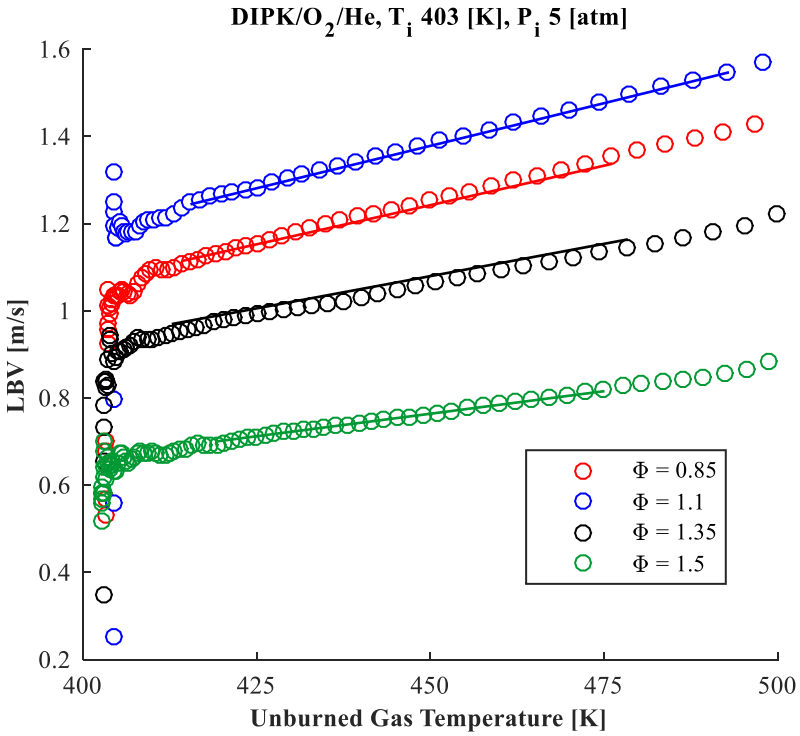

Figure 3.27. LBV vs unburned gas temperature for DIPK/O_2/He at initial conditions of 403 [K] and 5 [atm] for several equivalence ratios.

3.2.7 Conclusions for the LBV Measurements of DIPK

The laminar burning velocity (LBV) of DIPK - an advanced liquid biofuel ketone produced by endophytic conversion of cellulose - has been measured at several initial conditions. The constant volume approach with a Multilayer model was used to evaluate the laminar burning velocity from measured pressure at 100 kHz. Flame visualization at a rate of 20,000 fps ensured that the reported experiments have spherical and stable flames. The current experimental method verification is

carried out by using C_8H_{18}/air mixtures, a relatively well-characterized liquid fuel. LBV values for C_8H_{18}/air are compared against previous data and predictions by literature kinetics mechanism and found to be in reasonable agreement. The current Multilayer model gave insights into the temperature distribution and the entropy production during the combustion event. Also, the classical LBV trend was observed for both C_8H_{18} and DIPK fuels, however, the maximum LBV values of DIPK tended toward a richer mixture. At 1 atm and 393 K initial conditions, the maximum LBV of C_8H_{18}/air is 56.14 cm/s at $\Phi = 1.05$; while that of DIPK/air was 61.4 cm/s at $\Phi = 1.1$.

It has been noticed that the flame at an initial pressure of 5 atm suffered from hydrodynamic and diffusional-thermal instabilities for lean and rich mixtures respectively. N_2, Ar, and He diluents were used to suppress flame instability and to provide a wider range of data points. Ar was the most destabilizing diluent because of its low thermal diffusivity and provided a thin flame compared to other diluents. He with a diluent ratio D=5 offered a high thermal diffusivity that eliminated diffusional-thermal instabilities for rich mixtures and delayed hydrodynamic instability by providing a thicker flame relative to the density jump in lean mixtures. It is worth noting that the molar specific heat and thermal diffusivity are two important properties that influence fuel reactivity and LBV values. Under identical thermal diffusivity, the increase of LBV is directly related to the reduction of molar specific heat. Additionally, under identical molar specific heat, thermal diffusivity has a vast influence on the LBV. The classical LBV trend was observed for DIPK diluted with He, the maximum LBV of DIPK/O_2/He was 120.8 cm/s at $\Phi = 1.1$. Several data points along one isentrope (up to 10 atm and 503 K) were measured to provide numerous validation points for chemical kinetic mechanisms. Also, a correlation of laminar burning velocity was obtained to estimate the values in the range of pressures (5-9.5 atm), temperatures (403-495 K),

and equivalence ratios (0.8-1.5). The present method will be extended to other advanced biofuel candidates and blends as part of the U.S. Department of Energy's Co-Optimization of Fuels and Engines (Co-Optima) project [36].

CHAPTER 4: CONCLUSIONS

4.1 Summary of Results

In this doctoral study, advanced ignition systems were assessed using a constant volume combustion chamber and reciprocating engines to evaluate feasibility in lean reciprocating engine combustion. First, laser and spark ignition systems were used to initiate combustion for CH_4/air mixture to study the flammability limit, effect of pulse energy, flame kernel shape as well as laminar burning velocities (LBV). It has been found that the LBV is not a function of ignition energy; even though the maximum pressure occurs earlier with higher ignition energy, this is understood to happen because a larger volume is initially ignited. Toroidal and spherical flame propagations have been noticed during the experiments. However, the LBV values were almost identical with spark and laser ignition systems, nominally showing a difference of 1.5%, with a maximum difference of 2.8% at $\Phi = 1.3$. Discrepancies in the measured LBVs between SI and LI systems were within the uncertainty of experimental setup. The laminar burning velocity of the stoichiometric CH_4/air mixture is 57.02 cm/s at an initial pressure of 1 atm and 393 K initial temperature. The maximum value for the CH_4/air mixture occurs at an equivalence ratio of 1.05. Laser extends the CH_4 flammability limit to $\Phi = 0.5$-0.51 in this study, which is less than the values suggested by Tahtouh *et al.* [117] and Wang *et al.* [121] for spark ignition systems. The determination of LBV attributed to pressure increases after the ignition inside the UCF combustion chamber were characterized to have a cumulative uncertainty of 5.8% and 3.8% for LI and SI systems respectively.

A 6-cylinder natural gas engine study conducted at Argonne National Laboratory was successfully operated at a rated speed of 1800 RPM and 298 kW load with directly mounted

μlasers igniting all 6 cylinders. To the best of the author's knowledge, the multi cylinder directly mounted laser ignition, is the first time that this has ever been performed in the world. Ignition timing (IT) sweeps, and excess air ratio (λ) sweeps were performed while keeping the NO_x emissions below the EPA regulated value ($BSNO_x$ < 1.34 g/kW-hr), and maintaining ignition stability at industry acceptable values (COV_IMEP < 5%). The engine performance was compared for the cases of standard spark ignition (SI) and two pulse laser ignition (2P-LI). A brake thermal efficiency improvement of 2.6% points was observed with the use of 2P-LI. A detailed analysis shows that laser ignition leads to significantly improved ignition characteristics under advanced ignition timings, which, in turn, enables optimal phasing to result in efficiency improvements. Also, the cyclic variation in terms of indicated mean effective pressure, as well as location of maximum pressure, decreased dramatically by using laser ignition system and enable the use of leaner mixture. The optimum excess air ratio in case of laser ignition was λ 1.68, any further increase offsets the gain from the lean combustion mode because of the reduction of fuel reactivity and LBV.

Addressing the above concern, the reduced flame speeds can be compensated with the use of a prechamber to result in volumetric ignition, and thereby lead to faster combustion. Another study was performed to identify the optimal geometry of prechamber laser ignition (PCLI) through several tests in a single-cylinder engine as a compromise between autoignition, NO_x and soot formation within the prechamber. Subsequently, experiments were conducted to compare the performance of three ignition systems: standard electrical spark ignition (SI), single-point laser ignition (2P-LI), and prechamber equipped laser ignition (PCLI). Out of the three, the performance of PCLI was far superior compared to the other two. Efficiency gain of 2.1% points could be achieved while complying with EPA regulation and the industry standard for ignition stability.

Test results and data analysis are presented identifying the combustion mechanisms leading to the improved performance. The PCLI system was capable of achieving higher brake thermal efficiency because of the volumetric ignition which reduced the combustion duration dramatically. This fact allows the engine to operate at retarded ignition timings even though a leaner mixture were employed compared with other ignition systems. Also, the spatially distributed jets provided almost identical combustion on every cycle which reflects minimum cyclic variation. For example, the COV_LOMP of the optimum operating points for SI, 2P-LI, and PCLI systems were 13.5%, 9.5%, and 7% respectively. The PCLI system is expected to perform even better by using a multi-cylinder engine.

To assess the feasibility of new biofuels for automotive application, a spherical combustion chamber was designed, built, and assembled for studying laminar burning velocities of hydrocarbon fuels at high initial conditions. Methane and isooctane fuels were tested to validate the experimental setup for gas and liquid fuels respectively, by comparing the measured data points against values in literature and numerical predictions by CHEMKIN PRO [33]. In addition, those data points were used to examine the accuracy of the Multilayer thermodynamic model, and compare it with the Linear and Metghalchi and Keck models. Also, schlieren and shadowgraph imaging techniques were employed to capture the kernel development and flame propagation in each experiment. This approach ensured that the reported LBV is obtained by utilizing a spherical flame without hydrodynamic and diffusional-thermal instabilities.

After validating the experimental setup, procedure, and thermodynamic model, tests were conducted to measure the LBV of a new promising biofuel candidate for automotive application. The Laminar burning velocity of 2,4-Dimethyl-3-pentanone, also known as diisopropyl ketone (DIPK) has been measured at several initial conditions and diluents. Initial experiments with N_2

diluent is carried out at an initial temperature of 393 K and for two initial pressures (1 and 5 atm). The classical LBV trend was observed for both C_8H_{18} and DIPK fuels, however, the maximum LBV values of DIPK tended toward a richer mixture. The maximum LBV of C_8H_{18}/air is 56.14 cm/s at $\Phi = 1.05$; while that of DIPK/air was 61.4 cm/s at $\Phi = 1.1$. It is worth noting that the LBV values are slightly higher for DIPK than iso-octane but less than ethanol. In general, DIPK does not only provide auto-ignition enhancement and higher pressure and temperature sensitivities compared to gasoline but also higher flame speed that can reflects higher rate of heat release in reciprocating engines.

Flame instability was visualized in DIPK/air mixtures at 5 atm (initial pressure) for all rich mixtures from the onset of combustion. Also, under these pressure conditions in lean mixtures, a sudden discontinuity in LBV was recorded around 2/3 of the combustion duration. This sudden discontinuity is attributed to flame transitioning into instability, as combustion proceeds the flame thickness decreases due to the rise in pressure and temperature of the unburned mixture, while the density difference (across the flame) increases along one isentrope. Those two unfavorable factors triggered the hydrodynamic flame instability at high initial pressure.

Subsequent tests were conducted to suppress flame instability at high pressure using Ar, and He diluents with several diluent proportionalities. A slightly higher initial temperature of 403K and three initial pressure (1,3, and 5 atm) were used to eliminate any concern in regard to the fuel condensation. Ar was the most destabilizing diluent because it has low thermal diffusivity and provides a thin flame compared to other diluents. In contrast, He with a diluent ratio 5 offered a high thermal diffusivity that eliminates diffusional-thermal instabilities for rich mixtures and delayed hydrodynamic instability by providing a thicker flame relative to the density jump in lean

mixtures. It is worth noting that the specific heat and thermal diffusivity are two important properties that influence fuel reactivity and LBV values.

It is concluded that utilizing He at high proportionality is mandatory for LBV measurement at high initial pressure (targeting reciprocating engine conditions) in order to provide a stable flame. The classical laminar burning velocity trend was observed for DIPK fuel diluted with He, the maximum LBV of DIPK/O_2/He was 120.8 cm/s at $\Phi = 1.1$. Several data points along one isentrope (up to 10 atm and 503 K) were measured to provide numerous validation points for chemical kinetic mechanisms. Also, LBV correlation constants were obtained to estimate the values in the range of pressure (5-9.5 atm), temperature (403-495 K), and equivalence ratio (0.8-1.5).

4.2 Publications from this Dissertation

The research detailed in this dissertation has been published in the following conference and journal papers:

- B. Almansour, Joseph Lopez, Luke Thompson, Ghazal Barari, Subith S. Vasu, "Laser Ignition and Flame Speed Measurements in Oxy-Methane Mixtures Diluted With CO_2", **J. of Energy Resources Technology-Transactions of the ASME**, 2016, 138, 032201.
- B. Almansour, S. Vasu, S. Gupta, Q. Wang, R. Van Leeuwen, C. Ghosh, "Performance of a Laser Ignited Multi-Cylinder Lean Burn Natural Gas Engine", **Journal of Engineering for Gas Turbines and Power-Transactions of the ASME,** 2017, 139(11), 111501.
- B. Almansour, S. Vasu, S. Gupta, Q. Wang, R. Van Leeuwen, C. Ghosh, "Prechamber equipped laser ignition (PCLI) for improved performance in natural gas engines", **Journal of Engineering for Gas Turbines and Power-Transactions of the ASME**, 2017 139(10), 101501.

- B. Almansour, S. Alawadhi, S. Vasu, "Laminar burning velocity measurements in DIPK-an advanced biofuel", **SAE International Journal of Fuels and Lubricants**, SAE Paper No:2017-01-0863, 10(2):2017.
- B. Almansour; G Kim, S. Vasu; "The Effect of Diluent Gases on High Pressure Laminar Burning Velocity Measurements of an Advanced Biofuel Ketone", **SAE World Congress 2018**, accepted, SAE Technical Paper No 2018-01-0921.
- B. Almansour; S. Alawadhi, S. Vasu; "Laminar burning velocity measurements in DIPK-an advanced biofuel", **SAE World Congress 2017**, accepted, SAE Paper No 2017-01-0863.
- B. Almansour, S. Alawadhi, S. Vasu, "Comparison of Laser and Spark Ignition: Laminar Burning Velocity Measurements in Natural Gas/air Mixtures", **The 4th Laser Ignition Conference** 2016, Yokohama, Japan, May 2016.
- B. Almansour, S. Alawadhi, S.S. Vasu, "Flame Propagation in Premixed Mixtures of Liquid Biofuels", presented at the **ESS/CI Spring Technical meeting**, Princeton, NJ, 3/2016, paper #1B03.
- B. Almansour; J. Lopez; L. Thompson; G. Barari; S. Vasu; "Ignition and Flame Propagation in Oxy-Methane Mixtures Diluted with CO2", **Proceedings of the ASME Turbo Expo** 2015, Paper no: GT2015-43355.
- B. Almansour, L. Thompson, J. Lopez, S. Vasu, "Laser ignition and burning velocity measurements in natural gas/air mixtures", **The 3rd Laser Ignition Conference**, LIC15, Argonne National Lab, IL, 4/2015.
- L. Thompson, B. Almansour, J. Lopez, L. Glebov, S. Vasu, "Laser ignition and flame development in premixed conventional and alternative fuel mixtures", work-in-progress poster presented at the **35th Int. Symposium on Combustion**, SF, 8/2014.

- S. Vasu, B. Almansour, L. Thompson, J. Lopez, L. Glebov, "Fundamental Laser Ignition Studies of Hydrocarbon Fuels", **The 2nd Laser Ignition Conference** 2014, Yokohama, Japan, 22-25 April 2014.

Planned future publications are as follows:

- B. Almansour, S. Vasu, S. Gupta, " Reduction of cyclic variation in a lean-burn natural gas engine with advanced ignition systems ".
- B. Almansour; G Kim, S. Vasu; "The Effect of Diluent Gases on High Pressure Laminar Burning Velocity Measurements of DIPK".

4.3 Recommendations for Future Work

The current research highlighted the need to investigate in advance ignition systems that can ignite leaner mixtures to provide higher thermal efficiency in reciprocating engines. Out of the three ignition systems: spark ignition (SI), single-point laser ignition (2P-LI) and prechamber equipped laser ignition (PCLI), PCLI proved to have the best performance in the tested configurations. It does not only lead to the extension of the lean ignition limit but also shortened the ignition delay and combustion duration significantly which in turn reflects higher thermal efficiencies and lower COV_IMEP. However, the prechamber optimization process is extremely complicated, expensive and time-consuming if engine tests are carried out for each prechamber configuration. The optimization process must include the effect of several crucial parameters to achieve the optimum configuration (number of nozzles, their diameter and positions within the prechamber, prechamber volume relative to the clearance volume, and the prechamber shell thickness). Because of that reason, the development of a CFD model is recommended as a new research topic where the above-mentioned parameters can be altered easily. Furthermore,

efficiency gains can be envisioned with laser ignition as strategies promoting multi-point ignition with larger plasma spatial separation is attained. Therefore, innovative optics strategies that can provide excellent sealant and spatial plasma separation are suggested as another future topic.

In addition, constant volume combustion chamber are very useful tools for studying the heat release as we well as the laminar burning velocity. Measurements for CH_4, C_8H_{18}, and DIPK mixtures were taken using N_2, CO_2, Ar, and He diluents at several initial conditions. Since, the combustion chamber has been designed to withstand 140 atm, experiments at higher initial pressure are recommended. The range of initial pressure could be extended to 10-20 atm in a third research topic. Engine manufactures are pushing toward higher energy density engines; therefore, the high-pressure experiments will provide more insights in regards to fuel reactivity and ignition capabilities. In addition, since both ignition delay times and laminar burning velocity measurements exist for DIPK, the forth recommended future topic is to develop a detailed chemical kinetic mechanism where LBV values can be predicted in order to evaluate the fuel suitability for advance engine concepts through computational fluid dynamic (CFD) modeling.

APPENDIX A: UCF SPHERICAL CHAMBER EXPERIMENTAL SETUP

The experimental setup consists of the spherical combustion chamber, oven, mixing tank, optical system, ignition system, high-speed camera, and data acquisition system. The spherical combustion chamber is made of 316 stainless steel with an internal diameter of 165 mm and 10 mm shell thickness. Figure A1 shows a side view of the combustion chamber where spark ignition electrodes appear at the center. The flame propagation is captured during select experiments by using a high-speed camera (Phantom V12) at 20000 frames per second. Both flame shadowgraph and schlieren imagining are utilized throughout this dissertation. This approach ensured that only spherical, smooth flames without cellular structures are used to obtained LBV. A Kistler [195] 603B1 dynamic pressure transducer and 5010B1 charge amplifier are used to record the pressure at 100 kHz; while data was recorded using National Instruments [196] DAQ system NI 6259 that is capable of recording up to 1.25 Ms/s on a single channel. The schematic representation of the experimental setup is presented in Figure A2, and a detail description on each component is given below.

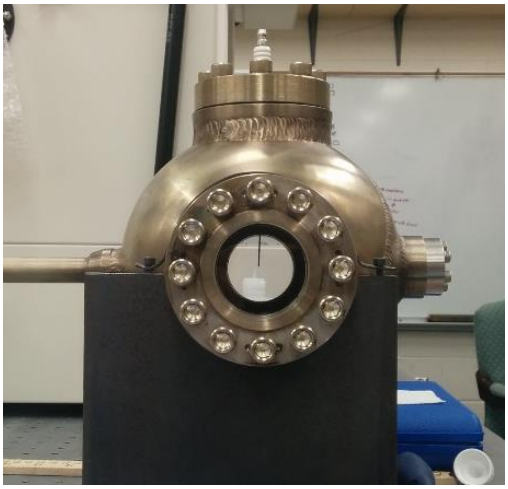

Figure A1. Side view of the spherical combustion chamber with a regular spark ignition system.

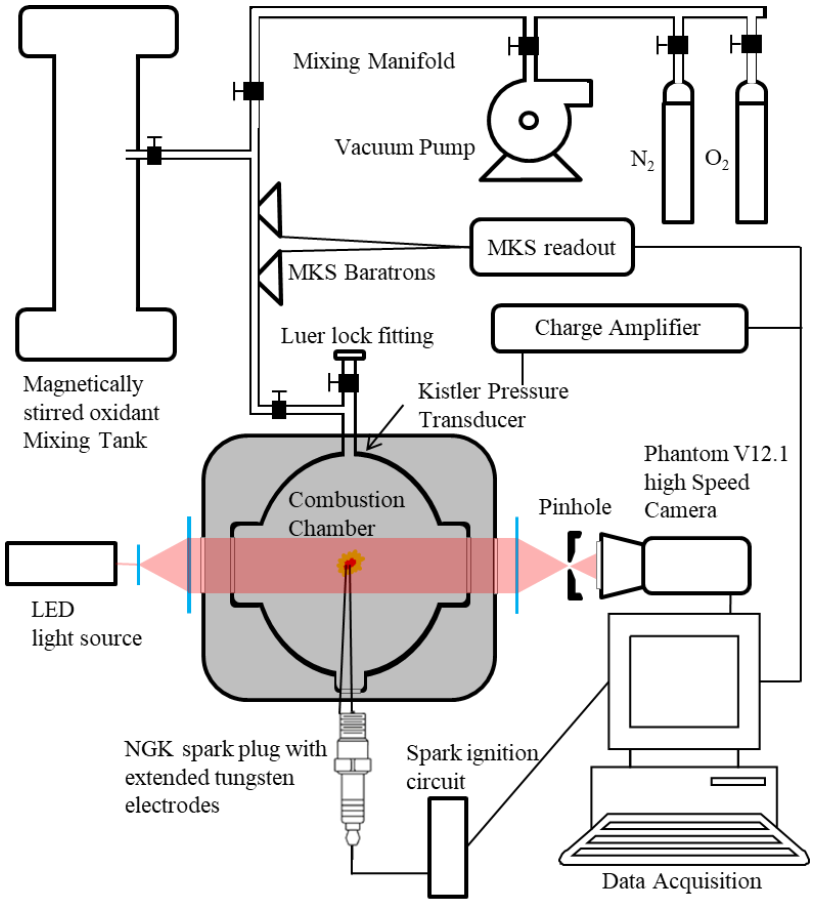

Figure A2. Schematic representation of the University of Central Florida spherical combustion chamber.

APPENDIX A1. *Design*

The spherical combustion chamber is made of 316 stainless steel with an internal diameter of 165 mm and 10 mm shell thickness. The vessel is designed and certified according to ASME Boiler and Pressure Code, Section VIII. It has four optical access with different sizes (13 – 64 mm) that can be used for schlieren photography, laser ignition, pressure transducer, and spectroscopy diagnostic techniques. A stainless steel 12.7 mm diameter pipe is welded to the chamber in order to attach the sphere to the manifold (shown in Figure A3). According to the Hoop stress analysis, the vessel can withstand 140 atm at 1000 K with a safety factor of 3.4. Namely, the stainless-steel structure can handle a maximum pressure of 478 atm at 1000 K.

Since the stainless-steel structure can withstand a very high pressure, the limiting factor in any combustion facility is the capability of optical windows. For example, the 12.7 mm sapphire window can withstand a maximum pressure of 140 atm, but with a lower safety factor. In the next paragraphs, the author presents design safety factors of quartz and sapphire windows based on Hoop stress, blind flange, and the optical equation suggested in [21].

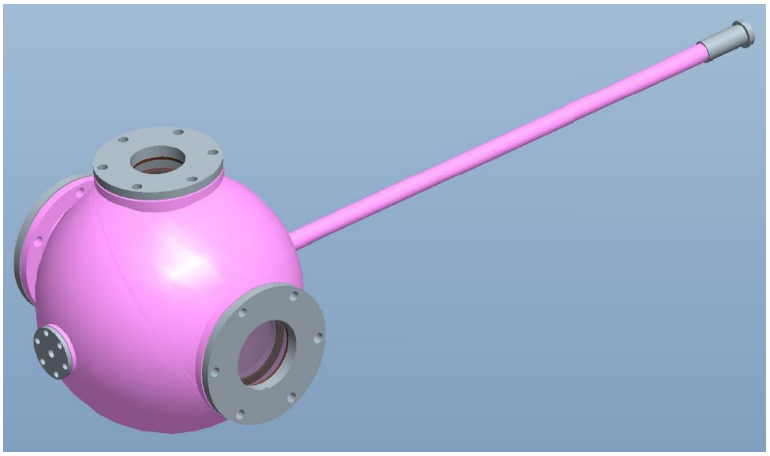

Figure A3. Combustion chamber model.

The window thickness is directly proportional to the diameter, all stress calculations carried out for the largest window (63.5 mm), and same thickness was used for the 50.8 mm window. A maximum pressure of 140 atm was chosen to ensure that the combustion chamber is capable of withstanding a combustion with an initial pressure of 20 atm. This initial condition is crucial to provide LBV values relevant to combustion in reciprocating engines (Otto and Diesel). Two window thicknesses are chosen for the stress calculation 9.525 and 12.7 mm; Table A1 shows the safety factor for Hoop stress (HS), blind flange (BF), and the optical equation (OE). The safety factor was found by dividing the window thickness by the designed thickness. It is apparent that the quartz window does not withstand the design parameter according to the BF and OE equations, and it is just above the safety factor 1 with hoop stress calculation. However, the sapphire windows

delivered a safety factor comparable to the one used for the stainless-steel structure. That is mainly because of the high tensile strength of sapphire 7000 kg/cm^2 compared to quartz 500 kg/cm^2.

Table A1. Window safety factors under several design equations.

	quartz			**sapphire**		
Thickness [mm]	HS	BF	OE	HS	BF	OE
9.525	1.04	0.785	0.51	14.5	2.4	1.89
12.7	1.4	0.86	0.68	19	3.21	2.5

APPENDIX A2. Ignition System

Spark and laser ignition systems are used throughout the dissertation to show the benefit of laser ignition. The result is evaluated based on the behavior of pressure trace, maximum pressure, flame propagation, and laminar burning velocity. The compression of the two ignition systems was presented by utilizing Methane mixtures (shown in section 2.2).

APPENDIX A2.1. Spark Ignition

Lucas ignition circuit was assembled and controlled by a LabVIEW program to provide spark ignition mechanism. A transistor (1RFP250) in conjunction with a 12 VDC relay were employed to disconnect the current from the primary circuit. The relay was powered by an external 9 V battery as shown in the schematic diagram (see Figure A4) while the transistor was controlled by a LabVIEW program. This configuration allows for direct control by using the DAQ analog output channel with a 7.5 V output. In spark ignition experiments, LABVIEW was used to synchronize the pressure measurement, camera system, and the spark timing by using a single triggering pulse. Since the preparation time for a single experiment is long, an on/off switch was utilized to charge the primary circuit before the ignition process.

A spark plug (NGK BR4HS) was modified by welding two tungsten electrodes with 1 mm diameter to produce a spark at the center of the combustion chamber. In our design, both electrodes were introduced from the same side as opposed to diametrically opposite configuration found in many spherical chamber configurations [142]. Because there is no electrode in one hemisphere, this arrangement would avoid thermal conduction losses and thereby produce a theoretically unperturbed flame in that section (opposite to electrodes). This concept allows for direct evaluation of heat transfer losses by comparing the flame position with respect to time on the two sides. The constant pressure approach is planned to be conducted in future experiments.

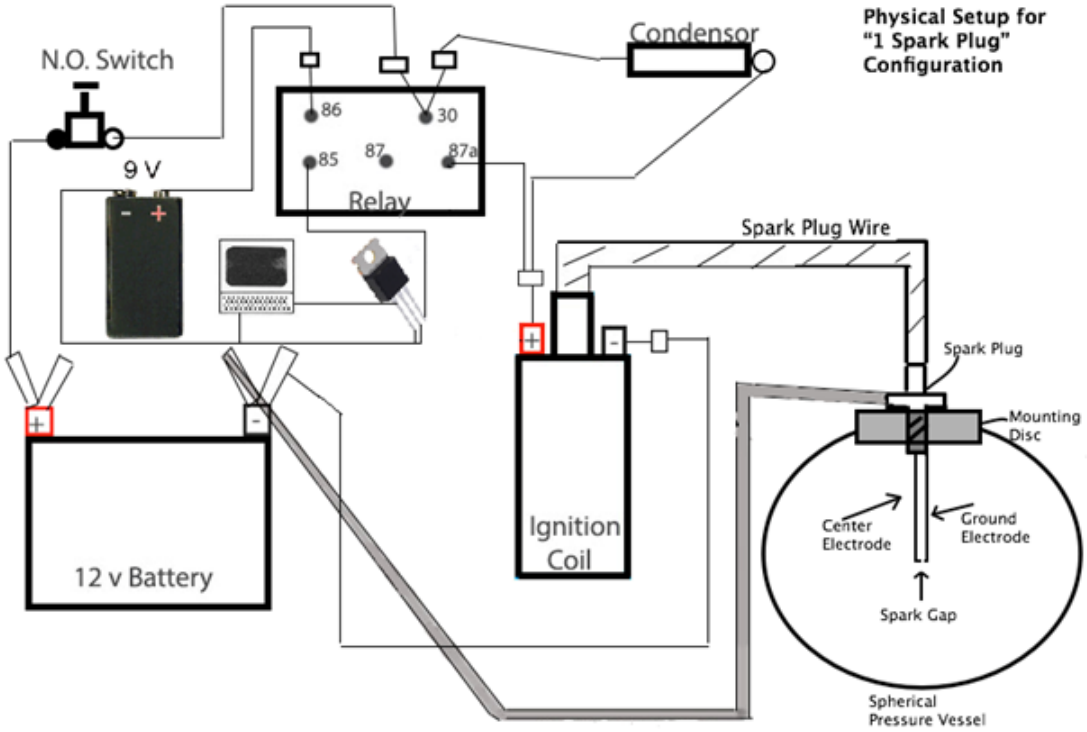

Figure A4. Lucas ignition circuit.

APPENDIX A2.2. Laser Ignition

The optical setup is comprised of two parts. One optical system was constructed to provide an ignition source for the chamber. A Quanta-Ray Lab 190 Q-switched Nd:Yag laser was used with a FWHM pulse width of approximately 10 ns. The ignition setup consisted of the 1064 nm laser

pulse passing through a series of mirrors and a simple bi-convex lens with the focal plane centered in the spherical combustion chamber. Two bi-convex lenses are utilized in this dissertation with a focal length of 250 mm and 500 mm. The laser peak power at the fundamental mode was measured at 1 J/pulse. Other harmonics 532 nm, 355 nm, and 266 nm can be obtained by using two BBO frequency doubling crystal and pairs of dichroic mirrors. Laser characterization is presented in section 2.2 by using Coherent J-50MB-YAG-1535 energy meter. Laser specifications are shown in Table A2.

Table A2. Laser specification

Model	**Quanta-Ray Lab 190**
Wavelength [nm]	1064
Pulse width [ns]	8-12
Beam diameter [mm]	< 10
Repetition rate [Hz]	10
Beam divergence [mrad]	< 0.5
Energy stability	< 3%

Since the laser power is significantly higher than that required to create a plasma, and 1064 nm neutral density filters were not available, the energy is reduced manually. This approach decreased the reported beam quality which may increase the required pulse energy to create a plasma in air. In the tests presented in this dissertation, a single pulse mode was used to ignite the mixture. A pulse energy of 155±10 mJ was used which was just above the minimum threshold energy for formation of plasma due to optical breakdown Unlike spark ignition tests, in laser ignition experiments LabVIEW was not used to trigger the ignition system. However, a Quanta-Ray laser triggering pulse was utilized to synchronize the high-speed camera, pressure transducer, and the laser firing.

APPENDIX A3. Optical Setup / Flame Propagation

The second half of the optical setup consists of the components necessary to record a shadowgraph/schlieren image of the kernel development and flame propagation. In the shadowgraph configuration, a CW He-Ne laser (HNL225R) was collimated to a 50.8 mm diameter and was passed perpendicular to the ignition spot. Due to the sharp density change along the flame front a high-resolution image allowing for flame tracking is obtainable through this method. Since the laser provides a Gaussian beam profile, the author noticed a brightness deviation in the captured image if the full laser diameter was utilized. Namely, images were too bright in the center, and the intensity decreases with the radius. This problem has been addressed by using a Bi-concave lens LD2568 in tandem with a Bi-convex lens LB1859, this configuration uses approximately 60% of the laser beam and provides a clear even image without any brightness deviation. A lens was employed after the combustion chamber in order to compress the picture so that the full window field may be imaged. The schematic representation of optical setup is shown in Figure A2.

On the other hand, schlieren image requires a broadband light source. A red LED light source was collimated to a 50.8 mm diameter by utilizing a similar lens arrangement. However, after passing the light beam through the tested media, a Bi-convex lens and a pinhole were employed to remove diffracted rays. In this configuration, a clear and bright flame surface area can be obtained and assessed. A Phantom v12.1 high-speed camera is used to capture frames at a resolution of 512x512 at a rate of 20000 fps. The camera can provide a higher frame rate up to 1 million fps. However, a low-resolution image and only small part of the 50.8 mm window will be captured.

APPENDIX A4. Manifold

A stainless-steel manifold has been assembled from Swagelok tube and VCR fittings to attach all components to a single platform. This setup allows for a better utilization of MKS Baratron, for

creating a mixture and referencing the pressure before the ignition process. Series of tubes, valves, and crosses are employed, all fittings are designed to withstand a maximum pressure and temperature of 200 atm and 477 K respectively. The targeted maximum initial pressure in this work was only 20 atm. However, the manifold was designed for a higher value because it is planned to be used for other studies like the supercritical carbon dioxide combustion. A strut channel in conjunction with vibration-damping clamp were employed to support the manifold on the optical table.

APPENDIX A5. Pressure Measurement

The pressure measurement setup is comprised of two parts for absolute and dynamic measurements. The absolute pressure measurements are carried out by using two temperature regulated capacitance manometers (MKS Baratron 628 and E27). The two Baratrons have been attached to the manifold in order to be used for mixture preparation as well as referencing the Kistler dynamic pressure transducer. Since the fuel partial pressure is very low when preparing a mixture at atmospheric pressure, a low-pressure range Baratron (E27) was employed to evaluate it accurately. MKS PDR2000 readout was powering the Baratrons for at least four hours before conducting tests to ensure that the optimal diaphragm temperature is achieved before preparing a mixture. The 628 Baratron output pressure signal (0 – 10 VDC) was fed to the National Instrument DAQ to record the initial pressure automatically. The pressure range and accuracy of the two Baratrons are given in Table A3.

Table A3. Specification of MKS capacitance manometers

MKS Baratron	**E27**	**628**
Pressure Range [atm]	0 – 0.13	0 - 26.3
Accuracy [%] (including non-linearity, hysteresis, and non-repeatability)	0.12	0.25 (ranges ≥ 1 Torr)

The Kistler 603B1 dynamic pressure transducer in tandem with the 5010B1 charge amplifier were used to record the combustion pressure at 100-200 kHz. The 603B1 is built for high-pressure measurements with a natural frequency beyond 300 kHz; the maximum operating pressure and temperature are 200 atm and 200 °C. The sensitivity and linearity of the transducer were 0.3695 pC/psi and ≤ 0.07% of the full-scale output respectively. Since dynamic pressure sensors are designed for measuring a pressure difference, the pressure before the ignition event was referenced to the value obtained by the MKS Baratron 628. This method eliminates the error associated with thermal sensitivity of Kistler pressure transducers. Half a second of pressure signal was recorded before employing a 1-D MATLAB smoothing function [174] to minimize the pressure fluctuation at the beginning of the combustion process. The smoothed trace was compared to the original signal at each experiment to ensure that the mean value of the pressure fluctuations was captured.

APPENDIX A6. Mixing Tank / Heating system

A 40 liters stainless steel mixing tank is used to prepare the fuel/air mixture. The design can withstand a maximum pressure and temperature of 40.3 atm and 260°C respectively. The internal surface was coated with Polytetrafluoroethylene (PTFE) to minimize absorption of liquid fuel and water. The tank has a magnetically actuated mixing system to ensure that the mixture is well-mixed and homogeneous before use in experiments. The mixing facility was heated and maintained at the target temperature by use of three insulated heating jackets each with an embedded K-type thermocouple and heating tape.

In addition to the magnetically actuated mixing tank, 1 gallon Swagelok sample cylinder coated with PFTE was purchased to prepare synthetic air. The sample cylinder is designed for a maximum pressure of 63 atm at 426°C respectively. The portable sample cylinder has two hemispheres ends

with NPT tube fitting. Two Swagelok adaptors were welded to provide VCR connection in order to eliminate leakage associated with NPT fittings. Since the sample cylinder will be used for various experiments, another benefit for the VCR fitting is to provide a simple way to disassemble the cylinder. The sample cylinder used in this dissertation for liquid fuel tests because fuel was directly injected into the combustion chamber.

Heating jacket and tapes are used to increase the temperature of the mixing tank, sample cylinder, and the Luer lock adaptor. Heating systems are essential for liquid fuel tests, where fuel and synthetic air must be at the same temperature in order to use Dalton's law of partial pressure. This approach minimizes uncertainties associated with mixing gases at a different temperature. Liquid fuel was injected into a heated volume to ensure complete vaporization. Similarly, the temperature of sample cylinder and manifold were maintained at the target temperature by using heating tapes and a control unit.

The spherical combustion chamber is placed in a 6 kW electric oven from Thermcraft (XSB-1C) in order to raise its temperature to the target value before conducting experiments. The oven chamber dimensions are 30.5 cm x 30.5 cm x 45.7 cm; a ceramic refractory heater with embedded resistance wire were used as a heating element. The oven has been modified to provide four optical access and can maintain a temperature as high as 1200 °C with a digital controller. For a greater accuracy, the author attached four k-type thermocouples to the spherical chamber to reference the temperature of the sphere directly.

APPENDIX A7. Mixture Preparation / Experimental Procedure

For the gas fuel experiments (CH_4), the magnetically actuated mixing tank was used to prepare the mixture. Before the creation of a fuel mixture, the mixing facility was vacuumed for at least 6

hours. This process ensures that no condensed water molecules from atmospheric air exist on the inner surface of the mixing facility. After that, the mixture was prepared by using the partial pressure method with the help of two manometers. The filling order was fuel, O_2, and diluent because the mass of fuel and oxygen are relatively small compared to the diluent. This approach increases the turbulence and hence the mixing process when diluent is filled. Since the mixture was homogenous in the mixing tank after blending for hours, only a wait time of 5 minutes was required after filling the chamber. A vacuum pump was used for 10-15 minutes before and after doing experiments to make sure that there is no air or residue from the previous run. Ultra-high purity gases are used throughout the dissertation with a purity of 99.999%.

On the other hand, for the liquid fuel experiments, another procedure was developed to ensure that each mixture is homogeneous and uncertainty in the composition is minimized. Since the liquid fuel requires a higher temperature to exist in the gas phase, experiments are conducted at 393-403 K. The heated (using heating jackets) synthetic air (1 O_2: 3.76 N_2) was created inside a sample cylinder (using partial pressure method) after evacuating for several hours. First, oxygen and then diluent were filled after determining the required partial pressure based on a target final value (10-20 atm). In the same time, the oven was used to raise the temperature of the evacuated combustion chamber. Mixtures of fuel and air were prepared by using the partial pressure method after first injecting a specified volume of fuel (Luer lock and syringe connection). Since the combustion chamber is maintained at high temperature, injected fuel evaporates completely because the partial pressure of the fuel was much below its vapor pressure. The combustion chamber temperature was monitored by using three thermocouples attached to different locations on the outside surface of the combustion chamber. The differences between the three thermocouple readings were less than 0.1°C. A second temperature controlled MKS E27 Baratron with a pressure

range of 0-0.13 atm was employed to increase the accuracy of determining the partial pressure of the injected fuel. Preheated oxidant was filled to achieve the target equivalence ratio and fuel/air mixtures were allowed to mix for roughly 10 minutes to ensure homogeneity.

APPENDIX B: MEASUREMENTS OF FLAME SPEED IN OXY-METHANE MIXTURES DILUTED WITH CO_2 USING LASER IGNITION

Ignition and flame propagation in CH_4/O_2 mixtures diluted with CO_2 are studied at room temperature and atmospheric pressure. The laminar burning velocity is evaluated for a range of equivalence ratios (Φ = 0.8-1.3, in steps of 0.1), and oxygen ratios, $D = O_2/(O_2+CO_2)$ (26-38% by volume). It was found that the LBV decreases by increasing the CO_2 proportionality. It was observed that the flame propagates towards the laser at a faster rate as the CO_2 proportionality increases, where it was not possible to obtain LBV due to the deviation from spherical flame shape. Current LBV data are in very good agreement with existing literature data. The premixed flame model from CHEMKIN PRO software and two mechanisms (GRI-Mech 3.0 and ARAMCO-Mech 1.3) are used to simulate the current experiment, providing reasonable agreement with the data. Additionally, a sensitivity analysis is carried out to understand the important reactions that influence the predicted flame speeds. Improvements to the GRI predictions are suggested after incorporating latest reaction rates from literature for key reactions. The work provided in Appendix B has been published in the Journal of Energy Resources Technology MAY 2016, Vol. 138 / 032201-1, and was presented in ASME Turbo Expo 2015, Montreal, QC, paper no: GT2015-43355.

APPENDIX B1. Introduction to Oxy-Methane Combustion with CO_2

Carbon capture and storage (CCS) is a promising technology for reducing CO_2 emission into the atmosphere by pumping it into a geological storage under the ground [197-199]. CO_2, which is a primary product of the combustion processes, promotes global warming due to the greenhouse gas effect that acts as a barrier to prevent the reflected waves from leaving the Earth. However, separating CO_2 from the emission gases is difficult in a normal combustion environment where fuel is burned with air. This is where oxy-fuel combustion holds great potential. Instead of burning

the fuel with air, pure oxygen can be utilized to convert each hydrogen and carbon atom to water and carbon dioxide. Ideally the products formed are CO_2 and H_2O, in which H_2O can be easily condensed out of the gas phase, and it is possible to store the remaining CO_2. It is possible to operate the flame in diffusion mode thereby eliminating concerns associated with combustion dynamics, which are typical concerns in lean premixed systems aimed at reducing NO_x. However, both the adiabatic temperature and the pressure during combustion process are extremely high where the combustion chamber might be affected (material safety issues).

Utilizing CO_2 from emission gases as a diluent reduces the temperature without adding another component in the combustion environment. The combustion of fuel in the presence of pure O_2 and CO_2 behaves differently because of the variation of transport and thermal properties in CO_2 and N_2 [200]. The laminar burning velocity is expected to be less than the value obtained by fuel-air mixtures because of the CO_2 participation in the chemical reaction [146]. It is understood that mixture properties and CO_2 participation rates are functions of CO_2 proportionality in the mixture and the adiabatic temperature. The dissociation of CO_2 increases with temperature, which enhances the chemical participation and decreases the free radicals. In this study, the laminar burning velocity has been investigated at room temperature and atmospheric pressure for different carbon dioxide proportionalities.

There are some studies in the literature regarding CO_2 diluted methane combustion using a variety of experimental techniques. Konnov and Dyakov [201] utilized a premixed planar flames stabilized on flat burners for studying the flame structure and the laminar burning velocities. Mazas *et al.* [202] measured flame speeds using a laminar conical premixed flames over a range of Φ at initial T = 373 K. Hu *et al.* [200] used a Bunsen burner method to derive laminar flame speeds of $CH_4/O_2/CO_2$ mixtures at 300 K and 1 atm. Xie *et al.* [146] studied the laminar burning velocity of

CH_4, O_2 and low proportionality of CO_2 in a spherical chamber. They obtained faster LBV values compared with the GRI-Mech 3.0 [34] mechanism predictions, and the difference increased with the reduction of CO_2 proportionalities.

The required energy for bond dissociation (BDE) of nitrogen and carbon dioxide are 945 and 531 KJ/mol respectively [146]. Heil *et al.* [203] and Liu *et al.* [204] studied the importance of CO_2 chemical effects on the combustion process experimentally and numerically respectively. They suggested that with the addition of CO_2, the reverse reaction of $CO+OH \leftrightarrow CO_2+H$ is favored, thereby reducing the availability of H radicals, which slows the crucial branching reaction $H+O_2 \leftrightarrow O+OH$. Namely, a reduction in combustion process is noticed because both CO_2 and O_2 are competing for the hydrogen radical. Heil *et al.* [203] tested this hypothesis by using a flameless combustor, which reduced the effect of molar heat capacity and thermal radiation on the combustion process. They used methane and hydrogen as fuel and found that the effects of CO_2 proportionality are less with hydrogen fuel because the H radicals are more available [203]. Also, it was noted that CO_2 has a significant impact on the chemical reaction but increasing O_2 concentration of the initial mixture counters that impact. Liu *et al.* [204] compared the combustion of methane by using CO_2 and a fictitious molecule, in simulations, that has the same thermodynamic properties but does not react during combustion. The obtained LBV with fictitious CO_2 is faster, which confirmed the chemical participation of CO_2 having a reduction in LBV.

Hinton and Stone [55] examined the effect of CO_2 proportionality on methane combustion with air at different initial conditions and equivalence ratios. LBV and flame stability studies were carried out in a constant volume combustion chamber. They found that the location of maximum LBV is shifting to a leaner mixture from $\Phi = 1$ as the CO_2 proportionality increases. The effect of

gravity on combustion process in CO_2 mixture is negligible for a flame faster than 15 cm/s [55, 142]. In addition, the radiation effects are significant for a flame slower than 15 cm/s [142, 200].

Di Benedetto *et al.* [205] determined the flammability limits of methane combustion with O_2 and CO_2 in a cylindrical vessel. They found that a transition from a normal combustion to a novel mode called: "combustion-induced rapid phase" is achieved by increasing the O_2 proportionality. De Persis *et al.* [206] reviewed different CO_2 separation techniques like absorption and membrane processes. Burning fuels with oxygen-enriched air is considered a valuable technology for low CO_2 capture process.

The current study represents the first CH_4/O_2 flame studies using laser ignition in a highly CO_2 diluted environment. The three CO_2 proportionalities are chosen such that the LBV values are fast enough to neglect the buoyancy and radiation effects. Also, these selected proportionalities provide a reasonable adiabatic flame temperature for gas turbine application. The most advanced gas turbines work at 1600 °C for turbine inlet temperature (TIT). Increasing the oxygen proportionality requires advanced cooling methods to deal with the increase in product temperature. In this study the mixture equivalence ratio range is changed from 0.8 to 1.3 in steps of 0.1. A wide range of equivalence ratios is chosen to compare and validate existing chemical kinetic mechanisms for oxy-methane combustion with high proportionality of CO_2. Also, the method of studying $CH_4/O_2/CO_2$ mixtures using laser ignition could aid the development of future supercritical CO_2 cycle utilizing oxy-methane combustion [207]. The ultimate goal of the long-term study is to conduct experiments at high initial pressure and temperature to reflect the gas turbine application.

APPENDIX B2. Combustion Model

In this section, the LBV has been calculated by using the Metghalchi and Keck [124, 141] Thermodynamic model. A detailed discussion on LBV theory and thermodynamic models is given in Chapter 3. The burned and unburned mixture properties are found by using NASA polynomials based on the highest thirteen species (H_2, H, O_2, O, OH, CO_2, CO, H_2O, HO_2, H_2O_2, CH_4, HCO, CH_2O) to reflect reliable values. NASA polynomials coefficients are taken from the GRI-Mech 3.0 [34] thermo file.

APPENDIX B3. Experimental Setup

Details of UCF spherical combustion chamber facility including fuel/oxidizer mixture preparation, ignition systems, pressure measurements, shadowgraph imaging system, and LABVIEW software are provided in Appendix A.

APPENDIX B4. Properties of Tested Mixtures

Since the combustion properties are directly related to the mixture proportionalities, several numerical predictions were conducted before proceeding with the LBV experiments. The proportionality, D (oxygen ratio), between O_2 and CO_2 is defined as $D = O_2/(O_2 + CO_2)$, all quantities in percentage by volume. In this work three proportionalities D = 0.38, 0.35, and 0.32 for six Φ's were used. Only at stoichiometric conditions (Φ = 1.0), an additional two proportionalities D = 0.29 and 0.26 were used to illustrate the reduction in laminar burning velocity. Even though the O_2 to CO_2 proportionalities is larger than the proportionality of O_2 to N_2 in experimental air, the current LBV values are slower (than N_2 diluent) due to the reasons discussed in the results section.

Heat capacity at constant pressure is defined as the amount of energy required to raise the temperature of a unit mass by one degree in unconstrained environment [208]. For a unit energy, the variation of gas temperature and heat capacity are inversely proportional. This property is used for the iterative solution of the energy equation, and directly related to the enthalpy and internal energy of the mixture. Except for monatomic gases, heat capacity increases with temperature for all gases and results in a lower temperature increase as the gas temperature increases [208]. This is attributed to larger amount of the input energy transfers to gas motions (translation, rotation, and vibration) rather than raising its temperature. Unfortunately, no specific law describes the behavior of C_p with respect to the temperature. For example, CO_2 has a higher variation of heat capacity with temperature relative to O_2 and N_2.

In this section, The author evaluated properties of the tested mixtures by utilizing Cantera [169] equilibrium code and ARAMCO-Mech 1.3 [56]. Table B1 shows the heat capacity for the tested gases at 295 K and atmospheric pressure. It is obvious that the heat capacity of methane is much bigger than the other gases. Also, the Carbon dioxide has a lower heat capacity in comparison with Nitrogen.

Table B1. Heat capacity for the tested gases at 295 [K] and 1 [atm].

	CH_4	**O_2**	**N_2**	**CO_2**
Heat capacity (C_p) [J/Kg.K]	2217.5	917.59	1039.6	840.58

Since mixture properties depend on species mole fractions, the author decided to evaluate the properties as a function of equivalence ratio. Figure B1 presents the specific heat for the mixtures with several oxygen ratios (D) versus the equivalence ratio. Also, the specific capacity of CH_4/air mixture is shown in green color for comparison. The specific heat increases as the equivalence ratio increases because of the higher value associated with the fuel molecule as shown in Table B1

Similarly, the specific heat decreases as the oxygen ratio decreases due to the same reason. In general, the heat capacity of a stoichiometric mixture at D = 35% decreased by 11.7% compared with CH_4/air. It is worth to mention that the trend in Figure B1 flips is the molar heat capacity is used because of the variation in species molecular weight.

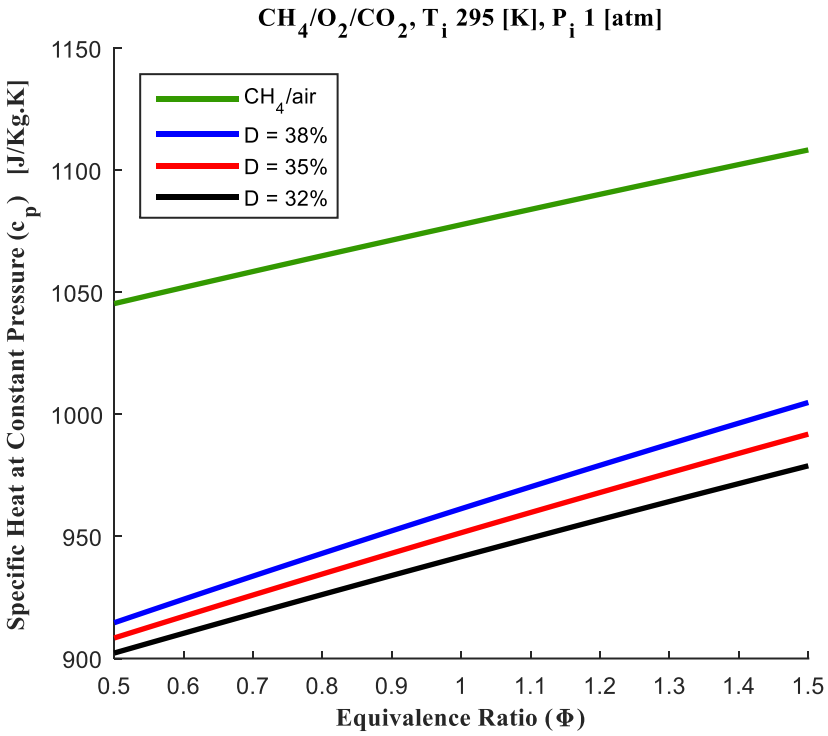

Figure B1. Heat capacity of Methane mixture diluted with several O_2 proportionalities.

Figure B2 presents Lewis number for mixtures diluted with CO_2. Overall, Lewis number decreases as the O_2 ratio decreases. However, the reduction of Lewis number for lean and rich mixtures affect the diffusional-thermal instability in opposite trends. For rich mixtures, decreasing O_2 ratio gave Lewis number closer to 1 (ideal condition). On the other hand, lean mixtures deviate more as the oxygen ratio decreases and promote diffusional-thermal instability. To conclude, diluting the mixture with CO_2 in the tested proportionality reduced the hydrodynamic instability, however, promoted the diffusional-thermal instability with lean mixtures.

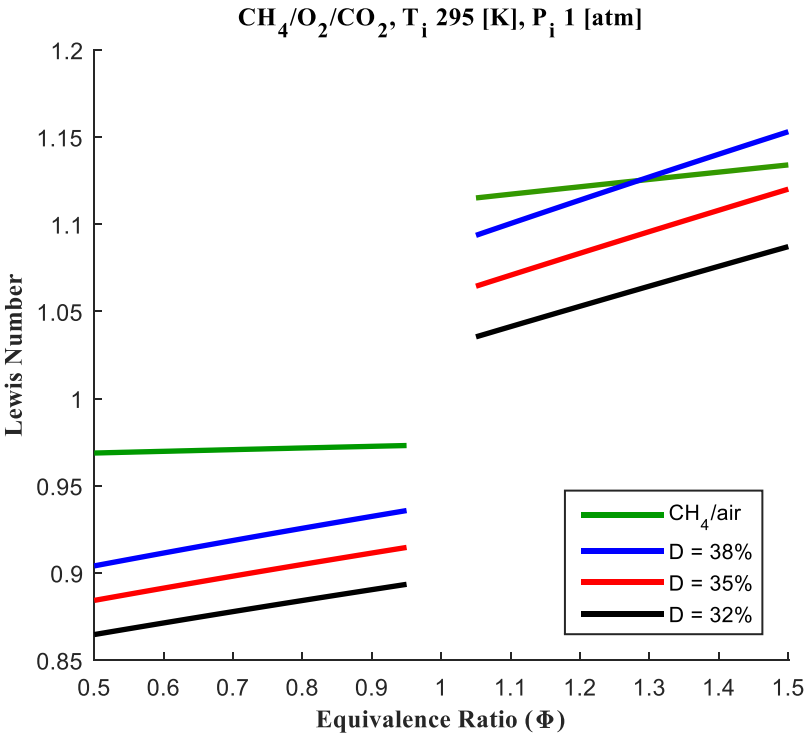

Figure B2. Lewis number comparison for Methane mixture diluted with several O2 proportionalities

APPENDIX B5. Results and Discussion

The LBV results presented in this work represent the average of at least 3 experiments conducted at every experimental condition to minimize random errors. The effect of CO_2 on the laminar burning velocity at an equivalence ratio of 1 for various oxygen ratio D is presented first. This result is presented in Figure B3 (pressure) and Figure B4 (LBV), where the expected behavior was noticed as a reduction in the LBV as the CO_2 proportionalities increases. The maximum pressure value decreases and location of maximum increases, respectively, with the reduction of O_2 proportionalities. This reasonable trend is due to the changes in thermal and transport mixture properties in addition to the chemical participation of CO_2 as explained previously by refs. [203, 204]. A nonlinear trend is noticed for the LBV with respect to O_2 ratio. Note that the LBV for oxygen ratio D = 26% should be neglected because of both buoyancy and radiation effects (i.e.,

LBV<15 cm/s), the result is shown in Figure B4 (solid triangle) for comparison only. Hence the three highest proportionalities are chosen for detailed analysis to compare with literature data and model predictions.

The pressure traces are shown from the beginning of combustion until the time where maximum value is reached. The maximum pressure for D = 38% is 8.1 atm after 44 ms from the ignition timing, similarly the maximum pressure for D = 26% is 5 atm after 256 ms. Even though at D = 26%, the CO_2 ratio in the mixture is still less than the N_2 ratio in air, the reaction is too slow for combustion application. The D ratio of 38% provides LBV values similar to the one obtained in synthetic air (O_2+3.76N_2) as oxidizer.

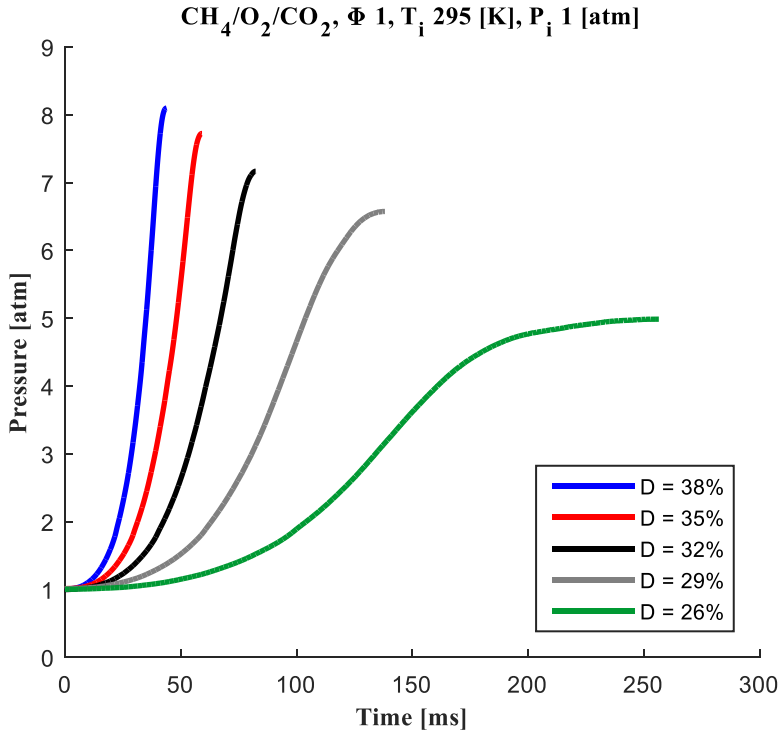

Figure B3. Combustion pressure traces at an equivalence ratio of 1 and different oxygen ratios.

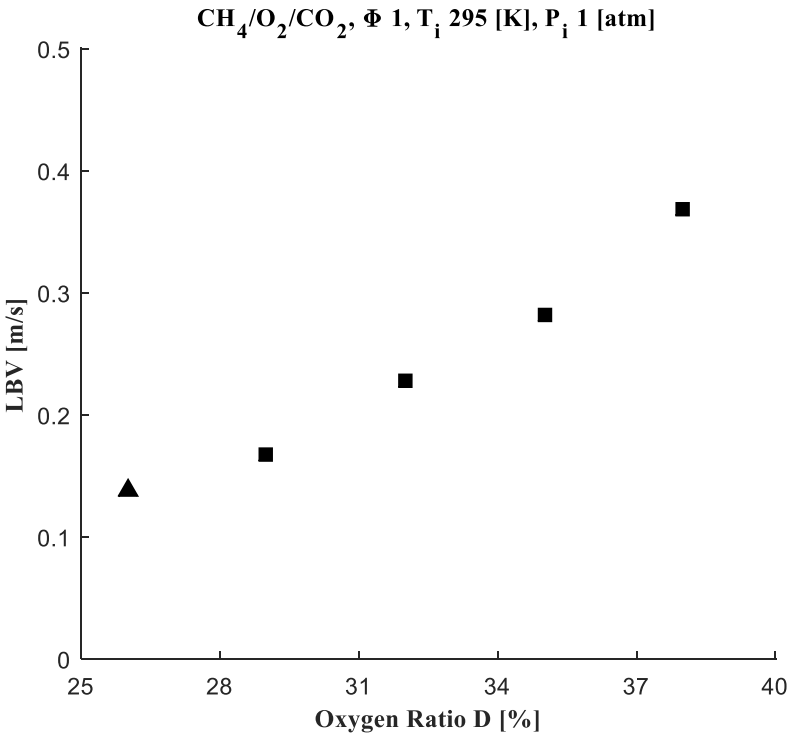

Figure B4. Measured LBV at an equivalence ratio of 1 as a function of oxygen ratio.

Since the TIT is a function of adiabatic flame temperature, Cantera equilibrium code [169] is used to calculate the adiabatic flame temperature as a function of equivalence ratio and oxygen ratio in Figure B5. Also, the trend of methane combustion in air is shown for comparison. The flame temperature increases as the O_2 concentration increases, also the maximum temperature occurs for a slight rich mixture. The location of the maximum temperature is shifting towards a lower equivalence ratio as the O_2 proportionality decreases. The O_2 ratio D = 32% (highest CO_2 proportionality) gives a similar adiabatic flame temperature trend as the one obtained by burning CH_4 in air. However, a wider concave down was noticed for all mixtures diluted with CO_2. A similar observation was also found for the LBV due to the its direct relation with adiabatic flame temperature.

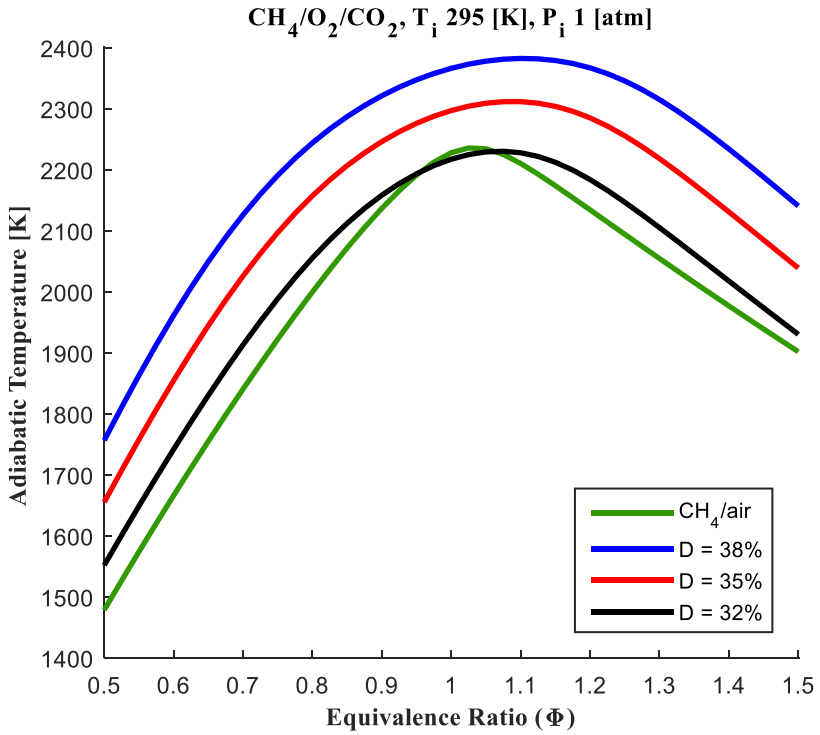

Figure B5. The adiabatic flame temperature versus equivalence ratio at different O2 ratios. Also, the result of CH4/air mixture is shown.

After obtaining the range of CO_2 proportionalities that provides acceptable values for LBV and adiabatic flame temperature, several experiments were conducted for the highest three D values at different equivalence ratios. Since the LBV is a function of mixture composition (equivalence ratio), the range of (Φ = 0.8-1.3, in steps of 0.1) is chosen to provide LBV faster than 15 cm/s for the lowest O2 ratio. At these chosen proportionalities, both gravity and radiation effect are very limited [142]. Figure B6 illustrates the pressure traces of D = 35% for the range of equivalence ratios. The fastest combustion occurred for an equivalence ratio of 1, which was nearly identical to the trace at an equivalence ratio of 1.1. This trend is noticed for two proportionalities, where at D = 38% the maximum burning velocity was at an equivalence ratio of 1.1.

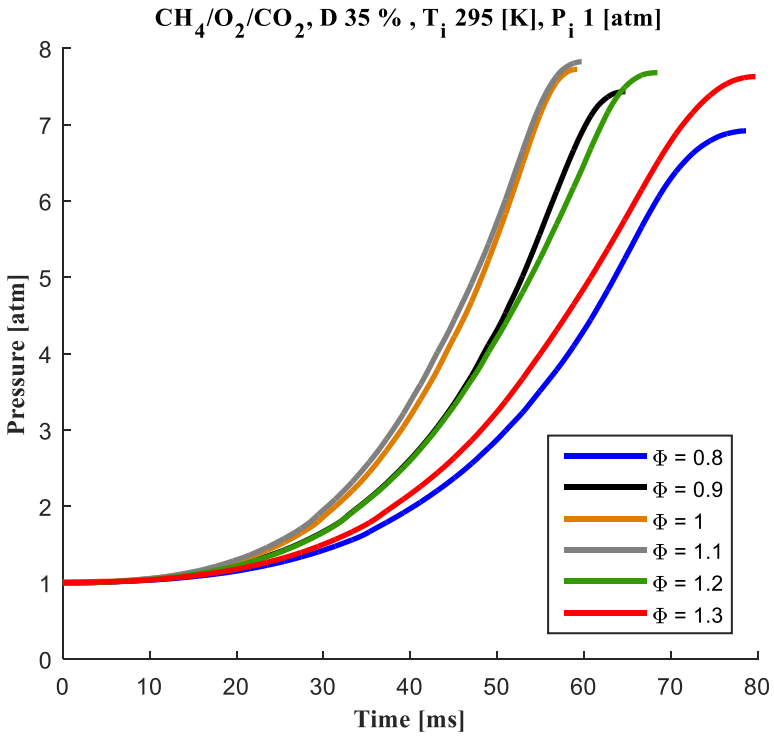

Figure B6. Combustion pressure traces at D = 35% and different equivalence ratios.

Figure B7 presents the LBV as a function of equivalence ratio for the three O_2 proportionalities. The classical LBV trend is found where the maximum burning velocity occurs near the stoichiometric condition and decreases for lean and rich mixtures. In the tested equivalence ratio

range (0.8-1.3), the effect of equivalence ratio on LBV is relatively small in comparison to the effect of CO_2 addition. The LBV decreases from 27.68 to 22.4 cm/s by lowering Φ from 1 to 0.8 for the O_2 ratio 35%, while the LBV at equivalence ratio 0.8 increases from 22.4 to 30.4 cm/s by increasing the oxygen ratio 3%. As expected the LBV value increases with increasing D values (due to the chemical effect of CO_2).

The shift of maximum LBV location to a leaner equivalence ratio when the D value decreased was noticed earlier by Hinton and Stone [55] during CH_4 combustion in air diluted with various CO_2 proportionalities. The simulation of adiabatic temperatures (as presented in Figure B5) using CANTERA [169] indicates the same trend, i.e., there is a slight shift of maximum adiabatic temperature towards Φ = 1 as the D value is decreased. Though this reason alone cannot explain the absolute changes in shift observed in experiments (Figure B7) differential diffusion, changes in Lewis number, CO_2 participation in chemical reactions and its collisional efficiency [209] (and its dependence on temperature) can also contribute to the difference.

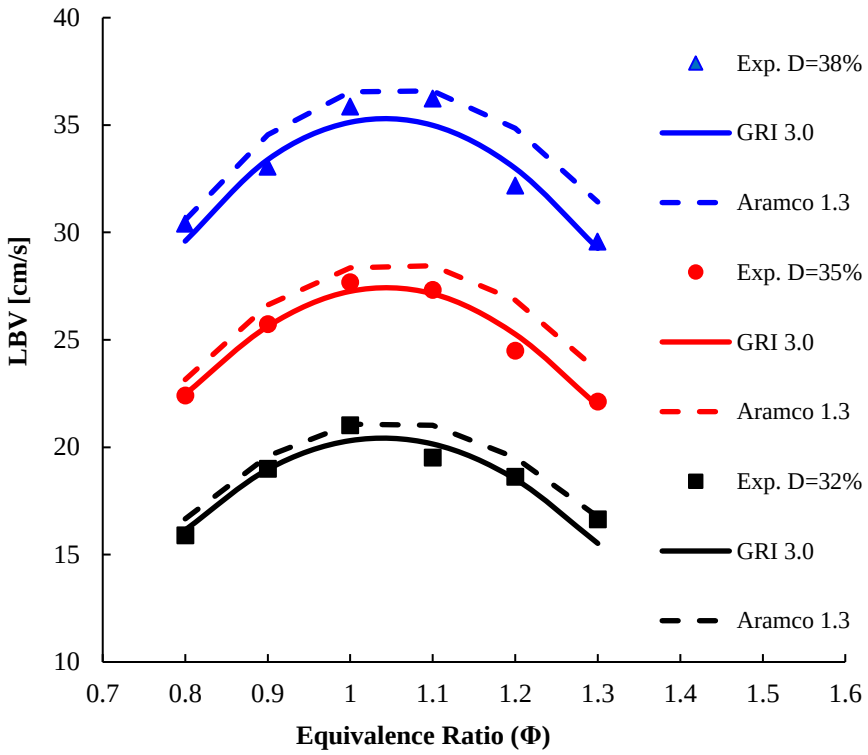

Figure B7. Measured LBV vs equivalence ratio at different O_2 ratios. Predictions of GRI-Mech 3.0 [34] and ARAMCO-Mech 1.3 [56] are also shown to be in good agreement with current data.

Figure B8 compares the laminar burning velocity with previous experiments for D = 35%. There is good agreement with past data except near the rich tails (ϕ = 1.2 and 1.3) where the LBV is slightly slower in current experiments. The current data is almost identical to the values obtained by Xie *et al.* [146] in the range of ϕ = 0.8-1.1; that is mainly because Xie utilized a spherical combustion approach (constant pressure), unlike Hu *et al.* and Konnov which utilize Bunsen burner and flat burners, respectively in their studies.

The LBV data obtained by Hu *et al.* is slightly over estimated compared to the other experiments. Egolfopoulos *et al.* [142] highlighted in a very recent article that none of the methods to obtain the flame speed data is without uncertainties, and the uncertainty of a stagnation flame

experiment is bigger than spherically expanding flame at some conditions. Moreover, it should be noted that each method has its own limitations.

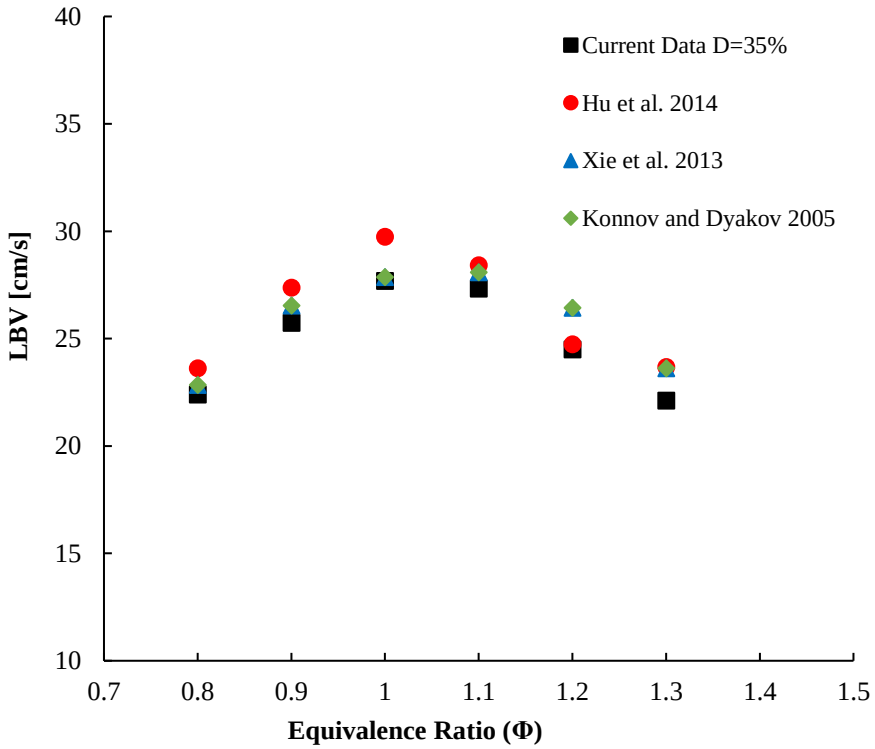

Figure B8. Current LBV data for mixture with D = 35% at different equivalence ratios with those from Xie et al.[146], Hu et al.[200], and Konnov and Dyakov [201].

Figure B9 shows a similar comparison between current data (D = 32%) and those from Konnov and Dyakov [201] at D = 31.5%. It is clear in both experiments the maximum LBV occurs at Φ = 1 and LBV profiles have similar trends, however, the difference in absolute values of LBV is due to the difference in oxygen ratio, which has a significant effect as illustrated in Figure B7.

An uncertainty analysis was carried out for the case of Φ = 1 and D = 0.35%; Table B2 provides the result of each parameter and the total uncertainty in current experiments is around 6.14%. Note that this total uncertainty includes contributions from random error (< 3%), which was determined by conducting multiple experiments at each experimental point.

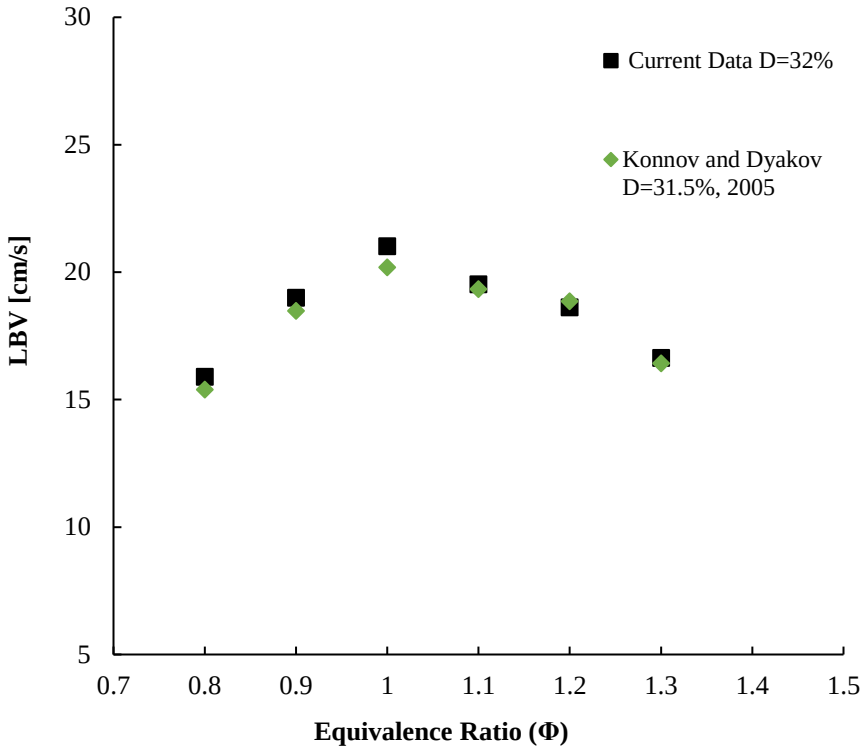

Figure B9. Current LBV data for mixture with D = 32% at different equivalence ratios with those from Konnov and Dyakov [201].

Table B2. Uncertainty analysis for CH4, O2 and CO2 mixture with Φ= 1 and D = 35%.

Uncertainty Source	**CH_4, O_2, & CO_2 (Φ= 1)**
Initial pressure	(+-) 0.04%
Initial temperature	(+-) 1.48%
Maximum pressure value	(-) 0.55%
LBV curve fitting	(+-) 4.19%
Mixture composition / phi	(+-) 3.25%
Smoothing pressure trace	(-) 0.738%
Random error for 3 experiments	(+-) 2.53%
Overall uncertainty	6.14%

To capture the flame shape and development, the combustion process was visualized by utilizing a high-speed camera. Figure B10 presents flame propagation for an extreme CO_2 case of D = 26% (Φ = 1) which has been neglected in the LBV results (presented in Figure B7). Two-stage toroidal flame propagation is noticed in most experiments. In the first stage the flame

propagates at a faster rate toward the incoming laser. After developing the toroidal shape, the flame propagates in the same rate for all directions. The proposed explanation of this toroidal behavior is that the gases before the focal point absorb some of the incident laser beam energy which results in a faster flame propagation toward the incoming laser [28, 210]. Other reasons have been given earlier in section 2.1. Additionally, it was observed that propagation toward the laser is consistently faster with higher CO2 proportionalities. To the authors' knowledge, this has not been reported earlier and can be seen clearly by comparing vertical flame propagation in Figure B10 and Figure B11.

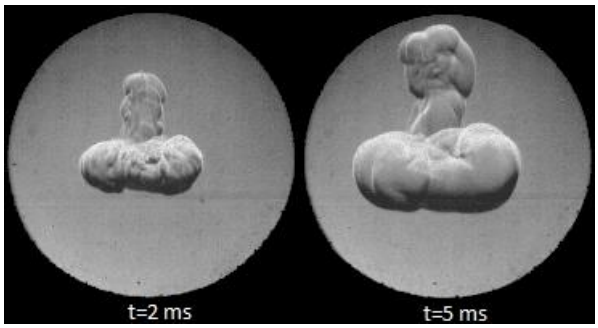

Figure B10. Flame propagation for CH_4, O_2 and CO_2 at an equivalence ratio of 1 and oxygen ratio 26%. Laser is incident from top. Window diameter is 47 mm. note that LBV data is neglected in this case due to nonspherical flame.

Figure B11 shows flame propagation for mixtures with oxygen ratio 38% and two equivalence ratios. Vertical flame propagation in Figure B10 is faster compared to other directions, whereas flame moves nearly spherical in Figure B11 Keep in mind that the early part of combustion process shown in the figures is not utilized for the LBV calculation because minimal variation of pressure trace as discussed in section 3.1. It is believed that after 7 ms, the flame tends toward a spherical shape and the constant volume analysis will be valid. The extreme CO_2 conditions ($D \leq 26\%$) require further study and comparisons with spark-ignition systems to see if the measured LBV values will be different for these two ignition methods.

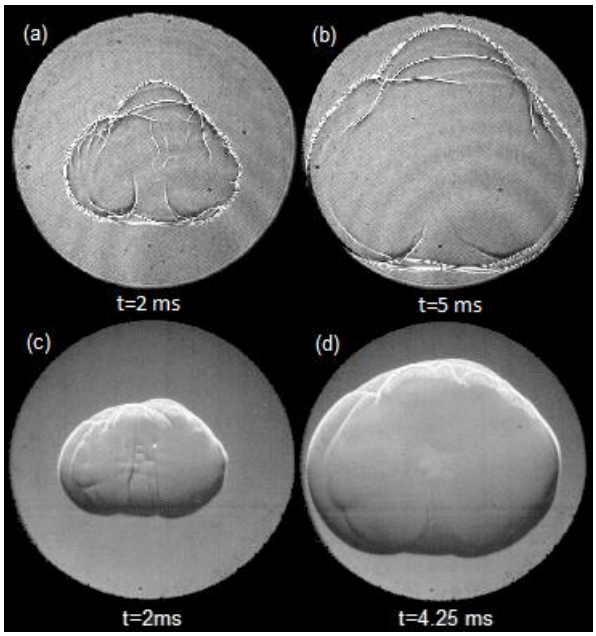

Figure B11. Flame propagation for CH_4, O_2, and CO_2 and D = 38%, at an equivalence ratio of 0.9 ((a) and (b)), and 1.1 ((c) and (d)). Laser is incident from top. Window diameter is 50.8 [mm].

The two-stage propagation is consistent with results seen by Srivastava *et al.* [28, 210]. Farrell and co-workers [123] reported that laser ignition gave rise to a highly turbulent flame kernel, however, for very lean mixtures, the turbulence dissipated before propagation and that the flame fronts remained smooth (unlike in the case of near-stoichiometric mixtures). Those perturbations had negligible effect on the surface area of the flame front and burning rate acceleration was not observed. Srivastava *et al.* [28, 210] observed a toroidal shape of the kernel, which grew before propagation, however, the shape of the kernel was structurally identical and did not vary with equivalence ratios. Initially the front lob of the flame propagated towards the incoming laser beam was also observed by [88, 89, 211].

The CHEMKIN PRO [33] predicted LBV values using the GRI-Mech 3.0 [34] and ARAMCO-Mech 1.3 [56] mechanisms are shown in Figure B7. The current LBV data are in between the two numerical predictions. In general, the ARAMCO-Mech 1.3 provides faster LBV values, while the

GRI-Mech 3.0 predictions are slightly slower than the current data in the stoichiometric region. The performance of the two mechanisms is considered to be reasonable, though the agreement between current data and GRI-Mech 3.0 is slightly better than that with ARAMCO-Mech 1.3. Note that the Soret diffusion effects were shown to be important in LBV simulations in recent publications [212-215] and is considered in the CHEMKIN PRO models presented in this paper to reflect the importance of heat diffusion for low molecular-weight species. Neglecting the Soret effect (results not shown here), the predictions resulted in faster LBVs due to decreased diffusion of radicals from the flame zone.

APPENDIX B6. Sensitivity Analysis

In order to better understand the differences between GRI-Mech 3.0 predictions and current data, a sensitivity analysis was performed using the CHEMKIN PRO sensitivity tool [33]. This tool shows a quantitative dependence of model parameters such as temperature, reactions, species fraction, etc. on CHEMKIN PRO numerical solution. The analysis was performed for $CH_4/CO_2/O_2$ mixture at different CO_2 concentrations at $\Phi = 1$, 1 atm, and an unburned gas temperature of 295 K. Figure B12 shows the normalized sensitivity for the top 10 most sensitive reactions that affects CO_2 concentrations during combustion.

As expected, the chain branching reaction of $H+O_2 \leftrightarrow O+OH$ rate is important in most combustion applications. It can be noted by comparing the sensitivity coefficient of this reaction in Figure B12, it increases relative to the other reactions by increasing the CO_2 fraction (i.e., reducing D). While, $OH+CO \leftrightarrow H+CO_2$ is another sensitive reaction for which the sensitivity coefficient decreases by increasing CO_2 fraction. Figure B13 provides the simulated concentrations of radicals (H, O, and OH). Increasing CO_2 mole fraction (from D = 38% to 32%)

reduces the available radicals and reflects in the reduction in reaction rates and thereby LBV values.

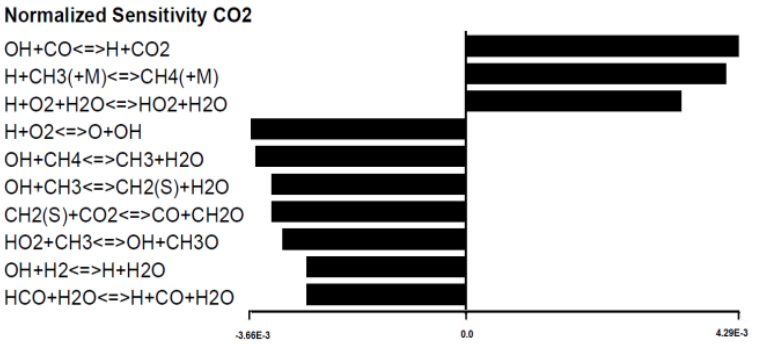

CO_2 SENSITIVITY FOR D = 38%, T = 1140 K

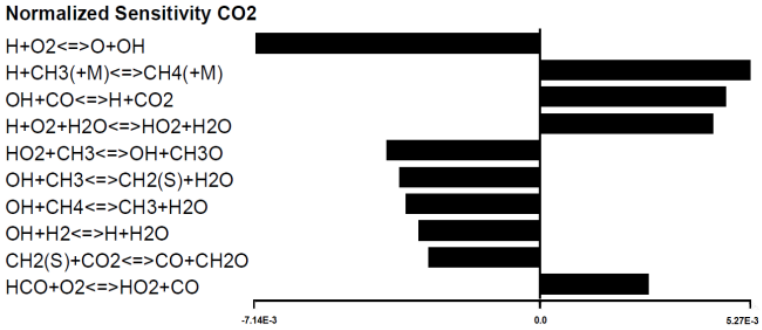

CO_2 SENSITIVITY FOR D = 35%, T = 1140 K

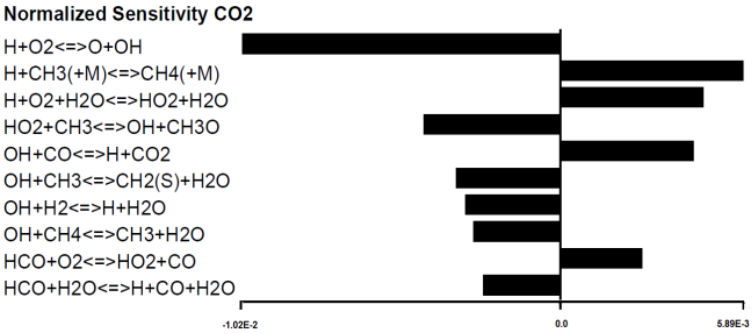

CO_2 SENSITIVITY FOR D = 32%, T = 1140 K

Figure B12. Sensitivity analysis for stochiometric mixtures and several oxygen ratios.

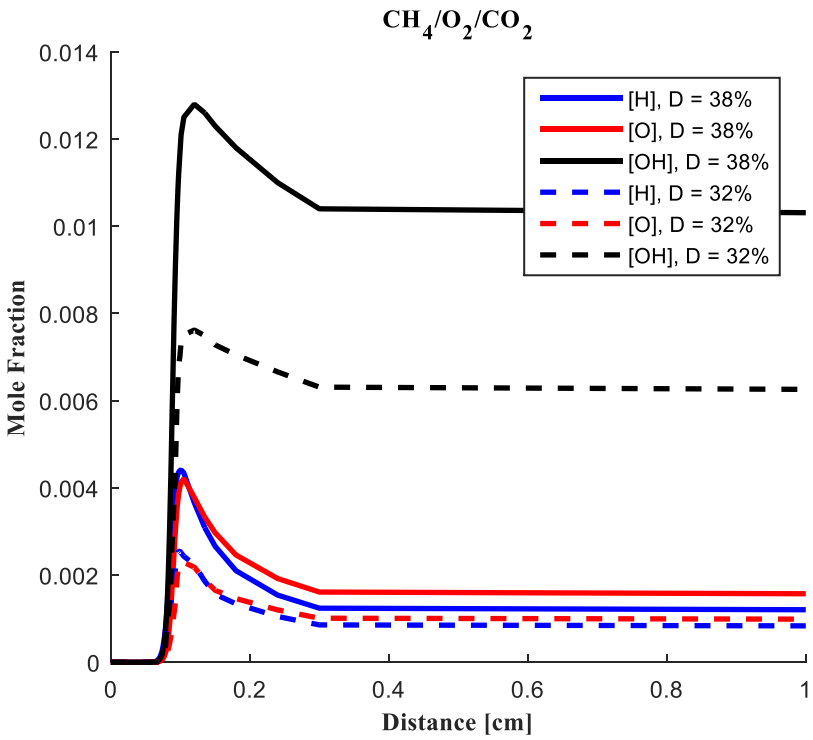

Figure B13. OH, O and H radicals mole fraction at different CO_2 fraction of $CH_4/CO_2/O_2$ mixture, Φ = 1. SOLID LINES-D = 38%, Dashed LINES-D = 32%.

There have been several experimental and theoretical studies (see Baulch *et al.* [216]) of key reactions shown in Figure B12 since the creation of GRI-Mech 3.0. Also, there were thermochemistry data updates for two important species, OH and HO_2 (see Goos *et al.* [217]) based on experiments. Influence of thermochemistry on predicted LBV values were probed for D = 32% by using the GRI 3.0 mechanism and updated thermochemistry from Goos *et al.* [217]. The obtained LBV by using the modified thermodynamic data is faster by 2% for a lean mixture at Φ = 0.8, while it remains unchanged for slightly rich mixture.

For the most sensitive $H+O_2 \leftrightarrow O+OH$ reaction, the rate used in the GRI-Mech 3.0 is very good when compared to recent measurements for that reaction (see [209]). Hence the effect of this reaction on predicted LBV was not examined. However, the effects of changing reaction rates are studied for the other three dominant reactions $CO+OH \leftrightarrow CO_2+H$, $HCO+O_2 \leftrightarrow HO_2+CO$, and

$OH+H_2 \leftrightarrow H+H_2O$ from the sensitivity analysis of CO_2. For the $CO+OH \leftrightarrow CO_2+H$ reaction, the rate constant was changed with the Baulch *et al.* recommended rate [216, 218]; the obtained LBV values over predicted experiments especially for lean mixture. The reaction rates for the $HCO+O_2 \leftrightarrow HO_2+CO$, and $OH+H_2 \leftrightarrow H+H_2O$ reactions were updated with values taken from Colberg and Friedrichs [219] and Krasnoperov and Michael [220], respectively. A slight reduction and increase in LBV was noticed for lean and rich mixtures, respectively. A better agreement was achieved with the current date (see Figure B14), where the maximum difference with predictions of updated GRI 3.0-Mech and experiments is only about 0.68 cm/s at $\Phi = 1$ (D = 32%).

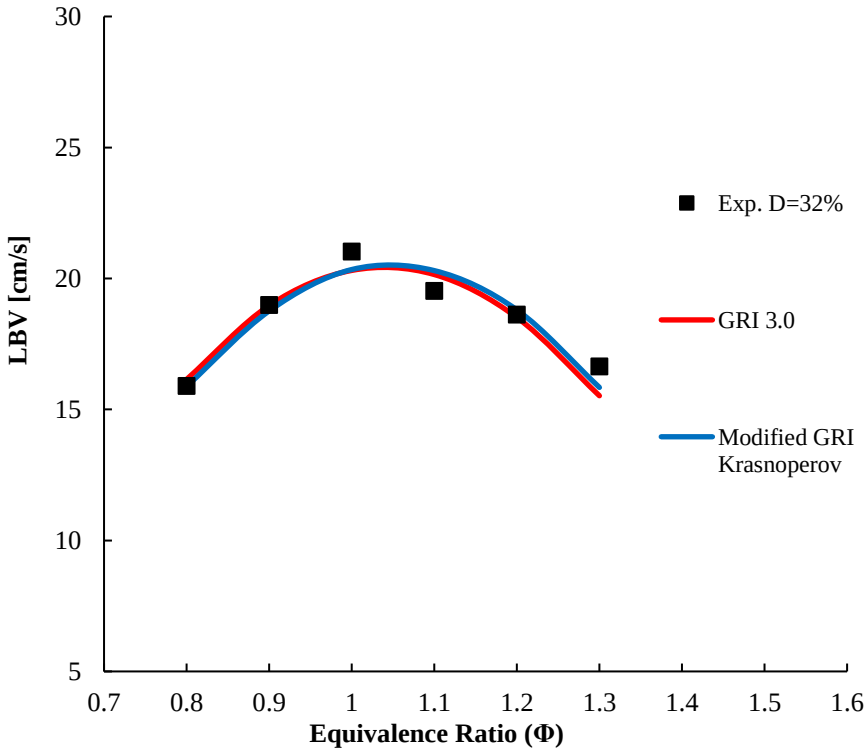

Figure B14. Comparison of current data with GRI-Mech 3.0 [34] predections (modified and un unmodificed mechanisms, see text for details).

The GRI-Mech 3.0 mechanism [34] is one of the most widely used CH_4 mechanism in the literature because it was optimized for a wide range of pressure, temperature and equivalence ratio [221] against experimental data. However, it was not validated against CO_2 diluted mixtures and

the mechanism has not been updated since 1999. The above calculations indicate that the GRI 3.0 mechanism should be revisited before applying to CH_4/O_2 combustion diluted with CO_2. The lack of GRI-Mech 3.0 performance was also noted by the current author for syngas combustion in highly diluted CO_2 mixtures [209]. As shown in this work (Figure B14) it is possible to improve the predictions of the GRI-Mech 3.0 (e.g., by using latest knowledge on key reactions) for use with CO_2 diluted mixtures. However, a complete re-optimization study incorporating updates to all dominant reactions is outside the scope of current work.

APPENDIX B7. Conclusion of Oxy-Methane Combustion with CO_2

Ignition and flame propagation in CH_4/O_2 mixtures diluted with CO_2 was conducted for a range of equivalence ratios (Φ = 0.8-1.3), and oxygen ratios, (D = 26-38% by volume) at 1 atm and room temperature. The laminar burning velocity (LBV) was obtained in a spherical combustion chamber using pressure during the combustion process. The LBV decreases dramatically by increasing the CO_2 fraction, for example, a 54% reduction in LBV was achieved by increasing CO_2 volume ratio by 9% at same equivalence ratio. The LBV profile has the classical LBV vs equivalence ratio shape. The maximum LBV occurs at slightly richer stoichiometric ratio and LBV values fall away for leaner and richer mixtures. The current data is in good agreement with previous experiments from literature. The predictions by two mechanisms (GRI-Mech 3.0 [34] and ARAMCO-Mech 1.3 [56]) agreed reasonably well with the experimental data. Current experiments will be extended to higher pressures, temperatures, and wider mixture ratios in our future work. In addition, a spark vs laser ignition experiment will be conducted to see the effectiveness of the LBV model in the presence of extremely high CO_2 dilutions ($D \leq 26\%$).

APPENDIX C: ADDITIONAL FIGURES FOR THE PRECHAMBER STUDY

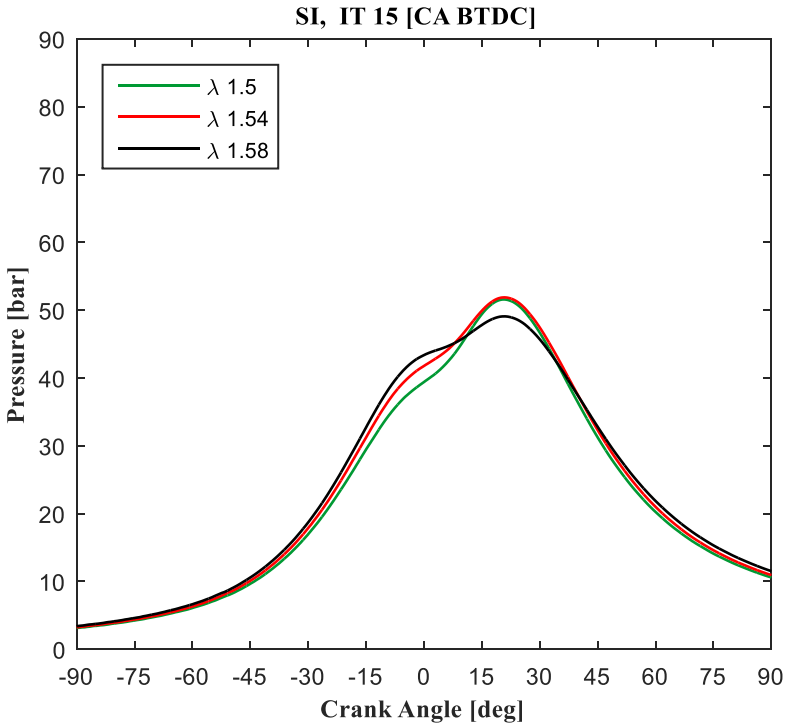

Figure C1. Pressure traces of natural gas reciprocating engine operated with spark ignition at a fixed ignition timing 15 CA BTDC and several air to fuel ratios.

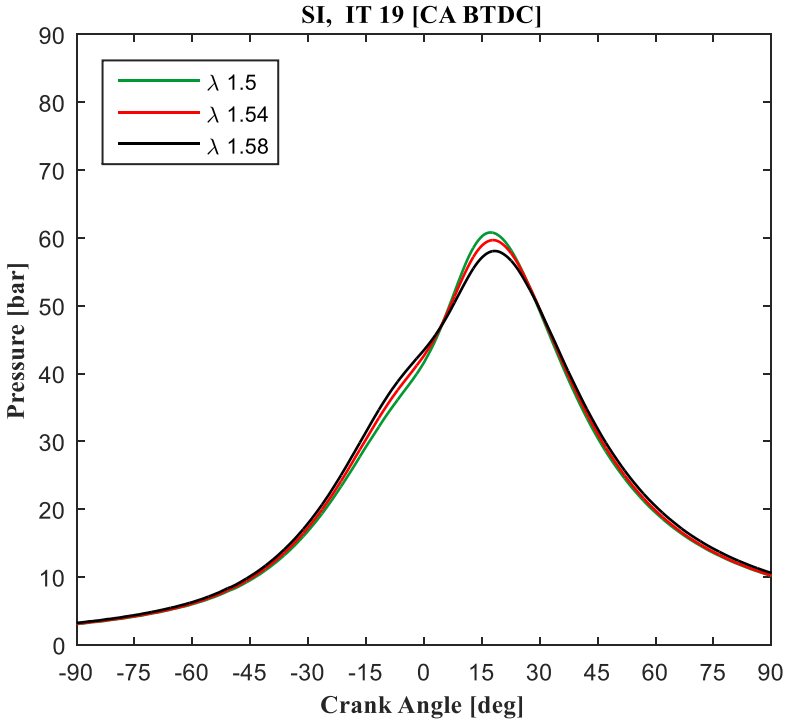

Figure C2. Pressure traces of natural gas reciprocating engine operated with spark ignition at a fixed ignition timing 19 CA BTDC and several air to fuel ratios.

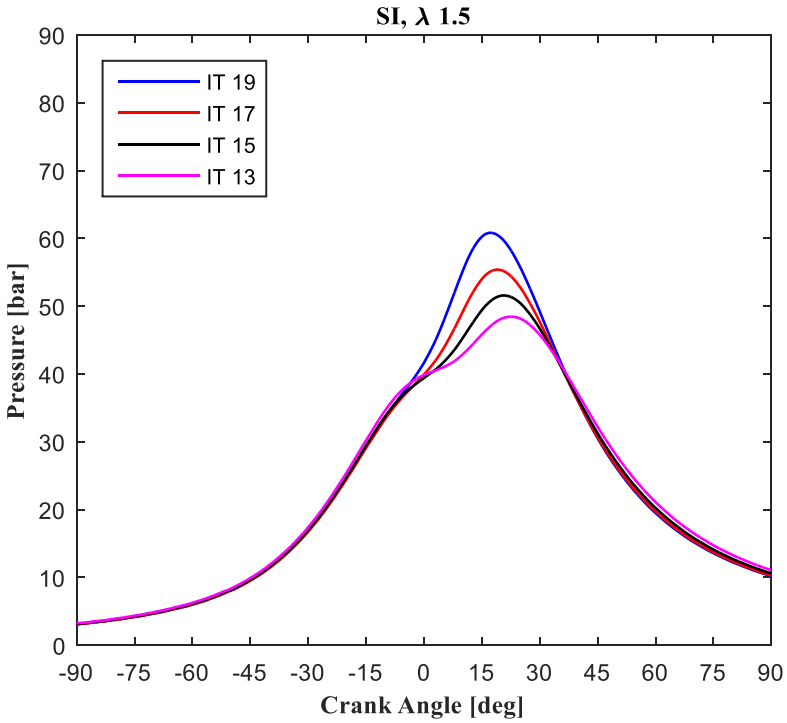

Figure C3. Pressure traces of natural gas reciprocating engine operated with spark ignition at a fixed air to fuel ratios λ = 1.5 and several ignition timings in CA BTDC.

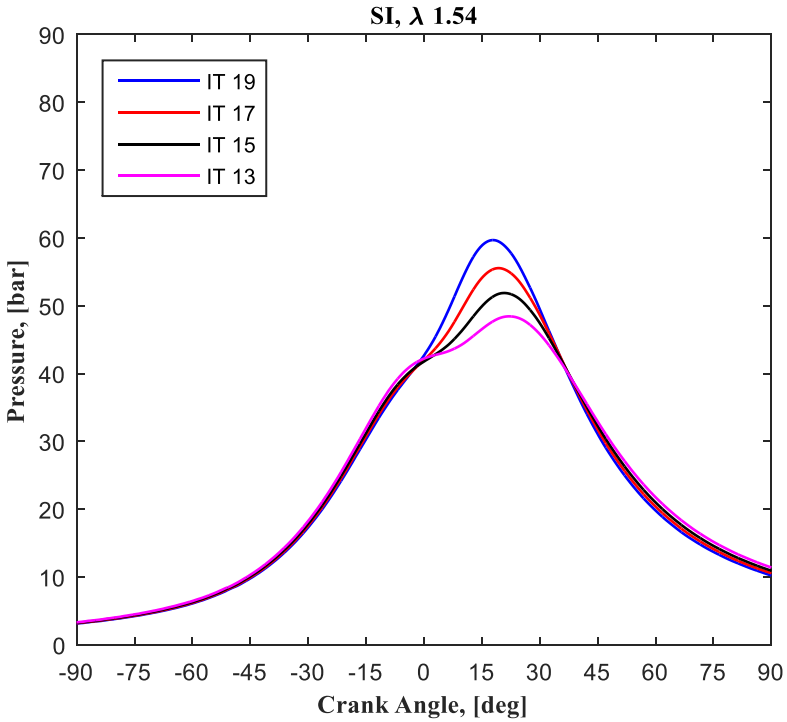

Figure C4. Pressure traces of natural gas reciprocating engine operated with spark ignition at a fixed air to fuel ratios λ = 1.54 and several ignition timings in CA BTDC.

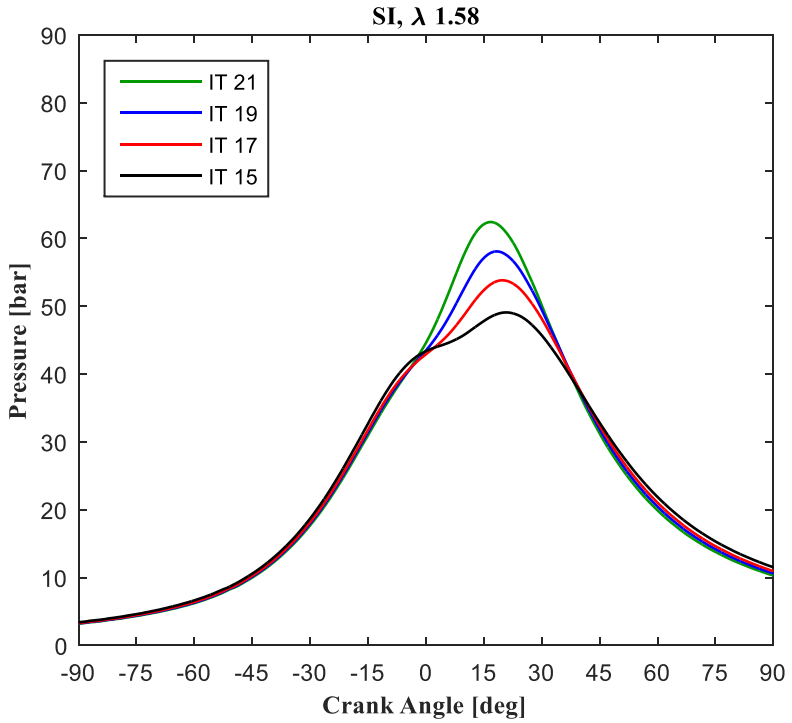

Figure C5. Pressure traces of natural gas reciprocating engine operated with spark ignition at a fixed air to fuel ratios λ = 1.58 and several ignition timings in CA BTDC.

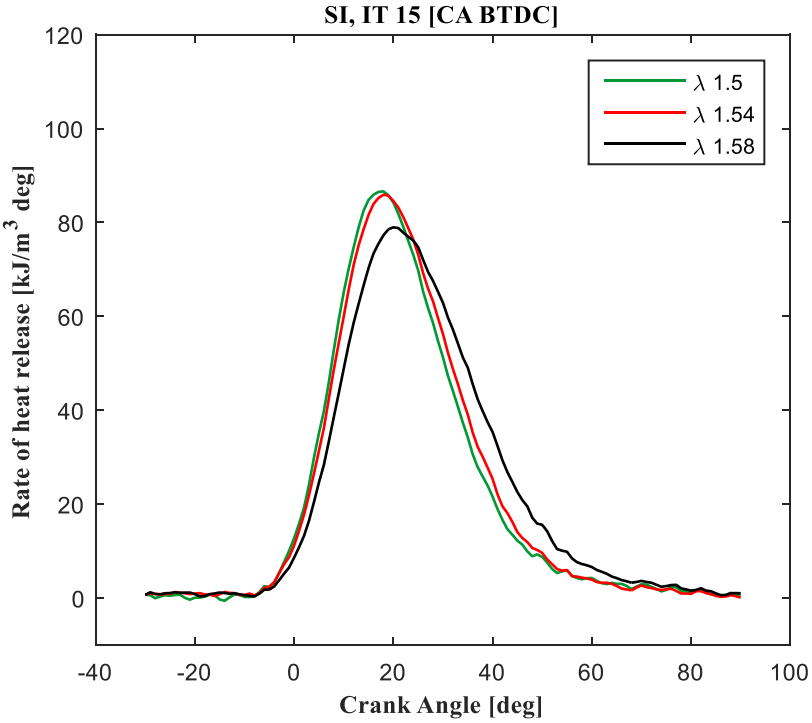

Figure C6. Rate of heat release of a natural gas reciprocating engine operated with spark ignition at fixed ignition timing 15 CA BTDC and several air to fuel ratios.

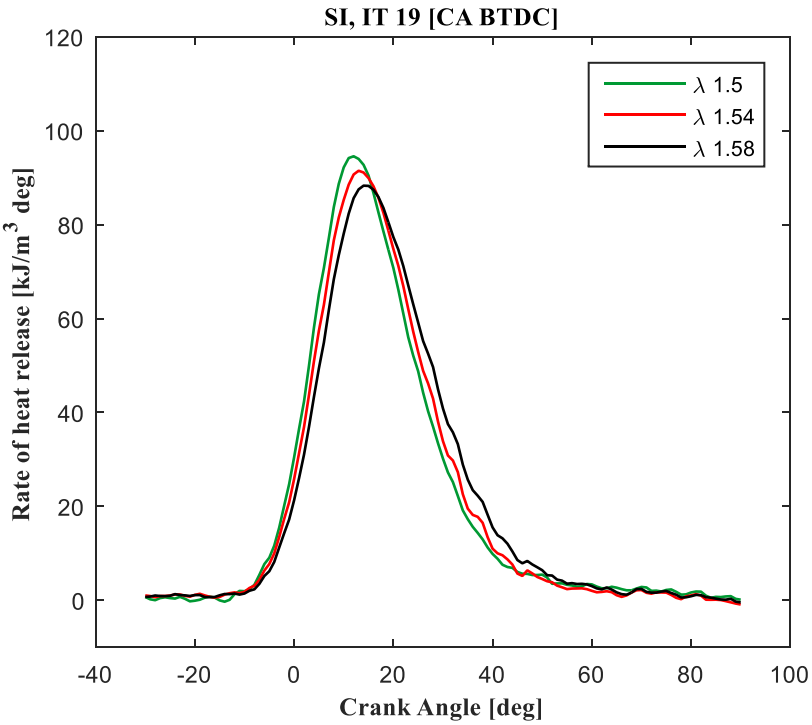

Figure C7. Rate of heat release of a natural gas reciprocating engine operated with spark ignition at fixed ignition timing 19 CA BTDC and several air to fuel ratios.

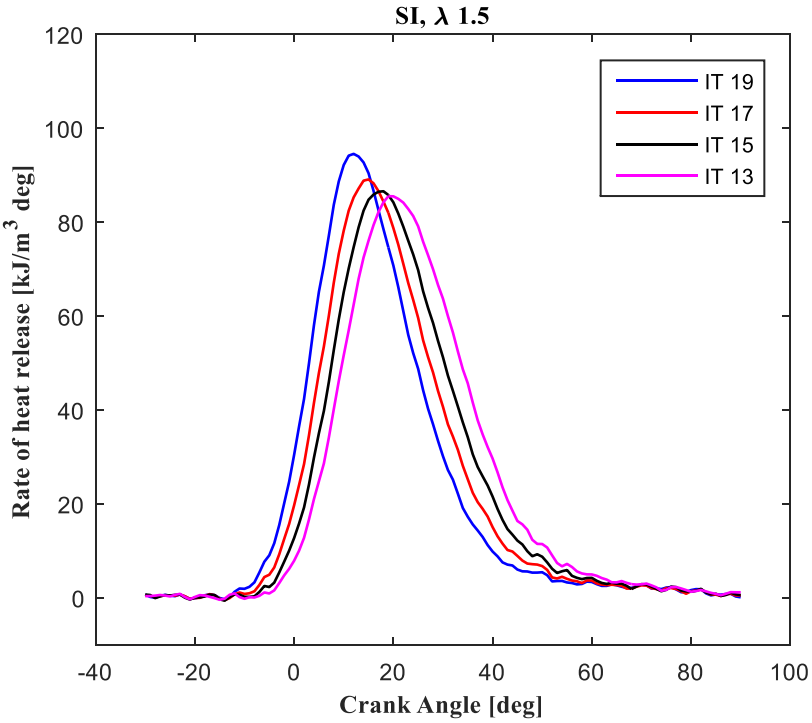

Figure C8. Rate of heat release of a natural gas reciprocating engine operated with spark ignition at fixed air to fuel ratios λ = 1.5 and several ignition timings in CA BTDC.

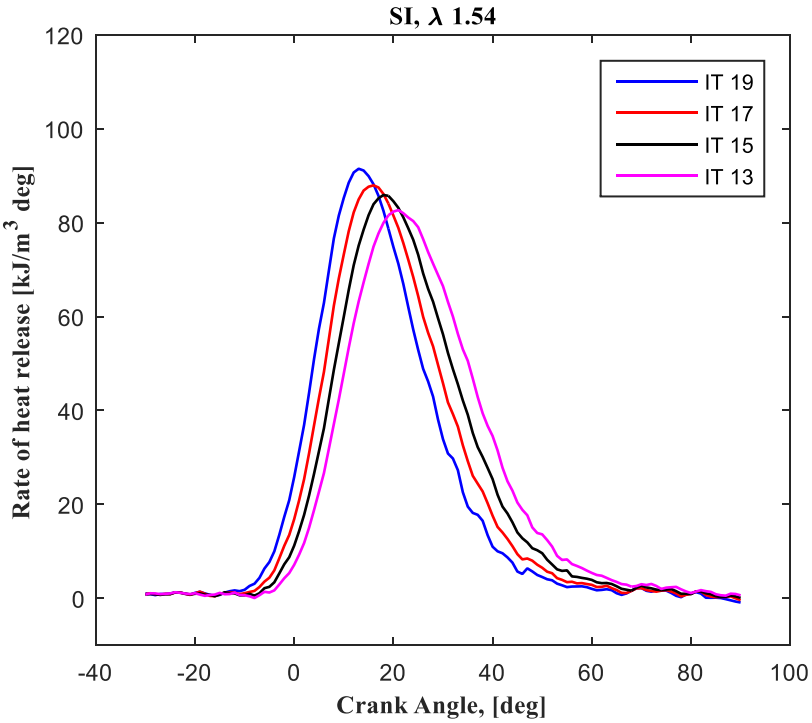

Figure C9. Rate of heat release of a natural gas reciprocating engine operated with spark ignition at fixed air to fuel ratios λ = 1.54 and several ignition timings in CA BTDC.

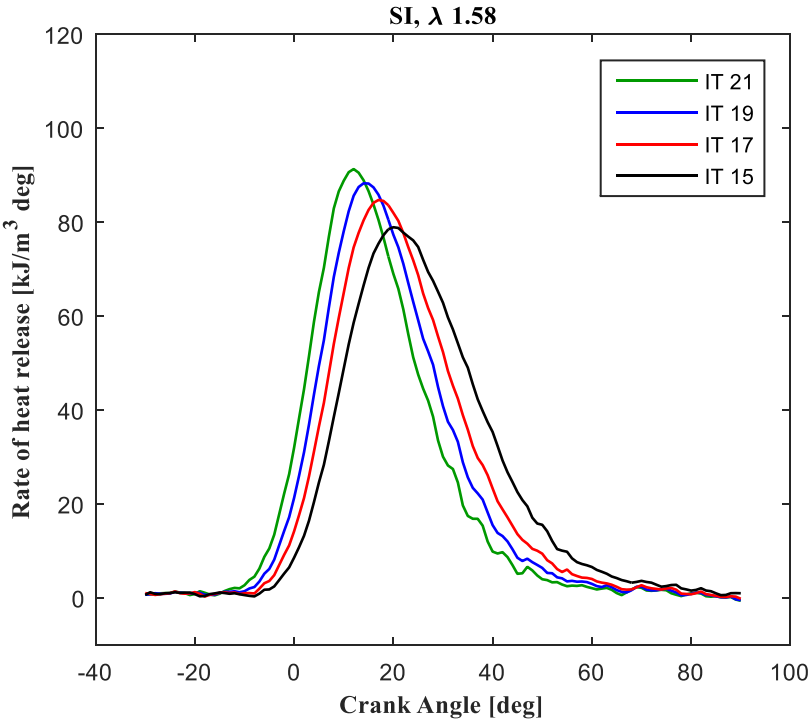

Figure C10. Rate of heat release of a natural gas reciprocating engine operated with spark ignition at fixed air to fuel ratios λ = 1.58 and several ignition timings in CA BTDC.

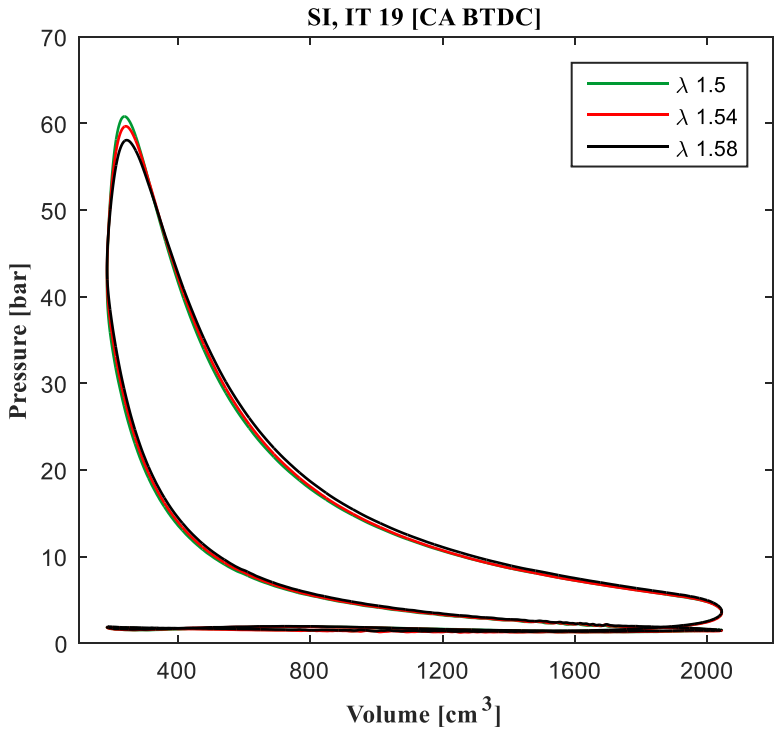

Figure C11. Pressure vs volume diagram of a natural gas reciprocating engine operated with spark ignition at fixed ignition timing 19 CA BTDC and several air to fuel ratios.

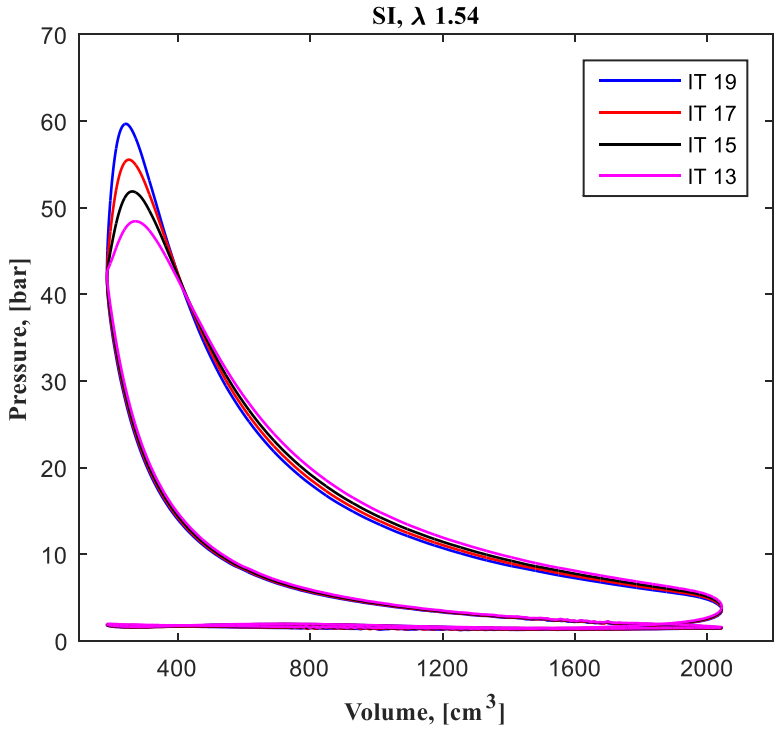

Figure C12. Pressure vs volume diagram of a natural gas reciprocating engine operated with spark ignition at fixed air to fuel ratios λ = 1.54 and several ignition timings in CA BTDC.

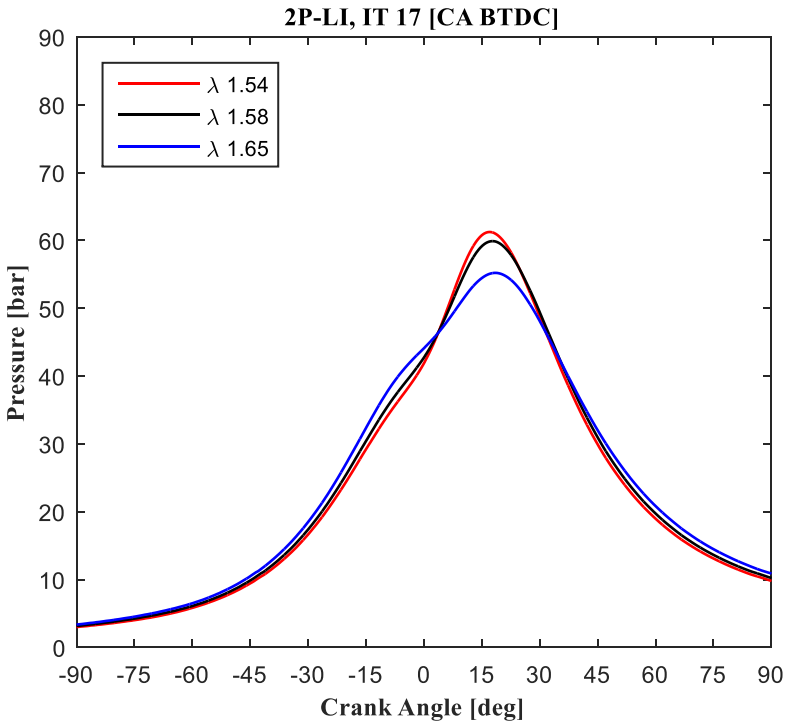

Figure C13. Pressure traces of natural gas reciprocating engine operated with laser ignition at a fixed ignition timing 17 CA BTDC and several air to fuel ratios.

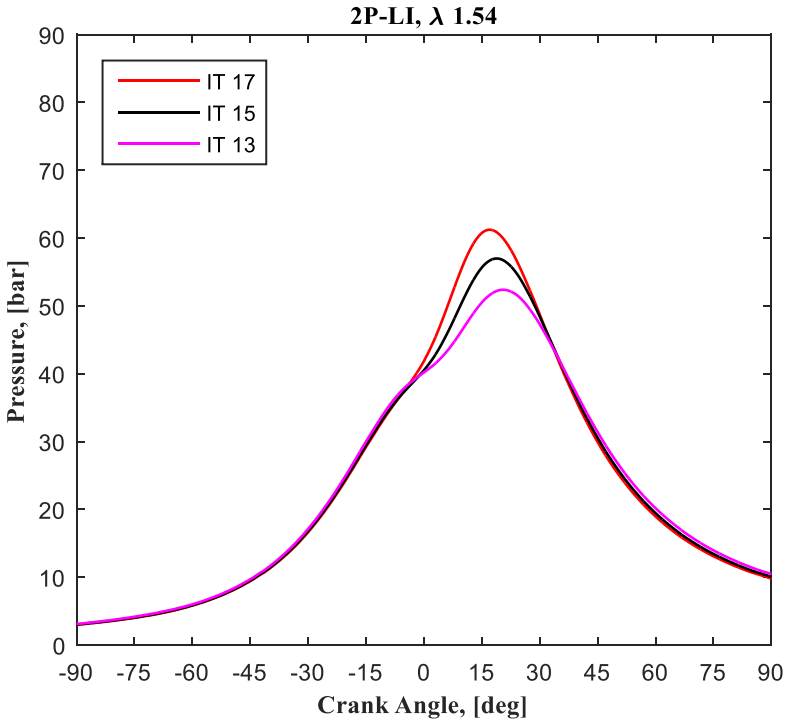

Figure C14. Pressure traces of natural gas reciprocating engine operated with laser ignition at a fixed air to fuel ratios λ = 1.54 and several ignition timings in CA BTDC.

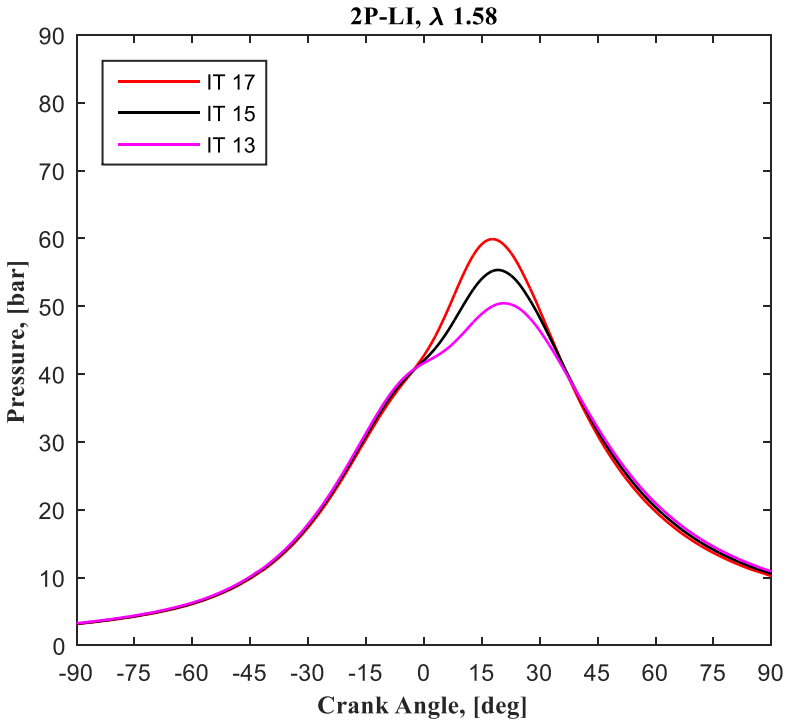

Figure C15. Pressure traces of natural gas reciprocating engine operated with laser ignition at a fixed air to fuel ratios λ = 1.58 and several ignition timings in CA BTDC.

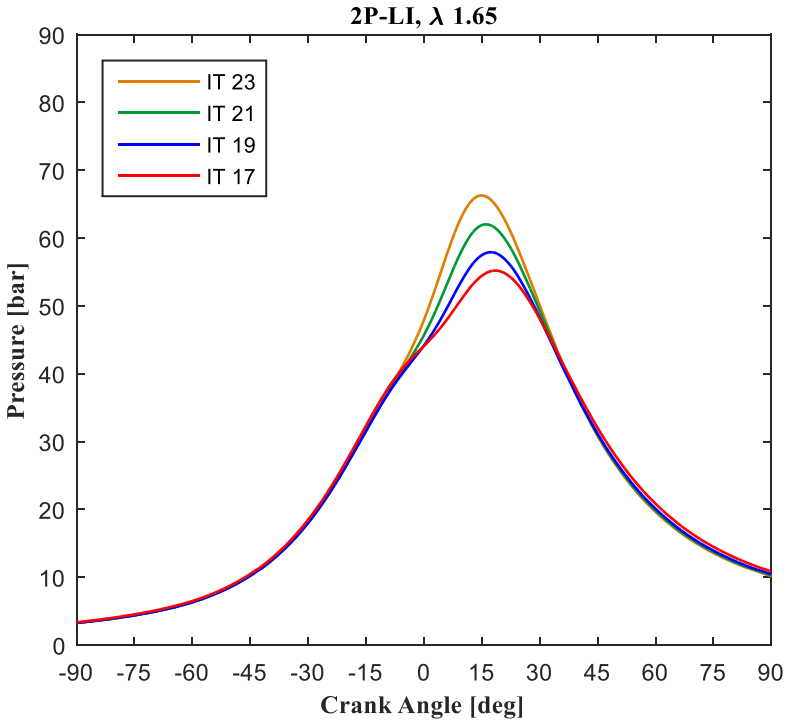

Figure C16. Pressure traces of natural gas reciprocating engine operated with laser ignition at a fixed air to fuel ratios λ = 1.65 and several ignition timings in CA BTDC.

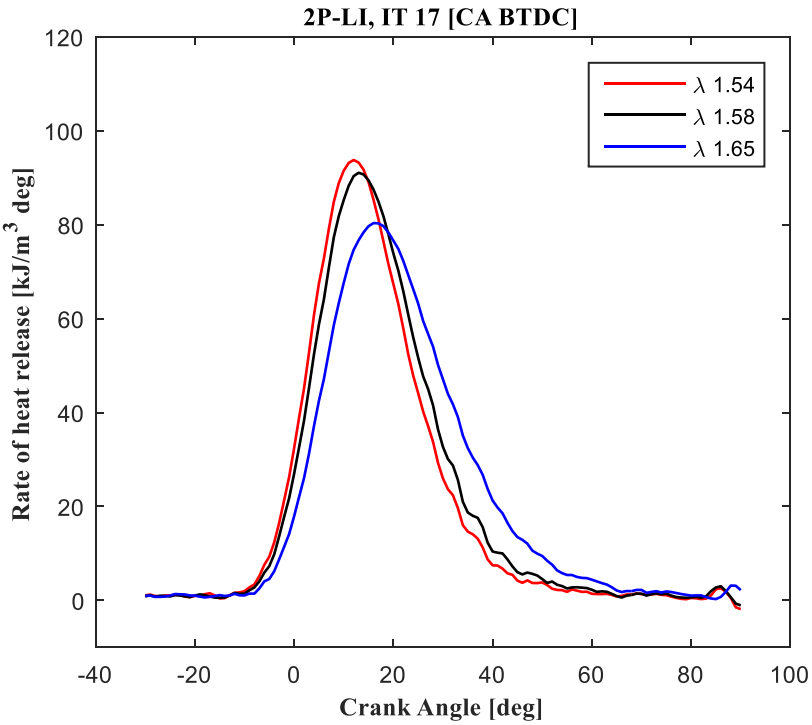

Figure C17. Rate of heat release of a natural gas reciprocating engine operated with laser ignition at fixed ignition timing 17 CA BTDC and several air to fuel ratios.

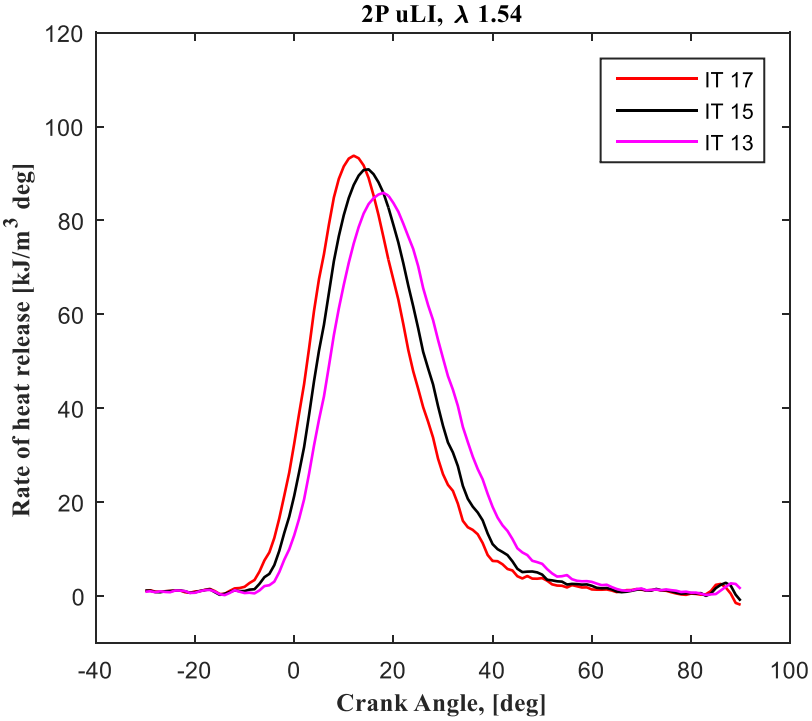

Figure C18. Rate of heat release of a natural gas reciprocating engine operated with laser ignition at fixed air to fuel ratios λ = 1.54 and several ignition timings in CA BTDC.

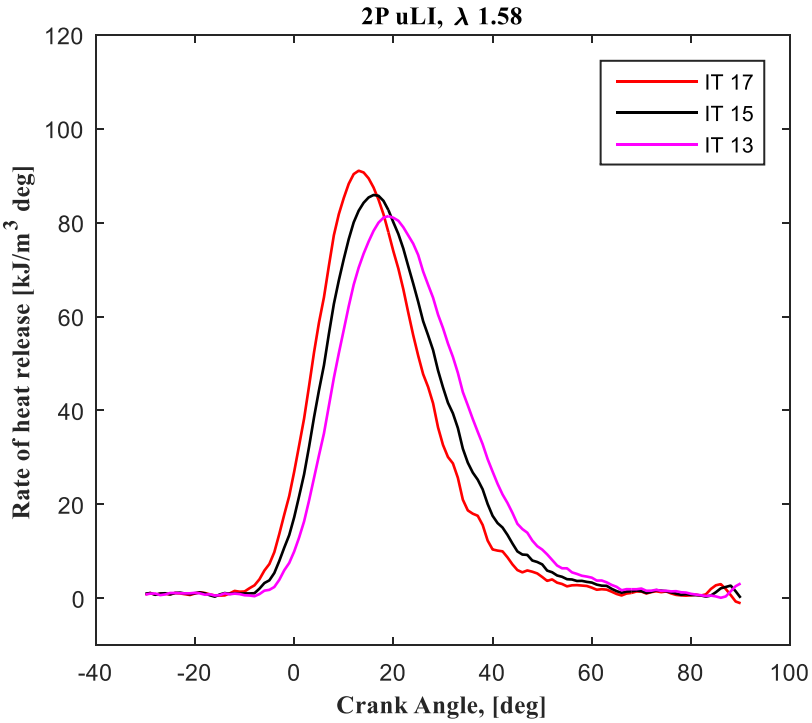

Figure C19. Rate of heat release of a natural gas reciprocating engine operated with laser ignition at fixed air to fuel ratios λ = 1.58 and several ignition timings in CA BTDC.

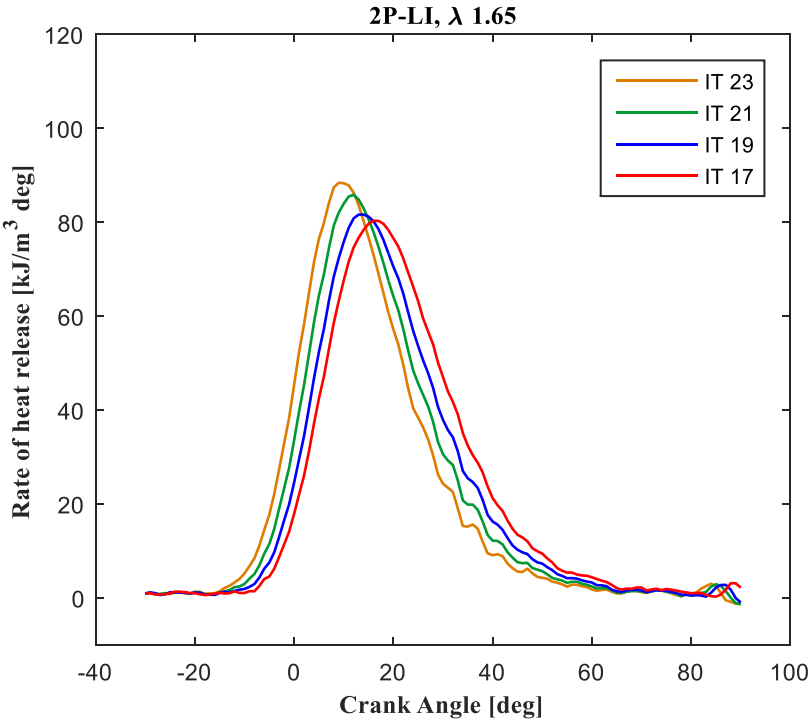

Figure C20. Rate of heat release of a natural gas reciprocating engine operated with laser ignition at fixed air to fuel ratios λ = 1.65 and several ignition timings in CA BTDC.

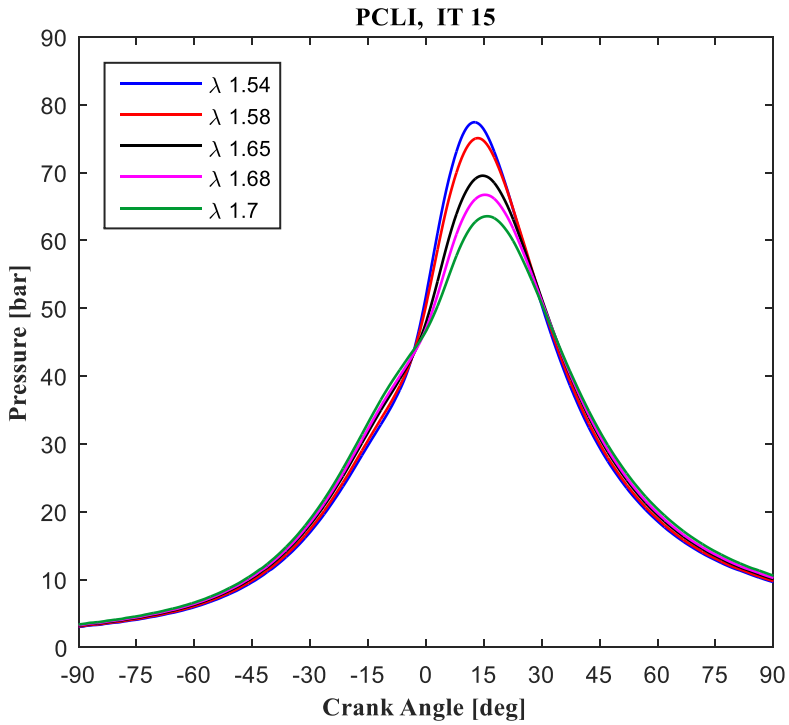

Figure C21. Pressure traces of natural gas reciprocating engine operated with prechamber laser ignition at a fixed ignition timing 15 CA BTDC and several air to fuel ratios.

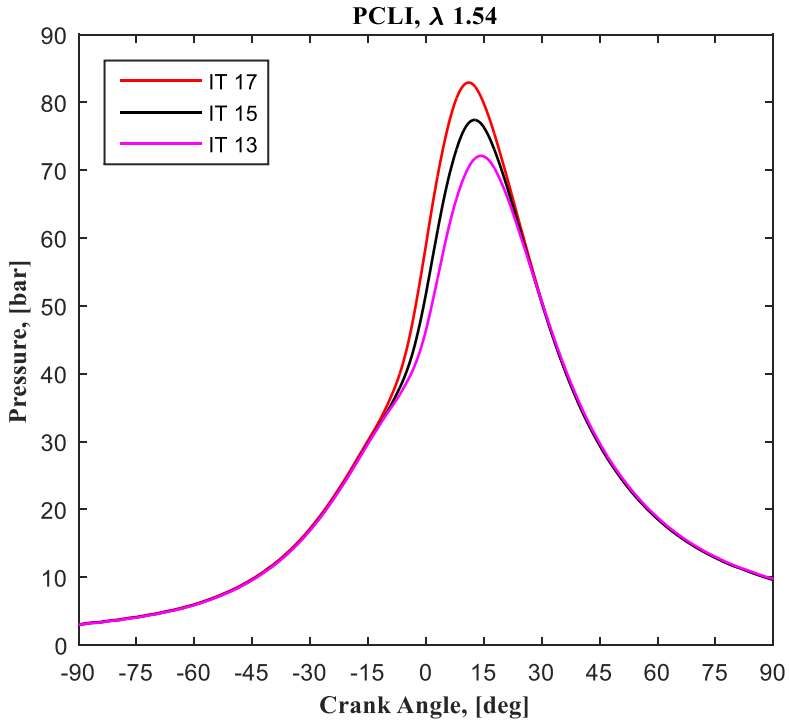

Figure C22. Pressure traces of natural gas reciprocating engine operated with prechamber laser ignition at a fixed air to fuel ratios λ = 1.54 and several ignition timings in CA BTDC.

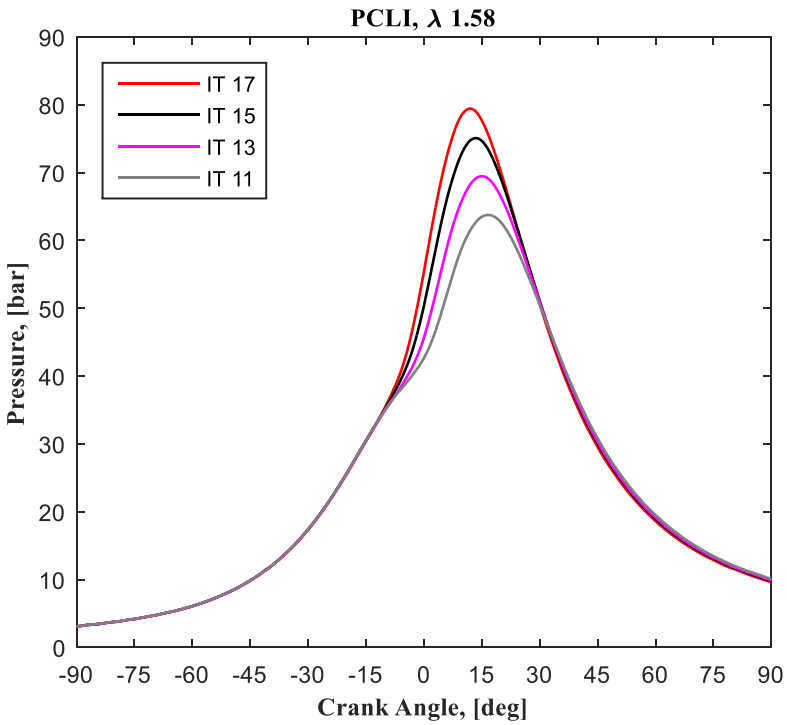

Figure C23. Pressure traces of natural gas reciprocating engine operated with prechamber laser ignition at a fixed air to fuel ratios λ = 1.58 and several ignition timings in CA BTDC.

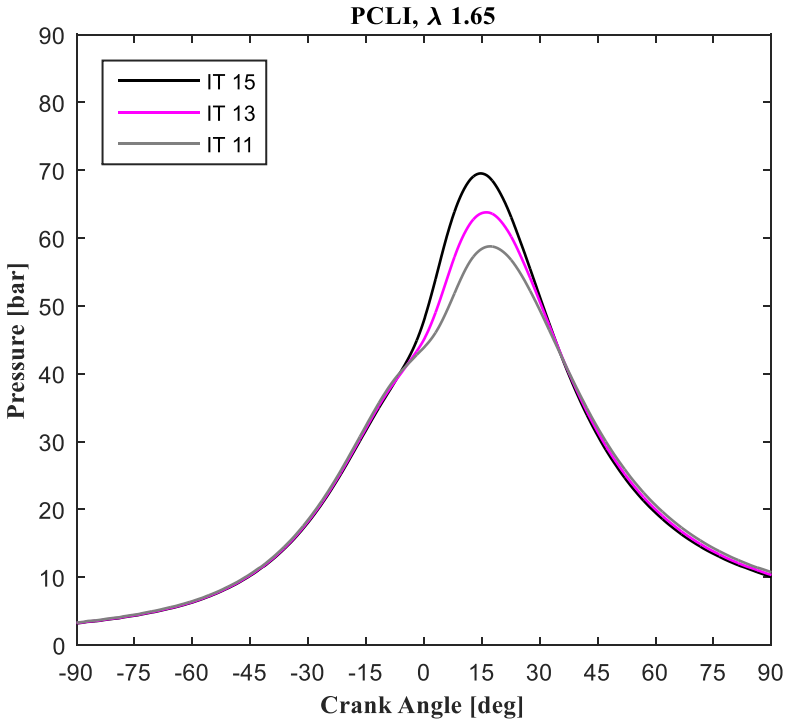

Figure C24. Pressure traces of natural gas reciprocating engine operated with prechamber laser ignition at a fixed air to fuel ratios λ = 1.65 and several ignition timings in CA BTDC.

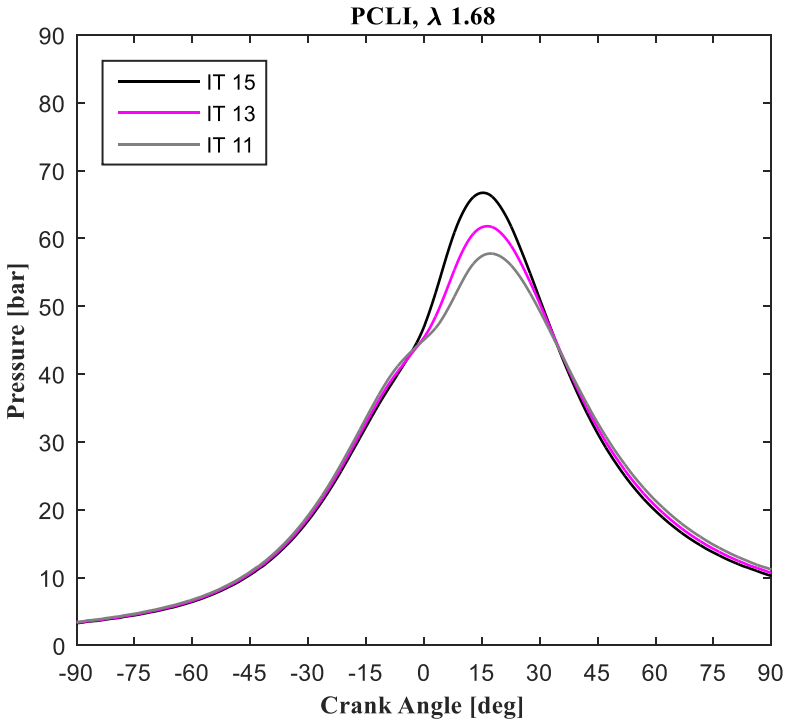

Figure C25. Pressure traces of natural gas reciprocating engine operated with prechamber laser ignition at a fixed air to fuel ratios λ = 1.68 and several ignition timings in CA BTDC.

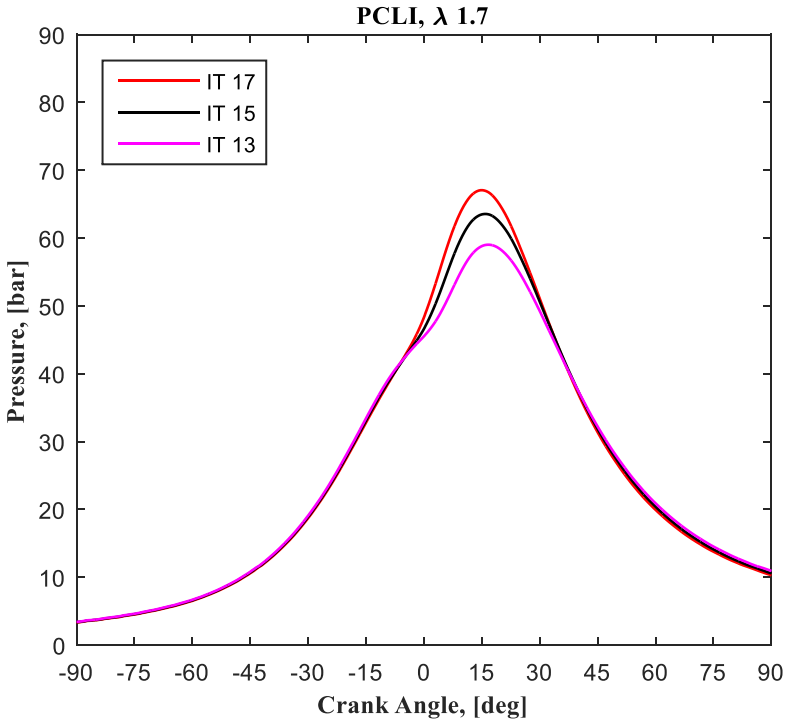

Figure C26. Pressure traces of natural gas reciprocating engine operated with prechamber laser ignition at a fixed air to fuel ratios λ = 1.7 and several ignition timings in CA BTDC.

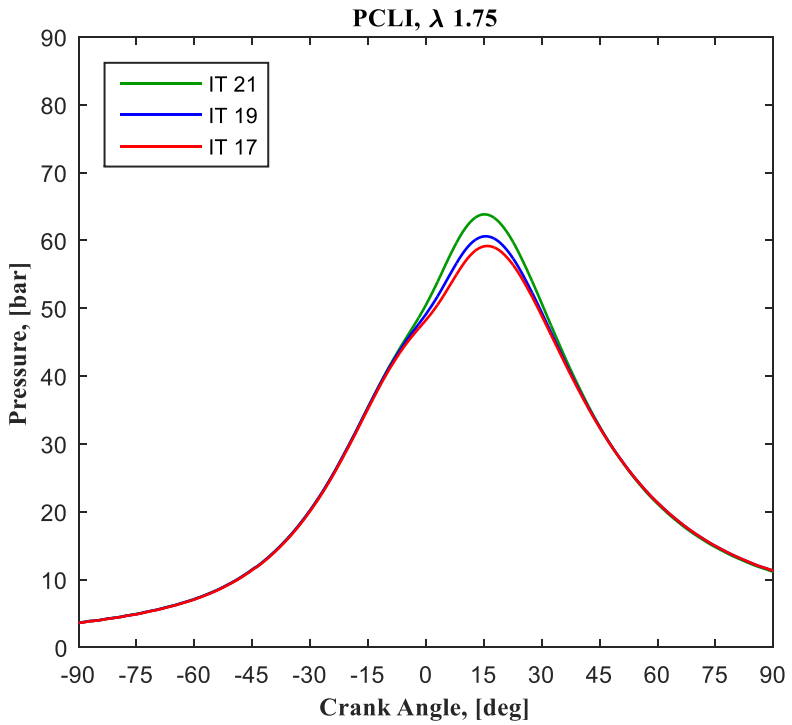

Figure C27. Pressure traces of natural gas reciprocating engine operated with prechamber laser ignition at a fixed air to fuel ratios λ = 1.75 and several ignition timings in CA BTDC.

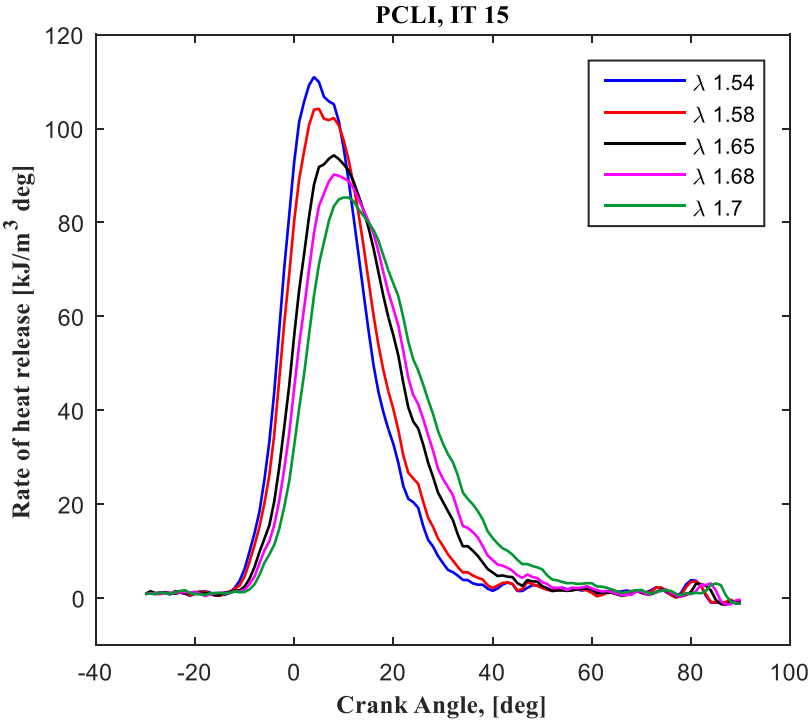

Figure C28. Rate of heat release of a natural gas reciprocating engine operated with prechamber laser ignition at fixed ignition timing 15 CA BTDC and several air to fuel ratios.

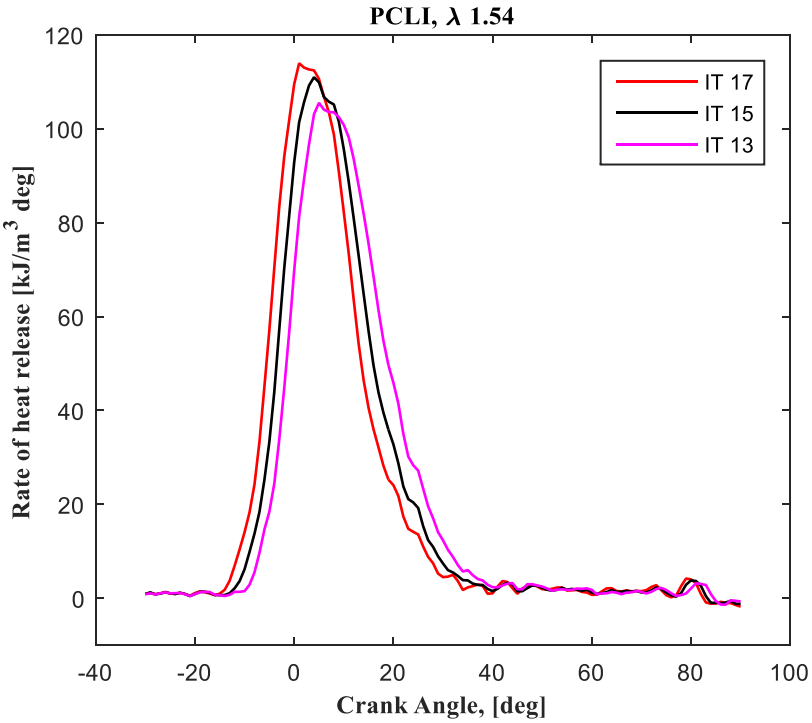

Figure C29. Rate of heat release of a natural gas reciprocating engine operated with prechamber laser ignition at fixed air to fuel ratios λ = 1.54 and several ignition timings in CA BTDC.

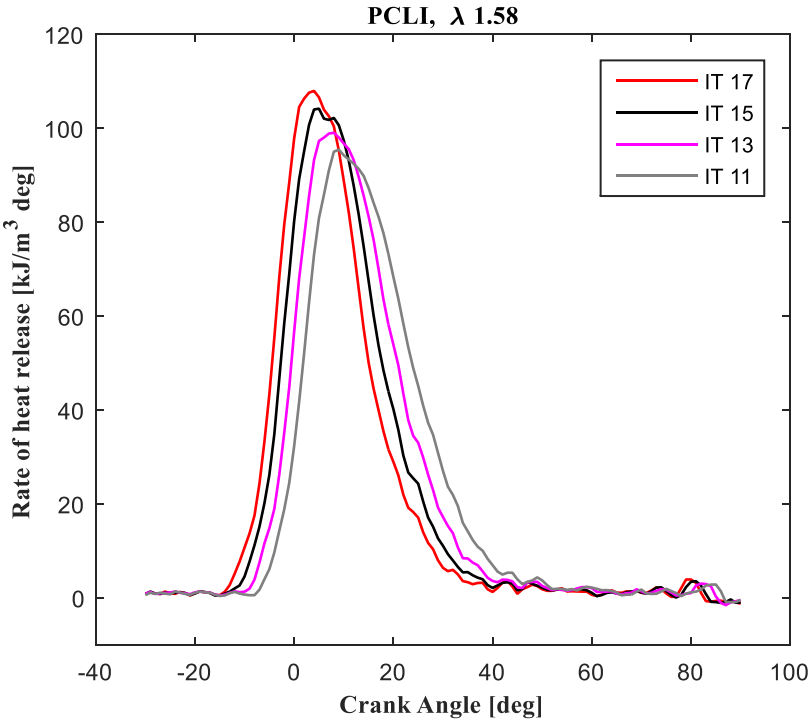

Figure C30. Rate of heat release of a natural gas reciprocating engine operated with prechamber laser ignition at fixed air to fuel ratios λ = 1.58 and several ignition timings in CA BTDC.

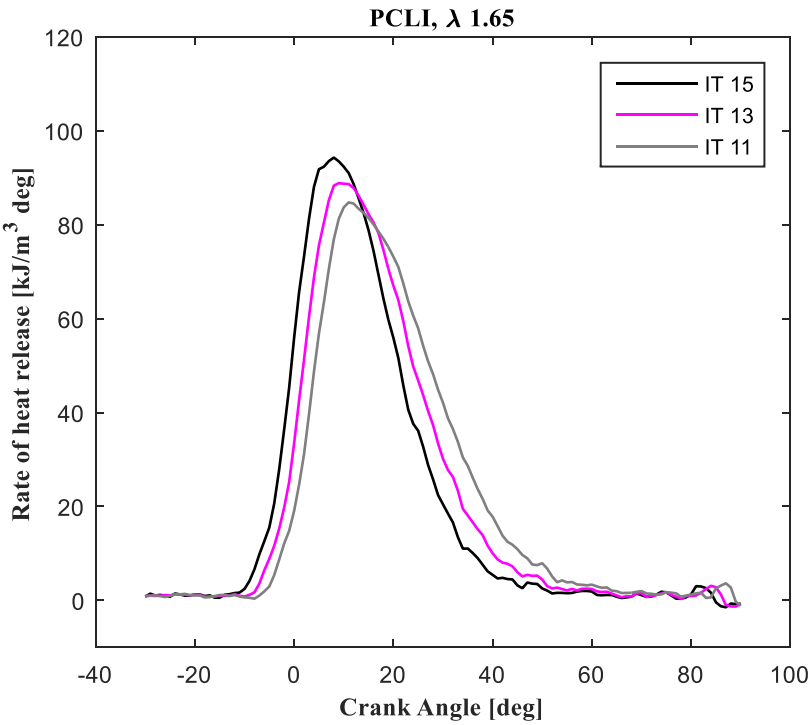

Figure C31. Rate of heat release of a natural gas reciprocating engine operated with prechamber laser ignition at fixed air to fuel ratios λ = 1.65 and several ignition timings in CA BTDC.

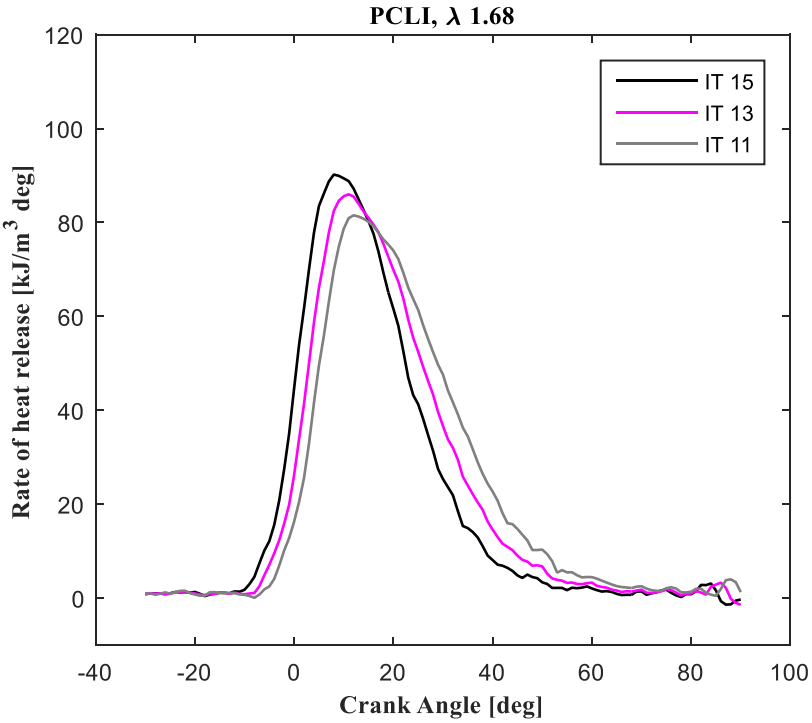

Figure C32. Rate of heat release of a natural gas reciprocating engine operated with prechamber laser ignition at fixed air to fuel ratios λ = 1.68 and several ignition timings in CA BTDC.

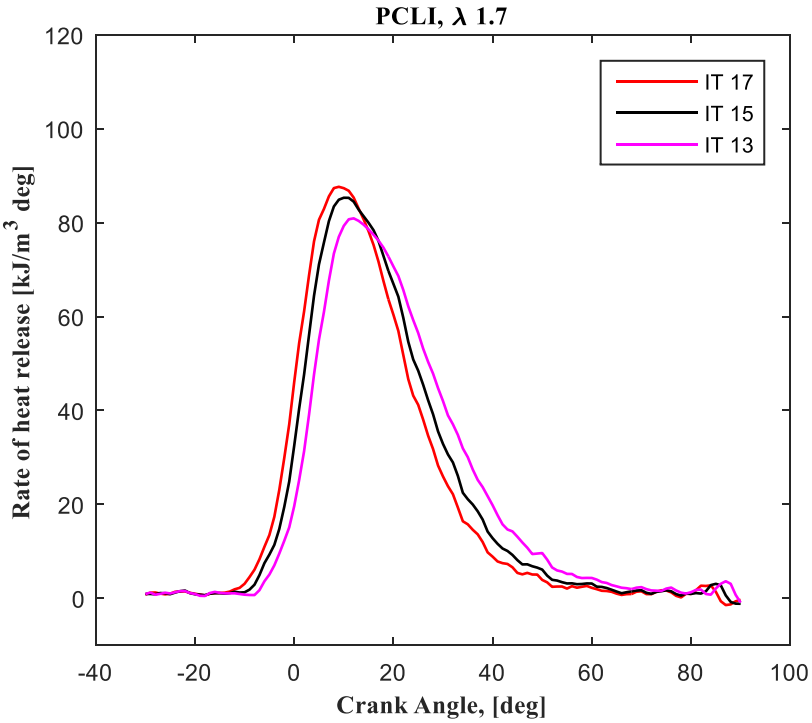

Figure C33. Rate of heat release of a natural gas reciprocating engine operated with prechamber laser ignition at fixed air to fuel ratios λ = 1.7 and several ignition timings in CA BTDC.

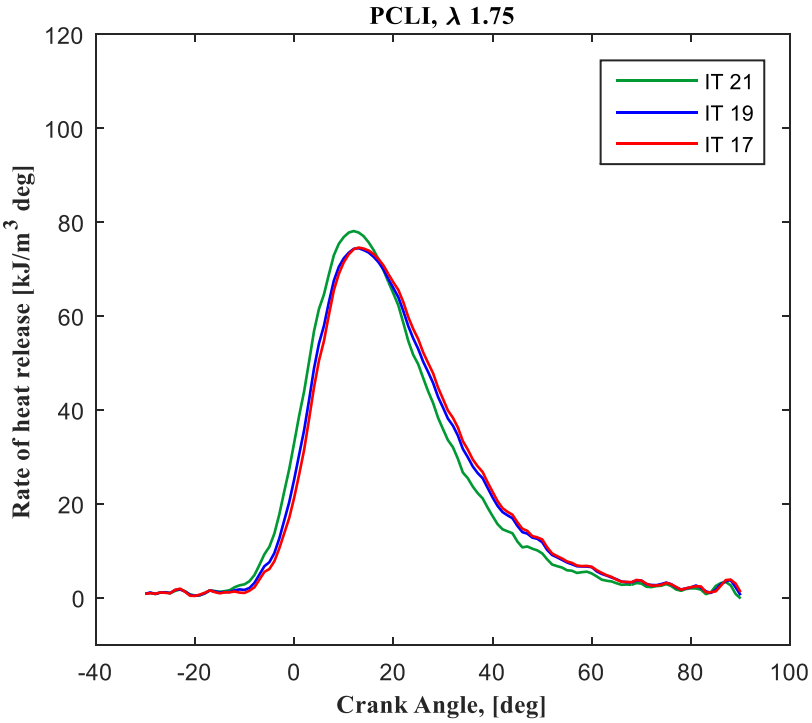

Figure C34. Rate of heat release of a natural gas reciprocating engine operated with prechamber laser ignition at fixed air to fuel ratios λ = 1.75 and several ignition timings in CA BTDC.

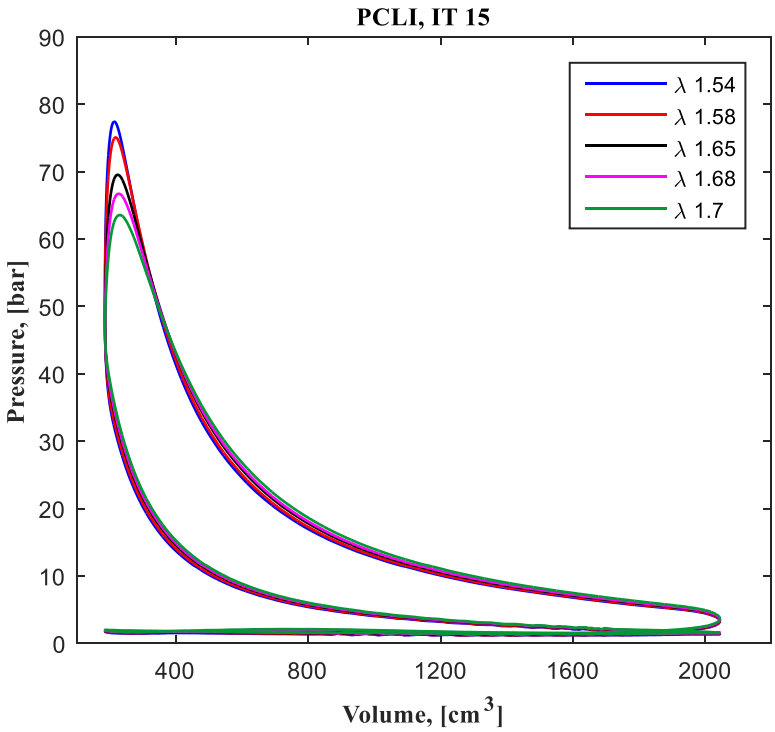

Figure C35. Pressure vs volume diagram of a natural gas reciprocating engine operated with prechamber laser ignition at fixed ignition timing 15 CA BTDC and several air to fuel ratios.

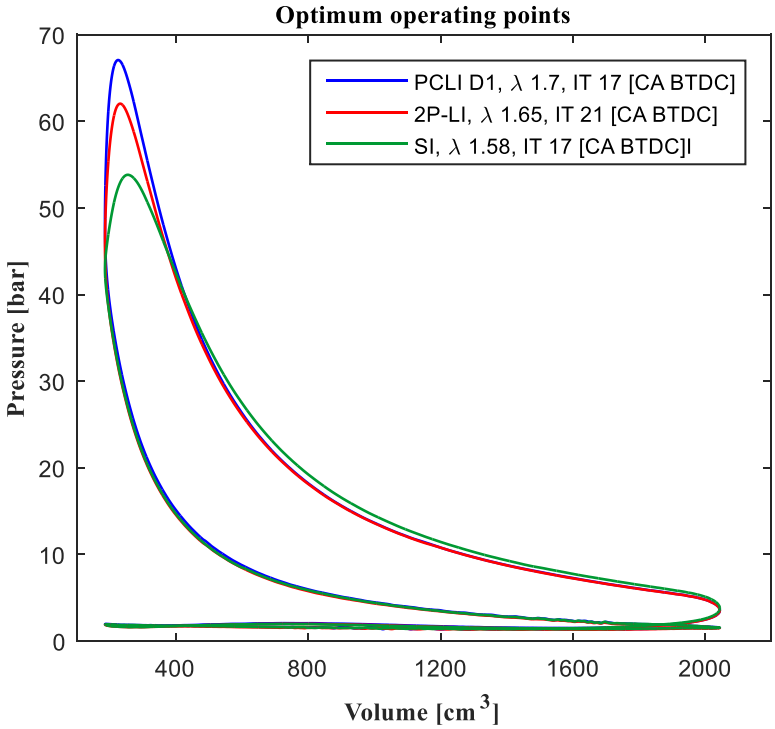

Figure C36. Pressure vs volume diagram of a natural gas reciprocating engine operated equipped with several ignition systems at 10 bar BMEP

APPENDIX D: PERMISSION LETTERS

Bader Almansour

From: InfoCtr (OC) <INFOCTR@eia.gov>
Sent: Wednesday, January 31, 2018 10:16 AM
To: Bader Almansour
Subject: RE: permission to use your data

Dear Bader Almansour,

Thank you for your inquiry to the U.S. Energy Information Administration (EIA) concerning permission to use our image/graph. You may view our copyright and reuse policy at http://www.eia.gov/about/copyrights_reuse.cfm.

Hope this information is helpful. Please contact us again for energy statistics or data.

Curley Andrews | Information Dissemination Specialist
Office of Communications
U.S. Energy Information Administration
www.eia.gov

Find us on Facebook | Follow us on Twitter

Check out what others are asking about energy, browse our frequently asked questions
Sign up for EIA data and report releases

From: Bader Almansour [mailto:bader@knights.ucf.edu]
Sent: Tuesday, January 30, 2018 8:40 PM
To: InfoCtr (OC) <INFOCTR@eia.gov>
Subject: permission to use your data

Dear Sir/Madam,

This email is in regards to some figures in your Annual Energy Outlook report 2017. My name is Bader Almansour; I am a graduate student at the University of Central Florida working on natural gas and biofuel research. I need permission to use some of your figures (energy production and consumption) in my dissertation introduction. I already cited the figures in my dissertation, but the school requires permission from the original author.

Can I use your figures in my dissertation?

Regards,

Bader

U.S. Energy Information Administration

About EIA
Copyrights and Reuse

Public domain and use of EIA content

U.S. government publications are in the public domain and are not subject to copyright protection. You may use and/or distribute any of our data, files, databases, reports, graphs, charts, and other information products that are on our website or that you receive through our email distribution service. However, if you use or reproduce any of our information products, you should use an acknowledgment, which includes the publication date, such as: "Source: U.S. Energy Information Administration (Oct 2008)."

Quoting EIA content and translations

When quoting EIA text, the acknowledgment should clearly indicate which text is EIA content and which is not. When translating EIA content into another language, please indicate the organization responsible for the translation and provide a link back to the original EIA web page in the acknowledgment.

Protected materials

You may see on our website documents, illustrations, photographs, or other information resources contributed or licensed by private individuals, companies, or organizations that may be protected by U.S. and foreign copyright laws. Transmission or reproduction of protected items beyond that allowed by fair use as defined in the copyright laws requires the written permission of the copyright owners.

The EIA logo is a registered trademark (Registration Number 4019501) of the U.S. Department of Energy and may not be used without the expressed consent of the U.S. Energy Information Administration. The mark consists of the acronym "EIA" with an associated design element of three curved lines above the literal element that extend to its right. For more information, please contact Dale Sweetnam at dale.sweetnam@eia.gov.

Please note that our "**Energy Ant**" (seen on our Energy Kids website at http://www.eia.gov/kids/) is a registered servicemark of the U.S. Department of Energy. For more information about use restrictions of this graphic item, please contact InfoCtr@eia.gov.

The photographs on our website are protected by private licensing agreements and may not be reproduced without EIA's and/or the licensor's prior written consent. Contact Us if you have any questions regarding the reproduction of any illustrations, photographs, or other protected information. For background material on other copyright issues, see Copyright Basics from the U.S. Copyright Office.

LIST OF REFERENCES

[1] Ma, F., Wang, M., Jiang, L., Deng, J., Chen, R., Naeve, N., and Zhao, S., 2010, "Performance and emission characteristics of a turbocharged spark-ignition hydrogen-enriched compressed natural gas engine under wide open throttle operating conditions," international journal of hydrogen energy, 35(22), pp. 12502-12509.

[2] Lecointe, B., and Monnier, G., 2003, "Downsizing a gasoline engine using turbocharging with direct injection," No. 0148-7191, SAE Technical Paper.

[3] Gray, C., 1988, "A review of variable engine valve timing," No. 0148-7191, SAE Technical Paper.

[4] Ceviz, M., and Akın, M., 2010, "Design of a new SI engine intake manifold with variable length plenum," Energy Conversion and Management, 51(11), pp. 2239-2244.

[5] Kalam, M., and Masjuki, H., 2011, "An experimental investigation of high performance natural gas engine with direct injection," Energy, 36(5), pp. 3563-3571.

[6] Automotive, D., 2017, " Worldwide Emissions Standards passenger vehicle and motorcycle booklet," DELPHI, USA, p. 118.

[7] Schnessl, E., and Wimmer, A., "Trends in the development of large gas engines for power generation," Proc. Proceedings of International Conference & Workshop REMOO, pp. 18-20.

[8] Agency, U. S. E. P., 2017, "Controlling Air Pollution from Stationary Engines," https://www.epa.gov/stationary-engines.

[9] Farrell, J., 2016, "Co-Optimization of Fuels and Engines," NREL (National Renewable Energy Laboratory (NREL), Golden, CO (United States)).

[10] Outlook, A. E., 2017, "Energy Information Administration," Department of Energy, AEO2017(1), p. 127.

[11] McKendry, P., 2002, "Energy production from biomass (part 3): gasification technologies," Bioresource technology, 83(1), pp. 55-63.

[12] McMillian, M. H., Woodruff, S. D., Richardson, S. W., and McIntyre, D. L., 2004, "Laser spark ignition:laser development and engine testing," Fall technical conference of the ASME ICE division, Long Beach, California, USA.

[13] Dale, J. D., Checkel, M., and Smy, P., 1997, "Application of high energy ignition systems to engines," Progress in energy and combustion science, 23(5), pp. 379-398.

[14] Sjöberg, M., Zeng, W., Singleton, D., Sanders, J. M., and Gundersen, M. A., 2014, "Combined effects of multi-pulse transient plasma ignition and intake heating on lean limits of

well-mixed E85 DISI engine operation," SAE International Journal of Engines, 7(2014-01-2615), pp. 1781-1801.

[15] Gao, H., Matthews, R. D., Hall, M. J., and Hari, S., 2004, "From spark plugs to railplugs–the characteristics of a new ignition system," No. 0148-7191, SAE Technical Paper.

[16] Gupta, S. B., Biruduganti, M., Bihari, B., and Sekar, R., 2012, "Natural gas fired reciprocating engines for power generation: Concerns and recent advances," Natural Gas-Extraction to End Use, Intech.

[17] Toulson, E., Huisjen, A., Chen, X., Squibb, C., Zhu, G., Schock, H., and Attard, W. P., 2012, "Visualization of Propane and Natural Gas Spark Ignition and Turbulent Jet Ignition Combustion," SAE International Journal of Engines, 5(2012-32-0002), pp. 1821-1835.

[18] Morsy, M. H., 2012, "Review and recent developments of laser ignition for internal combustion engines applications," Renewable and Sustainable Energy Reviews, 16, pp. 4849-4875.

[19] Heywood, J. B., 1988, Internal combustion engine fundamentals, Mcgraw-hill New York.

[20] Stanglmaier, R. H., and Roberts, C. E., 1999, "Homogeneous charge compression ignition (HCCI): benefits, compromises, and future engine applications," No. 0148-7191, SAE Technical Paper.

[21] Tauer, J., Kofler, H., and Wintner, E., 2010, "Laser-initiated ignition," Laser & Photon. Rev., 4(1), pp. 99-122.

[22] Srivastava, D. K., Wintner, E., and Agarwal, A. K., 2014, "Effect of laser pulse energy on the laser ignition of compressed natural gas fueled engine," Optical Engineering, 53(5), p. 9.

[23] Herdin, G., Klausner, J., Wintner, E., Weinrotter, M., Graf, J., and Iskra, K., "Laser ignition: a new concept to use and increase the potentials of gas engines," Proc. ASME 2005 Internal Combustion Engine Division Fall Technical Conference, American Society of Mechanical Engineers, pp. 673-681.

[24] Ikeda, Y., Nishiyama, A., Katano, H., Kaneko, M., and Jeong, H., 2009, "Research and development of microwave plasma combustion engine (Part II: engine performance of plasma combustion engine)," No. 0148-7191, SAE Technical Paper.

[25] Saito, H., Sakurai, T., Sakonji, T., Hirashima, T., and Kanno, K., 2001, "Study on lean burn gas engine using pilot oil as the ignition source," No. 0148-7191, SAE Technical Paper.

[26] Richardson, S., McMillian, M. H., Woodruff, S. D., and McIntyre, D., 2004, "Misfire, knock and NOx mapping of a laser spark ignited single cylinder lean burn natural gas engine," No. 0148-7191, SAE Technical Paper.

[27] Tsunekane, M., Inohara, T., Kanehara, K., and Taira, T., 2010, "Micro-solid-state laser for ignition of automobile engines," Advances in Solid-State Lasers: Development and Applications, pp. 195-212.

[28] Srivastava, D. K., Dharamshi, K., and Agarwal, A. K., 2011, "Flame kernel characterization of laser ignition of natural gas–air mixture in a constant volume combustion chamber," Optics and Lasers in Engineering, 49(9), pp. 1201-1209.

[29] Pineda, D. I., Wolk, B., Sennott, T., Chen, J.-Y., Dibble, R. W., and Singleton, D., "Nanosecond pulsed discharge in a lean methane-air mixture," Proc. Laser Ignition Conference, Optical Society of America, p. T5A. 2.

[30] Schenk, A., Rixecker, G., and Bohne, S., "Results from Gasoline and CNG Engine Tests with the Corona Ignition System EcoFlash," Proc. Laser Ignition Conference, Optical Society of America, p. W4A. 4.

[31] Strozzi, C., Gillard, P., and Minard, J.-P., 2014, "Laser-Induced Spark Ignition of Gaseous and Quiescent N-Decane–Air Mixtures," Combustion Science and Technology, 186(10-11), pp. 1562-1581.

[32] Musazzi, S., and Perini, U., 2014, Laser-induced breakdown spectroscopy: theory and applications, Springer.

[33] Design, R., 2017, "ANSYS Chemkin-Pro," http://www.ansys.com/products/fluids/ansys-chemkin-pro, San Diego, CA.

[34] Smith, G. P., Golden, D. M., Frenklach, M., Moriarty, N. W., Eiteneer, B., Goldenberg, M., Bowman, C. T., Hanson, R. K., Song, S., Gardiner Jr., W. C., Lissianski, V. V., and Qin, Z., 1999, "The GRI 3.0 chemical kinetic mechanism," http://www.me.berkeley.edu/gri_mech/.

[35] Shah, A., Tunestal, P., and Johansson, B., 2012, "Investigation of performance and emission characteristics of a heavy duty natural gas engine operated with pre-chamber spark plug and dilution with excess air and EGR," SAE International Journal of Engines, 5(2012-01-1980), pp. 1790-1801.

[36] Shah, A., Tunestal, P., and Johansson, B., 2015, "Effect of Pre-Chamber Volume and Nozzle Diameter on Pre-Chamber Ignition in Heavy Duty Natural Gas Engines," No. 0148-7191, SAE Technical Paper.

[37] Roethlisberger, R., and Favrat, D., 2003, "Investigation of the prechamber geometrical configuration of a natural gas spark ignition engine for cogeneration: part I. Numerical simulation," International journal of thermal sciences, 42(3), pp. 223-237.

[38] Gentz, G., Thelen, B., Gholamisheeri, M., Litke, P., Brown, A., Hoke, J., and Toulson, E., 2015, "A study of the influence of orifice diameter on a turbulent jet ignition system through combustion visualization and performance characterization in a rapid compression machine," Applied Thermal Engineering, 81, pp. 399-411.

[39] Princiotta, F. T., and Loughlin, D. H., 2014, "Global climate change: The quantifiable sustainability challenge," Journal of the Air & Waste Management Association, 64(9), pp. 979-994.

[40] Hill, J., Nelson, E., Tilman, D., Polasky, S., and Tiffany, D., 2006, "Environmental, economic, and energetic costs and benefits of biodiesel and ethanol biofuels," Proceedings of the National Academy of sciences, 103(30), pp. 11206-11210.

[41] 2013, "International Energy Outlook 2013," D. o. Energy, ed.http://www.eia.gov/forecasts/ieo/pdf/0484(2013).pdf.

[42] 2011, "International Energy Outlook," Energy Information Administration.

[43] Splitter, D. A., and Szybist, J. P., 2013, "Experimental Investigation of Spark-Ignited Combustion with High-Octane Biofuels and EGR. 1. Engine Load Range and Downsize Downspeed Opportunity," Energy & Fuels, 28(2), pp. 1418-1431.

[44] Splitter, D. A., and Szybist, J. P., 2013, "Experimental Investigation of Spark-Ignited Combustion with High-Octane Biofuels and EGR. 2. Fuel and EGR Effects on Knock-Limited Load and Speed," Energy & Fuels, 28(2), pp. 1432-1445.

[45] Energy, U. S. D. o., 2016, "Use of Energy in the United State," https://www.eia.gov/energyexplained/?page=us_energy_transportation#tab1.

[46] Beeckmann, J., Cai, L., and Pitsch, H., 2014, "Experimental investigation of the laminar burning velocities of methanol, ethanol, n-propanol, and n-butanol at high pressure," Fuel, 117, pp. 340-350.

[47] Burluka, A., Harker, M., Osman, H., Sheppard, C., and Konnov, A., 2010, "Laminar burning velocities of three C 3 H 6 O isomers at atmospheric pressure," Fuel, 89(10), pp. 2864-2872.

[48] Dirrenberger, P., Glaude, P.-A., Bounaceur, R., Le Gall, H., da Cruz, A. P., Konnov, A., and Battin-Leclerc, F., 2014, "Laminar burning velocity of gasolines with addition of ethanol," Fuel, 115, pp. 162-169.

[49] Allen, J. W., Scheer, A. M., Gao, C. W., Merchant, S. S., Vasu, S. S., Welz, O., Savee, J. D., Osborn, D. L., Lee, C., Vranckx, S., Wang, Z., Qi, F., Fernandes, R. X., Green, W. H., Hadi, M. Z., and Taatjes, C. A., 2014, "A Coordinated Investigation of the Combustion Chemistry of Diisopropyl Ketone, a Prototype for Biofuels Produced by Endophytic Fungi," Combust. Flame, 161, pp. 711-724.

[50] Yang, Y., Dec, J. E., Dronniou, N., and Simmons, B. A., 2010, "Characteristics of Isopentanol as a Fuel for HCCI Engines," SAE Technical Paper, 2010-01-2164.

[51] Yao, M., Zheng, Z., and Liu, H., 2009, "Progress and recent trends in homogeneous charge compression ignition (HCCI) engines," Prog. Energ. Combust. Sci., 35(5), pp. 398-437.

[52] Dec, J., and Yang, Y., 2013, "Bio-Ketones: Autoignition Characteristics and Their Potential as Fuels for HCCI Engines," SAE Int. J. Fuels Lubr., 6(3).

[53] Gladden, A., Taatjes, C. A., Gao, C., Powell, A. J., Scheer, A. M., Turner, K., Wu, W., and Yu, E. T., 2013, "Tailoring Next-Generation Biofuels and Their Combustion in Next-Generation Engines."

[54] Saeed, K., and Stone, C. R., 2004, "Measurements of the laminar burning velocity for mixtures of methanol and air from a constant-volume vessel using a multizone model," Combustion and Flame, 139(1–2), pp. 152-166.

[55] Hinton, N., and Stone, R., 2014, "Laminar burning velocity measurements of methane and carbon dioxide mixtures (biogas) over wide ranging temperatures and pressures," Fuel, 116, pp. 743-750.

[56] Metcalfe, W. K., Burke, S. M., Ahmed, S. S., and Curran, H. J., 2013, "A Hierarchical and Comparative Kinetic Modeling Study of C1 − C2 Hydrocarbon and Oxygenated Fuels," International Journal of Chemical Kinetics, 45(10), pp. 638-675.

[57] LEWIS, B., and ELBE, V., 1987, "Combustion, flames and explosions of gases//((Book))," Orlando, FL, Academic Press, Inc., 1987, 763.

[58] Law, C. K., 2006, Combustion physics, Cambridge university press.

[59] Abdel-Gayed, R., Bradley, D., and Lung, F.-K., 1989, "Combustion regimes and the straining of turbulent premixed flames," Combustion and Flame, 76(2), pp. 213-218.

[60] Cui, G., Li, Z., Yang, C., Zhou, Z., and Li, J., 2016, "Experimental Study of Minimum Ignition Energy of Methane–Air Mixtures at Low Temperatures and Elevated Pressures," Energy & Fuels, 30(8), pp. 6738-6744.

[61] Kim, H. J., Chung, S. H., and Sohn, C. H., 2004, "Numerical calculation of minimum ignition energy for hydrogen and methane fuels," KSME international journal, 18(5), pp. 838-846.

[62] Cui, G., Zeng, W., Li, Z., Fu, Y., Li, H., and Chen, J., 2016, "Experimental study of minimum ignition energy of methane/air mixtures at elevated temperatures and pressures," Fuel, 175, pp. 257-263.

[63] Kopecek, H., Maier, H., Reider, G., Winter, F., and Wintner, E., 2003, "Laser ignition of methane–air mixtures at high pressures," Exp. Therm. Fluid Sci., 27, pp. 499-503.

[64] Ronney, P. D., 1994, "Laser versus conventional ignition of flames," Optical Engineering, 33(2), pp. 510-521.

[65] Tsunekane, M., Inohara, T., Kanehara, K., and Taira, T., 2010, "Micro-Solid-State Laser for Ignition of Automobile Engines," Advances in Solid State Lasers Development and Applications, M. Grishin, ed., InTech, Croatia, pp. 195–212.

[66] Dearden, G., and Shenton, T., 2013, "Laser ignited engines: progress, challenges and prospects," Optics express, 21(106), pp. A1113-A1125.

[67] Liedl, G., Schuoecker, D., Geringer, B., Graf, J., Klawatsch, D., Lenz, H. P., Piock, W., Jetzinger, M., and Kapus, P., "Laser-induced ignition of gasoline direct-injection engines," Proc. Prague--2004 DL over, International Society for Optics and Photonics, pp. 955-960.

[68] Takizawa, K., Takahashi, A., Tokuhashi, K., Kondo, S., and Sekiya, A., 2005, "Burning velocity measurement of fluorinated compounds by the spherical-vessel method," Combustion and Flame, 141(3), pp. 298-307.

[69] Xu, C., Fang, D., Luo, Q., Ma, J., and Xie, Y., 2014, "A comparative study of laser ignition and spark ignition with gasoline–air mixtures," Optics & Laser Technology, 64, pp. 343-351.

[70] Morgan, C. G., 1975, "Laser-induced breakdown of gases," Reports on Progress in Physics, 38(5), p. 621.

[71] Almansour, B., Vasu, S., Gupta, S. B., Wang, Q., Van Leeuwen, R., and Ghosh, C., 2017, "Performance of a Laser Ignited Multicylinder Lean Burn Natural Gas Engine," Journal of Engineering for Gas Turbines and Power, 139(11), p. 111501.

[72] Harris, D. C., 1998, "Durable 3–5 μm transmitting infrared window materials," Infrared Physics & Technology, 39(4), pp. 185-201.

[73] Lackner, M., Kofler, H., Ranner, H., Winter, F., Klausner, J., and Herdin, G., "The optical spark plug: window-related issues," Proc. Proc. Eur. Combustion Meeting (ECM 2005)(Lovain-la-Neuve, Belgium, 4 March–4 June 2005).

[74] Rudz, S., Chetehouna, K., Strozzi, C., and Gillard, P., 2014, "Minimum ignition energy measurements for α-pinene/air mixtures," Combustion Science and Technology, 186(10-11), pp. 1597-1605.

[75] Kopecek, H., Charareh, S., Lackner, M., Forsich, C., Winter, F., Klausner, J., Herdin, G. n., Weinrotter, M., and Wintner, E., 2005, "Laser ignition of methane-air mixtures at high pressures and diagnostics," Journal of Engineering for Gas Turbines and Power, 127(1), pp. 213-219.

[76] Gupta, S. B., Sekar, R. R., Xu, Z., Leong, K. H., Reed, C. B., Pal, S., Cramer, J., and Santoro, R. J., "Laser Based Ignition of Natural Gas-Air Mixtures," Proc. ASME 2003 Internal Combustion Engine Division Spring Technical Conference, American Society of Mechanical Engineers, pp. 187-195.

[77] Ternel, C., Lecordier, B., Trinité, M., and Cessou, A., "Laser-induced spark ignition of propane-air and isooctane-air," Proc. Proceedings of the European Combustion Meeting, Belgium.

[78] Kopecek, H., Maier, H., Reider, G., Winter, F., and Wintner, E., 2003, "Laser ignition of methane–air mixtures at high pressures," Experimental Thermal and Fluid Science, 27(4), pp. 499-503.

[79] Bradley, D., Sheppard, C., Suardjaja, I., and Woolley, R., 2004, "Fundamentals of high-energy spark ignition with lasers," Combustion and Flame, 138(1), pp. 55-77.

[80] Lorenz, S., Bärwinkel, M., Heinz, P., Lehmann, S., Mühlbauer, W., and Brüggemann, D., 2015, "Characterization of energy transfer for passively Q-switched laser ignition," Optics express, 23(3), pp. 2647-2659.

[81] Endo, T., Takenaka, Y., Sako, Y., Johzaki, T., Namba, S.-i., and Shimokuri, D., 2017, "An experimental study on the ignition ability of a laser-induced gaseous breakdown," Combustion and Flame, 178, pp. 1-6.

[82] Ghosh, S., and Mahesh, K., 2008, "Numerical simulation of the fluid dynamic effects of laser energy deposition in air," Journal of Fluid Mechanics, 605, pp. 329-354.

[83] Phuoc, T. X., 2006, "Laser-induced spark ignition fundamental and applications," Optics and Lasers in Engineering, 44(5), pp. 351-397.

[84] Chen, Y. L., Lewis, J. W. L., and Parigger, C., 2000, "Spatial and temporal profiles of pulsed laser-induced air plasma emissions," Journal of Quantitative Spectroscopy and Radiative Transfer, 67(2), pp. 91-103.

[85] Yalçin, Ş., Crosley, D., Smith, G., and Faris, G. W., 1999, "In uence of ambient conditions on the laser air spark," Applied Physics B: Lasers and Optics, 68(1), pp. 121-130.

[86] Almansour, B., Thompson, L., Lopez, J., Barari, G., and Vasu, S. S., 2015, "Laser Ignition and Flame Speed Measurements in Oxy-Methane Mixtures Diluted With CO2," Journal of Energy Resources Technology, 138(3), pp. 032201-032201.

[87] Thompson, L., Almansour, B., Lopez, J., Glebov, L., and Vasu, S. S., 2014, "Laser ignition and flame development in premixed conventional and alternative fuel mixtures," work-in-progress poster, 35th Int. Symp. on Combustion, SF, 8/2014. .

[88] Morsy, M. H., and Chung, S. H., 2002, "Numerical simulation of front lobe formation in laser-induced spark ignition of CH4/Air mixtures.," Proc. Combust. Inst., 29, pp. 1613-1619.

[89] Bradley, D., Sheppard, C. G. W., Suardjaja, I. M., and Woolley, R., 2004, "Fundamental of highenergy ignition with lasers.," Combust Flame, 138, pp. 55-77.

[90] Spiglanin, T. A., Mcilroy, A., Fournier, E. W., Cohen, R. B., and Syage, J. A., 1995, "Time resolved imaging of flame kernels: laser spark ignition of H2/O2/Ar mixtures.," Combust Flame, 102, pp. 310-328.

[91] Phuoc, T. X., 2000, "Single-point versus multi-point laser ignition: experimental measurements of combustion times and pressures," Combustion and Flame, 122(4), pp. 508-510.

[92] Böker, D., and Brüggemann, D., 2011, "Advancing lean combustion of hydrogen–air mixtures by laser-induced spark ignition," International Journal of Hydrogen Energy, 36(22), pp. 14759-14767.

[93] Endo, T., Takenaka, Y., Sako, Y., Honda, T., Johzaki, T., and Namba, S., 2016, "Reinjection of transmitted laser light into laser-produced plasma for efficient laser ignition," Applied optics, 55(5), pp. 1132-1137.

[94] Morsy, M. H., Ko, Y. S., and Chung, S. H., 1999, "M.H. Morsy, Laser-induced ignition using a conical cavity in CH4–air mixtures," Combust Flame, 119, pp. 473-482.

[95] Ryu, S., Won, S., and Chung, S., 2009, "Laser-induced multi-point ignition with single-shot laser using conical cavities and prechamber with jet holes," Proceedings of the Combustion Institute, 32(2), pp. 3189-3196.

[96] Dale, J., Smy, P., and Clements, R., 1978, "Laser ignited internal combustion engine-an experimental study," No. 0148-7191, SAE Technical Paper.

[97] Mullett, J., Dodd, R., Williams, C., Triantos, G., Dearden, G., Shenton, A., Watkins, K., Carroll, S., Scarisbrick, A., and Keen, S., 2007, "The influence of beam energy, mode and focal length on the control of laser ignition in an internal combustion engine," Journal of Physics D: Applied Physics, 40(15), p. 4730.

[98] Srivastava, D., and Agarwal, A. K., 2013, "Laser ignition of single cylinder engine and effects of ignition location," SAE Paper(2013-01), p. 1631.

[99] Ahrens, D. L., Olsen, D. B., and Yalin, A. P., 2005, "Development of an open path laser ignition system for a large bore natural gas engine: Part 2 single cylinder demonstration," ASME Paper No. ICES2005-1317.

[100] Srivastava, D. K., and Agarwal, A. K., 2014, "Comparative experimental evaluation of performance, combustion and emissions of laser ignition with conventional spark plug in a compressed natural gas fuelled single cylinder engine," Fuel, 123, pp. 113-122.

[101] McMillian, M., Richardson, S., Woodruff, S. D., and McIntyre, D., 2004, "Laser-spark ignition testing in a natural gas-fueled single-cylinder engine," No. 0148-7191, SAE Technical Paper.

[102] Richardson, S. W., McMillian, M. H., Woodruff, S. D., Worstell, T., and McIntyre, D. L., "Laser spark ignition of a blended hydrogen-natural gas fueled single cylinder engine," Proc.

ASME 2006 Internal Combustion Engine Division Spring Technical Conference, American Society of Mechanical Engineers, pp. 411-419.

[103] Joshi, S., Loccisano, F., Yalin, A. P., and Montgomery, D. T., 2011, "On comparative performance testing of prechamber and open chamber laser ignition," Journal of Engineering for Gas Turbines and Power, 133(12), p. 122801.

[104] Graf, J., Weinrotter, M., Kopecek, H., and Wintner, E., "Laser ignition, optics and contamination of optics in an IC engine," Proc. ASME 2004 Internal Combustion Engine Division Fall Technical Conference, American Society of Mechanical Engineers, pp. 11-17.

[105] Mullett, J., Dickinson, P., Shenton, A., Dearden, G., and Watkins, K., 2008, "Multi-cylinder laser and spark ignition in an IC gasoline automotive engine: a comparative study," No. 0148-7191, SAE Technical Paper.

[106] Bihari, B., Gupta, S. B., Sekar, R. R., Gingrich, J., and Smith, J., "Development of advanced laser ignition system for stationary natural gas reciprocating engines," Proc. ASME 2005 Internal Combustion Engine Division Fall Technical Conference, American Society of Mechanical Engineers, pp. 601-608.

[107] Joshi, S., Yalin, A. P., and Galvanauskas, A., 2007, "Use of hollow core fibers, fiber lasers, and photonic crystal fibers for spark delivery and laser ignition in gases," Applied optics, 46(19), pp. 4057-4064.

[108] Yalin, A. P., 2013, "High power fiber delivery for laser ignition applications," Optics express, 21(106), pp. A1102-A1112.

[109] Tsunekane, M., Inohara, T., Ando, A., Kido, N., Kanehara, K., and Taira, T., 2010, "High Peak Power, Passively $ Q $-switched Microlaser for Ignition of Engines," IEEE Journal of Quantum Electronics, 46(2), pp. 277-284.

[110] Gupta, S. B., Bihari, B., Sekar, R., 2014, "Performance of a 6-cylinder natural gas engine on laser ignition," 2nd Laser Ignition Conference, pp. 22-25.

[111] Almansour, B., Vasu, S., Gupta, S. B., Wang, Q., Van Leeuwen, R., and Ghosh, C., 2017, "Prechamber Equipped Laser Ignition for Improved Performance in Natural Gas Engines," Journal of Engineering for Gas Turbines and Power, 139(10), p. 101501.

[112] Kroupa, G., Franz, G., and Winkelhofer, E., 2009, "Novel miniaturized high-energy Nd-YAG laser for spark ignition in internal combustion engines," Optical engineering, 48(1), pp. 014202-014202-014205.

[113] Myers, M. J., Myers, J. D., Guo, B., Yang, C., and Hardy, C. R., "Practical internal combustion engine laser spark plug development," Proc. Photonic Devices+ Applications, International Society for Optics and Photonics, pp. 66620E-66620E-66627.

[114] Griffiths, J., Lawrence, J., and Fitzsimons, P., 2013, "Effect of ignition location on the in-process removal of combustion deposits from the output window of a gas turbine laser ignition system," Optics & Laser Technology, 48, pp. 326-330.

[115] Ranner, H., Tewari, P. K., Kofler, H., Lackner, M., Wintner, E., Agarwal, A. K., and Winter, F., 2007, "Laser cleaning of optical windows in internal combustion engines," Optical Engineering, 46(10), pp. 104301-104301-104308.

[116] Alfier, A., Pasqualotto, R., Giudicotti, L., Cervaro, V., and Franchin, L., "Optimized in-situ window cleaning system by laser blow-off through optical fiber," Proc. Journal of Physics: Conference Series, IOP Publishing, p. 012036.

[117] Tahtouh, T., Halter, F., and Mounaïm-Rousselle, C., 2009, "Measurement of laminar burning speeds and Markstein lengths using a novel methodology," Combustion and Flame, 156(9), pp. 1735-1743.

[118] Miao, H., and Liu, Y., 2014, "Measuring the laminar burning velocity and Markstein length of premixed methane/nitrogen/air mixtures with the consideration of nonlinear stretch effects," Fuel, 121(0), pp. 208-215.

[119] Bradley, D., Gaskell, P., and Gu, X., 1996, "Burning velocities, Markstein lengths, and flame quenching for spherical methane-air flames: a computational study," Combustion and Flame, 104(1), pp. 176-198.

[120] Jayachandran, J., Zhao, R., and Egolfopoulos, F. N., 2014, "Determination of laminar flame speeds using stagnation and spherically expanding flames: Molecular transport and radiation effects," Combustion and Flame, 161(9), pp. 2305-2316.

[121] Wang, S.-F., Zhang, H., Jarosinski, J., Gorczakowski, A., and Podfilipski, J., 2010, "Laminar burning velocities and Markstein lengths of premixed methane/air flames near the lean flammability limit in microgravity," Combustion and Flame, 157(4), pp. 667-675.

[122] Ciprian, D., Marc, B., Andrew, B., Anthony, M., Azer, P. Y., Amir, M., and John, R., 2015, "Laser Ignition of Methane-Air Mixtures with a Rapid Compression Machine," 53rd AIAA Aerospace Sciences Meeting, American Institute of Aeronautics and Astronautics.

[123] Farrell, J. T., Johnston, R. J., and Androulakis, I. P., 2004, "Molecular Structure Effects On Laminar Burning Velocities At Elevated Temperature And Pressure," SAE Paper 2004-01-2936, p. 24.

[124] Metghalchi, M., and Keck, J. C., 1982, "Burning velocities of mixtures of air with methanol, isooctane, and indolene at high pressure and temperature," Combustion and flame, 48, pp. 191-210.

[125] Bradley, D., Hicks, R. A., Lawes, M., Sheppard, C. G. W., and Woolley, R., 1998, "The Measurement of Laminar Burning Velocities and Markstein Numbers for Iso-octane–Air and

Iso-octane–n-Heptane–Air Mixtures at Elevated Temperatures and Pressures in an Explosion Bomb," Combustion and Flame, 115(1–2), pp. 126-144.

[126] Srivastava, D. K., Weinrotter, M., Iskra, K., Agarwal, A. K., and Wintner, E., 2009, "Characterisation of laser ignition in hydrogen–air mixtures in a combustion bomb," international journal of hydrogen energy, 34(5), pp. 2475-2482.

[127] Duffy, J. E., 2000, Modern automotive technology, Goodheart-Willcox Company.

[128] Schwarz, J., Stoppel, K., Nübel, K., and Engelhardt, J., "Pumping concepts for laser spark plugs–requirements, options, solutions," Proc. OPIC 2nd Laser Ignition Conference, Yokohama, Japan, pp. 21-24.

[129] Van Leeuwen, R., Xu, B., Chen, T., Wang, Q., Seurin, J.-F., Xu, G., Zhou, D., and Ghosh, C., "VCSEL-pumped passively Q-switched monolithic solid-state lasers," Proc. SPIE LASE, International Society for Optics and Photonics, pp. 97260U-97260U-97266.

[130] Biruduganti, M., Gupta, S., Bihari, B., Kanehara, K., Polcyn, N., and Hwang, J., "Performance evaluation of a DENSO developed micro-laser ignition system on a natural gas research engine," Proc. Laser Ignition Conference, Optical Society of America, p. T5A. 4.

[131] Sjöberg, M., and Zeng, W., 2016, "Combined effects of fuel and dilution type on efficiency gains of lean well-mixed DISI engine operation with enhanced ignition and intake HEating for enabling mixed-mode combustion," SAE International Journal of Engines, 9(2016-01-0689), pp. 750-767.

[132] Roethlisberger, R., and Favrat, D., 2003, "Investigation of the prechamber geometrical configuration of a natural gas spark ignition engine for cogeneration: part II. Experimentation," International journal of thermal sciences, 42(3), pp. 239-253.

[133] Zhu, G. G., Daniels, C. F., and Winkelman, J., 2003, "MBT timing detection and its closed-loop control using in-cylinder pressure signal," No. 0148-7191, SAE Technical Paper.

[134] Kalghatgi, G. T., 1987, "Spark ignition, early flame development and cyclic variation in IC engines," No. 0148-7191, SAE Technical Paper.

[135] Ozdor, N., Dulger, M., and Sher, E., 1994, "Cyclic variability in spark ignition engines a literature survey," No. 0148-7191, SAE Technical Paper.

[136] Reyes, M., Tinaut, F., Giménez, B., and Pérez, A., 2015, "Characterization of cycle-to-cycle variations in a natural gas spark ignition engine," Fuel, 140, pp. 752-761.

[137] Ghorbani, A., Steinhilber, G., Markus, D., and Maas, U., 2015, "Ignition by transient hot turbulent jets: An investigation of ignition mechanisms by means of a PDF/REDIM method," Proceedings of the Combustion Institute, 35(2), pp. 2191-2198.

[138] Lewis, B., and Von Elbe, G., 2012, Combustion, flames and explosions of gases, Elsevier, UK.

[139] Turns, S. R., 1996, An introduction to combustion, McGraw-hill New York.

[140] Lieuwen, T. C., 2012, Unsteady Combustor Physics, Cambridge University Press.

[141] Metghalchi, M., 1976, "Laminar burning velocity of Isooctane-air, methane-air and methanol-air mixtures at high temperature and pressure,"Master's Thesis, Massachusetts Institute of Technology.

[142] Egolfopoulos, F. N., Hansen, N., Ju, Y., Kohse-Höinghaus, K., Law, C. K., and Qi, F., 2014, "Advances and challenges in laminar flame experiments and implications for combustion chemistry," Progress in Energy and Combustion Science, 43, pp. 36-67.

[143] Chen, Z., 2009, "Studies on the Initiation, Propagation, and Extinction of Premixed Flames,"Doctor of Philosophy Thesis, Princeton University.

[144] Jerzembeck, S., Peters, N., Pepiot-Desjardins, P., and Pitsch, H., 2009, "Laminar burning velocities at high pressure for primary reference fuels and gasoline: Experimental and numerical investigation," Combustion and Flame, 156(2), pp. 292-301.

[145] Johnston, R., and Farrell, J., 2005, "Laminar burning velocities and Markstein lengths of aromatics at elevated temperature and pressure," Proceedings of the combustion institute, 30(1), pp. 217-224.

[146] Xie, Y., Wang, J., Zhang, M., Gong, J., Jin, W., and Huang, Z., 2013, "Experimental and Numerical Study on Laminar Flame Characteristics of Methane Oxy-fuel Mixtures Highly Diluted with CO2," Energy & Fuels, 27(10), pp. 6231-6237.

[147] Chen, Z., Burke, M. P., and Ju, Y., 2009, "Effects of compression and stretch on the determination of laminar flame speeds using propagating spherical flames," Combustion Theory and Modelling, 13(2), pp. 343-364.

[148] De Persis, S., Foucher, F., Pillier, L., Osorio, V., and Gökalp, I., 2013, "Effects of O 2 enrichment and CO 2 dilution on laminar methane flames," Energy, 55, pp. 1055-1066.

[149] Miao, H., and Liu, Y., 2014, "Measuring the laminar burning velocity and Markstein length of premixed methane/nitrogen/air mixtures with the consideration of nonlinear stretch effects," Fuel, 121, pp. 208-215.

[150] Chen, Z., 2011, "On the extraction of laminar flame speed and Markstein length from outwardly propagating spherical flames," Combustion and Flame, 158(2), pp. 291-300.

[151] Khan, A., Anbusaravanan, S., Kalathi, L., Velamati, R., and Prathap, C., 2017, "Investigation of dilution effect with N 2/CO 2 on laminar burning velocity of premixed methane/oxygen mixtures using freely expanding spherical flames," Fuel, 196, pp. 225-232.

[152] Markstein, G. H., 2012, "Experimental and theoretical studies of flame-front stability," Journal of the Aeronautical Sciences.

[153] Ronney, P. D., and Sivashinsky, G. I., 1989, "A theoretical study of propagation and extinction of nonsteady spherical flame fronts," SIAM Journal on Applied Mathematics, 49(4), pp. 1029-1046.

[154] Kelley, A., and Law, C., 2009, "Nonlinear effects in the extraction of laminar flame speeds from expanding spherical flames," Combustion and Flame, 156(9), pp. 1844-1851.

[155] Kelley, A., Bechtold, J., and Law, C., "Propagation of confined premixed flames," Proc. 7th US National Technical Meeting of the Combustion Institute, pp. 1-24.

[156] Peters, N., 2000, Turbulent combustion, Cambridge university press.

[157] Parsinejad, F., Keck, J. C., and Metghalchi, H., 2007, "On the location of flame edge in Shadowgraph pictures of spherical flames: a theoretical and experimental study," Experiments in Fluids, 43(6), pp. 887-894.

[158] Fiock, E. F., Marvin Jr, C. F., Caldwell, F. R., and Roeder, C. H., 1940, "Flame speeds and energy considerations for explosions in a spherical bomb."

[159] O'Donovan, K., and Rallis, C. J., 1959, "A modified analysis for the determination of the burning velocity of a gas mixture in a spherical constant volume combustion vessel," Combustion and Flame, 3, pp. 201-214.

[160] Bradley, D., and Mitcheson, A., 1976, "Mathematical solutions for explosions in spherical vessels," Combustion and Flame, 26(0), pp. 201-217.

[161] Hill, P., and Hung, J., 1988, "Laminar burning velocities of stoichiometric mixtures of methane with propane and ethane additives," Combustion science and technology, 60(1-3), pp. 7-30.

[162] Rahim, F., Far, K. E., Parsinejad, F., Andrews, R. J., and Metghalchi, H., 2008, "A Thermodynamic Model to Calculate Burning Speed of Methane-Air-Diluent Mixtures," International Journal of Thermodynamics, 11(4), pp. 151-160.

[163] Elia, M., Ulinski, M., and Metghalchi, M., 2001, "Laminar burning velocity of methane–air–diluent mixtures," Journal of engineering for gas turbines and power, 123(1), pp. 190-196.

[164] Clarke, A., 1994, "Measurement of laminar burning velocity of air/fuel/diluent mixtures in zero gravity," University of Oxford.

[165] Omari, A., Shapiro, M., and Tartakovsky, L., 2015, "Laminar Burning Velocity of Alcohol Reforming Products and Effects of Cellularity on Flame Propagation," No. 0148-7191, SAE Technical Paper.

[166] Moghaddas, A., Eisazadeh-Far, K., and Metghalchi, H., 2012, "Laminar burning speed measurement of premixed n-decane/air mixtures using spherically expanding flames at high temperatures and pressures," Combustion and Flame, 159(4), pp. 1437-1443.

[167] Metghalchi, M., and Keck, J. C., 1980, "Laminar Burning Velocity of Propane-Air Mixtures at High Temperature and Pressure," Combust Flame, 38, pp. 143-154.

[168] Eisazadeh-Far, K., Moghaddas, A., Rahim, F., and Metghalchi, H., 2010, "Burning Speed and Entropy Production Calculation of a Transient Expanding Spherical Laminar Flame Using a Thermodynamic Model," Entropy, 12(12), pp. 2485-2496.

[169] David G. Goodwin, H. K. M., and Raymond L. Speth., 2016, "Cantera: An object- oriented software toolkit for chemical kinetics, thermodynamics, and transport processes.," http://www.cantera.org,.

[170] Luijten, C., Doosje, E., and de Goey, L., 2009, "Accurate analytical models for fractional pressure rise in constant volume combustion," International Journal of Thermal Sciences, 48(6), pp. 1213-1222.

[171] Luijten, C., Doosje, E., Van Oijen, J., and de Goey, L., 2009, "Impact of dissociation and end pressure on determination of laminar burning velocities in constant volume combustion," International Journal of Thermal Sciences, 48(6), pp. 1206-1212.

[172] Askari, O., Vien, K., Wang, Z., Sirio, M., and Metghalchi, H., 2016, "Exhaust gas recirculation effects on flame structure and laminar burning speeds of H 2/CO/air flames at high pressures and temperatures," Applied Energy, 179, pp. 451-462.

[173] Askari, O., Moghaddas, A., Alholm, A., Vien, K., Alhazmi, B., and Metghalchi, H., 2016, "Laminar burning speed measurement and flame instability study of H 2/CO/air mixtures at high temperatures and pressures using a novel multi-shell model," Combustion and Flame, 168, pp. 20-31.

[174] Garcia, D., 2010, "Robust smoothing of gridded data in one and higher dimensions with missing values," Computational statistics & data analysis, 54(4), pp. 1167-1178.

[175] Askari, O., Wang, Z., Vien, K., Sirio, M., and Metghalchi, H., 2017, "On the flame stability and laminar burning speeds of syngas/O 2/He premixed flame," Fuel, 190, pp. 90-103.

[176] Spadaccini, L., and Colket, M., 1994, "Ignition delay characteristics of methane fuels," Progress in Energy and Combustion Science, 20(5), pp. 431-460.

[177] Frenklach, M., and Bornside, D. E., 1984, "Shock-initiated ignition in methane-propane mixtures," Combustion and flame, 56(1), pp. 1-27.

[178] Petersen, E. L., Davidson, D. F., and Hanson, R. K., 1999, "Ignition delay times of Ram accelerator CH/O/diluent mixtures," Journal of Propulsion and Power, 15(1), pp. 82-91.

[179] Li, Y., Zhou, C.-W., Somers, K. P., Zhang, K., and Curran, H. J., 2017, "The oxidation of 2-butene: A high pressure ignition delay, kinetic modeling study and reactivity comparison with isobutene and 1-butene," Proceedings of the Combustion Institute, 36(1), pp. 403-411.

[180] Kwon, O., Rozenchan, G., and Law, C., 2002, "Cellular instabilities and self-acceleration of outwardly propagating spherical flames," Proceedings of the combustion Institute, 29(2), pp. 1775-1783.

[181] Jomaas, G., Law, C., and Bechtold, J., 2007, "On transition to cellularity in expanding spherical flames," Journal of fluid mechanics, 583, pp. 1-26.

[182] Barari, G., Pryor, O., Koroglu, B., Sarathy, S. M., Masunov, A. E., and Vasu, S. S., 2017, "High temperature shock tube experiments and kinetic modeling study of diisopropyl ketone ignition and pyrolysis," Combustion and Flame, 177, pp. 207-218.

[183] Pryor, O., Barari, G., Koroglu, B., Lopez, J., Nash, L., and Vasu, S., "Shock Tube Ignition Studies of Advanced Biofuels," Proc. 52nd AIAA/SAE/ASEE Joint Propulsion Conference, p. 4691.

[184] Barari, G., Sarathy, S. M., and Vasu, S. S., 2016, "Improved combustion kinetic model and HCCI engine simulations of di-isopropyl ketone ignition," Fuel, 164, pp. 141-150.

[185] Hu, E., Jiang, X., Huang, Z., and Iida, N., 2012, "Numerical study on the effects of diluents on the laminar burning velocity of methane–air mixtures," Energy & Fuels, 26(7), pp. 4242-4252.

[186] Galmiche, B., Halter, F., Foucher, F., and Dagaut, P., 2011, "Effects of dilution on laminar burning velocity of premixed methane/air flames," Energy & Fuels, 25(3), pp. 948-954.

[187] Zhu, D., Egolfopoulos, F., and Law, C., "Experimental and numerical determination of laminar flame speeds of methane/(Ar, N2, CO2)-air mixtures as function of stoichiometry, pressure, and flame temperature," Proc. Symposium (International) on Combustion, Elsevier, pp. 1537-1545.

[188] Rozenchan, G., Zhu, D. L., Law, C. K., and Tse, S. D., 2002, "Outward propagation, burning velocities, and chemical effects of methane flames up to 60 Atm," Proc. Combust. Inst., 29, pp. 1461-1470.

[189] Eisazadeh-Far, K., Moghaddas, A., Metghalchi, H., and Keck, J. C., 2011, "The effect of diluent on flame structure and laminar burning speeds of JP-8/oxidizer/diluent premixed flames," Fuel, 90(4), pp. 1476-1486.

[190] Curran, H. J., Gaffuri, P., Pitz, W. J., and Westbrook, C. K., 2002, "A comprehensive modeling study of iso-octane oxidation," combustion and flame, 129(3), pp. 253-280.

[191] Blanquart, G., Pepiot-Desjardins, P., and Pitsch, H., 2009, "Chemical mechanism for high temperature combustion of engine relevant fuels with emphasis on soot precursors," Combustion and Flame, 156(3), pp. 588-607.

[192] Chaos, M., Kazakov, A., Zhao, Z., and Dryer, F. L., 2007, "A high-temperature chemical kinetic model for primary reference fuels," International Journal of Chemical Kinetics, 39(7), pp. 399-414.

[193] Li, Q., Fu, J., Wu, X., Tang, C., and Huang, Z., 2012, "Laminar flame speeds of DMF/iso-octane-air-N2/CO2 mixtures," Energy & Fuels, 26(2), pp. 917-925.

[194] Broustail, G., Seers, P., Halter, F., Moréac, G., and Mounaïm-Rousselle, C., 2011, "Experimental determination of laminar burning velocity for butanol and ethanol iso-octane blends," Fuel, 90(1), pp. 1-6.

[195] USA, K., "Piezoelectric Pressure Sensor," http://www.kistler.com/us/en/.

[196] Corporation, N. I., "NI PCI-6259," http://sine.ni.com/nips/cds/view/p/lang/en/nid/14128.

[197] Pires, J. C. M., Martins, F. G., Alvim-Ferraz, M. C. M., and Simões, M., 2011, "Recent developments on carbon capture and storage: An overview," Chemical Engineering Research and Design, 89(9), pp. 1446-1460.

[198] Dostal, V., Hejzlar, P., and Drscoll, M. J., 2006, The supercritical carbon dioxide power cycle : Comparison to other advanced power cycles, American Nuclear Society, La Grange Park, IL, ETATS-UNIS.

[199] Gibbins, J., and Chalmers, H., 2008, "Carbon capture and storage," Energy Policy, 36(12), pp. 4317-4322.

[200] Hu, X., Yu, Q., Liu, J., and Sun, N., 2014, "Investigation of laminar flame speeds of CH4/O2/CO2 mixtures at ordinary pressure and kinetic simulation," Energy, 70, pp. 626-634.

[201] Konnov, A. A., and Dyakov, I. V., 2005, "Measurement of propagation speeds in adiabatic cellular premixed flames of CH4+O2+CO2," Experimental Thermal and Fluid Science, 29(8), pp. 901-907.

[202] Mazas, A. N., Lacoste, D. A., and Schuller, T., 2010, "Experimental and Numerical Investigation on the Laminar Flame Speed of CH4/O2 Mixtures Diluted With CO2 and H2O," Proc. of ASME Turbo Expo, Paper No. GT2010-22512, pp. 411-421.

[203] Heil, P., Toporov, D., Förster, M., and Kneer, R., 2011, "Experimental investigation on the effect of O2 and CO2 on burning rates during oxyfuel combustion of methane," Proceedings of the Combustion Institute, 33(2), pp. 3407-3413.

[204] Liu, F., Guo, H., and Smallwood, G. J., 2003, "The chemical effect of CO2 replacement of N2 in air on the burning velocity of CH4 and H2 premixed flames," Combustion and Flame, 133(4), pp. 495-497.

[205] Di Benedetto, A., Cammarota, F., Di Sarli, V., Salzano, E., and Russo, G., 2012, "Reconsidering the flammability diagram for CH4/O2/N2 and CH4/O2/CO2 mixtures in light of combustion-induced Rapid Phase Transition," Chemical Engineering Science, 84, pp. 142-147.

[206] de Persis, S., Foucher, F., Pillier, L., Osorio, V., and Gökalp, I., 2013, "Effects of O2 enrichment and CO2 dilution on laminar methane flames," Energy, 55, pp. 1055-1066.

[207] Dinçer, İ., and Zamfirescu, C., 2014, Advanced Power Generation Systems, Elsevier Science, UK.

[208] Gupta, H. N., 2012, Fundamentals of internal combustion engines, PHI Learning Pvt. Ltd.

[209] Vasu, S. S., Davidson, D. F., and Hanso, R. K., 2011, "Shock Tube Study of Syngas Ignition in Rich CO2 Mixtures and Determination of the Rate of H + O2 + CO2 -> HO2 + CO2," Energy and Fuels, 25, pp. 990-997.

[210] Srivastava, D. K., Wintner, E., and Agarwal, A. K., 2014, "Effect of laser pulse energy on the laser ignition of compressed natural gas fueled engine," Optical Engineering, 53(5), pp. 056120-056120.

[211] Bo¨ker, D., and Bru¨ggemann, D., 2011, "Advancing lean combustion of hydrogeneair mixtures by laser-induced spark ignition," Int. J. Hydrogen Energy, 36, pp. 14759-14767.

[212] Liang, W., Chen, Z., Yang, F., and Zhang, H., 2013, "Effects of Soret diffusion on the laminar flame speed and Markstein length of syngas/air mixtures," Proceedings of the Combustion Institute, 34(1), pp. 695-702.

[213] Xin, Y., Sung, C.-J., and Law, C. K., 2012, "A mechanistic evaluation of Soret diffusion in heptane/air flames," Combustion and Flame, 159(7), pp. 2345-2351.

[214] Yang, F., Law, C. K., Sung, C. J., and Zhang, H. Q., 2010, "A mechanistic study of Soret diffusion in hydrogen–air flames," Combustion and Flame, 157(1), pp. 192-200.

[215] Yang, F., Zhang, H. Q., and Wang, X. L., 2011, "Effects of soret diffusion on the laminar flame speed of n-butane-air mixtures," Proceedings of the Combustion Institute, 33(1), pp. 947-953.

[216] Baulch, D. L., Bowman, C. T., Cobos, C. J., Cox, R. A., Just, T., Kerr, J. A., Pilling, M. J., Stocker, D., Troe, J., Tsang, W., Walker, R. W., and Warnatz, J., 2005, J. Phys. Chem. Ref. Data, 34, p. 757.

[217] Goos, E., Burcat, A., and Ruscic, B., 2011, "EXTENDED THIRD MILLENIUM IDEAL GAS AND CONDENSED PHASE THERMOCHEMICAL DATABASE FOR COMBUSTION

WITH UPDATES FROM ACTIVE THERMOCHEMICAL TABLES,"
http://garfield.chem.elte.hu/Burcat/THERM.DAT.

[218] Baulch, D. L., Cobos, C. J., Cox, R. A., Esser, C., Frank, P., Just, T., Kerr, J. A., Pilling, M. J., Troe, J., Walker, R. W., and Warnatz, J., 1992, J. Phys. Chem. Ref. Data, 21, p. 411.

[219] Colberg, M., and Friedrichs, G., 2005, "Room Temperature and Shock Tube Study of the Reaction HCO + O2 Using the Photolysis of Glyoxal as an Efficient HCO Source," The Journal of Physical Chemistry A, 110(1), pp. 160-170.

[220] Krasnoperov, L. N., and Michael, J. V., 2004, "Shock Tube Studies Using a Novel Multipass Absorption Cell: Rate Constant Results For OH + H2 and OH + C2H6," The Journal of Physical Chemistry A, 108(26), pp. 5643-5648.

[221] Nadezhda, S., and Oskar, H., 2011, "Kinetic Mechanism For Low Pressure Oxygen / Methane Ignition and Combustion," 49th AIAA Aerospace Sciences Meeting including the New Horizons Forum and Aerospace Exposition, American Institute of Aeronautics and Astronautics.